UNIVERSITY OF OKLAHOMA

GRADUATE COLLEGE

THE EFFECT OF LIGAND DENTICITY IN STABILIZING ACTINIDE-ELEMENT MULTIPLE BOND FUNCTIONALITIES

A DISSERTATION

SUBMITTED TO THE GRADUATE FACULTY

in partial fulfillment of the requirements for the

Degree of

DOCTOR OF PHILOSOPHY

By

BRIAN C. STOBBE
Norman, Oklahoma
2017

Downloaded from SHAREOK. Persistent Handle URL: https://hdl.handle.net/11244/51947

THE EFFECT OF LIGAND DENTICITY IN STABILIZING ACTINIDE-ELEMENT MULTIPLE BOND FUNCTIONALITIES

A DISSERTATION APPROVED FOR THE
DEPARTMENT OF CHEMISTRY AND BIOCHEMISTRY

BY

_____
Dr. Robert Thomson, Chair

_____
Dr. Lloyd Bumm

_____
Dr. Kenneth Nicholas

_____
Dr. Ronald Halterman

_____
Dr. Charles Rice

© Copyright by BRIAN C. STOBBE 2017
All Rights Reserved.

For my grandfather, Marco Rodriguez, a man of science.

Acknowledgements

I would like to thank the University of Oklahoma and the Department of Chemistry and Biochemistry for allowing me to pursue my Ph.D. studies. Additionally, I would like to formally thank the members of my committee: Dr. Halterman, Dr. Nicholas, Dr. Rice and Dr. Bumm for their guidance and assistance with my development as a scientist.

Importantly, I would like to thank my research advisor, Dr. Robert K. Thomson, for giving me the opportunity to pursue my Ph.D. research in his lab. I am eternally grateful for his guidance and continued support, for without it, I would not have been nearly as successful in my endeavors. Additionally, I would like to thank Dr. Thomson for helping me to develop not only my laboratory research skills, but my presentation skills as they will be extremely useful to me in the future. Again, I am extremely grateful for all of the assistance and guidance provided to me by Dr. Thomson.

I also would like to thank the members of the Thomson Lab – both past and present – for their friendship and fruitful research discussions and for helping to push me to become the best chemist I can be.

I am eternally grateful to my parents, Andy and Yoky Stobbe, for their continued support, as well as their encouragement to keep pushing on even when times were tough. On this note, words cannot express my gratitude for the support, encouragement, and advice my fiancé, Tiffany, has provided me with, as it is because of this support that I have been successful thus far.

Table of Contents

Acknowledgements iv

List of Tables xi

List of Figures xiii

List of Schemes xix

Abbreviations xxii

Abstract xxv

Chapter 1 Introduction 1

1.1: U.S. energy demands and the search for a more sustainable fuel source 2

1.2: Concerns with nuclear energy as a long-term, sustainable fuel source 5

1.2.1: Public opinion and economic concerns with nuclear energy .. 5

1.2.2: Concerns with radioactive nuclear waste 6

1.2.3: Management of high level radioactive waste and funding initiatives for actinide science 8

1.3: Important breakthroughs in fundamental actinide science 10

1.3.1: Understanding the inverse trans influence (ITI) 10

1.3.2: Prior research into the inverse trans influence (ITI) 13

1.3.3: Understanding methods of quantifying actinide covalency .. 14

1.4: Project goals 16

1.5: References 18

Chapter 2 Synthesis and characterization of uranium(IV) & thorium(IV) tris(trimethylsilyl(anilido)) complexes: Divergent chemistry influenced by alkali metal salt identity 23

2.1: Background 24

2.2: Stabilization of U(IV) complexes using amido ligands 27

2.3: Synthesis and characterization of chloro tris(anilido) uranium complexes 36

2.4: Synthesis and characterization of bromo anilido uranium complexes 43

2.5: Attempts to generate (F)U[N(SiMe$_3$)(3,5-(CH$_3$)$_2$(C$_6$H$_3$)]$_3$ 56

2.6: Synthesis of Th[N(SiMe$_3$)(3,5-(CH$_3$)$_2$)(C$_6$H$_3$)]$_4$ 63

2.7: Analysis of ^{1}H NMR chemical shift trends for the [L]$_3$U(X) series ... 70

2.8: Attempts to generate uranium-element multiple bonds using halo tris(anilido) uranium platform 73

2.9: Concluding remarks 89

2.10: Experimental 92

2.10.1: General experimental procedures 92

2.10.2: Synthesis of [K][N(SiMe$_3$)(3,5-(CH$_3$)$_2$(C$_6$H$_3$)] 93

2.10.3: Synthesis of $[L]_3U(I)$ (2.1) from [Li][N(Si(CH_3)$_3$)(3,5-dimethylphenyl)] 94

2.10.4: Synthesis of $[Li(Cl)(THF)_2][[L]_3U(Cl)]$ (2.2) 94

2.10.5: Synthesis of $[L]_3U(Cl)$ (2.3) 95

2.10.6: Synthesis of $[L]_3U(Br)$ (2.4) 95

2.10.7: Synthesis of $[L]_2U(Br)(\mu\text{-}Br)_3U(Br)[L]_2$ (2.5) 96

2.10.8: Synthesis of $[L]_4U$ from K[L] (2.6) 96

2.10.9: Synthesis of $[L]_4Th$ (2.7) 97

2.10.10: Synthesis of $[L]_3U(THF)$ (2.8) via reduction pathway 97

2.10.11: Synthesis of $[L]_3U(THF)$ (2.8) from K[L] 98

2.11: References 98

Chapter 3 An unexpected alkylation: Redox non-innocent ligand reactivity of a bis(amido)pyridine uranium complex 107

3.1: Exploring the use of a new ligand framework 108

3.2: An unexpected alkylation resulting in [BDPP']U($CH_2Ph)_2$ 109

3.3: Rational synthesis of [K][BDPP′]U($CH_2Ph)_2$ from [BDPP]U($CH_2Ph)_2$ 115

3.4: Attempts at elucidating a mechanism for the observed alkylation. 118

3.5: Scope of nucleophilicity 121

3.6: Concluding Remarks 127

3.7: Experimental 128

3.7.1: General experimental procedures 128

3.7.2: Synthesis of K[BDPP']U($CH_2(C_6H_5)$)$_2$ (3.1) from U(CH_2Ph)$_4$ 129

3.7.3: Synthesis of [K][BDPP']U(CH_2Ph)$_2$ (3.1) from [BDPP]U(CH_2Ph)$_2$ 130

3.7.4: Synthesis of [BDPP]U($CD_2C_6D_5$)$_2$ 130

3.7.5: Synthesis of K[BDPP']U($CD_2C_6D_5$)$_2$ 131

3.8: References 131

Chapter 4 A new hope for generating An=E functionalities: Synthesis, characterization and reactivity of Th(IV) and U(IV) dichloro Schiff base complexes 136

4.1: Background 137

4.2: Synthesis and characterization of [L]An(Cl)$_2$($Solv$)$_2$ complexes 140

4.3: Salt metathesis reactivity of the [L]An(Cl)$_2$($Solv$)$_2$ complexes with NaN_3 149

4.4: Salt metathesis reactivity of [L]An(Cl)$_2$($Solv$)$_2$ complexes with carbon nucleophiles 158

4.5: σ-Bond metathesis reactivity of [L]An(Cl)$_2$(Solv)$_2$ complexes with Me$_3$Si-Br 174

4.6: Attempts at generating [L]An=E functionalities via oxidative pathways 183

4.7: Concluding remarks 197

4.8: Experimental 200

4.8.1: General Experimental Procedures 200

4.8.2: Synthesis of (L)UCl$_2$(THF)$_2$ (4.1) 201

4.8.3: Synthesis of (L)UCl$_2$(Py)$_2$ (4.1-(Py)) 202

4.8.4: Synthesis of (L)ThCl$_2$(THF)$_2$ (4.2) 203

4.8.5: Synthesis of (L)U(N$_3$)$_2$(Py)$_2$ (4.3) 204

4.8.6 Synthesis of (L)Th(N$_3$)$_2$(Py)$_2$ (4.4) 205

4.8.7: Synthesis of [L]U(Cp*)(Cl)(1,4-dioxane) (4.5) 206

4.8.8: Synthesis of [L]U(Cp)$_2$(1,4-dioxane) (4.6) 207

4.8.9: Synthesis of [L]Th(Cp)$_2$(1,4-dioxane) (4.7) 207

4.8.10: Synthesis of [L]U(Br)$_2$(Py)$_2$ (4.8) 208

4.8.11: Synthesis of [L]Th(Br)$_2$(Py)$_2$ (4.9) 209

4.8.12: Synthesis of [L]U(I)$_2$(THF)$_2$ (4.10) 209

4.8.13: Synthesis of (L)UO$_2$(Py) (4.11) 210

4.9: References 211

Appendix A X-ray diffraction data for complexes described in Chapter 2..... 219

Appendix B X-ray diffraction data for complex described in Chapter 3..... 226

Appendix C X-ray diffraction data for complexes described in Chapter 4..... 228

List of Tables

Table 2-1: Selected bond distances (Å) and angles (°) for **2.1** 32

Table 2-2: Bond distances (Å) for U(1)-N and U(1)-C(aryl) interactions for **2.1** 34

Table 2-3: Comparison of ^{1}H NMR chemical shifts (ppm) of complex **2.1** and IU[N(^{t}Bu)(3,5-$Me_2C_6H_3$)]$_3$ 35

Table 2-4: Table of selected bond distances (Å) and angles (°) for **2.2** 38

Table 2-5: Comparison of ^{1}H NMR chemical shifts (ppm) for **2.1** and **2.2**..... 40

Table 2-6: Selected bond distances (Å) for **2.5**..... 47

Table 2-7: Selected bond angles (°) for **2.5** 48

Table 2-8: Selected bond distances (Å) for hapticity analysis for **2.5**..... 50

Table 2-9: Selected bond lengths (Å) and angles (°) for **2.6** 62

Table 2-10: Selected bond lengths (Å) and angles (°) for **2.7** 66

Table 2-11: Comparison of ^{1}H NMR chemical shifts (ppm) for complexes **2.1**, **2.3**, **2.4** and **2.6** 71

Table 2-12: Selected bond distances (Å) and angles (°) for **2.8**..... 77

Table 2-13: Selected bond distances (Å) for hapticity analysis for **2.8**..... 77

Table 3-1: Selected bond distances (Å) and angles (°) for **3.1** 111

Table 4-1: Selected bond distances (Å) for **4.1-(Py)** and **4.2-(Py)** 142

Table 4-2: Selected bond angles (°) for **4.1-(Py)** and **4.2-(Py)** 143

Table 4-3: Selected bond lengths (Å) for **4.3-Endo** and **4.3-Exo**..... 152

Table 4-4: Selected bond angles (°) for **4.3-Endo** and **4.3-Exo**..... 152

Table 4-5: Selected bond lengths (Å) and angles (°) for **4.5** 162

Table 4-6: Selected bond lengths (Å) and angles (°) for **4.6** 165

Table 4-7: Selected bond lengths (Å) and angles (°) for **4.7** 170

Table 4-8: Selected bond lengths (Å) and angles (°) for **4.8** 175

Table 4-9: Selected bond lengths (Å) and angles (°) for **4.11** 186

Table A-1: X-ray diffraction data for $L_3U(I)$ (**2.1**) 220

Table A-2: X-ray diffraction data for $[Li(Cl)(THF)_2][L_3U(Cl)]$ (**2.2**) 221

Table A-3: X-ray diffraction data for $L_2U(Br)(\mu\text{-}Br)_3U(Br)L_2$ (**2.5**) 222

Table A-4: X-ray diffraction data for $U[L]_4$ (**2.6**) 223

Table A-5: X-ray diffraction data for $Th[L]_4$ (**2.7**) 224

Table A-6: X-ray diffraction data for $[L]_3U(THF)$ (**2.8**) 225

Table B-1: X-ray diffraction data for $[K][BDPP']U(CH_2Ph)_2$ (**3.1**) 227

Table C-1: X-ray diffraction data for $(L)UCl_2(Py)_2$ (**4.1-(Py)**) 229

Table C-2: X-ray diffraction data for $(L)ThCl_2(Py)_2$ (**4.2-(Py)**) 230

Table C-3: X-ray diffraction data for endo-$(L)U(N_3)_2(Py)_2$ (**4.3-Endo**) 231

Table C-4: X-ray diffraction data for exo-$(L)U(N_3)_2(Py)_2$ (**4.3-Exo**) 232

Table C-5: X-ray diffraction data for (L)U(Cp*)(Cl)(1,4-dioxane) (**4.5**) 233

Table C-6: X-ray diffraction data for $(L)U(Cp)_2$(1,4-dioxane) (**4.6**) 234

Table C-7: X-ray diffraction data for $(L)Th(Cp)_2$(1,4-dioxane) (**4.7**) 235

Table C-8: X-ray diffraction data for $(L)U(Br)_2(Py)_2$ (**4.8**) 236

Table C-9: X-ray diffraction data for $(L)U(O)_2(Py)$ (**4.11**) 237

Table C-10: X-ray diffraction data for $(L)U(Cl)(N_3)_2(Py)_2$ (**4.12**) 238

List of Figures

Figure 1-1: Contribution of various energy sources (%) to U.S energy consumption in 2016 2

Figure 1-2: Simplified depiction of U-235 undergoing nuclear fission. 4

Figure 1-3: Explaining the origin of the inverse trans influence (ITI)..... 12

Figure 2-1: Target actinide complexes for studying the ITI..... 26

Figure 2-2: Structure of $U[N(SiMe_3)_2]_3$ 27

Figure 2-3: Space filling model of $U[N(SiMe_3)_2]_3$ 29

Figure 2-4: Targeted anilido type complexes..... 30

Figure 2-5: ORTEP Depiction of $(I)U[N(SiMe_3)\{3,5\text{-}(CH_3)_2(C_6H_3)]$ (**2.1**) with elliposoids shown at 50% probability. Hydrogen atoms omitted for clarity. 31

Figure 2-6: 300 MHz ^1H NMR Spectrum of $(I)U[N(SiMe_3)(3,5\text{-}(CH_3)_2(C_6H_3)]_3$ (**2.1**) in C_6D_6..... 35

Figure 2-7: ORTEP Depiction of $[(THF)(Et_2O)LiCl][\ (Cl)U[N(SiMe_3)(3,5\text{-}(CH_3)_2(C_6H_3)]_3$ (**2.2**) with ellipsoids shown at 30% probability. Hydrogen atoms and aryl-CH_3s omitted for clarity. 37

Figure 2-8: 300 MHz ^1H NMR spectrum of $(THF)_2[LiCl]\bullet$ $[(Cl)U[N(SiMe_3)(3,5\text{-}(CH_3)_2(C_6H_3)]_3$ (**2.2**) in C_6D_6..... 40

Figure 2-9: 300 MHz ^1H NMR Spectrum of $(Cl)U[N(SiMe_3)(3,5\text{-}(CH_3)_2(C_6H_3)]_3$ (**2.3**) in C_6D_6 42

Figure 2-10: 300 MHz ^1H NMR spectrum of $(Br)U[N(SiMe_3)(3,5\text{-}(CH_3)_2(C_6H_3)]_3$ **2.4** in C_6D_6..... 44

Figure 2-11: ORTEP depiction of $[L]_2U(\mu(\eta^1:\eta^1)Br)_2(\mu(\eta^1:\eta^1:\eta^1)BrLi(THF)_2)U[L]_2$ (**2.5**) shown at 30% probability. Hydrogen atoms and aryl-CH_3s removed for clarity. 47

Figure 2-12: Hetero trimetallic core of complex **2.5** 49

Figure 2-13: 300 MHz ^{1}H NMR spectrum of isolated products from reaction of **2.2** with excess Me_3Si-Br in C_6D_6. The major product (**2.5**) is shown inset. 52

Figure 2-14: Possible mechanism for the formation of complex **2.5** 53

Figure 2-15: ORTEP depiction of $U[N(SiMe_3)(3,5\text{-}(CH_3)_2(C_6H_3)]_4$ complex (**2.6**) with ellipsoids shown at 30% probability. Aryl-CH_3s and hydrogen atoms removed for clarity. 61

Figure 2-16: 300 MHz ^{1}H NMR spectrum of $U[N(SiMe_3)(3,5\text{-}(CH_3)_2)(C_6H_3)]_4$ (**2.6**) in C_6D_6 63

Figure 2-17: ORTEP depiction of $Th[N(SiMe_3)(3,5\text{-}(CH_3)_2)(C_6H_3)]_4$ (**2.7**) with ellipsoids shown at 30% probability. Aryl-CH_3s and hydrogen atoms removed for clarity. 66

Figure 2-18: 400 MHz ^{1}H NMR spectrum of $Th[N(SiMe_3)(3,5\text{-}(CH_3)_2)(C_6H_3)]_4$ (**2.7**) in C_6D_6 68

Figure 2-19: 400 MHz ^{13}C NMR spectrum of $Th[N(SiMe_3)(3,5\text{-}(CH_3)_2)(C_6H_3)]_4$ complex (**2.7**) in C_6D_6 69

Figure 2-20: Correlation between halogen electronegativity (X_p) and the ^{1}H NMR chemical shift (ppm) of selected protons. 72

Figure 2-21: ORTEP Depiction of $(THF)U[N(SiMe_3)(3,5\text{-}(CH_3)_2)(C_6H_3)]_3$ (**2.8**) with ellipsoids shown at 50% probability. Hydrogen atoms omitted for clarity. . 76

Figure 2-22: Comparison of the space-filling models of complex **2.8** and Andersen's tris(amido) complex U[N(Si(Me$_3$)$_2$)]$_3$ 79

Figure 2-23: 300 MHz ^{1}H NMR spectrum of (THF)U[N(SiMe$_3$)(3,5-(CH$_3$)$_2$)(C$_6$H$_3$)]$_3$ (**2.8**) generated by salt metathesis from UI$_3$(dioxane)$_{1.5}$ in C$_6$D$_6$ 80

Figure 2-24: ORTEP depiction of Mes*P=PMes* dimer isolated from Path 2 with ellipsoids shown at 30% probability. Hydrogen atoms omitted for clarity. 84

Figure 2-25: Phosphaindole byproduct generated from Path 3 (Scheme 2-14) 86

Figure 2-26: 300 MHz ^{1}H NMR spectrum of K[N(SiMe$_3$)(3,5-(CH$_3$)$_2$(C$_6$H$_3$)] in C$_6$D$_6$ 93

Figure 3-1: Structural comparison between the BDPP ligand framework and the core of the structurally-similar BIP ligand. 109

Figure 3-2: ORTEP depiction of [K]([BDPP']U(CH$_2$Ph)$_2$) (**3.1**) with ellipsoids shown at 30% probability. 2,6-diisopropyl groups and most hydrogen atoms removed for clarity. 111

Figure 3-3: Crystal packing depiction of **3.1** illustrating intermolecular interactions between K$^+$ ions and benzyl ligands. η^4-benzyl ligands displayed in orange, η^1-benzyl ligands displayed in brown and pyridine alkylated benzyl groups shown in red. Hydrogen atoms and BDPP aryl groups omitted for clarity. 114

Figure 3-4: 300 MHz ^{1}H NMR spectrum of complex **3.1** in C$_6$D$_6$ at 298 K..... 115

Figure 3-5: Stacked 300 MHz ^{1}H NMR spectra of [BDPP]Zr(NMe_2)$_2$ (top, blue) and possible alkylation product [BDPP´]Zr(NMe_2)$_2$ (bottom, red) in C_6D_6 at 298 K 125

Figure 3-6: Stacked 300 MHz ^{1}H NMR spectra of [BDPP]Zr(NMe_2)$_2$ (top, blue) and the attempted alkylation product [BDPP-O^{t}Bu]Zr(NMe_2)$_2$ (bottom, red) in C_6D_6 at 298 K 127

Figure 4-1: Highlighted κ^4 bonding motif of the Schiff base ligand (salen)..... 138

Figure 4-2: ORTEP depiction of [L]U(Cl)$_2$(Py)$_2$ (**4.1-(Py)**) (left) and [L]Th(Cl)$_2$(Py)$_2$ (**4.2-(Py)**, right) with ellipsoids shown at 50% probability. Hydrogen atoms omitted for clarity. 142

Figure 4-3: 300 MHz ^{1}H NMR spectrum of [L]U(Cl)$_2$(THF)$_2$ (**4.1**) in $CDCl_3$ at 298 K 145

Figure 4-4: 400 MHz ^{1}H NMR spectrum of [L]U(Cl)$_2$(Py)$_2$ **4.1-(Py)** in $CDCl_3$ at 298 K 146

Figure 4-5: 300 MHz ^{1}H NMR spectrum of complex **4.2-(Py)** in $CDCl_3$ at 298 K 147

Figure 4-6: 400 MHz ^{1}H NMR spectrum of [L]Th(Cl)$_2$(Py)$_2$ **4.2-(Py)** in D_5-pyridine at 298 K 148

Figure 4-7: 100 MHz ^{13}C NMR spectrum of [L]Th(Cl)$_2$(Py)$_2$ (**4.2-(Py)**) in D_5-pyridine at 298 K 149

Figure 4-8: Solid-state structures of endo and exo conformers of complex **4.3**, with ellipsoids shown at 50% probability. Hydrogen atoms omitted for clarity. 151

Figure 4-9: 300 MHz ^{1}H NMR spectrum of [L]U$(N_3)_2(Py)_2$ (**4.3)** (bulk material) in $CDCl_3$ at 298 K 155

Figure 4-10: 400 MHz ^{1}H NMR spectrum of [L]Th$(N_3)_2(Py)_2$ (**4.4**) in $CDCl_3$ at 298 K 156

Figure 4-11: 400 MHz ^{1}H NMR spectrum of [L]Th$(N_3)_2(Py)_2$ (**4.4**) in D_5-pyridine at 298 K 157

Figure 4-12: 100 MHz ^{13}C NMR spectrum of [L]Th$(N_3)_2(Py)_2$ (**4.4**) in D_5-pyridine at 298 K 158

Figure 4-13: ORTEP depiction of [L]U(Cp*)(Cl)(1,4-dioxane) (**4.5**) with ellipsoids shown at 50% probability. Hydrogen atoms omitted for clarity. 161

Figure 4-14: 300 MHz ^{1}H NMR spectrum of complex **4.5** in C_6D_6 at 298 K ... 163

Figure 4-15: ORTEP depiction of [L]U$(Cp)_2$(1,4-dioxane) (**4.6**) with ellipsoids shown at 30% probability. Hydrogen atoms and cocrystallized 1,4-dioxane removed for clarity. 165

Figure 4-16: 300 MHz ^{1}H NMR spectrum of the linear uranium metallocene (**4.6**) in C_6D_6 at 298 K 168

Figure 4-17: ORTEP depiction of [L]Th$(Cp)_2$(1,4-dioxane) (**4.7**) with ellipsoids shown at 30% probability. Hydrogen atoms and 2 cocrystallized 1,4-dioxane molecules removed for clarity. 169

Figure 4-18: 400 MHz ^{1}H NMR spectrum of [L]Th$(Cp)_2$(1,4-dioxane) (**4.7**) spiked with excess 1,4-dioxane in C_6D_6 at 298 K 172

Figure 4-19: 100 MHz ^{13}C NMR spectrum of [L]Th$(Cp)_2$(1,4-dioxane) (**4.7**) in D_5-pyridine at 298 K 173

Figure 4-20: ORTEP depiction of [L]U(Br)$_2$(Py)$_2$ (**4.8**) and [L]Th(Br)$_2$(Py)$_2$ (**4.9**) with ellipsoids shown at 50% probability. Hydrogen atoms omitted for clarity. 175

Figure 4-21: 300 MHz ^{1}H NMR spectrum of [L]U(Br)$_2$(Py)$_2$ (**4.8**) in $CDCl_3$ at 298 K 177

Figure 4-22: 400 MHz ^{1}H NMR spectrum of [L]Th(Br)$_2$(Py)$_2$ (**4.9**) in $CDCl_3$ at 298 K 178

Figure 4-23: 100 MHz ^{13}C NMR spectrum of [L]Th(Br)$_2$(Py)$_2$ (**4.9**) in $CDCl_3$ at 298 K 179

Figure 4-24: 300 MHz ^{1}H NMR spectrum of [L]U(I)$_2$(THF)$_2$ (**4.10**) in $CDCl_3$ at 298 K 181

Figure 4-25: ^{1}H NMR chemical shifts of the diagnostic imine peaks in **4.1**, **4.8**, and **4.10** compared to the Pauling electronegativity value of the halides 183

Figure 4-26: ORTEP depiction of [L]U(O)$_2$(Py) (**4.11**) with ellipsoids shown at 30% probability. Hydrogen atoms omitted for clarity. 185

Figure 4-27: 300 MHz ^{1}H NMR spectrum for [L]U(O)$_2$(Py) (**4.11**) in $CDCl_3$ at 298 K 188

Figure 4-28: 100 MHz ^{13}C NMR spectrum of [L]U(O)$_2$(Py) (**4.11**) in $CDCl_3$ at 298 K 189

Figure 4-29: ORTEP depiction of [L]U(Cl)(N_3)(Py)$_2$ (**4.12**), the major product of Path 1 (Scheme 4-8) with ellipsoids shown at 30% probability. Hydrogen atoms omitted for clarity. 194

List of Schemes

Scheme 2-1: C-H activation reactivity of $U[N(SiMe_3)_2]_4$ 28

Scheme 2-2: Attempted synthesis of $U[N(SiMe_3)(3,5\text{-}Me_2C_6H_3)]_3$ by salt metathesis with a U(III) starting material. 30

Scheme 2-3: Synthesis of $[L]_3U(I)$ (**2.1**) from $UI_4(1,4\text{-dioxane})_2$ 31

Scheme 2-4: Attempted synthesis of $(Cl)U[N(SiMe_3)(3,5\text{-}(CH_3)_2(C_6H_3))]_3$ (**2.3**) from UCl_4 and $[Li(OEt_2)][N(Si(Me_3)(3,5\text{-}(CH_3)_2(C_6H_3)]$ 37

Scheme 2-5: Synthesis of $(Cl)U[[N(SiMe_3)(3,5\text{-}(CH_3)_2(C_6H_3)]_3$ (**2.3**) from UCl_4 and $K[N(Si(Me_3)(3,5\text{-}(CH_3)_2(C_6H_3)]$ 41

Scheme 2-6: Synthetic pathways for generating $(Br)U[N(SiMe_3)(3,5\text{-}(CH_3)_2(C_6H_3)]_3$ (**2.4**) 43

Scheme 2-7: Proposed pathway to generate complex **2.4** from complex **2.2** .. 46

Scheme 2-8: Divergent reactivity influenced by ligand salt alkali metal counterion identity 54

Scheme 2-9: Synthetic pathways used to try to generate $(F)U[N(SiMe_3)(3,5\text{-}(CH_3)_2(C_6H_3)]_3$ 57

Scheme 2-10: Rational synthesis of $U[L]_4$ (**2.6**) from UCl_4 or $UI_4(1,4\text{-dioxane})_2$ 60

Scheme 2-11: Proposed synthesis of $[L]_3Th(Cl)$ 64

Scheme 2-12: Synthetic pathways attempted to generate $[L]_3U(O)(X)$ 74

Scheme 2-13: Synthetic approaches for generating the uranium imido (U=N) functionality 81

Scheme 2-14: Synthetic pathways used to attempt to generate the U=P(Ar) functionality 83

Scheme 2-15: Possible mechanism for the formation of the phosphaindole ... 86

Scheme 2-16: Attempted synthetic pathway to access $(Cl)_2U(N(SiMe_3)(3,5\text{-}(CH_3)_2(C_6H_3))]_3$ 89

Scheme 3-1: Proposed protonolysis pathway to BDPP stabilized U=E functionalities (E = N, P). 108

Scheme 3-2: Direct and multistep procedures used to generate complex **3.1** 117

Scheme 3-3: Possible mechanisms for the formation of $[BDPP´]U(CH_2Ph)_2$ (**3.1**) 118

Scheme 3-4: Isotopic labeling studies probing the mechanism of formation of $[BDPP´]U(CH_2Ph)_2$ (**3.1**) 119

Scheme 3-5: Scope of nucleophilicity for alkylation of $[BDPP]Zr(X)_2$ complexes (X = (CH_2Ph) or $N(Me_2)$) 122

Scheme 4-1: Synthesis of Schiff base proligand $[L]H_2$ 139

Scheme 4-2: Synthesis of Th(IV) and U(IV) dichloro Schiff base complexes 141

Scheme 4-3: Synthesis of $[L]An(N_3)_2(Py)_2$ complexes from $[L]An(Cl)_2(THF)_2$ where An = U, Th 150

Scheme 4-4: Synthetic approaches for generating dialkyl Schiff base actinide complexes 159

Scheme 4-5: σ-Bond metathesis reactivity used to generate $[L]An(Br)_2(Py)_2$, complexes **4.6** (An = U) and **4.7** (An = Th) 174

Scheme 4-6: Synthetic approaches to generate the diiodo and difluoro Schiff base complexes of the type $[L]U(X)_2(Solv)_2$ 180

Scheme 4-7: Oxidative pathways used to generate (R)E=U=E(R) functionalities 184

Scheme 4-8: Methods attempted to generate the uranium nitride functionality 193

Abbreviations

An	Actinide
o-Ar	*ortho*-Aryl
p-Ar	*para*-Aryl
avg	Average
BDPP	Bis(2,6-diisopropylanilidomethyl)pyridine
BDPP*	2,6-Bis(2,6-diisopropylanilidomethyl)(4-tertbutoxy)dihydropyridonate
BDPP'	(4-benzyl) bis(2,6-diisopropylanilidomethyl)dihydropyridonate
BIP	Bis(imino)pyridine
BTU	British thermal unit
n-Bu	*n*-Butyl or normal butyl (-$CH_2CH_2CH_2CH_3$)
^{t}Bu	*tert*-Butyl [-$C(CH_3)_3$]
Cp	cyclopentadienyl (C_5H_5)
Cp*	1,2,3,4,5-pentamethylcyclopentadienyl (C_5Me_5)
DFT	Density functional theory
DME	1,2-dimethoxyethane
DMF	Dimethylformamide
DOE	United States Department of Energy
E	Energy or specified element
e^-	Electron
EPR	Electron paramagnetic resonance

eq	Equivalent
equiv.	Equivalent
Et	Ethyl (-CH_2CH_3)
Et_3N	Triethylamine
FT-IR	Fourier transform-infrared
Gen	Generation
HLW	High level radioactive waste
HSAB	Hard-Soft Acid-Base
hv	Light
ILW	Intermediate level radioactive waste
ITI	Inverse *trans* influence
L	Chapter 2: [$N(SiMe_3)(3,5\text{-}(Me)_2(C_6H_3)$]
L	Chapter 4: ±-trans-6,6’-diethoxy-2,2’-cyclohexane-1,2-diylbis(nitrilomethanylyidene)diphenolate
LLW	Low level radioactive waste
M	Metal
Me	Methyl (-CH3)
Mes*	2,4,6-tritertbutylphenyl
MHz	Megahertz
MJ	Megajoule
MS	Mass spectrometry
MW	Megawatt
NMR	Nuclear magnetic resonance

ORTEP	Oak Ridge Thermal Ellipsoid Plot
Ph	Phenyl
ppm	Parts per million
^{i}Pr	Isopropyl [-C(CH_3)$_2$]
PUREX	Plutonium and uranium redox extraction
Py	Pyridine
R	Generic functional group
RT	Room temperature
salen	N,N’-Bis(salicylidene)ethylenediamine
Solv	Solvent
TEMPO	(2,2,6,6-tetramethylpiperidin-1-yl)oxyl
THF	Tetrahydrofuran
UREX	Uranium extraction
U.S.	United States of America
VAC	Vacuum Atmospheres
XANES	K-edge X-ray absorption near edge spectroscopy
XRD	X-ray diffraction
xs	Excess
χ_p	Pauling electronegativity

Abstract

Different synthetic approaches to the development of complexes with X-An=E and E=An=E functionalities (where An = U, Th) for use in studying the inverse *trans* influence (ITI) and the role *f*-orbitals play in early actinide bonding are expounded upon in this work. Chapter 1 gives a brief overview of the context of early actinide complexes in the nuclear fuel cycle, the grand challenges associated with understanding the inverse *trans* influence (ITI) and the participation of f-orbitals in bonding between actinides and main group elements.

Chapter 2 discusses the use of a κ^1-ancillary anilido ligand [N(SiMe$_3$)(3,5-(Me)$_2$(C$_6$H$_3$)] to support actinide complexes to accommodate bulky U=E(R) moieties that can protect the reactive U=E bonds. This scaffold can be used to isolate tris(amido) halide (X)U[N(SiMe$_3$)(3,5-(Me)$_2$(C$_6$H$_3$)]$_3$ (X = Cl, Br and I; complexes 2.3, 2.4 and 2.1 respectively) and homoleptic tetrakis(amido) complexes of uranium (complex 2.6), where a correlation between halogen electronegativity and ^{1}H NMR chemical shift is observed. The identity of the alkali metal counterion (M) used in salt metathesis reactions of [M][N(SiMe$_3$)(3,5-(Me)$_2$(C$_6$H$_3$)] with AnX$_4$ (An = U, Th; X = Cl, I) plays a significant role in the reactivity of the resultant halo tris(anilido) uranium species. All attempts at isolating U=E multiple bonds were unsuccessful and resulted in either no reaction or isolation of a disproportionation byproduct, U[N(SiMe$_3$)(3,5-(Me)$_2$(C$_6$H$_3$)]$_4$.

Chapter 3 explores the use of a bulkier κ^3-bis(diisopropylanilidomethyl) pyridine (BDPP) ligand, for stabilizing mid-valent uranium complexes. Previous studies with lanthanides and transition metals have shown this ligand scaffold to

avoid non-innocent ligand-based reactivity. The BDPP ligand is shown to undergo non-innocent ligand based reactivity through alkylation at the 4-position of the BDPP pyridine backbone to generate a dihydropyridonate species (complex 3.1). All attempts at elucidating a plausible mechanism for this unwanted alkylation were unsuccessful; however, generality for this reaction is demonstrated through reactivity studies with [BDPP]Zr(NMe_2)$_2$.

Chapter 4 highlights the use of κ^4-salen type Schiff base ligand (±)-*trans*-6,6'-diethoxy-2,2'-[cyclohexane-1,2-diylbis(nitrilomethanylylidene)]diphenol. This ligand system enables isolation of pseudo-*trans* dihalo actinide complexes [L]An(X)$_2$(Solv)$_2$ (X = Cl, Br, I; Solv = THF or pyridine; L = Schiff base ligand) (complexes 4.1, 4.1-(Py), 4.2, 4.2-(Py), 4.8, 4.9, and 4.10). Ligand innocence in [L]An(Cl)$_2$(Solv)$_2$ is maintained during reactions with both weak and strong nucleophiles and metal-based salt metathesis reactivity. This scaffold supports rare pseudo-*trans* diazido complexes [L]An(N_3)$_2$(Py) generated by reaction of [L]An(Cl)$_2$(Solv)$_2$ with excess NaN_3 (complexes 4.3 and 4.4). Remarkably, this ligand framework can support the linear metallocene functionalities [L]An(Cp)$_2$(1,4-dioxane) (complexes 4.6 and 4.7) upon reaction of [L]An(Cl)$_2$(Solv)$_2$ with 2 equiv. of NaCp, including the rare uranium linear metallocene (complex 4.6) and the first example of a thorium linear metallocene (complex 4.7). This ligand system also enables the preparation of a uranyl complex, [L]U(O)$_2$(Py), through oxidation of the dichloro complexes with $NaNO_2$ (complex 4.11).

Chapter 1

Introduction

1.1: U.S. energy demands and the search for a more sustainable fuel source

With the U.S. population increasing to over 325 million people in 2017, the pressure to provide enough energy to sustain the current population has increased dramatically over the past few decades.[1] It was estimated that by the end of 2016, roughly 97.4 quadrillion BTUs of energy were consumed across all sectors.[2] By 2050, the U.S. population is expected to increase to over 400 million people with an expected population growth of 2.1 million people per year.[3] Consequently, the challenge to meet the population's energy demands will only increase for the foreseeable future.

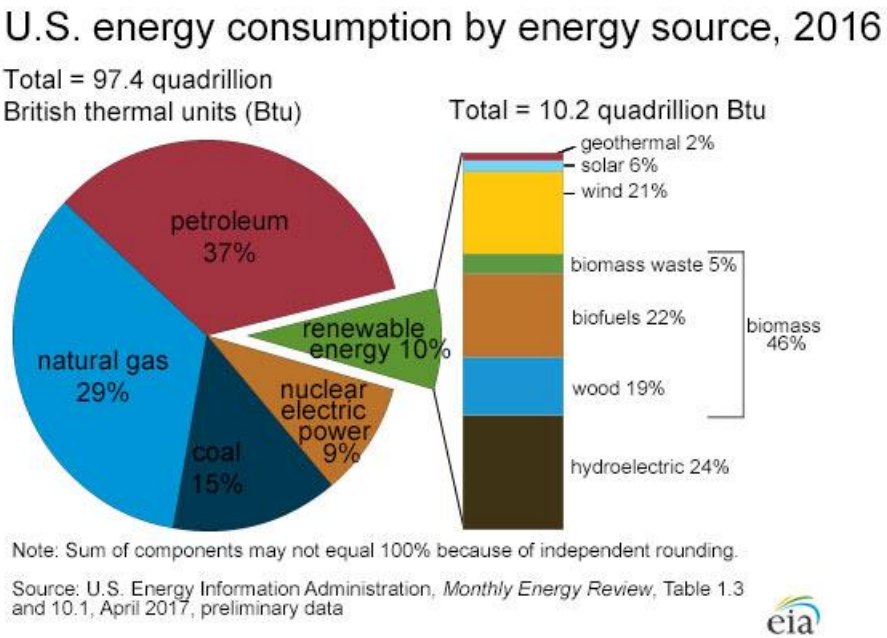


Figure 1-1: *Contribution of various energy sources (%) to U.S energy consumption in 2016*

As of 2014, roughly 53% of energy produced in the U.S. comes from non-renewable and non-carbon neutral sources like coal and oil.[4] As these resources

are finite, it is likely that these materials will run out in the foreseeable future, creating a deficit in energy production unless a more reliable source of energy can be found. Aside from the inability to sustain the growing population long term, continued use of non-renewable fuel sources like coal and oil pose additional problems. One of the main concerns with burning coal and other hydrocarbon fuels sources is their emission of greenhouse gases like CO_2.[5] High emissions of these gases are believed to be the main contributor to global climate change.[5,6] Currently, the burning of coal accounts for roughly half of all CO_2 emissions associated with the burning fossil fuels.[7] Despite this, approximately 40% of the world's electricity is produced through the combustion of coal and other hydrocarbon solids.[5-7] Due to the decreasing reserves of fossil fuel sources like coal, and the environmental concerns with their continued use, cleaner, less environmentally hazardous sources of fuel that can sustain the growing population are currently being explored. One possible alternative fuel candidate that easily has the ability to support the world's growing population is nuclear fuel.[7] Currently, nuclear energy is generated primarily through fission of heavy actinide isotopes, namely uranium and plutonium (Figure 1-2).[8]

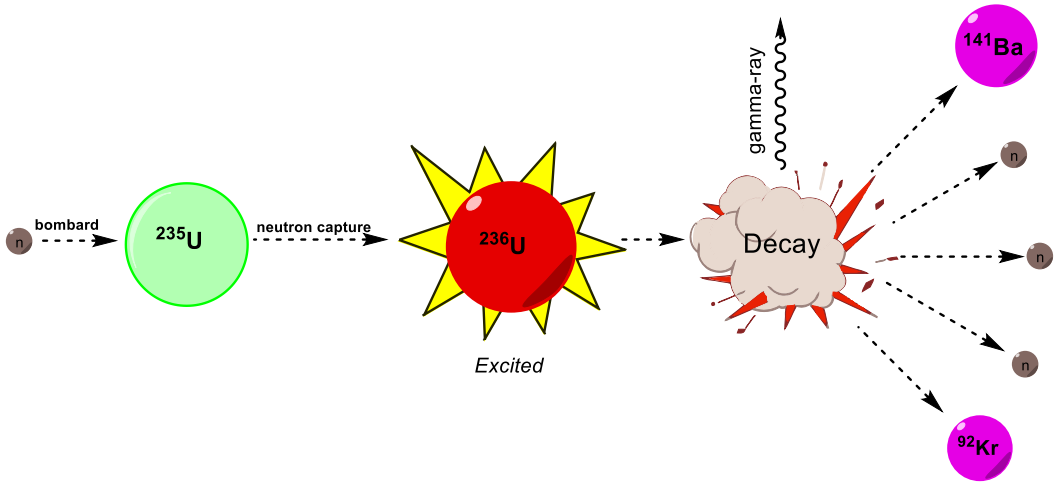


Figure 1-2: *Simplified depiction of U-235 undergoing nuclear fission.*

During a fission event, a U-235 atom is bombarded with a neutron, which is captured by the U-235 atom to temporarily become an excited U-236 atom. The U-236 nuclide then splits or decays into two smaller fragments, releasing three additional neutrons, which can in turn participate in additional fission events, along with gamma-rays and energy in the form of heat. The heat generated from this process is then harnessed to convert liquid water to steam, which is then used to drive electricity producing turbines without producing carbon emissions.[9] Interestingly, just one kilogram of fissile uranium fuel, has the ability to generate about 500,000 MJ of energy.[7] To illustrate the efficiency of uranium as a fuel source, the equivalent mass (1 kg) of non-renewable black coal is produces only 24-30 MJ of energy.[7] This difference in energy density, or the amount of energy produced per unit of mass of the fuel source (MJ/kg) between a uranium nuclear fuel source and coal can further be demonstrated by the amount of each fuel source consumed by a power plant annually. It is estimated that a one million kilowatt (1000 MW) coal burning power plant consumes approximately 3.2 million

tons of black coal per annum, whereas a one million kilowatt nuclear power plant, uses only 27 tons of uranium fuel (UO_2) each year.[7, 10] Through this comparison, we can see that nuclear fuel, is a far more efficient fuel source than fossil fuels like coal. Despite this, and the fact that nuclear fuel is able to produce energy with minimal carbon emissions, there are still many concerns with using nuclear power to meet world demands.

1.2: Concerns with nuclear energy as a long-term, sustainable fuel source

1.2.1: Public opinion and economic concerns with nuclear energy

The safe and reliable operation of nuclear power plants is of paramount interest to the general public.[5] Recent nuclear accidents, which led to significant leaks of harmful radiation into the surrounding environment at the Fukushima Daiichi nuclear power plant in Japan and historic releases of radioactive material at the Chernobyl plant in Pripyat, Ukraine, have caused people to criticize the use of this fuel source for fear of potential exposure to harmful radiation generated as a byproduct of the fission process.[11] Although catastrophic accidents where significant amounts of radiation are released into the environment are extremely rare, this fear of potential exposure to harmful radiation has created a negative public opinion for the use of nuclear fuels.[12] This negative opinion has, in turn, prompted countries like Belgium, Germany and Switzerland to begin phasing out the use of nuclear power by the year 2035.[5, 13] In an effort remedy public safety concerns, many countries have begun to explore the development of safer reactor designs, which are theoretically better equipped to handle a catastrophic

accident in the very unlikely event one were to occur.[14] In addition to fear of accidental exposure to radiation, economic pressures that limit the cost effectiveness of nuclear power are an additional concern for long-term sustainability of nuclear power. Due to falling natural gas prices, many old coal-burning power plants have been replaced with new plants that run on natural gas rather than nuclear power.[5] In addition to this, subsides for solar and wind energy have prompted the construction of wind and solar farms rather than new nuclear power plants,[5, 15] and government subsidies for renewable energy have driven power generated by these methods, "so low that nuclear power cannot feasibly compete" at this time.[15] With nuclear power being responsible for the production of roughly 20% of the electricity produced in the U.S. – and nearly 60% of the nation's "carbon-free" electricity – the inability for nuclear power to compete effectively in the energy industry may be problematic for the future of the nation's carbon-free energy production.[16] As such, in 2016, the United States Department of Energy (DOE) awarded two companies a combined sum of $80 million dollars to develop safer, more cost-effective Gen IV nuclear reactors.[16] It was their hope that by awarding this grant, that the U.S. would be able to provide cleaner, carbonless nuclear energy for decades to come.[16]

1.2.2: Concerns with radioactive nuclear waste

Although efforts have been made to address nuclear plant operation safety and the long-term economic viability of nuclear power, many qualms still exist about the use of nuclear power due to the production of highly toxic nuclear waste

as a byproduct of the nuclear fuel cycle. Nuclear fission generally results in radioactive waste belonging to one of three different categories.[17] The first type of radioactive waste produced from fission is known as low level radioactive waste (LLW). This type of waste makes up roughly 90% of the volume of all radioactive waste produced, but accounts for only 1% of all radioactivity for the entire nuclear waste inventory.[17] LLW typically contains paper, clothing and tools that have been exposed to minor contamination.[17, 18] The second category of waste is known as intermediate level radioactive waste (ILW) and typically is comprised of resins, metal fuel cladding and “sludge”.[17] This type of waste accounts for 7% of the volume of radioactive waste produced, but only 4% of the total radioactivity.[17] ILW is often solidified in concrete before being stored in holding yards. The last type of waste produced as a result of nuclear power is classified as high level radioactive waste (HLW) and is often comprised of spent nuclear fuel and waste generated during the reprocessing of used fuel.[19] This type of waste accounts for about 3% of the volume of nuclear waste produced, but nearly 95% of the total radioactivity.[17] HLW is generally stored under water at an onsite location at a nuclear power plant, allowing the highly radioactive isotopes found in the waste to have time to decay.[17] Due to the long half-lives for many of the radioactive isotopes found in this type of waste, storage of HLW is required for 40-50 years – or longer in the case of long-lived isotopes – before proper disposal can occur.[17] As this type of waste must be properly stored for many years before disposal, buildup of HLW waste at nuclear power plants is a concern. It is estimated that roughly 300,000 tonnes of HLW waste is distributed

across nuclear power plants worldwide, with annual additions of new HLW waste reaching approximately 10,500 tonnes annually.[17] Buildup of this type of waste is a concern not only from proliferation and storage standpoints, but from a national security perspective as well. As this waste contains high levels of radioactivity, it must be closely monitored to ensure that it is not stolen or intercepted and used for illicit purposes.[19] As this waste continues to accumulate, it becomes more difficult and more expensive to monitor. As a result, efforts are being made to find more suitable storage solutions and to reduce the amount of HLW waste generated each year.

1.2.3: Management of high level radioactive waste and funding initiatives for actinide science

Currently, it is internationally accepted that the best solution for storing HLW waste is to bury it deep underground in a secure repository.[17, 19] Despite consensus on this matter, no government has been able to institute the use of long-term repositories due to negative public opinion concerning their use. Public opinion regarding long-term repositories is negative due to fears that highly radioactive waste will breach containment and seep out into the environment. As a result, “not in my backyard” protests of radioactive waste storage have become commonplace.[20] Due to continued pressure on the government, this negative opinion played a significant role in shutting down construction of Yucca Mountain, the only long term nuclear waste storage facility in the U.S.[17] With construction

on this nuclear waste repository halted, other means of dealing with the buildup of HLW waste were needed.

In an effort to remedy this issue, the DOE began investing in ways to reprocess or recycle spent nuclear waste such that the amount of HLW waste produced each year could be minimized.[21] Currently, the Plutonium and Uranium Redox Extraction (PUREX) and URanium EXtraction (UREX) processes are the most widely used methods for recycling spent high level nuclear waste. It is estimated that these methods have the ability to remove greater than 99% of useable plutonium and uranium from spent nuclear fuel.[10] Although this is the case, the post PUREX raffinate or the material containing the desired fissionable isotopes after the PUREX process, is still contaminated with lanthanides and minor actinides like neptunium, americium and curium.[10, 22] Contamination of uranium and plutonium with minor actinide byproducts is responsible for a large portion of the long-term radiotoxicity and heat load of the post PUREX material.[22-24] As the desired plutonium and uranium isotopes are still contaminated with other *f*-elements, methods for improving current separation technologies to obtain a more pure raffinate are being investigated. In an effort expedite the improvement of current separations technologies, the DOE is sponsoring fundamental actinide research to better understand the differences in bonding between 4*f* and 5*f* elements, and early and late actinides such that a better sequestering agent can be developed to further purify the desired plutonium and uranium products from reprocessed nuclear fuel.[25] Currently, The DOE considers understanding the nature of *f*-element bonding to be one of the three “grand challenges” of *f*-element

chemistry.[25] With this in mind, funding has been made available for government and academic labs seeking to perform research related to uncovering the role *f*-electrons play in bonding.

1.3: Important breakthroughs in fundamental actinide science

1.3.1: Understanding the inverse trans *influence (ITI)*

With support from agencies like the DOE, research has shown that the 5*f*-orbitals play a significant role in bonding for actinide complexes and materials that are required for advanced energy systems.[25] Since this discovery, significant work has been done to determine the extent to which *f*-orbitals participate in bonding for actinide complexes. A great deal of this work has been focused on understanding the bonding in uranyl, $[O=U=O]^{2+}$, as it is the most environmentally prevalent form of uranium and makes up a significant portion of the uranium found in spent nuclear waste. Studies of uranyl species have shown that uranium displays a fairly unique phenomenon not observed in bonding with transition metals. Upon further investigation, it was determined that there was a "cooperative stabilization of the metal-oxo bonds *trans* to one another."[26] As this is opposite to what is observed in transition metal bonding, this phenomenon has become known as the inverse *trans* influence, or the ITI.[27] The uranium-oxo bond strengthening observed with uranyl complexes, which derives from the inverse *trans* influence is now accepted to be an underlying feature for the stability of uranyl complexes.[26, 27] Considering that ITI bond strengthening is a common

characteristic of high valent actinide complexes, considerable effort has been invested into understanding the origins of this phenomenon.

Denning and coworkers suggested that the inverse trans influence may be explained by the “electrostatic interaction between a strong anionic ligand and the metal core electrons,”[28] which leads to a polarization of these electrons. If the highest filled core orbitals have the opposite parity, or symmetry with respect to inversion, as the symmetry of the valence shell orbitals, then the resulting polarization of the electrons is dipolar in nature. Conversely, if the highest filled core orbitals have the same symmetry with respect to inversion as the symmetry of the valence shell orbitals, then the resulting induced polarization of the electrons is quadrupolar in nature.[27] For transition metals, the highest filled core atomic orbitals are generally *p*-orbitals (antisymmetric with respect to inversion), whereas the valence shell orbitals are *d*-orbitals (which are symmetric with respect to inversion). As the core and valence shell orbitals for transition metals have different symmetries with respect to inversion, the resulting polarization of electrons in L-M=E functionalities is dipolar for d-block transition metal complexes.[27, 29] This results in buildup of negative charge *trans* to a strongly bound ligand (typically an M=E functionality), thus causing the M-L bond to weaken by electron-electron repulsion (Figure 1-3).[27] For early high valent actinide complexes, the highest filled core atomic orbitals are *p*-orbitals, and the valence shell orbitals are *f*-orbitals, both of which are antisymmetric with respect to inversion. Since both the highest filled core atomic orbitals and the valence shell orbitals have the same symmetry with respect to inversion for high valent

early actinide complexes, the resulting polarization of the electrons in the L-M=E functionality is quadrupolar. This results in negative charge build up *cis* to the strongly bound M=E functionality.[27] A consequence of this charge distribution is a weakening of the M-L bonds *cis* to the strongly bound M=E functionality, and the observed ITI strengthening of the M-X bond *trans* to the M=E functionality (Figure 1-3).[27]

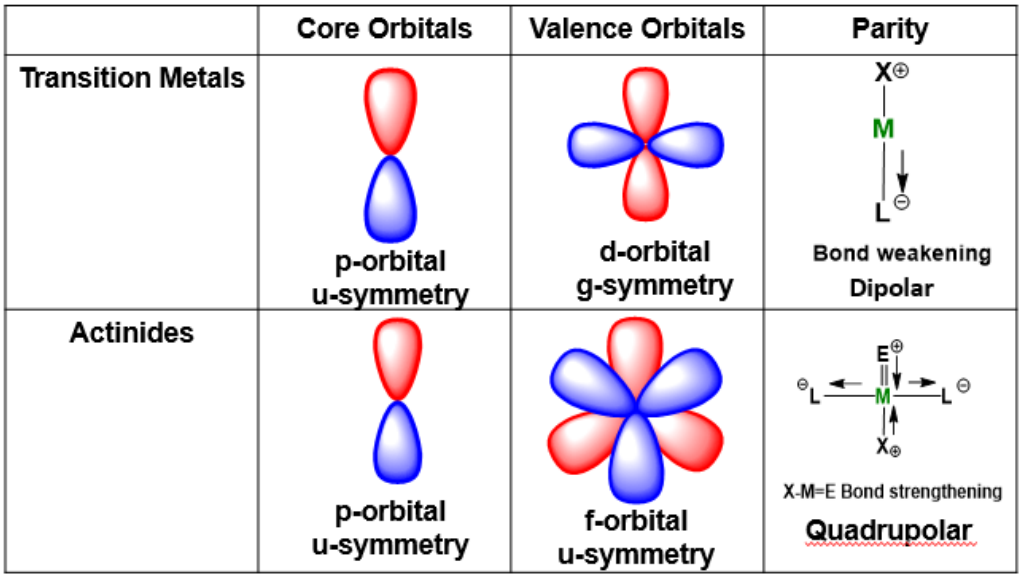


Figure 1-3: *Explaining the origin of the inverse* trans *influence (ITI)*

More simply put, it can be rationalized in part that the bond strengthening observed with the ITI originates form the donation of electron density from the semi-core 6p orbitals of the high valent uranium complex to the empty valence 5*f*-orbitals. This electron donation creates a hole in electron density which is compensated for by donation from the strong π-donor ligand in the *trans* position relative to the M=E functionality.[30, 31] This donation by the ligand *trans* to the M=E functionality causes the observed bond strengthening seen in the ITI. Until recently, evidence for the ITI was only observed with U(VI) uranyl complexes.[31]

A major reason for this observation is the difficulty associated with synthesizing non-uranyl complexes that exhibit this behavior.[27] Synthesis of non-uranyl complexes that exhibit ITI behavior is complicated by the susceptibility of low valent uranium precursor complexes to undergo unwanted side reactivity like disproportionation.[32] Additionally, preparation of examples of non-uranyl ITI behavior have not been observed due to the difficulties associated with installing more electropositive multiply bound ligands such as imides, nitrides and phosphinidenes on the uranium center.[33]

Although methods for readily accessing the M=N(R) functionality have long existed for Group 6 Mo and W complexes, suitable methods for installing the imido functionality on uranium have only recently been developed.[33,34] With this in mind, recent efforts have been made to generate non-uranyl complexes that exhibit the ITI with the aim of providing more experimental data that can help accurately depict the electronic structure of these complexes. Information about the electronic structure of these complexes is desired such that the role that 6*p*, 6*d* and 5*f* -orbitals play in actinide bonding can be elucidated.

1.3.2: Prior research into the inverse trans *influence (ITI)*

Through persistent pursuit of non-uranyl complexes that exhibit ITI behavior, Meyer and coworkers were able to fully characterize a uranium imido complex that exhibits the iconic bond strengthening characteristics of the inverse *trans* influence.[33] From this work, Meyer and coworkers were able to show that the inverse trans influence can be observed in non-uranyl complexes, and is not

specific to the O=U=O moiety of uranyl. Similarly, Boncella and coworkers were able to generate a bis(imido) U(VI) uranyl analog, through which they were able to illustrate that trans E=U=E functionalities are also able to experience the bond strengthening effects of the ITI.[35] Additionally, Schelter and coworkers were able to develop a tris(amido) uranium platform that is able to support a series of non-uranyl X-U=O functionalities.[26] From this work, Schelter and coworkers were able to observe how the ITI bond strengthening changes as the identity of the group (X) *trans* to the uranium oxo bond is altered. Although this work answered fundamental questions about how the magnitude of ITI bond strengthening changes as the identity of a σ-bound ligand *trans* to a U=O bond is varied, many questions arose from this work about how the magnitude of ITI bond strengthening would change as the identity of the uranium element multiple bond is altered. From these studies, questions about other ways to tune the ITI bond strengthening arose, and investigations are ongoing to better understand how the ITI bond strengthening can be altered.[30, 36]

1.3.3: Understanding methods of quantifying actinide covalency

In addition to uncovering the ITI, the DOE-sponsored research has also uncovered that early actinide complexes display a degree of covalency in bonding unlike their lanthanide counterparts.[25] This discovery is of particular interest to the DOE and the nuclear energy community since it provides a potential lead into finding a way to better separate lanthanide and actinide fission

byproducts during nuclear waste reprocessing. This has spawned many experimental investigations into the nature of actinide-ligand bond covalency.

It is currently understood that both orbital overlap driven covalency and orbital near degeneracy driven covalency play a significant role in actinide-ligand bonding interactions.[37, 38] It is also known that actinide covalency is dependent on the "hard-soft nature of the ligand set, the formal oxidation state of the actinide ion, and the degeneracy that results from simple energy matching of metal and ligand valence orbitals."[39] These components of actinide covalency have been extensively studied by computational methods.[39, 40] Unfortunately, experimental validation of the these computational studies are lacking.[39] This is in part due to the fact that it is difficult to quantify actinide covalency experimentally.[39] Currently K-edge X-ray absorption near-edge spectroscopy (XANES) is one of the main methods used to experimentally quantify actinide covalency.[37, 39, 41-43] Unfortunately, this technique is not broadly available, as it requires a synchrotron for its implementation.[42] Where it can be successfully applied, the XANES technique is able to effectively measure transition intensities after a core ligand electron is excited to a vacant metal-ligand antibonding orbital. The extent of covalency in an M-L bond can be quantified by this technique since it involves an electric dipole allowed transition from a ligand core 1s electron to an np orbital. The intensity of this transition determines the amount of ligand p character in the valence molecular orbital. As this is the case, this technique investigates both unoccupied and singly-occupied acceptor orbitals of the metal complex that contain ligand np contribution and directly probes the covalency of the metal-

ligand bond.[41] It has also recently been shown that pulse based electron paramagnetic resonance spectroscopy (EPR) can reliably measure covalency in actinide complexes using the 'superhyperfine' interaction of primarily metal-based unpaired electrons with ligand nuclei that have a non-zero nuclear spin.[39] These pulse based EPR methods can detect much weaker metal-ligand interactions and provide information on spin-dynamics/time resolution and spin delocalization.[39] Despite these breakthroughs in quantifying actinide covalency, more experimental studies that quantify actinide covalency are needed to help develop theoretical calculations that accurately model actinide bonding behavior.

1.4: Project goals

Although considerable effort has been directed to trying to understand the ITI and the role *f*-electrons play in actinide bonding, there are still plenty of unanswered questions related to these topics. Our actinide research tries to answer these questions in a manner that is of relevance to the needs of funding agencies like the DOE. As such, we set up our research targets into three main phases described below:

Phase 1: The design and development of suitable ligand scaffolds that are able to support X-An=E functionalities for studies related to the inverse trans influence (ITI). Additionally during this phase of research, we intend to generate and fully characterize suitable low valent actinide precursor complexes that can be readily oxidized to support X-An=E functionalities. Generation of low valent actinide complexes will be accomplished through salt-metathesis reactivity or

protonolysis reactivity. Full characterization of these complexes will be accomplished mainly through X-ray diffraction studies and relevant spectroscopic studies.

Phase 2: Generation and characterization of X-An=E functionalities, where E=O, N(R) and P(R). Attempts at generating these uranyl analogs will be made using oxidative methods, protonolysis methods, and salt metathesis reactivity. Additionally, during this phase of research, we intend to vary the identity of X for each type of X-An=E functionality generated for use in studies related to the inverse trans influence. Full characterization of these complexes will be performed using X-ray diffraction and relevant spectroscopic methods.

Phase 3: Collaborative studies will examine the bond strengthening observed with the X-An=E functionalities generated in Phase 2. This will be accomplished through electronic structure analysis using DFT calculations performed by a collaborator, and will allow us to understand the role f-electrons play in the bonding picture for complexes generated in phases 1 and 2. Covalency will be quantified through XANES or EPR methods performed with assistance from a collaborator.

As the work represented in this dissertation is the beginning of our research efforts in actinide science, the research described herein focuses mainly on the aims described in phases 1 and 2. We attempted to generate suitable ligand scaffolds that can stabilize X-An=E functionalities using ligands that employ different denticities. Chapter 2 will focus on our efforts at utilizing a κ^1-anilido ligand scaffold, and our attempts at generating X-An=E functionalities with

this ligand framework. Chapter 3 will focus on the use of a κ^3-bis(anilido)pyridine ligand for the synthesis of a low valent uranium precursor complex that has potential to stabilize X-An=E functionalities. Finally, Chapter 4 focuses on the development of a κ^4-Schiff base ligand scaffold that is able to stabilize low oxidation state uranium and thorium precursor complexes that can stabilize the desired X-An=E functionalities.

1.5: References

1. U.S. Census Bureau. U.S. and World Population Clock. https://www.census.gov/popclock/ (Accessed Jul 1, 2017).

2. Mobilia, M.; Comstock, O. *U.S energy consumption rose slightly in 2016 despite a significant decline in coal use*. U.S. Energy Information Administration: Washington, DC, 2017. https://www.eia.gov/todayinenergy/detail.php?id=30652 (Accessed Jul 1, 2017).

3. Colby, S. L.; Ortman, J. M. *Projections of the Size and Composition of the U.S. Population: 2014-2060*; U.S. Census Bureau: Washington, DC, 2015. https://www.census.gov/content/dam/Census/library/publications/2015/demo/p25-1143.pdf (Accessed Jul 3, 2017).

4. U.S. Energy Information Administration Office of Energy Statistics. *Monthly Energy Review March 2015*. U.S. Energy Information Administration: Washington, DC, 2015. https://www.eia.gov/totalenergy/data/monthly/archive/00351503.pdf (Accessed Jul 3, 2017).

5. Fellet, M. *A Global Transition to Clean Energy: Challenges and Opportunitie*s; ACS-*extraInsights!*: Washington, DC, 2016.

6. International Energy Agency. World Energy Outlook 2015. https://www.iea.org/Textbase/npsum/WEO2015SUM.pdf (Accessed Jul 4, 2017).

7. World Nuclear Association. Energy for the World - Why Uranium? 2012. http://www.world-nuclear.org/information-library/nuclear-fuel-cycle/introduction/energy-for-the-world-why-uranium.aspx (Accessed Jul 4, 2017).

8. World Nuclear Association. How a nuclear reactor makes electricity. http://www.world-nuclear.org/nuclear-basics/how-does-a-nuclear-reactor-make-electricity.aspx (Accessed Jul 4, 2017).

9. Nuclear Energy Institute. How Nuclear Reactors Work. https://www.nei.org/Knowledge-Center/How-Nuclear-Reactors-Work (Accessed Jul 5, 2017)

10. World Nuclear Association. Processing of Used Nuclear Fuel. 2016. http://www.world-nuclear.org/information-library/nuclear-fuel-cycle/fuel-recycling/processing-of-used-nuclear-fuel.aspx (Accessed Jul 6, 2017).

11. Windridge, M. Fear of nuclear power is out of all proportion to the actual risks. *The Guardian*, April 4, 2011. https://www.theguardian.com/science/blog/2011/apr/04/fear-nuclear-power-fukushima-risks (Accessed Jul 6, 2011).

12. World Nuclear Association. Safety of Nuclear Power Reactors. 2016. http://www.world-nuclear.org/information-library/safety-and-security/safety-of-plants/safety-of-nuclear-power-reactors.aspx (Accessed Jul 6, 2017).

13. Nuclear Energy Agency and International Energy Agency. Technology Roadmap: Nuclear Energy 2015 edition. https://www.oecd-nea.org/pub/techroadmap/techroadmap-2015.pdf (Accessed Jul 10, 2017).

14. World Nuclear Association. Advanced Nuclear Power Reactors. 2017. http://www.world-nuclear.org/information-library/nuclear-fuel-cycle/nuclear-power-reactors/advanced-nuclear-power-reactors.aspx (Accessed Jul 10, 2017).

15. Gross, D., Half-Life of America's Nuclear Plants. *Slate,* May 16, 2016. http://www.slate.com/articles/business/the_juice/2016/05/america_is_getting_new_nuclear_plants_in_tennessee_and_georgia_we_need_more.html (Accessed Jul 10, 2017).

16. U.S. Department of Energy. Energy Department announces new investments in advanced nuclear power reactors to help meet America's carbon emission reduction goal. Jan 15, 2016. https://www.energy.gov/articles/energy-department-announces-new-investments-advanced-nuclear-power-reactors-help-meet (Accessed Jul 10, 2017).

17. World Nuclear Association. Radioactive Waste Management. 2017. http://www.world-nuclear.org/information-library/nuclear-fuel-cycle/nuclear-wastes/radioactive-waste-management.aspx (Accessed Jul 10, 2017).

18. United States Nuclear Regulatory Commission. Low-Level Waste. https://www.nrc.gov/waste/low-level-waste.html (Accessed Jul 10, 2017).

19. United States Nuclear Regulatory Commission. High-Level Waste. https://www.nrc.gov/waste/high-level-waste.html (Accessed Jul 10, 2017).

20. Cohen, S., Not in my backyard syndrome and sustainability infrastructure. *Huffington Post*, Jan 4, 2017. http://www.huffingtonpost.com/steven-cohen/the-not-in-my-backyard-sy_b_8910632.html (Accessed Jul 12, 2017).

21. U.S. Department of Energy Office of Nuclear Energy. Mission. https://energy.gov/ne/mission (Accessed Jul 20, 2017).

22. Afsar, A.; Distler, P.; Harwood, L. M.; John, J.; Westwood, J., Extraction of minor actinides, lanthanides and other fission products by silica-immobilized BTBP/BTPhen ligands. *Chem. Commun.* **2017,** *53* (28), 4010-4013.

23. Panak, P. J.; Geist, A., Complexation and Extraction of Trivalent Actinides and Lanthanides by Triazinylpyridine N-Donor Ligands. *Chem. Rev.* **2013,** *113* (2), 1199-1236.

24. Lan, J. H.; Shi, W. Q.; Yuan, L. Y.; Li, J.; Zhao, Y. L.; Chai, Z. F., Recent advances in computational modeling and simulations on the An(III)/Ln(III) separation process. *Coord. Chem. Rev.* **2012,** *256* (13-14), 1406-1417.

25. U.S. Department of Energy Office of Science. Heavy Element Chemistry. https://science.energy.gov/~/media/bes/pdf/brochures/bes-cras/2010-apr/cra_22_heavy_element_chemistry.pdf (Accessed Jul 18, 2017).

26. Lewis, A. J.; Mullane, K. C.; Nakamaru-Ogiso, E.; Carroll, P. J.; Schelter, E. J., The Inverse Trans Influence in a Family of Pentavalent Uranium Complexes. *Inorg. Chem.* **2014,** *53* (13), 6944-6953.

27. Lam, O. P.; Franke, S. M.; Nakai, H.; Heinemann, F. W.; Hieringer, W.; Meyer, K., Observation of the Inverse Trans Influence (ITI) in a Uranium(V) Imide Coordination Complex: An Experimental Study and Theoretical Evaluation. *Inorg. Chem.* **2012,** *51* (11), 6190-6199.

28. Denning, R. G., Electronic-structure and bonding in actinyl ions. *Struct. Bond.* **1992,** *79*, 215-276.

29. Denning, R. G., Electronic structure and bonding in actinyl ions and their analogs. *J. Phys. Chem. A* **2007,** *111* (20), 4125-4143.

30. Gregson, M.; Lu, E.; Mills, D. P.; Tuna, F.; McInnes, E. J. L.; Hennig, C.; Scheinost, A. C.; McMaster, J.; Lewis, W.; Blake, A. J.; Kerridge, A.; Liddle, S. T., The inverse-trans-influence in tetravalent lanthanide and actinide bis(carbene) complexes. *Nat. Commun.* **2017,** *8*.

31. La Pierre, H. S.; Rosenzweig, M.; Kosog, B.; Hauser, C.; Heinemann, F. W.; Liddle, S. T.; Meyer, K., Charge control of the inverse trans-influence. *Chem. Commun.* **2015,** *51* (93), 16671-16674.

32. Brown, D.; Hurtgen, C., Preparation and properties of halogeno-, oxyhalogeno-, and ethoxyhalogeno-complexes of uranium(V). *J. Chem. Soc. Dalton* **1979,** (11), 1709-1713.

33. La Pierre, H. S.; Meyer, K., Uranium-Ligand Multiple Bonding in Uranyl Analogues, L=U=L (n+), and the Inverse Trans Influence. *Inorg. Chem.* **2013,** *52* (2), 529-539.

34. Kolitsch, W.; Dehnicke, K., Complex chemical behavior of nitride chlorides $MoNCl_3$ and $WNCl_3$. *Zeitschrift Fur Naturforschung Part B-Chemie Biochemie Biophysik Biologie Und Verwandten Gebiete* **1970,** *B 25* (10), 1080.

35. Spencer, L. P.; Gdula, R. L.; Hayton, T. W.; Scott, B. L.; Boncella, J. M., Synthesis and reactivity of bis(imido) uranium(VI) cyclopentadienyl complexes. *Chem. Commun.* **2008,** (40), 4986-4988.

36. Anderson, N. H.; Xie, J.; Ray, D.; Zeller, M.; Gagliardi, L.; Bart, S. C., Elucidating bonding preferences in tetrakis(imido)uranate(VI) dianions. *Nat. Chem.* **2017,** *9*, 850-855.

37. Neidig, M. L.; Clark, D. L.; Martin, R. L., Covalency in f-element complexes. *Coord. Chem. Rev.* **2013,** *257* (2), 394-406.

38. Kozimor, S. A.; Yang, P.; Batista, E. R.; Boland, K. S.; Burns, C. J.; Clark, D. L.; Conradson, S. D.; Martin, R. L.; Wilkerson, M. P.; Wolfsberg, L. E., Trends in Covalency for d- and f-Element Metallocene Dichlorides Identified Using Chlorine K-Edge X-ray Absorption Spectroscopy and Time-Dependent Density Functional Theory. *J. Am. Chem. Soc.* **2009,** *131* (34), 12125-12136.

39. Formanuik, A.; Ariciu, A. M.; Ortu, F.; Beekmeyer, R.; Kerridge, A.; Tuna, F.; McInnes, E. J. L.; Mills, D. P., Actinide covalency measured by pulsed electron paramagnetic resonance spectroscopy. *Nat. Chem.* **2017,** *9* (6), 578-583.

40. Smiles, D. E.; Wu, G.; Hrobarik, P.; Hayton, T. W., Use of Se-77 and Te-125 NMR Spectroscopy to Probe Covalency of the Actinide-Chalcogen Bonding in Th(E-n){N(SiMe3)(2)}(3) (-) (E = Se, Te; n=1, 2) and Their Oxo-Uranium(VI) Congeners. *J. Am. Chem. Soc.* **2016,** *138* (3), 814-825.

41. Solomon, E. I.; Hedman, B.; Hodgson, K. O.; Dey, A.; Szilagyi, R. K., Ligand K-edge X-ray absorption spectroscopy: covalency of ligand-metal bonds. *Coord. Chem. Rev.* **2005,** *249* (1-2), 97-129.

42. Denecke, M. A., Synchrotron applications to f-element research in the nuclear fuel cycle. *Dalton Trans.* **2015,** *44* (6), 2606-2612.

43. Ekberg, C.; Lofstrom-Engdahl, E.; Aneheim, E.; Foreman, M.; Geist, A.; Lundberg, D.; Denecke, M.; Persson, I., The structures of CyMe4-BTBP complexes of americium(III) and europium(III) in solvents used in solvent extraction, explaining their separation properties. *Dalton Trans.* **2015,** *44* (42), 18395-18402.

Chapter 2

Synthesis and characterization of uranium(IV) & thorium(IV) tris(trimethylsilyl(anilido)) complexes: Divergent chemistry influenced by alkali metal salt identity

2.1: Background

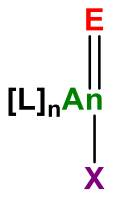
Over the course of a year, a typical commercial nuclear power plant produces about 20 metric tons of processed fuel.[17] This material contains a large mixture of high and low level radioactive waste that is typically accumulated and stored on site.[17] During the last four decades, it is estimated that the industry as a whole has produced roughly 76,430 metric tons of nuclear waste.[44] If stacked side-by-side and end-on-end, this is enough waste to cover an American football field that is over 8 yards deep.[44] Accordingly, there is a strong desire to process unspent nuclear fuel and dispose of the waste safely to prevent a large build-up of nuclear waste on site.[10] One such method suggested for helping to process this waste is the recycling of fissionable materials. A significant portion of the composition of nuclear waste is made up from 4*f*- and 5*f*-elements.[22] Currently, technology is available to selectively remove uranium and plutonium from nuclear waste for reuse in nuclear fission for energy applications. These recycling processes are collectively known as Plutonium Uranium Redox and EXtraction (PUREX) and URanium EXtraction (UREX).[10] UREX utilizes acetohydroxamic acid to selectively remove ~99.9% of uranium and > 95% of technetium from each other and from the other fission products.[10] These methods do not, however, extract and recycle other potentially useful 4*f*- and 5*f*-elements that are produced as a result of the fission process.[22] Finding a suitable sequestering agent that can bind specifically to a desired *f*-element holds a lot of potential value for the future of nuclear waste reprocessing.[21, 25] Understanding how this can be achieved

necessitates the study of how uranium, a 5*f*-element, can be selectively removed from other fission products.[25, 42]

One of the most environmentally prevalent forms of uranium is the uranyl dication: $[UO_2]^{2+}$.[45] This species contains two U=O bonds and is believed to be the significant form of uranium recovered from nuclear waste.[46] It has been observed that this species exhibits unique behavior, where the U=O fragments undergo a bond contraction or strengthening when a strong *π*-donor is *trans* (or about 180°) from the U=O fragment.[27, 28, 30, 31, 33] In the case of uranyl, the mutually *trans* U=O bonds are approximately 180° from each other, and serve as each other's strong *π*-donor. This interaction creates a system that contains very strong U=O bonds, that are extremely resistant to reactivity.[47-50] The bond strengthening observed with this system is opposite to what is typically seen with analogous transition metal complexes, and as such it has become known as the inverse *trans* influence (ITI).[27, 28] Many questions still remain concerning the nature of the inverse *trans* influence, such as: can this phenomenon be tuned by adding different *π*-donating groups *trans* to a U=O bond? To what extent is a U=E bond strengthened, when E is not oxygen? Understanding the answers to these questions along with determining the role that *f*-electrons play in bonding and covalency observed for *f*-element complexes will help us better understand actinide-ligand interactions such that improved sequestering technology could be developed for the reprocessing nuclear waste.[25, 51]

In an effort to better understand the inverse *trans* influence and *f*-electron participation in bonding for compounds that contain U=E bonds, a significant

effort has been made to generate complexes that contain X-U=E fragments[49 52] (example shown in Figure 2-1 below). Generating these types of complexes would provide insight into the extent to which a U=E bond is strengthened when different *π*-donors *trans* to the U=E bond are present. The information obtained from generating these complexes is directly relevant to the development of improved nuclear waste separations technology since, the inverse *trans* influence occurs in UO_2, the main form of fissile uranium in spent nuclear waste. Additionally, making analogous f^0 Th(IV) complexes of the type X-Th=E are also of interest. The generation of these complexes provides an opportunity to study actinide bonding for systems that lack valence 5*f*-electrons, since Th(IV) complexes have a closed shell [Rn] electronic configuration, with no valence *f*-electrons. When juxtaposed with their uranium(IV) counterparts, which have a [Rn]$5f^2$ electronic configuration, a direct comparison can be made between the two systems and insight into the role that *f*-electrons play in bonding can be obtained experimentally through the aid of spectroscopic techniques.[40]



E = O, N, P, S, Se, Te
X = Strong π–donor ligand
An = Th, U

Figure 2-1: *Target actinide complexes for studying the ITI*

Currently, a large effort is being made to explore the use of lower oxidation state thorium and uranium complexes as precursors to stable An=E(R)

fragments.[48, 53, 54] Unfortunately, the chemistry of low oxidation state uranium and thorium is heavily influenced by steric properties.[50, 52, 54] As such, a significant portion of the work done with these systems utilizes bulky cyclopentadienyl type ligands to stabilize the lower oxidation state metal centers.[55-77] Finding additional ancillary ligands that support the chemistry of low oxidation state uranium and thorium has proven to be a challenging endeavor that is often plagued with unwanted side reactivity, such as C-H activation and disproportionation.[78] This unwanted reactivity can make isolating desired X-An=E functionalities for investigating the ITI quite difficult. Ligands selected for use in accessing X-An=E functionalities must not only be able to adequately sterically protect the actinide metal center, but also must not engage in unwanted side reactivity.

2.2: Stabilization of U(IV) complexes using amido ligands

Recently, it has been shown that amido ligands can support lower oxidation state uranium chemistry.[52, 54, 74, 79-83] Work by Anderson and coworkers demonstrates that low valent uranium(III) can be stabilized by the bulky amido ligand [$N(SiMe_3)_2$] without unwanted disproptionation reactivity.[80]

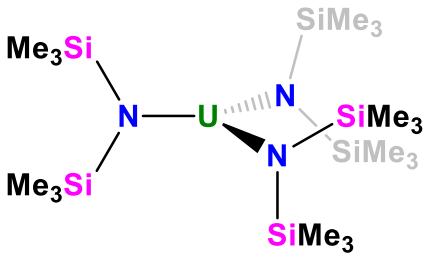
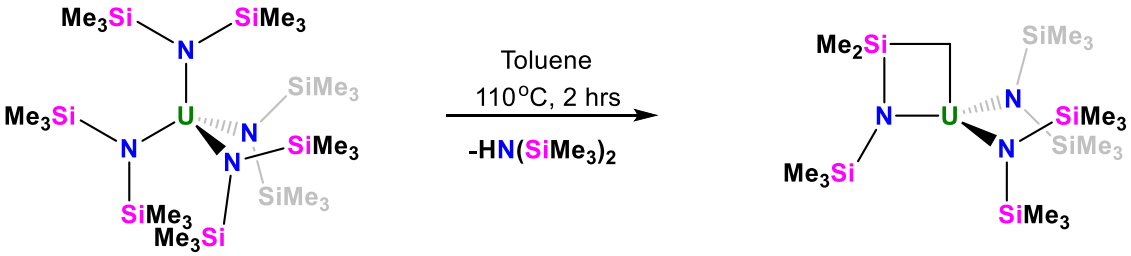


Figure 2-2: *Structure of $U[N(SiMe_3)_2]_3$*

Interestingly, this system has proven to be versatile and effective in supporting oxidation chemistry to generate stable U(IV),[84] U(V)[48, 52, 59, 85-87] and U(VI) species containing U=E multiple bonds, (where E = C, O, N, S, Se and Te).[49]Although a great deal of success has been experienced with this system, it still has a number of limitations, including the propensity to readily undergo potentially unwanted C-H activation reactivity as illustrated in Scheme 2-1.[78, 88, 89]



Scheme 2-1: *C-H activation reactivity of U[N(SiMe$_3$)$_2$]$_4$*

Aside from C-H activation, the size of the amido ancillary ligand also limits access to the metal center, and thereby affects the reactivity of the system. From the space-filling model below (Figure 2-2), it can be seen that the size of the reagents used during the oxidation chemistry of the system is limited to smaller functionalities, such that the steric bulk of the resulting complex can be accommodated.[78, 84]

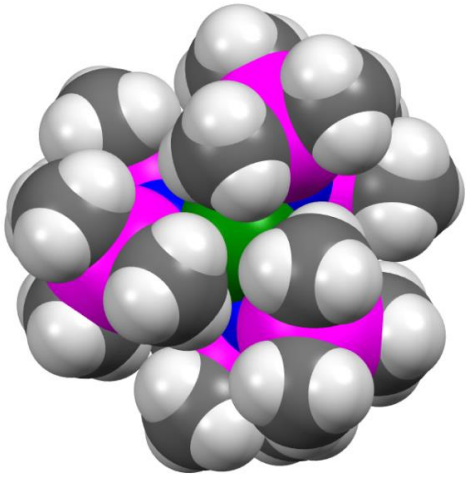
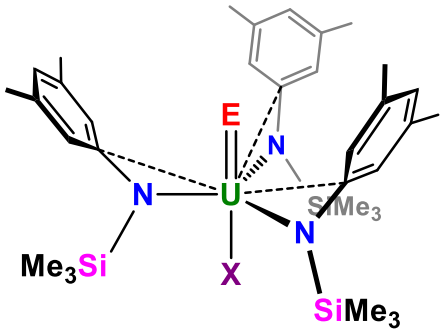


Figure 2-3: *Space filling model of $U[N(SiMe_3)_2]_3$*

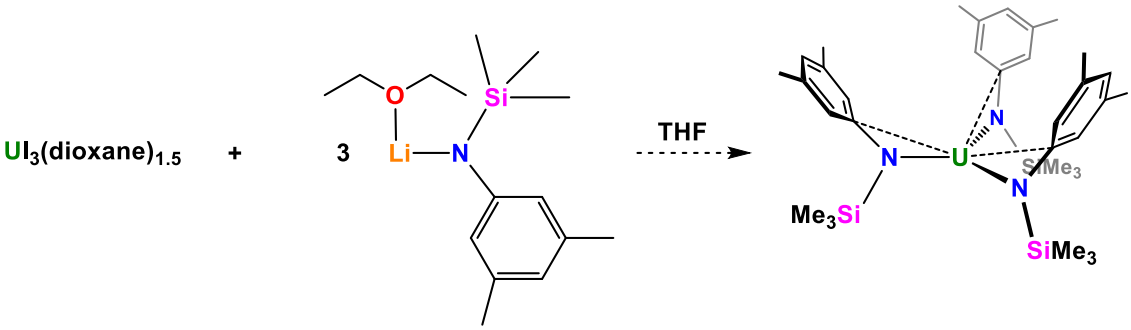
Due to the limitations associated with this ligand platform, and the success it has had in stabilizing U=E functionalities, we endeavored to fine tune the ancillary amido ligand. When designing the new framework, it was desired to utilize a ligand that would provide increased access to the metal center to accommodate a wider array of U=E(R) functionalities. It was reasoned that, by keeping the $SiMe_3$ functionality in the ligand, it could provide a potential platform for Me_3Si-X elimination under oxidative conditions, enabling the synthesis of uranium imido complexes. Consequently, we chose to utilize the $[N(SiMe_3)(3,5\text{-}Me_2C_6H_3)]$ ligand pioneered by Mashima and coworkers for our subsequent studies.[90] The 3,5-dimethylaryl functionality was chosen as it is planar and can allow for more steric access to the metal center. With this in mind, we hoped to generate new X-U=E complexes of the type shown below in (Figure 2-4) to enable the study of the extent of bond strengthening observed in the ITI.



E = C, N, O, P, S, Se, Te
X = Strong π-donor

Figure 2-4: *Targeted anilido type complexes*

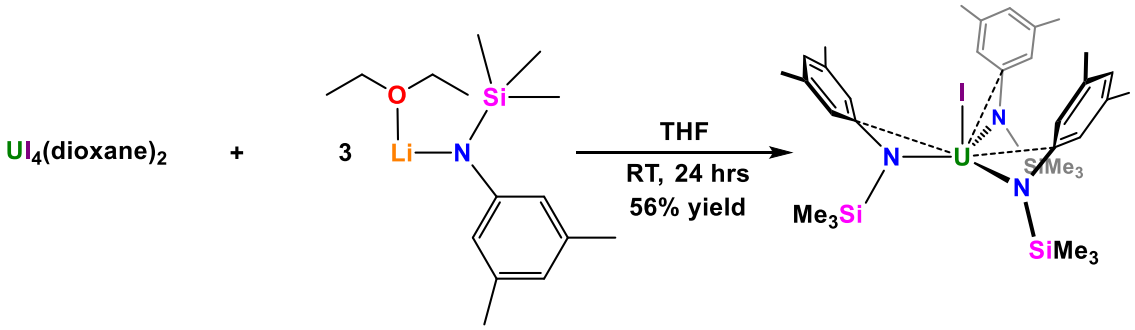
To test the utility of this anilido framework, 3 equiv. of the lithium salt of the ligand [Li•(OEt_2)][N($SiMe_3$)(3,5-$Me_2C_6H_3$)] were added to one equiv. of the readily prepared trivalent uranium starting material UI_3(1,4-dioxane)$_{1.5}$ in tetrahydrofuran (THF), in an attempt to prepare a tris(amido) complex analogous to what was observed by Anderson and coworkers as shown in Scheme 2-2.[80, 88]



Scheme 2-2: *Attempted synthesis of U[N($SiMe_3$)(3,5-$Me_2C_6H_3$)]$_3$ by salt metathesis with a U(III) starting material.*

Rather than generating the desired U[N($SiMe_3$)(3,5-$Me_2C_6H_3$)]$_3$ complex, an unexpected disproportionation reaction was observed to generate a uranium(IV) complex: [L]$_3$UI (**2.1**) and an uncharacterized byproduct. Iodo complex **2.1** was recrystallized from hexanes at room temperature in 26%

isolated yield and characterized by ^{1}H NMR spectroscopy and single crystal X-ray diffraction. Complex **2.1** was also synthesized rationally from one equiv. of the readily prepared uranium (IV) precursor $UI_4(1,4\text{-dioxane})_2$ and 3 equiv. of $[Li•(OEt_2)][N(SiMe_3)(3,5\text{-}Me_2C_6H_3)]$ as shown in Scheme 2-3. Using this approach, **2.1** was isolated as a highly hexanes soluble red-orange powder in 56% isolated yield.



Scheme 2-3: *Synthesis of $[L]_3U(I)$ (**2.1**) from $UI_4(1,4\text{-dioxane})_2$*

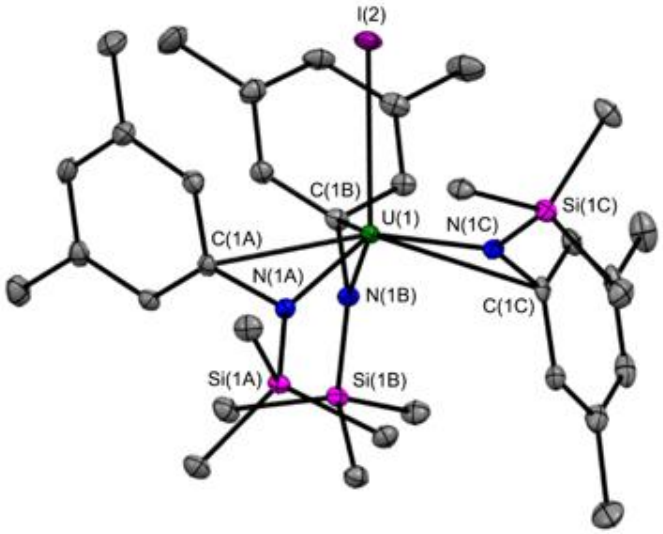


Figure 2-5: *ORTEP Depiction of $(I)U[N(SiMe_3)\{3,5\text{-}(CH_3)_2(C_6H_3)\}]$ (**2.1**) with elliposoids shown at 50% probability. Hydrogen atoms omitted for clarity.*

Table 2-1: *Selected bond distances (Å) and angles (°) for* ***2.1***

Bond	Bond Distance (Å)	Bond Angle	Angle (°)
U(1)-I(2)	3.0358(3)	I(2)-U(1)-N(1A)	117.70(5)
U(1)-N(1A)	2.211(2)	I(2)-U(1)-N(1B)	121.21(5)
U(1)-N(1B)	2.214(2)	I(2)-U(1)-N(1C)	94.34(5)
U(1)-N(1C)	2.193(2)	N(1A)-U(1)-C(1A)	31.14(7)
U(1)-C(1A)	2.769(2)	N(1B)-U(1)-C(1B)	30.94(7)
U(1)-C(1B)	2.764(2)	N(1C)-U(1)-C(1C)	29.92(7)
U(1)-C(1C)	2.823(3)	N(1A)-U(1)-N(1B)	101.79(7)
N(1A)-Si(1A)	1.745(2)	N(1A)-U(1)-N(1C)	100.89(7)
N(1B)-Si(1B)	1.737(2)	N(1B)-U(1)-N(1C)	120.05(7)
N(1C)-Si(1C)	1.746(2)	Si(1A)-N(1A)-U(1)	146.33(11)
		Si(1B)-N(1B)-U(1)	141.51(11)
		Si(1C)-N(1C)-U(1)	146.33(11)

Complex **2.1** exhibits solvatochromism changing color from red-orange to green upon dissolution in THF. This complex is formally U(IV) and adopts a pseudo tetrahedral environment, as demonstrated by the solid-state structure shown in Figure 2-5. Complex **2.1** exhibits a U(1)-I(2) bond distance of 3.0358(3) Å (Table 2-1), which is similar to other reported U(IV) U-I bond distances.[82] Additionally, this complex showcases the electrophilic nature of the U(IV) metal center with a short average U-C_{ipso} distance of 2.785 Å, indicating donation from the aryl π-system to the metal center. This length is shorter by about 0.12 Å than the average U-C_{ipso} distances for the U(III) tris(anilido) complex (THF)U[N(^{t}Bu)(3,5-$Me_2C_6H_3$)]$_3$ reported by Cummins and coworkers.[81] This indicates increased π-donation from the aryl system in the U(IV) complex **2.1** than in the U(III) tris(anilido) complex reported by Cummins and coworkers. Interestingly, in complex **2.1,** one of the anilido ligands differs in its bonding vs. the other two. The U(1)-N(1C) bond distance is ~0.02 Å shorter than the U(1)-N(1A) and U(1)-N(1B) distances with a distance of 2.193(2) Å. Additionally, the

anilido group bound through N(1C) exhibits a longer U-C_{ipso} distance than the other two anilido ligands by approximately 0.06 Å. This observation also correlates well with the 3.9° increase in C_{ipso}-N(1C)-U(1) bond angle. The difference in bonding observed for the N(1C) amido ligand can be attributed in part to steric requirements that enable all three anilido ligands and the iodo ligand to be accommodated by the metal center. The *ipso*-C coordinated [N($SiMe_3$)(3,5-$Me_2C_6H_3$)] ligand is structurally similar to the benzyl (CH_2Ph) ligand in its higher hapticity bonding capabilities. Kiplinger and coworkers have shown that a [N($SiMe_3$)(Ph)] ligand in (η^5-C_5Me_5)$_2$U(Cl)[N($SiMe_3$)(Ph)] binds in an η^3-(N, C, C′) fashion.[74] In order to quantify the extent of aryl to metal interaction found in these anilido systems, the following parameters have been identified: Δ and Δ′. Δ= [MC_{ortho}-MN]-[MC_{ipso}-MN] and Δ′=[MC_{ortho}′-MN]-[MC_{ipso}-MN], where MC_{ortho} is the shorter metal to ortho carbon bond distance, MN is the metal to anilido nitrogen distance, and MC_{ortho}′ is the longer metal to ortho carbon distance.[74, 91, 92] It is been determined that larger differences between Δ and Δ′ are indicative of η^3-interactions and smaller differences indicate η^4-behavior.[74] In **2.1**, the differences between Δ and Δ′ are considerably smaller than that reported for (η^5-C_5Me_5)$_2$U(Cl)[N($SiMe_3$)(Ph)] (avg: 1.013).[74] Additionally, the average U-C_{ipso} distance in complex **2.1** is substantially shorter (~2.786 Å) than for (η^5-C_5Me_5)$_2$U(Cl)[N($SiMe_3$)(Ph)] (2.979 Å). The U-C_{ortho} distances are, however, comparable (avg: ~3.252 Å) for complex **2.1** and 3.179 Å for (η^5-C_5Me_5)$_2$U(Cl)[N($SiMe_3$)(Ph)]. From these distances, we can conclude that the bonding interaction for the aryl system is η^4 for two of the anilido ligands in **2.1**.

The difference in hapticity of the aryl systems between complex **2.1** and (η^5-$C_5Me_5)_2U(Cl)[N(SiMe_3)(Ph)]$ may be explained by the increased steric access to the metal center complex **2.1** has as a result of the lack of bulky (η^5-C_5Me_5) ancillary ligands.

Table 2-2: *Bond distances (Å) for U(1)-N and U(1)-C(aryl) interactions for* ***2.1***

Ligand	U-N	U-C_{ipso}	U-C_{ortho}[a]	U-$C_{ortho'}$[b]	Δ[c]	Δ′[d]	Δ′-Δ[c,d]
(1A)	2.211(2)	2.769(2)	3.214	3.604	0.4448	0.8348	0.39
(1B)	2.214(2)	2.764(2)	3.203	3.593	0.4388	0.8288	0.39
(1C)	2.193(2)	2.823(3)	3.341	3.662	0.5177	0.8387	0.321

[a] C_{ortho} is the aromatic *ortho* carbon closer to the uranium center
[b] C_{ortho}' is the aromatic *ortho* carbon further from the uranium center
[c] $\Delta=[(U\text{-}C_{ortho})\text{-}(U\text{-}N)]\text{-}[(U\text{-}C_{ipso})\text{-}(U\text{-}N)]$
[d] $\Delta'=[(U\text{-}C_{ortho'})\text{-}(U\text{-}N)]\text{-}[(U\text{-}C_{ipso})\text{-}(U\text{-}N)]$

In solution, **2.1** exhibits C_{3v} symmetry, explained with a simple paramagnetically shifted ^1H NMR spectrum (Figure 2-6). Complex **2.1** exhibits drastically different ^1H NMR chemical shifts to $IU[N(^tBu)(3,5\text{-}Me_2C_6H_3)]_3$ reported by Cummins and coworkers.[81] This is interesting because the only difference between the two complexes is the use of $SiMe_3$ in complex **2.1** instead of CMe_3 in $IU[N(^tBu)(3,5\text{-}Me_2C_6H_3)]_3$.

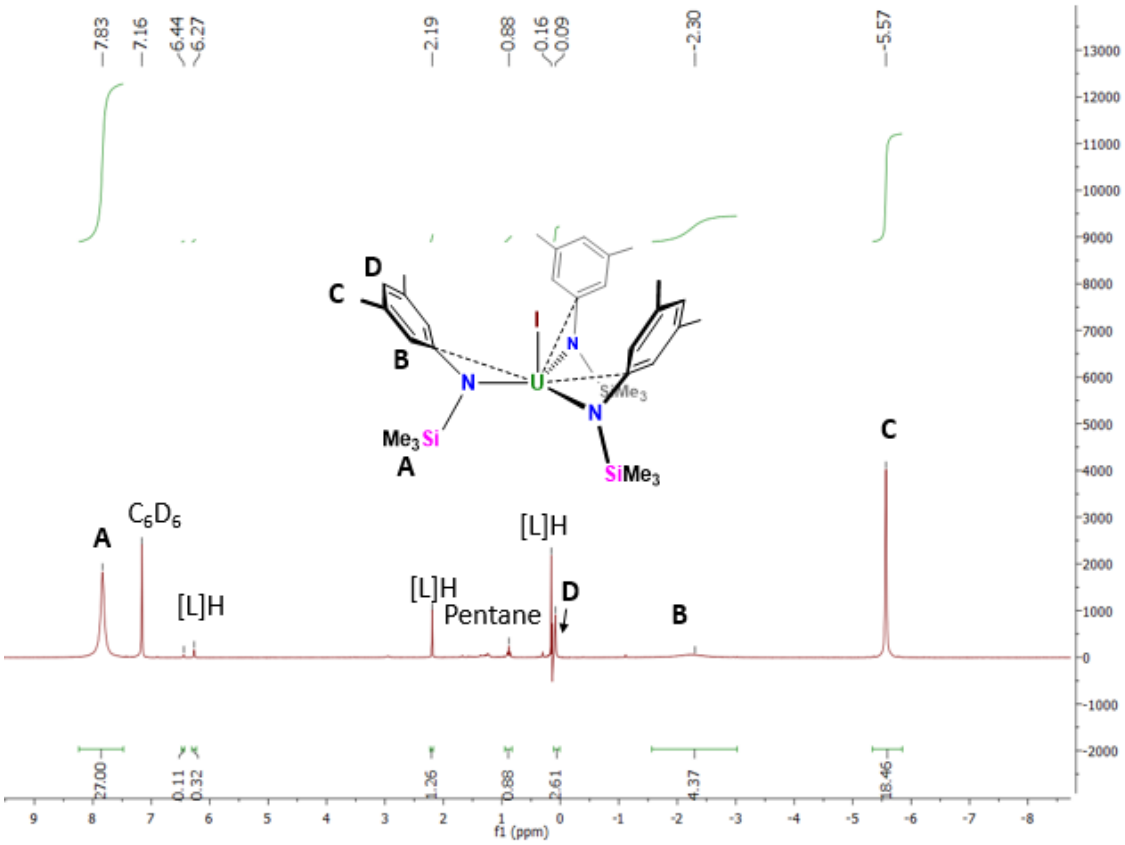


Figure 2-6: *300 MHz ^{1}H NMR Spectrum of (I)U[N(SiMe$_3$)(3,5-(CH$_3$)$_2$(C$_6$H$_3$)]$_3$ (**2.1**) in C$_6$D$_6$*

Table 2-3: *Comparison of ^{1}H NMR chemical shifts (ppm) of complex **2.1** and IU[N(^{t}Bu)(3,5-Me$_2$C$_6$H$_3$)]$_3$*

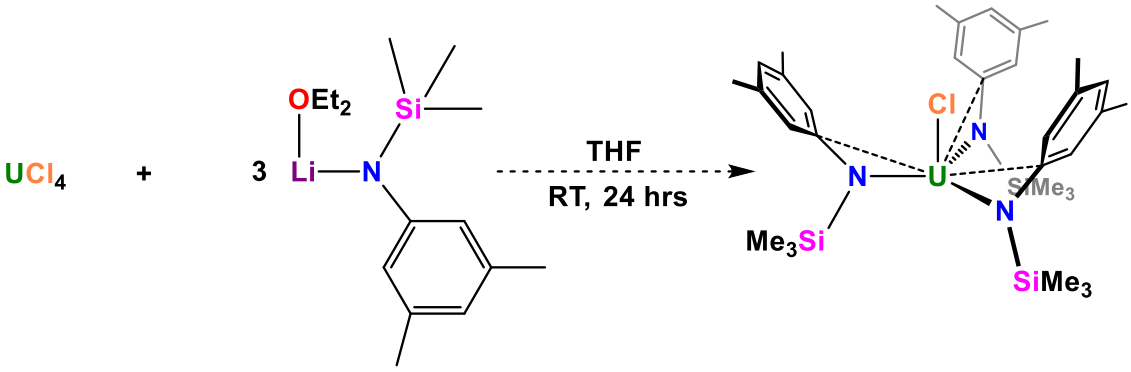
Complex 2.1		**IU[N(^{t}Bu)(3,5-Me$_2$C$_6$H$_3$)]$_3$**	
Proton Type	**Chemical Shift (ppm)**	**Proton Type**	**Chemical Shift (ppm)**
Si(C*H*$_3$)$_3$	7.83	C(C*H*$_3$)$_3$	11.26
o-Ar	-2.30	*o*-Ar	6.6
Aryl-C*H*$_3$	-5.57	Aryl-C*H*$_3$	-4.77
p-Ar	0.09	*p*-Ar	-0.30

The chemical shift for the SiMe$_3$ group is considerably upfield shifted from the CMe$_3$ peak in (I)U[N(^{t}Bu)(3,5-Me$_2$C$_6$H$_3$)]$_3$ (*vide supra*). This, however, can be attributed to the greater shielding nature of the more diffuse 3*p* orbitals of silicon. The chemical shift assigned for the aryl-methyl protons in **2.1** is slightly more shielded with a peak at δ -5.57 vs. δ -4.77 in (I)U[N(^{t}Bu)(3,5-Me$_2$C$_6$H$_3$)]$_3$. The *para*

protons of the aryl system are similar between the two complexes with a peak at δ 0.09 for complex **2.1** and δ -0.30 for (I)U[N(^{t}Bu)(3,5-$Me_2C_6H_3$)]$_3$. Additionally, the chemical shifts for the *ortho*-protons of the aryl system for the two complexes differ significantly with a peak at δ -2.30 for complex **2.1** and a peak at δ 6.60 for (I)U[N(^{t}Bu)(3,5-$Me_2C_6H_3$]$_3$.[81] From these results, it can be concluded that the use of a silicon atom in the ancillary ligand backbone in **2.1** plays a significant role in altering the electronics of the uranium tris(anilido) complex.

2.3: Synthesis and characterization of chloro tris(anilido) uranium complexes

Since UI_4(1,4-dioxane)$_2$ is prepared from uranium turnings, which are not always readily available, and the other common U(IV) starting material UCl_4, is prepared from the more readily available oxide UO_3, it was determined that it would be useful to generate the chloro analog (Cl)U[N($SiMe_3$)(3,5-$(CH_3)_2(C_6H_3)$)]$_3$ via synthesis from UCl_4 and 3 equiv. of [Li•(OEt_2)][N($SiMe_3$)(3,5-$(Me_2C_6H_3)$] (Scheme 2-4).[88, 93] This preparation would have a greater universal utility as a potential platform for generating U=E bonds, since UCl_4 can be generated from easier to obtain uranium starting materials. Upon characterizing the product of this reaction, it was determined that a solvated LiCl adduct [(THF)(Et_2O)LiCl]•(Cl)U[N($SiMe_3$)(3,5-$(CH_3)_2(C_6H_3)$)]$_3$ (**2.2**) was isolated (Figure 2-7) instead of the intended product (Cl)U[N($SiMe_3$)(3,5-$(CH_3)_2(C_6H_3)$)]$_3$.



Scheme 2-4: *Attempted synthesis of (Cl)U[N(SiMe$_3$)(3,5-(CH$_3$)$_2$(C$_6$H$_3$))]$_3$ (**2.3**) from UCl$_4$ and [Li(OEt$_2$)][N(Si(Me$_3$)(3,5-(CH$_3$)$_2$(C$_6$H$_3$)]*

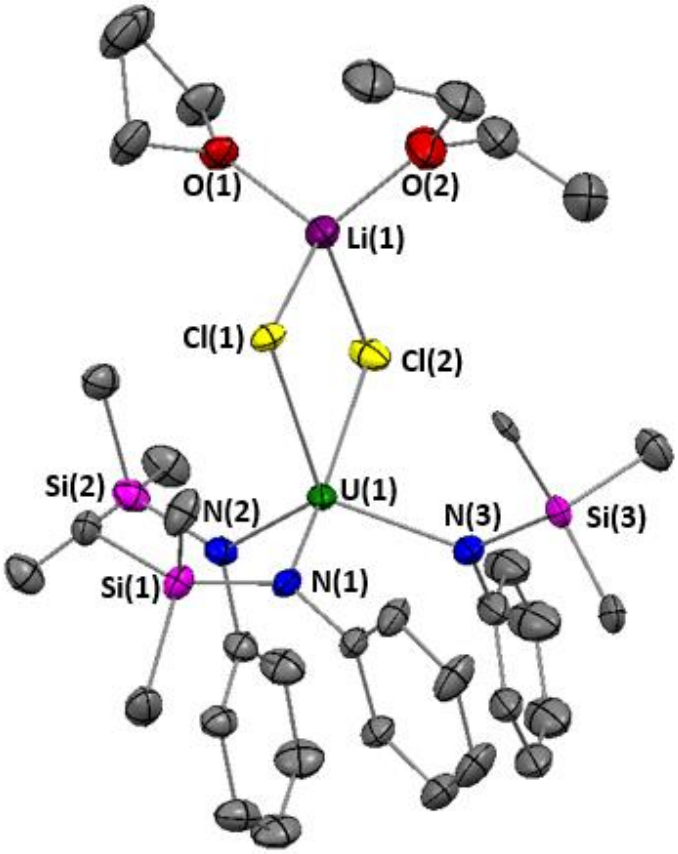


Figure 2-7: *ORTEP Depiction of [(THF)(Et$_2$O)LiCl][(Cl)U[N(SiMe$_3$)(3,5-(CH$_3$)$_2$(C$_6$H$_3$)]$_3$ (**2.2**) with ellipsoids shown at 30% probability. Hydrogen atoms and aryl-CH$_3$s omitted for clarity.*

Table 2-4: *Table of selected bond distances (Å) and angles (°) for* ***2.2***

Bond[a,b]	Bond Distance (Å)	Bond Angle	Bond Angle (°)
U(1)-N(1)	2.221(4)	C_{ipso}(1)-U(1)-N(1)	21.5(1)
U(1)-N(2)	2.217(4)	C_{ipso}(2)-U(1)-N(2)	25.4(1)
U(1)-N(3)	2.251(4)	C_{ipso}(3)-U(1)-N(3)	22.5(1)
U(1)-Cl(1)	2.7429(10)	Cl(1)-U(1)-N(1)	88.79(1)
U(1)-Cl(2)	2.7696(13)	Cl(1)-U(1)-N(2)	116.64(10)
U(1)-C_{ipso}(1)	3.080	Cl(1)-U(1)-N(3)	126.42(11)
U(1)-C_{ipso}(2)	3.194	Cl(2)-U(1)-N(1)	165.49(9)
U(1)-C_{ipso}(3)	3.251	Cl(2)-U(1)-N(2)	88.29(10)
Si(1)-N(1)	1.738(4)	Cl(2)-U(1)-N(3)	86.92(11)
Si(2)-N(2)	1.763(7)	Si(1)-N(1)-U(1)	125.49(18)
Si(3)-N(3)	1.744(4)	Si(2)-N(2)-U(1)	131.43(19)
Cl(1)-Li(1)	2.402(9)	Si(3)-N(3)-U(1)	119.9(3)
Cl(2)-Li(1)	2.338(8)	N(1)-U(1)-N(2)	103.10(13)
O(1)-Li(1)	1.935(9)	N(1)-U(1)-N(3)	96.43(14)
O(2)-Li(1)	1.914(10)	N(2)-U(1)-N(3)	113.86(15)
U-C_{ortho}(1)	3.657	Cl(1)-U(1)-Cl(2)	77.95(3)
U-C_{ortho}(2)	3.831	O(1)-Li(1)-O(2)	106.0(4)
U-C_{ortho}(3)	3.924	O(1)-Li(1)-Cl(1)	110.2(4)
U-C_{ortho}'(1)	4.013	O(2)-Li(1)-Cl(2)	110.7(4)
U-C_{ortho}'(2)	4.104	Cl(1)-Li(1)-Cl(2)	94.0(3)
U-C_{ortho}'(3)	4.191		

[a]U-C_{ortho} denotes shorter U-C aromatic *ortho* carbon bond distance for each ligand (1, 2, 3)
[b]U-C_{ortho}' denotes longer U-C aromatic *ortho* carbon bond distance for each ligand (1, 2, 3)

Structurally, complex **2.2** adopts a distorted trigonal bipyramidal geometry about the uranium metal center, with N(1) and Cl(2) being axial, and a distorted tetrahedral geometry about the lithium metal center. Bond angles about the trigonal bipyramidal uranium metal center are distorted from an idealized geometry in order to accommodate three fairly bulky anilido ligands and two chlorido ligands. Additionally, in order to accommodate a distorted trigonal bipyramidal geometry about the uranium metal center (preferred Cl(1)-U(1)-Cl(2) bond angle of 90°), the Cl(1)-Li(1)-Cl(2) bond angle distorts from an idealized 109.5° to 94.02° to accommodate both the preferred tetrahedral geometry for the lithium center and the trigonal bipyramidal geometry for the uranium center. The

average U-Cl bond distance for **2.2** is about 2.7563 Å and is considerably longer than the U-Cl bond distance of 2.593 Å for U(Cl)[N(SiMe$_3$)$_2$]$_3$, a similar U(IV) tris(amido) uranium complex reported by Ephritikhine and coworkers.[94] Additionally the U-Cl bond distance for complex **2.2** is significantly longer than the U-Cl bond distance reported in a uranium anilido complex that utilizes a similar anilido ligand frame work; 2.5991 Å for (C$_5$Me$_5$)$_2$U(Cl)[N(SiMe$_3$)(Ph)] reported by Kiplinger and coworkers.[74] The average U-N bond distance of 2.230 Å for complex **2.2**, however, is in good agreement with U-N bond distances reported for other U(IV) tris(amido/anilido) complexes.[74, 83, 94] Unlike **2.1**, the average U-C$_{ipso}$ and U-C$_{ortho}$ bond lengths are quite long, indicating a significant decrease in π-electron donation from the aryl system to the metal center. As a result, it can be concluded that the aryl system does not bond η^4 like in complex **2.1**, but is only bound κ^1 through the anilido nitrogen.

In solution, **2.2** displays C$_{3v}$ symmetry when triturated with THF followed by removal of the solvent *in vacuo* (Figure 2-8). From the ^{1}H NMR spectrum (*vide infra*), we can see a down field shift for the Si(C*H*$_3$)$_3$ protons in complex **2.2** from the same group in complex **2.1**. For all other protons in complex **2.2**, we observe up field shifts when compared to the same groups in complex **2.1**. This observation is most likely explained by the difference in electronegativity between Cl and I for the two complexes.

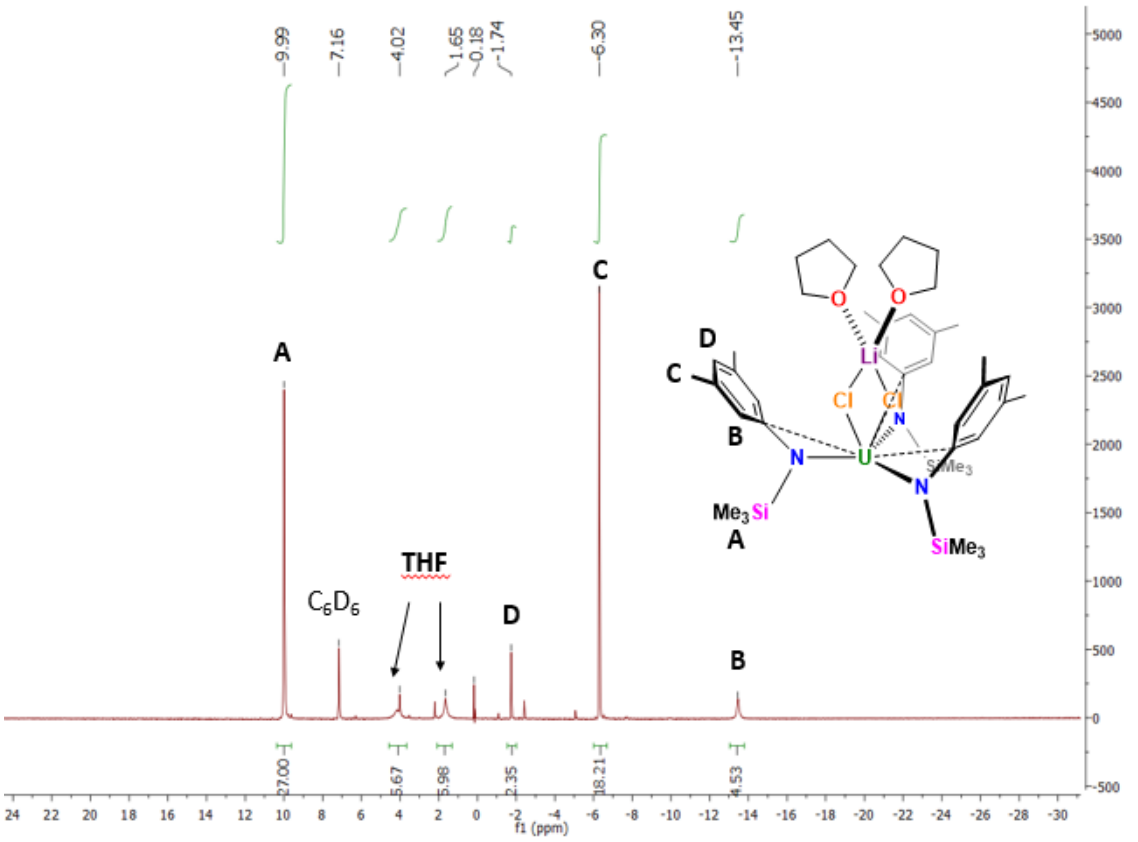


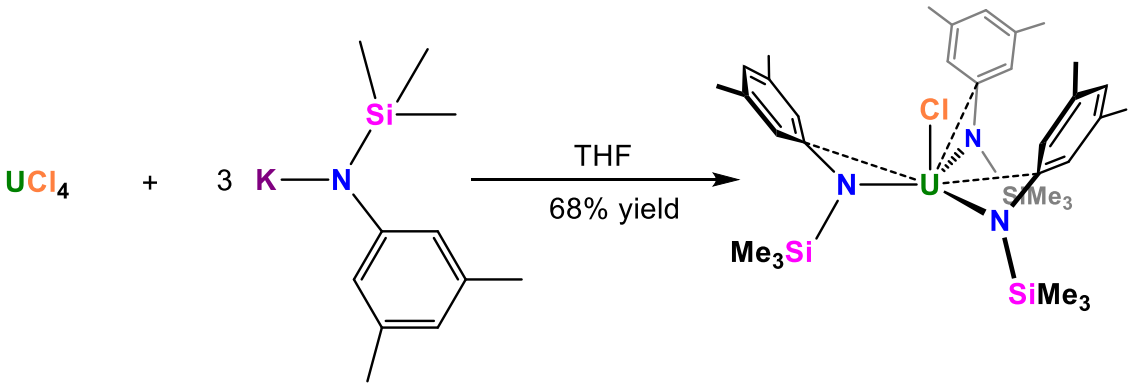
Figure 2-8: *300 MHz ^{1}H NMR spectrum of $(THF)_2$[LiCl]• [(Cl)U[N(SiMe$_3$)(3,5-$(CH_3)_2(C_6H_3)]_3$ (**2.2**) in C_6D_6*

Table 2-5: *Comparison of ^{1}H NMR chemical shifts (ppm) for **2.1** and **2.2***

Proton Type	Complex 2.1	Complex 2.2
Si(CH_3)$_3$	7.83	9.99
o-Ar	-2.30	-13.45
Ar-CH_3	-5.57	-6.30
p-Ar	0.09	-1.74

LiCl can be removed from complex **2.2** through extraction with pentane. This, however, leads to subsequent decomposition of **2.2** by means of disproportionation to generate varying amounts of proligand H[N(SiMe$_3$)(3,5-$(CH_3)_2(C_6H_3)$] and a homoleptic complex U[N(SiMe$_3$)(3,5-$(CH_3)_2(C_6H_3)]_4$ discussed *vide infra.*

(Cl)U[N(SiMe$_3$)(3,5-(CH$_3$)$_2$(C$_6$H$_3$)]$_3$ (**2.3**) can be generated from UCl$_4$ upon reaction with 3 equiv. of the potassium salt K[N(SiMe$_3$)(3,5-(CH$_3$)$_2$(C$_6$H$_3$)] as shown in Scheme 2-5. The use of the potassium salt of the ligand presumably does not generate an ate salt adduct complex[MCl]•[U(Cl)L$_3$] as seen with complex **2.2**.



Scheme 2-5: *Synthesis of (Cl)U[[N(SiMe$_3$)(3,5-(CH$_3$)$_2$(C$_6$H$_3$)]$_3$ (**2.3**) from UCl$_4$ and K[N(Si(Me$_3$)(3,5-(CH$_3$)$_2$(C$_6$H$_3$)]*

Complex **2.3** can be isolated as a golden-yellow powder, but all attempts to recrystallize this complex were unsuccessful. Complex **2.3** was, however, characterized by ^{1}H NMR spectroscopy (Figure 2-9) and displays C$_{3v}$ symmetry in solution. The simplicity of the spectrum and the integrations for each peak support a single ligand environment (i.e. the assignment of symmetry) in solution.

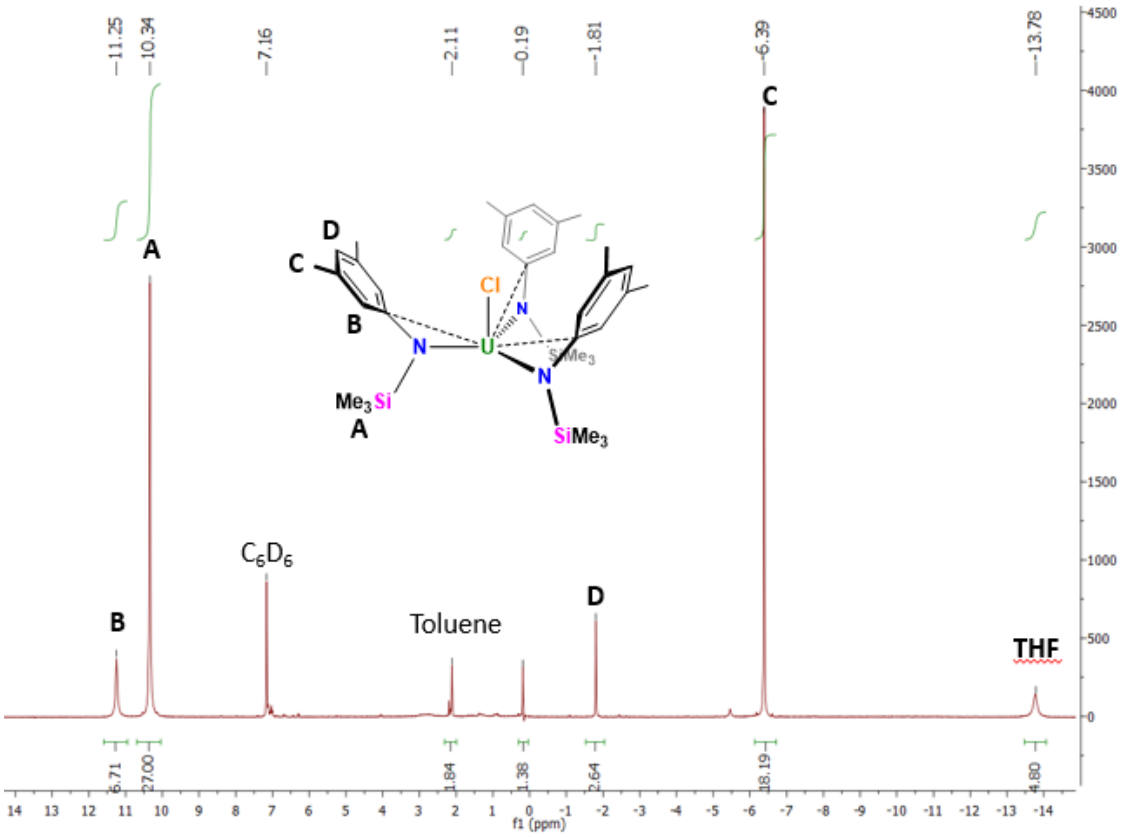
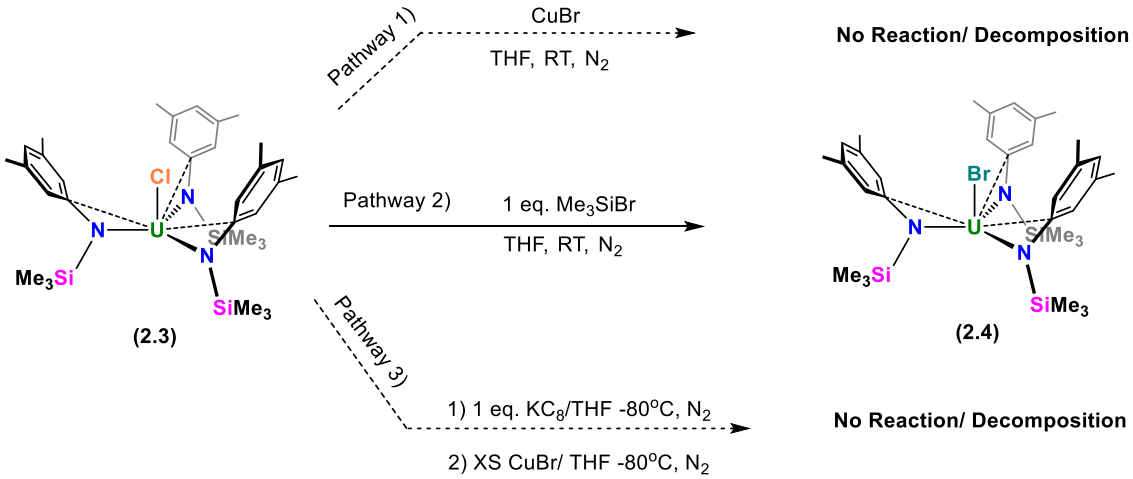


Figure 2-9: *300 MHz ^{1}H NMR Spectrum of (Cl)U[N(SiMe$_3$)(3,5-(CH$_3$)$_2$(C$_6$H$_3$)]$_3$ (**2.3**) in C$_6$D$_6$*

Complex **2.3** displays similar chemical shift behavior to complex **2.2** with a few notable exceptions. An additional down field shift of about δ 0.35 for the Si(C*H*$_3$)$_3$ protons is noted when compared to complex **2.2**. More noteworthy, however, is the chemical shift change for the *o*-aryl protons when compared to complex **2.2** from δ 13.45 in complex **2.2** to δ 11.25 in complex **2.3**. The reason for the magnitude of this chemical shift change is unknown, but may be attributed to the removal of an unusual shielding environment provided by the LiCl adduct in **2.2**. All other protons in **2.3** experience only a very slight up field shift when compared to analogous groups in complex **2.2**.

2.4: Synthesis and characterization of bromo anilido uranium complexes

Drastic changes observed in the chemical shifts for analogous protons in the ^{1}H NMR spectra for complexes **2.1**, **2.2** and **2.3** prompted attempts to prepare $[L]_3U(Br)$ and $[L]_3U(F)$. The generation of these complexes would be beneficial for cataloging the effect halogen identity has on ^{1}H NMR chemical shift for paramagnetic U(IV) anilido species. Despite the wide spread use of amido type ligands in stabilizing low valent uranium centers, only one study has examined how halogen identity affects ^{1}H NMR chemical shift for amido ligand containing uranium complexes.[74] A study examining this effect would have utility in the field since the present dearth of information on the subject makes it a herculean task to predict the ^{1}H NMR chemical shifts for paramagnetic uranium complexes. While attempting to generate $L_3U(Br)$, several approaches were attempted (Scheme 2-6).



Scheme 2-6: *Synthetic pathways for generating (Br)U[N(SiMe$_3$)(3,5-(CH$_3$)$_2$(C$_6$H$_3$)]$_3$* ***(2.4)***

Recently, Kiplinger and coworkers pioneered the use of CuBr and other copper halide salts to install U-X functionalities on low valent uranium systems.[48,

[95] Accordingly, this method was attempted first (Scheme 2-6, Path 1). Unfortunately, the reaction was unsuccessful, yielding only proligand [L]H and a disproportionation reaction product $U[N(SiMe_3)(3,5\text{-}(CH_3)_2(C_6H_3)]_4$ (*vide infra)*. The second attempt at generating this complex involved the use of 1 equiv. of $(CH_3)_3Si\text{-}Br$ with 1 equiv. of **2.3**. A completely pure powder not isolable from this reaction; however, characterization of the product by ^1H NMR spectroscopy suggests evidence for the formation of $(Br)U[N(SiMe_3)(3,5\text{-}(CH_3)_2(C_6H_3)]_3$ **2.4** (Figure 2-10).

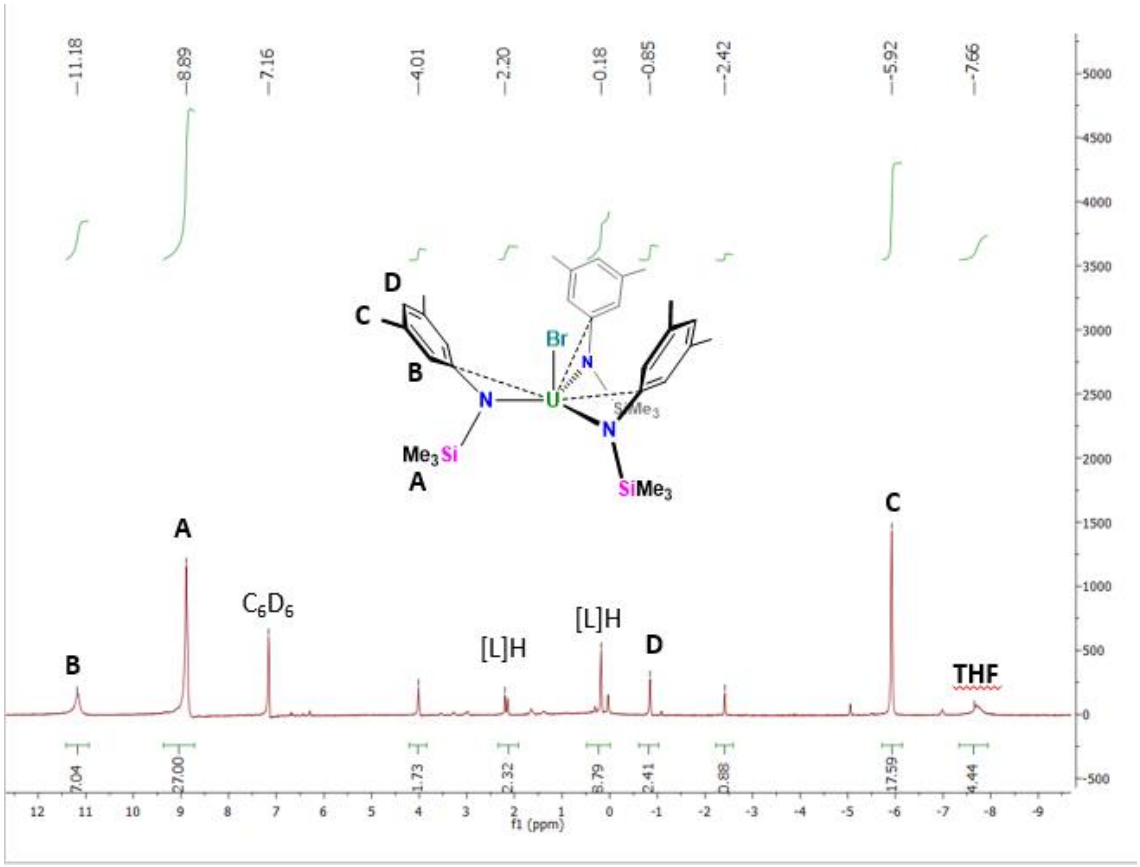


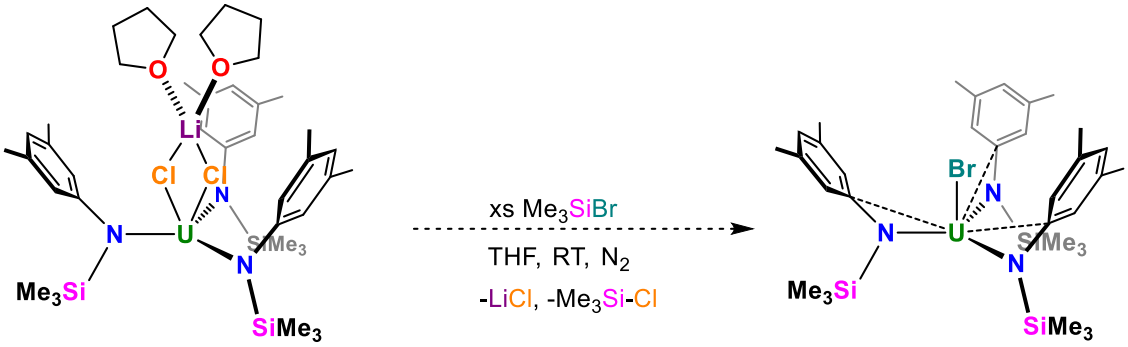
Figure 2-10: *300 MHz ^1H NMR spectrum of $(Br)U[N(SiMe_3)(3,5\text{-}(CH_3)_2(C_6H_3)]_3$* ***2.4*** *in C_6D_6*

Herein we observe downfield-shifted peaks at δ 11.18 (6H) for the *o*-aryl protons and δ 8.89 (27H) for the $Si(CH_3)_3$ protons. Additionally, upfield peaks are

observed at δ -0.85 (4H) for *p*-aryl protons and δ -5.92 (18H) for Ar-C*H*$_3$ protons. These observations coincide with chemical shift trends observed for complexes **2.1**, **2.2** and **2.3**. Since the ^{1}H NMR chemical shift trends match the trend observed with the chloro and iodo tris(anilido) analogs and the integrations match the values needed for (Br)U[N(SiMe$_3$)(3,5-(CH$_3$)$_2$(C$_6$H$_3$)]$_3$, it can be assumed that this complex is being generated as the major product for the reaction in Path 2 (Scheme 2-6). Due to the high solubility of both complex **2.4** and the proligand H[N(SiMe$_3$)(3,5-(CH$_3$)$_2$(C$_6$H$_3$)]$_3$ in most organic solvents, separation and complete isolation of **2.4** was unsuccessful. A third path that would hopefully generate **2.4** in higher purity was devised (Scheme 2-6, Path 3). This path utilized 1 equiv. of KC$_8$ to induce a one-electron reduction of complex **2.3**. This would in turn generate a transient U[L]$_3$ species *in situ* that would then be oxidized by an excess of CuBr. By design, this approach would take advantage of the propensity for a U(III) species to undergo rapid oxidation to U(IV) in the presence of an oxidizing agent. By adding an excess of CuBr, it was anticipated that the U(III) species would more than likely react with the CuBr generating the desired (Br)U[N(SiMe$_3$)(3,5-(CH$_3$)$_2$(C$_6$H$_3$)]$_3$ species. This would in turn limit the possibility for an unwanted disproportionation reaction to occur. Unfortunately, due to the poor solubility of CuBr and the strong propensity for the U(III) species to be oxidized, only the disproportionation product U[L]$_4$ (*vide infra*) was isolated.

While attempting to design a reaction pathway that would generate **2.4** in high purity, it was rationalized that complex **2.2** might serve as a more suitable starting material due to the added stability provided to the complex by the

coordination of LiCl. The presence of LiCl in this complex was hypothesized to provide enough steric protection to prevent unwanted disproprtionation reactivity from occurring, thereby making this complex an ideal starting material for the generation of complex (**2.4**). With this in mind, the synthesis shown in Scheme 2-7 was attempted.



2.2 **2.4**

Scheme 2-7: *Proposed pathway to generate complex **2.4** from complex **2.2***

Upon workup, green plate crystals were isolated from THF. To our surprise, instead of isolating complex **2.4** as intended, a trimetallic complex, $[L]_2U(\mu(\eta^1{:}\eta^1)Br)_2(\mu(\eta^1{:}\eta^1{:}\eta^1)BrLi(THF)_2)U[L]_2$ (where L = $[N(SiMe_3)(3,5\text{-}(CH_3)_2(C_6H_3)]$) (**2.5**), was isolated (Figure 2-11).

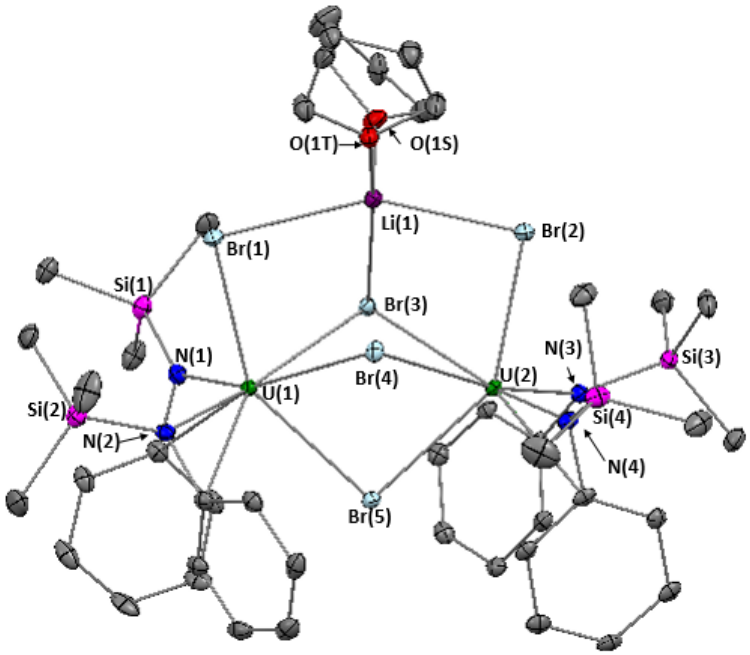


Figure 2-11: *ORTEP depiction of $[L]_2U(\mu(\eta^1{:}\eta^1)Br)_2(\mu(\eta^1{:}\eta^1{:}\eta^1)BrLi(THF)_2)U[L]_2$ (**2.5**) shown at 30% probability. Hydrogen atoms and aryl-CH_3s removed for clarity.*

Table 2-6: *Selected bond distances (Å) for **2.5***

Bond[a,b]	Distance (Å)	Bond[a,b]	Distance (Å)
U(1)-N(1)	2.214(3)	U(2)-N(3)	2.193(3)
U(1)-N(2)	2.187(3)	U(2)-N(4)	2.215(3)
U(1)-Br(1)	2.8253(4)	U(2)-Br(2)	2.8286(4)
U(1)-Br(3)	2.9489(3)	U(2)-Br(3)	3.0876(3)
U(1)-Br(4)	3.1184(4)	U(2)-Br(4)	2.9609(3)
U(1)-Br(5)	2.9605(3)	U(2)-Br(5)	2.9757(3)
U(1)-C_{ipso}(1)	2.843(3)	U(2)-C_{ipso}(3)	2.790(3)
U(1)-C_{ipso}(2)	2.788(3)	U(2)-C_{ipso}(4)	2.816(3)
U(1)-C_{ortho}(1)	3.253	U(2)-C_{ortho}(3)	3.422
U(1)-C_{ortho}'(1)	3.810	U(2)-C_{ortho}'(3)	3.472
U(1)-C_{ortho}(2)	3.410	U(2)-C_{ortho}(4)	3.196
U(1)-C_{ortho}'(2)	3.508	U(2)-C_{ortho}'(4)	3.778
Si(1)-N(1)	1.757(3)	Si(3)-N(3)	1.744(3)
Si(2)-N(2)	1.750(3)	Si(4)-N(4)	1.748(3)
Li(1)-Br(1)	2.906(5)	Li(1)-Br(2)	2.744(5)
Li(1)-Br(3)	2.907(6)	Li(1)-Br(4)	3.042(5)
Li(1)-O(1T)	1.956(6)	Li(1)-O(1S)	1.980(6)

[a]U-C_{ortho} denotes shorter U-C aromatic *ortho* carbon bond distance for each ligand (1 and 2)
[b]U-C_{ortho}' denotes longer U-C aromatic *ortho* carbon bond distance for each ligand (1 and 2)

Table 2-7: *Selected bond angles (°) for* ***2.5***

Bond Angle	Angle (°)	Bond Angle	Angle (°)
N(1)-U(1)-N(2)	99.84(10)	N(3)-U(2)-N(4)	97.30(10)
Br(1)-U(1)-N(1)	88.87(7)	Br(2)-U(2)-N(3)	90.69(7)
Br(1)-U(1)-N(2)	91.04(7)	Br(2)-U(2)-N(4)	91.98(7)
Br(1)-U(1)-Br(3)	80.448(10)	Br(2)-U(2)-Br(3)	75.860(10)
Br(1)-U(1)-Br(4)	77.968(10)	Br(2)-U(2)-Br(4)	80.330(10)
Br(1)-U(1)-Br(5)	146.054(10)	Br(2)-U(2)-Br(5)	143.954(10)
Br(3)-U(1)-N(1)	86.55(7)	Br(3)-U(2)-N(3)	95.52(7)
Br(3)-U(1)-N(2)	169.30(7)	Br(3)-U(2)-N(4)	160.10(7)
Br(3)-U(1)-Br(4)	74.756(9)	Br(3)-U(2)-Br(4)	74.774(9)
Br(3)-U(1)-Br(5)	74.517(9)	Br(3)-U(2)-Br(5)	72.294(9)
Br(4)-U(1)-N(1)	158.59(7)	Br(4)-U(2)-N(3)	169.83(7)
Br(4)-U(1)-N(2)	97.23(8)	Br(4)-U(2)-N(4)	87.83(7)
Br(4)-U(1)-Br(5)	73.620(9)	Br(4)-U(2)-Br(5)	75.445(9)
Br(5)-U(1)-N(1)	111.77(7)	Br(5)-U(2)-N(3)	110.18(7)
Br(5)-U(1)-N(2)	110.46(7)	Br(5)-U(2)-N(4)	113.09(7)
U(1)-N(1)-C_{ipso}(1)	100.32	U(2)-N(3)-C_{ipso}(3)	98.34
U(1)-N(2)-C_{ipso}(2)	98.44	U(2)-N(4)-C_{ipso}(4)	98.60
N(1)-U(1)-C_{ipso}(1)	29.68	N(3)-U(2)-C_{ipso}(3)	30.62
N(2)-U(1)-C_{ipso}(2)	30.67	N(4)-U(2)-C_{ipso}(4)	30.34
Si(1)-N(1)-U(1)	143.44(15)	Si(3)-N(3)-U(2)	141.54(15)
Si(2)-N(2)-U(1)	144.18(16	Si(4)-N(4)-U(2)	144.79(15)
U(1)-Br(3)-U(2)	91.392(9)	U(1)-Br(1)-Li(1)	90.03(10)
U(1)-Br(4)-U(2)	90.188(9)	U(2)-Br(2)-Li(1)	92.03(11)
U(1)-Br(5)-U(2)	93.423(9)	U(1)-Br(3)-Li(1)	87.63(10)
U(1)-Br(4)-Li(1)	82.30(11)	U(2)-Br(3)-Li(1)	83.91(11)
U(2)-Br(4)-Li(1)	83.47(10)	O(1T)-Li(1)-O(1S)	101.3(3)
Br(1)-Li(1)-Br(2)	153.6(2)	Br(2)-Li(1)-Br(3)	80.22(14)
Br(1)-Li(1)-Br(3)	79.83(14)	Br(2)-Li(1)-Br(4)	80.59(14)
Br(1)-Li(1)-Br(4)	78.03(13)	Br(3)-Li(1)-Br(4)	76.53(13)

In complex **2.5**, the uranium center is hexacoordinate and adopts a pseudo octahedral geometry, whereas the lithium center is pentacoordinate and adopts a trigonal bipyramidal geometry. This geometric assignment for the uranium center can be supported by the fact that many of the bond angles about the uranium center adopt angles close to the idealized angle of 90° for *cis* ligands within a true octahedral complex. An angle contraction is noted for many of the groups *trans* to one another within complex **2.5**. Optimally the angle between

these groups should be about 180° in a true octahedral complex, but the need to accommodate the octahedral environments of both uranium centers and the trigonal bipyramidal environment of the lithium center, forces many of the bond angles to contract and become more acute. This contraction allows for the formation of an idealized pseudo-octahedral equilibrium geometry for each uranium center in the complex. In general, the U-N and U-Br distances reported for complex **2.5** are in good agreement with other U-N and U-Br bond distances for related U(IV) species.[94, 96] The unique hetero trimetallic core of complex **2.5** (Figure 2-12) displays a U(μ(η^1:η^1)Br)$_2$(μ(η^1:η^1:η^1)Br Li(THF)$_2$)U halogen bridging motif. To date only one other complex reported by Marks and coworkers has a core similar to the core found in complex **2.5**.[97]

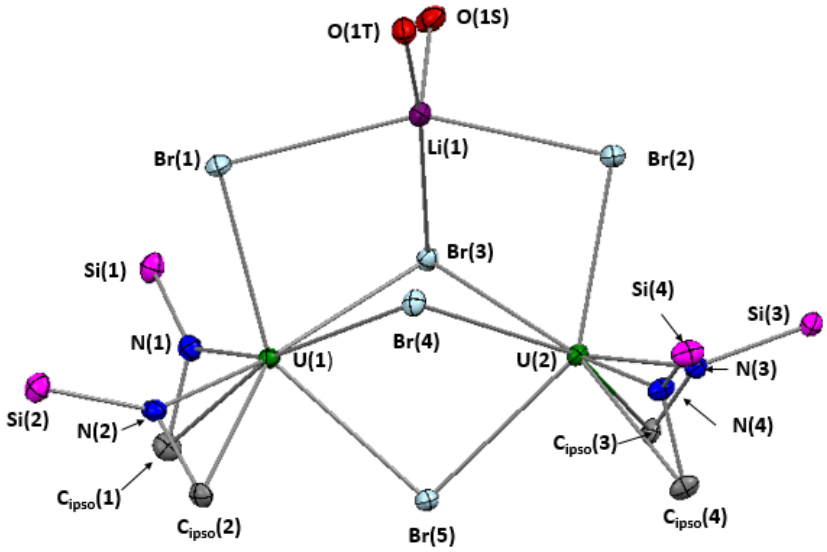


Figure 2-12: *Hetero trimetallic core of complex* ***2.5***

Table 2-8: *Selected bond distances (Å) for hapticity analysis for* ***2.5***

Ligand	U-N	U-C_{ipso}	U-C_{ortho}[a]	U-C_{ortho}'[b]	Δ[c]	Δ'[d]	Δ-Δ'[c,d]
L[N(1)]	2.214	2.843	3.253	3.810	0.41	0.967	0.557
L[N(2)]	2.187	2.788	3.410	3.508	0.622	0.72	0.098
L[N(3)]	2.193	2.790	3.422	3.477	0.632	0.687	0.055
L[N(4)]	2.215	2.816	3.196	3.778	0.38	0.962	0.582

[a]U-C_{ortho} denotes shorter U-C aromatic *ortho* carbon bond distance for each ligand (1, 2, 3, 4)
[b]U-C_{ortho}' denotes longer U-C aromatic *ortho* carbon bond distance for each ligand (1, 2, 3, 4)
[c]Δ=[(U-C_{ortho})-(U-N)]-[(U-C_{ipso})-(U-N)]
[d]Δ'=[(U-C_{ortho}')-(U-N)]-[(U-C_{ipso})-(U-N)]

From the hapticity analysis of complex **2.5** (Table 2-8), it was determined that the complex displays two different types of bonding interactions from the ligand aryl π- systems. Interestingly, each uranium metal center – U(1) and U(2) – contains a ligand that has the aryl system bound η^2: ligand L[N(2)] on U(1) and L[N(3)] on U(2). Each metal center also contains a ligand that has the aryl π-system bound η^3: L[N(1)] on U(1) and L[N(4)] on U(2). The η^2 designation was determined for ligands L[N(2)] and L[N(3)] since these ligands contain the shortest U-C_{ipso} bond distances and much longer U-C_{ortho} bond distances. The short U-C_{ipso} bond distances suggests a strong U-C_{ipso} interaction signifying that these ligands are at least bound η^2 from the aryl π-system and not just κ^1 through the anilido nitrogen. The average U-C_{ortho} bond distance for these ligands is about 0.192 Å longer than the average U-C_{ortho} bond distance for ligands L[N(1)] and L[N(4)]. This distance, however, is still about 0.4 Å shorter than the shortest U-C_{ortho} bond distance for complex **2.2**, which had no discernable U-C_{ortho} ligand interactions. This suggests that there is still a minor U-C_{ortho} interaction occurring with ligands L[N(2)] and L[N(3)]. Assuming this to be the case, it was determined that at least two ligand aryl carbons are interacting with the uranium metal centers for ligands L[N(2)] and L[N(3)], justifying the η^3 designation used with these

ligands. As discussed previously, the η^3 designation for ligands L[N(1)] and L[N(2)] was determined since the average U-C_{ortho}' bond distance (3.794 Å) is 0.361 Å shorter than the U-C_{ortho}' bond distance observed with Kiplinger's η^3 bound $(C_5Me_5)_2U(Cl)[N(SiMe_3)(C_6H_5)]$ anilido complex, indicating a possible U-C_{ortho}' interaction.[74] This result along with a moderate difference between Δ and Δ' suggest that these ligands are more than likely bound η^3 through the C_{ortho}', C_{ipso} and C_{ortho} carbons of the aryl π-system.

The unique difference in hapticity observed with the two sets of ligands on each uranium center can in part be explained by the sterics of the system. In the case of **2.5**, the anilido ligands adopt N-U-N' bond angles of less than 100°. In complexes **2.1** and **2.2**, however, the N-U-N' anilido bond angles are all greater than 100°. The contraction observed with the N-U-N' bond angles experienced in complex **2.5** forces the bulky anilido ligands to be in closer proximity to one another. This in turn adds unwanted steric pressure to the system. From Figure 2-11, we can also see that the aryl groups are all down on the bottom half of the molecule near Br(5).This forces the aryl groups to be in close proximity to one another and can lead to some repulsion between the groups. This repulsion is partly responsible for the difference in hapticity observed for the sets of anilido ligands as two of the aryl groups may be forced further away from the uranium centers preventing necessary U-C_{ortho}' interactions for η^3 binding.

A ^{1}H NMR spectrum representative of the bulk material isolated from the reaction pathway displayed in Scheme 2-7 was collected (Figure 2-12). It can be

determined from the ^{1}H NMR spectrum that a mixture of **2.4**, **2.5**, U[L]$_4$ (*vide infra*) and [L]H was generated during the reaction.

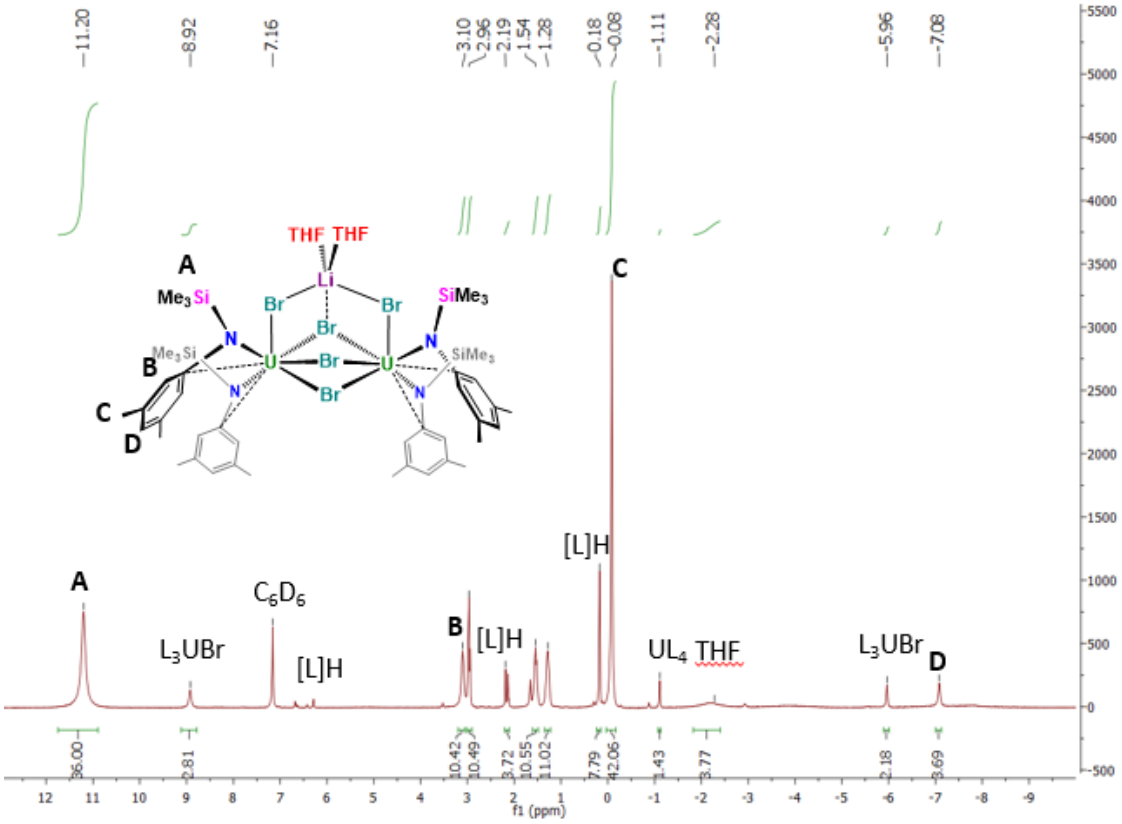


Figure 2-13: *300 MHz ^{1}H NMR spectrum of isolated products from reaction of* ***2.2*** *with excess Me_3Si-Br in C_6D_6. The major product (**2.5**) is shown inset.*

Although complex **2.5** is the major product, it is clear that other pathways are occurring during the reaction, resulting in the generation of other products. In an effort to cleanly isolate **2.5**, the reaction was repeated several times with varying amounts of Me_3Si-Br. All attempts to remake and isolate this complex, however, were unsuccessful. In an effort to better understand how complex **2.5** formed, a possible mechanism was rationalized and is displayed in Figure 2-14.

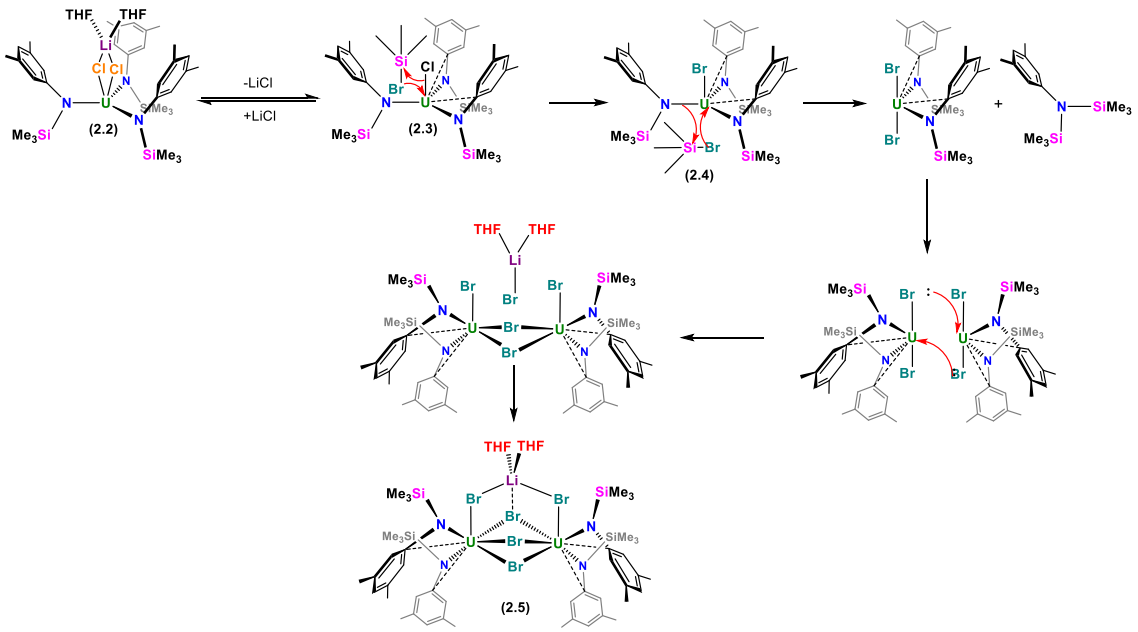
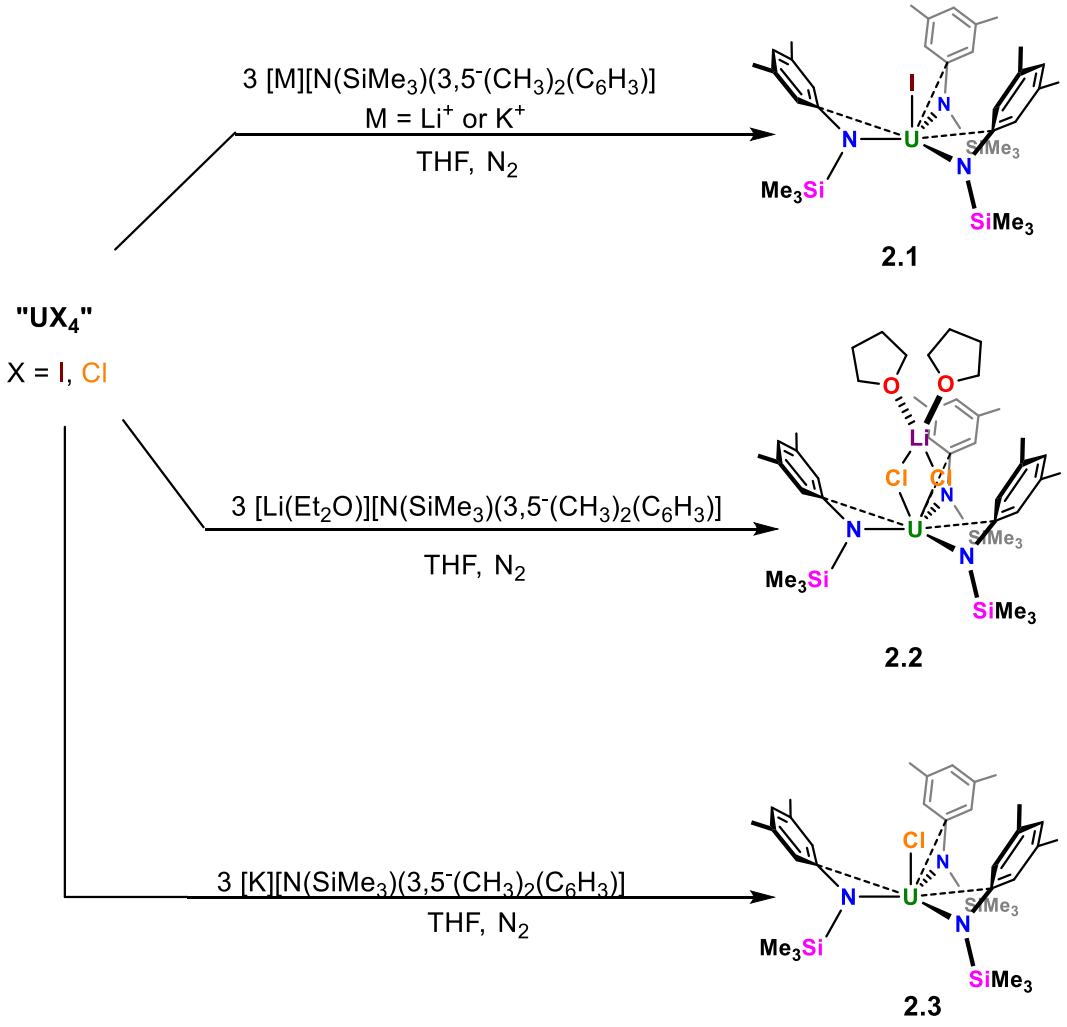


Figure 2-14: *Possible mechanism for the formation of complex* ***2.5***

It was rationalized that the first step of the process involves dissociation of LiCl from complex **2.2** to generate complex **2.3**. Next, complex **2.3** undergoes a σ-bond metathesis with 1 equiv. of Me_3Si-Br to generate complex **2.4**. Subsequently, a second equivalent of Me_3Si-Br presumably undergoes a second σ-bond metathesis with one of the [$N(SiMe_3)(3,5\text{-}(CH_3)_2(C_6H_3)$] ligands, thereby eliminating an equivalent of [$N(SiMe_3)_2(3,5\text{-}(CH_3)_2(C_6H_3)$] and generating $[L]_2U(Br)_2$ as an intermediate. Unfortunately, experimental evidence for the formation of [$N(SiMe_3)_2(3,5\text{-}(CH_3)_2(C_6H_3)$] was not observed. At this point, bromido ligands from two species of $[L]_2U(Br)_2$ form a bridging interaction, generating a homo bimetallic intermediate, which is then capped and stabilized with an equivalent of LiBr (formed by a σ-bond metathesis between LiCl and excess Me_3Si-Br), forming complex **2.5**.

Through the isolation of complexes **2.2** and **2.5**, it was discovered that the alkali metal counterion identity of the ligand salt [M][N(SiMe$_3$)(3,5-(CH$_3$)(C$_6$H$_3$)] (where M = Li$^+$ or K$^+$) used to generate the uranium tris(anilido) complexes, plays a significant role in the reactivity and stability of the [L]$_3$U(X) anilido complexes formed (Scheme 2-8), allowing some control over reactivity patterns.



Scheme 2-8: *Divergent reactivity influenced by ligand salt alkali metal counterion identity*

When using the lithium salt of the ligand to generate the uranium anilido complexes, it was found that the lithium halide byproduct generated during the reaction would end up coordinated to the uranium center(s) during the formation of (X)U[N($SiMe_3$)(3,5-(CH_3)$_2$(C_6H_3)]$_3$ (where X= Cl or Br). When the potassium salt of the ligand was used, however, coordination of the potassium halide byproduct to the uranium center(s) was not observed. Although potassium halides were not found to coordinate to the uranium centers of the tris(anilido) complexes, a disproportionation byproduct U[N($SiMe_3$)(3,5-(CH_3)$_2$(C_6H_3)]$_4$ was often observed by ^{1}H NMR spectroscopy when the potassium salt of the anilido ligand was used to generate the uranium anilido complexes. The homoleptic byproduct was not observed when the lithium salt of the anilido ligand was used to generate the tris(anilido)halo uranium complexes. From this observation, it was rationalized that coordination of a lithium halide salt to the uranium center stabilized the tris(anilido)halo uranium complexes and prevented formation of the disproportionation byproduct U[N($SiMe_3$)(3,5-(CH_3)$_2$(C_6H_3)]$_4$ (*vide infra*). To support this theory, the LiCl was removed from complex **2.2** to directly generate complex **2.3**. This was accomplished by extracting the (Cl)U[N($SiMe_3$)(3,5-(CH_3)$_2$(C_6H_3)]$_3$ complex with pentane and removing the LiCl byproduct via filtration over Celite. The uranium complex has high solubility in hydrocarbon solvents, making its extraction facile. As **2.3** is isolable using this extraction process, it demonstrates that the coordination of LiCl in complex **2.2** is a weak interaction. Upon removal of the LiCl from complex **2.2** and subsequent analysis of the uranium complex by ^{1}H NMR, it was found that the [L]$_3$U(Cl) complex

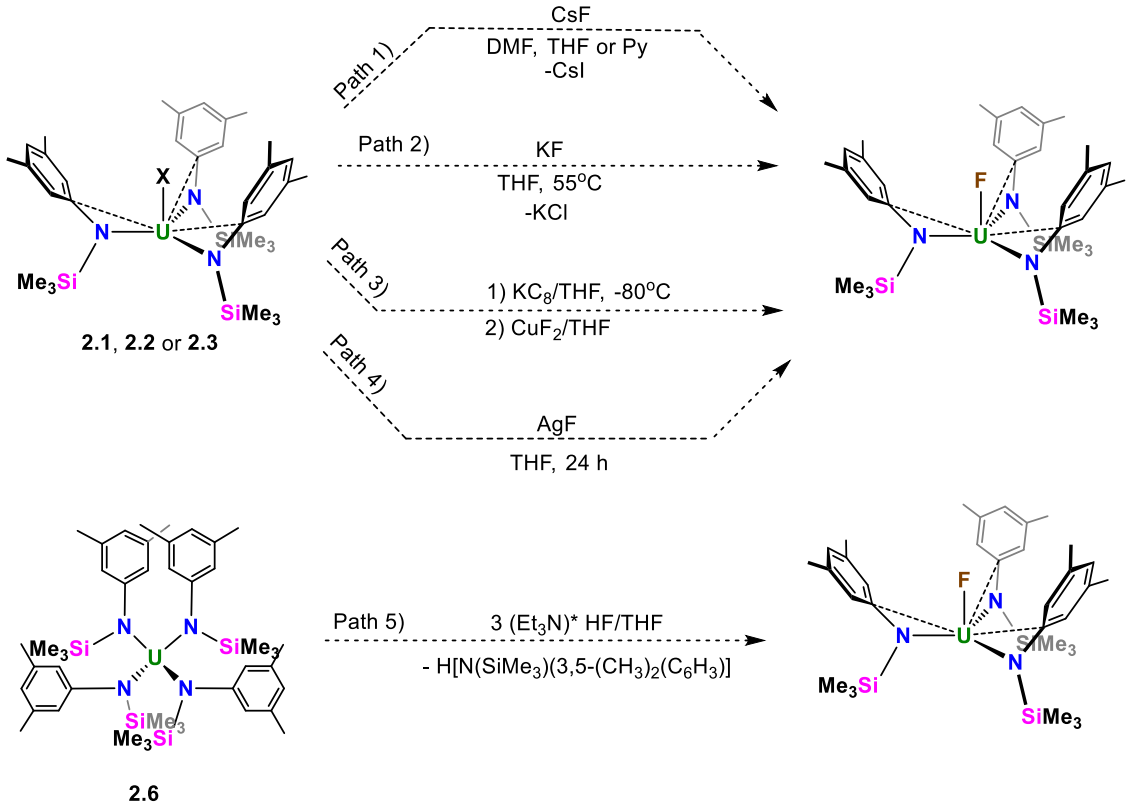
generated from this process readily disproportionates to generate a significant amount U[N(SiMe$_3$)(3,5-(CH$_3$)$_2$(C$_6$H$_3$)]$_4$ and an additional uncharacterized disproportionation byproduct. This in turn, supports the notion that the coordination of the lithium halide salt to the uranium center of the tris(anilido) complexes prevents unwanted disproportionation from occurring. Interestingly, when generating the iodo complex **2.1**, the identity of alkali metal counter ion of the ligand did not matter, as coordination of lithium iodide to the uranium center was not observed when [Li•(Et$_2$O)][N(SiMe$_3$)(3,5-(CH$_3$)(C$_6$H$_3$) was used to generate the tris(anilido) uranium complex, presumably because of the lower stability of LiI due to hard soft acid base theory.[98]

Aside from stabilizing the uranium tris(anilido)halo complexes from disproportionation, the coordination of these salts to the uranium tris(anilido) complexes also alters the reactivity of these uranium complexes. This observation can be seen with the formation of complexes **2.4** and **2.5**. When a lithium halide salt is present during the reaction intended to generate [L]$_3$U(Br), the lithium halide salt remains coordinated to the uranium center(s) and complex **2.5** is preferentially generated. In the absence of the lithium halide salt, however, the intended uranium tris(anilido) (**2.4**) is generated.

2.5: Attempts to generate (F)U[N(SiMe$_3$)(3,5-(CH$_3$)$_2$(C$_6$H$_3$)]$_3$

According to hard-soft acid base theory, fluorine is known to form a stronger interaction than either chlorine or bromine with lithium.[98] As this is the case, it was rationalized that divergent reactivity might also be seen during the

formation of $[L]_3U(F)$ depending on which alkali metal salt of the $[N(SiMe_3)(3,5\text{-}(CH_3)_2(C_6H_3)]$ ligand is used for the reaction. Additionally, by generating $[L]_3U(F)$ a more complete ^1H NMR spectroscopic study can be performed to better understand the effect halogen identity has on ^1H NMR chemical shift for paramagnetic uranium anilido complexes. With this in mind, efforts were made to generate $[L]_3U(F)$ as shown in Scheme 2-9.



Scheme 2-9: *Synthetic pathways used to try to generate $(F)U[N(SiMe_3)(3,5\text{-}(CH_3)_2(C_6H_3)]_3$*

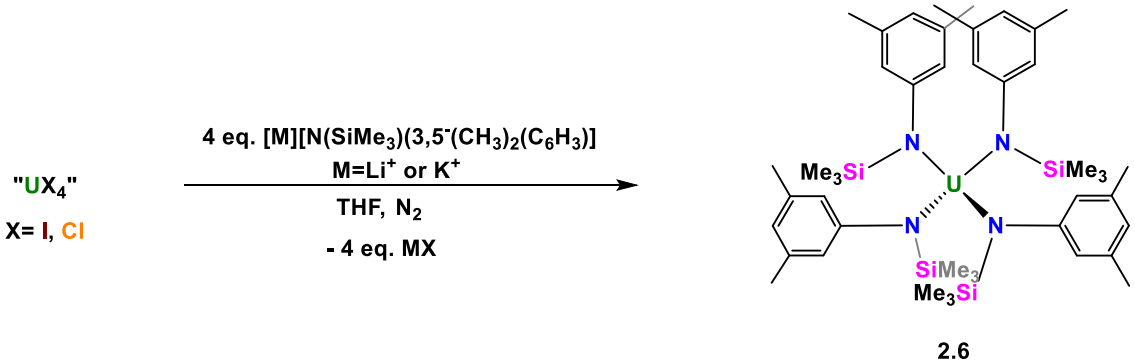
Path 1 was attempted first with the belief that $[L]_3U(X)$ would undergo a simple salt metathesis reaction with CsF to generate more favorable CsI and U-F interactions. As both U(IV) and F are considered to be hard, the formation of a U-F bond is a favorable process. Both Cs and I are considered to be softer, so

the formation of a Cs-I interaction is also favorable according to Hard-Soft Acid-Base Theory.[98] Although seemingly favorable, this process was unfortunately unsuccessful due to the poor solubility of CsF in most organic solvents. The same logic was applied for Path 2. The formation of KCl would be a better hard-soft Lewis acid base match than U(IV) and Cl, while a U-F interaction would be more favorable than a U-Cl interaction.[98] This pathway also was unsuccessful in yielding $[L]_3U(F)$ due to the poor solubility of KF in organic solvents. Unlike Paths 1 and 2, Path 3 attempted to generate the desired $[L]_3U(F)$ complex by means of a similar reduction and oxidation pathway used by Kiplinger and coworkers. In step 1 of this pathway, the starting tris(anilido)halo uranium complex was reduced *in situ* with KC_8, a very strong reducing agent, to generate a transient U(III) tris(anilido) species. Then, the uranium(III) tris(anilido) complex was treated with CuF_2 in hopes of oxidizing the U(III) species to the desired U(IV) complex. Like the other pathways, this route too was unsuccessful. Upon characterization of the product from Path 3, it was found that only a disproportionation byproduct $U[L]_4$ (*vide infra)* was generated. This means that after the reduction of the $[L]_3U(X)$ complex, the transient U(III) species most likely rapidly underwent disproportionation, before being oxidized by the CuF_2. The rapid disproportionation experienced by the U(III) species *in situ* can be explained in part due to the lack of steric protection provided to the uranium center by only 3 equiv. of the ligand. Unlike the bulky $[N(SiMe_3)_2]$ amido ligand used to stabilize U(III) by Anderson and coworkers, the $[N(SiMe_3)(3,5\text{-}(CH_3)_2(C_6H_3)]$ ligand seems to be unable to indefinitely stabilize a U(III) center from disproportionation.[80] As

a result, further reduction pathways that generated a U(III) species *in situ* were not attempted. Path 4, on the other hand, attempted to utilize a transmetallation reaction in which AgF and $[L]_3UCl$ would exchange halogens to generate AgCl and $[L]_3UF$.[48] By design, this reaction makes use of AgCl's poor solubility in most organic solvents by having it precipitate out of solution as the reaction proceeds. As this happens, the reaction should theoretically be driven forward by Le Chatlier's Principle, generating the intended $[L]_3UF$ complex. Unfortunately, Path 4 did not show any evidence of a reaction occurring by ^1H NMR spectroscopy. With Paths 1-4 failing to generate the intended $[L]_3UF$ complex, a new pathway that made use of protonolysis was devised. In this reaction, U-L and H-X bonds are broken and L-H and U-X bonds are formed. This is accomplished by exposing the U-L bond to only one equivalent of an acidic proton. When this occurs, the electrons in the U-L bond attack the acidic proton generating the new L-H bond (in this case H-[N($SiMe_3$)(3,5-$(CH_3)_2(C_6H_3)$] and an equivalent of X^- and leaving behind a formal positive charge on at the metal center. Finally, the X^- anion attacks the metal center generating the desired U-X bond (in this case the U-F bond). Although this type of pathway was shown to be effective for generating a similar chloro tris(amido) uranium complex by Ephritikhine and coworkers, this pathway did not generate the desired $[L]_3UF$ complex. Instead, only [L]H was observed by ^1H NMR spectroscopy.[94] In each of these pathways, either the disproportionation byproduct $U[L]_4$ was generated or no reaction was detected by ^1H NMR spectroscopy. It was rationalized that if the $[L]_3UF$ complex was generated through any of the above pathways, it most likely underwent

disproportionation to generate an equivalent of $U[L]_4$ and another uncharacterized uranium byproduct. This is most likely due to the poor steric protection provided by the anilido ligands and the smaller fluorido ligand. Since the $[L]_3U(X)$ complexes can be isolated when X=Cl, Br and I and given the fact that F is considerably smaller than the other halides, it is reasonable to assume that it may not provide the same type of steric protection that the other halides can provide the metal center. It is possible that the $[L]_3UF$ complex undergoes rapid ligand exchange to generate the sterically more encumbering $U[L]_4$ complex. For these reasons, further attempts to isolate $[L]_3UF$ were abandoned.

While attempting to generate $[L]_3UF$ and complexes **2.1**-**2.5**, it was discovered by ^1H NMR spectroscopy that there was often a small amount of a disproportionation byproduct, $U[L]_4$ present in the bulk material for these complexes. In order to more accurately determine which ^1H NMR peaks belonged to the intended tris(anilido) halo uranium complexes and which belonged to the $U[L]_4$ byproduct, the $U[L]_4$ complex (**2.6**) was synthesized rationally (Scheme 2-10).



2.6

Scheme 2-10: *Rational synthesis of $U[L]_4$ (**2.6**) from UCl_4 or $UI_4(1,4\text{-dioxane})_2$*

It was found that **2.6** could be generated from UCl_4 or $UI_4(1,4\text{-dioxane})_2$ with 4 equiv. of either the lithium or potassium salt of the anilido ligand. Complex **2.6** can be isolated cleanly through recrystallization from hydrocarbon or ethereal solvents.

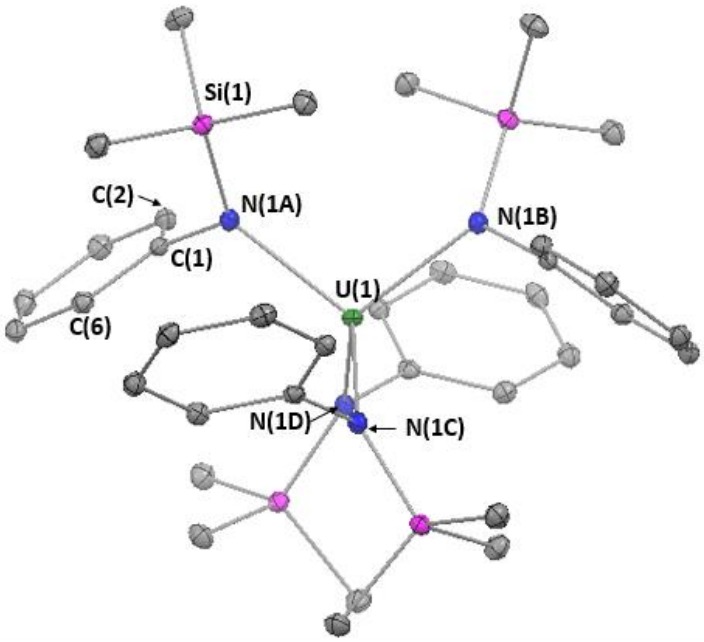


Figure 2-15: *ORTEP depiction of $U[N(SiMe_3)(3,5\text{-}(CH_3)_2(C_6H_3)]_4$ complex (**2.6**) with ellipsoids shown at 30% probability. Aryl-CH_3s and hydrogen atoms removed for clarity.*

Complex **2.6** displays S_4 symmetry in the solid state and adopts a pseudo tetrahedral geometry as shown in Figure 2-15. Crystallographically, all four anilido ligands are equivalent. The U-N bond distances (Table 2-8) for this complex are in good agreement with the U-N bond distances for complexes **2.1**-**2.5** and are similar to the U-N bond distances of related anilido uranium complexes.[84] The U-C_{ipso} bond distance (U(1)-C(1)) for complex **2.6** is about 0.250 Å longer than the average U-C_{ipso} bond distance for complex **2.1** (U-C_{ipso} avg = 2.785 Å), and about 0.226 Å longer than the average U-C_{ipso} bond distance

in complex **2.5** (U-C_{ipso} avg = 2.809 Å). This U-C_{ipso} bond elongation for complex **2.6** relative to complexes **2.1** and **2.5** suggests that there is a greatly diminished U-C_{ipso} interaction for complex **2.6**. This U-C_{ipso} bond elongation can be attributed to the increased steric congestion of the complex, as there are now four anilido ligands about the metal center with this system instead of the three or two for complexes **2.1** and **2.5**, respectively. The increased congestion caused by these additional ligands forces the aryl groups of the ligands to be further away from the uranium center, preventing strong U-C_{ipso} interactions (such as those observed in complexes **2.1** and **2.5**) from occurring. The anilido ligands in complex **2.6** thus only bind κ^1 through the anilido nitrogens and have little to no π-aryl donation to the uranium center. This bonding designation is supported with the fact that the U-C_{ipso} bond distance of complex **2.6** more closely matches the U-C_{ipso} bond distances found in the κ^1 bound anilido ligands of complex **2.2**. Additionally, **2.6** contains fairly long U-C_{ortho} bond distances, which signify little to no U-C_{ortho} interactions.

Table 2-9: *Selected bond lengths (Å) and angles (°) for* ***2.6***

Bond	Distance (Å)	Bond Angle	Angle (°)
U(1)-N(1)	2.2473(12)	N(1A)-U(1)-N(1B)	104.21(6)
U(1)-C(1)	3.0352(14)	N(1A)-U(1)-N(1C)	112.17(3)
U(1)-(C2)	3.669	N(1A)-U(1)-N(1D)	112.17(3)
U(1)-C(6)	3.868	N(1B)-U(1)-N(1C)	112.17(3)
Si(1)-N(1)	1.7433(13)	N(1B)-U(1)-N(1D)	112.17(3)
N(1)-C(1)	1.4331(18)	N(1C)-U(1)-N(1D)	104.21(6)
		C(1)-U(1)-N(1)	26.50
		Si(1)-N(1)-U(1)	135.04(7)

In solution, as in the solid state, complex **2.6** displays high symmetry, as indicated by the simplicity of its ^{1}H NMR spectrum (Figure 2-16). The spectrum

contains only four peaks, indicating that the ligands are equivalent on the NMR time scale. This means that there is free rotation of the anilido ligands about the U-N bonds despite the increased steric congestion of the system with four equivalents of the anilido ligand. This is consistent with the high symmetry observed with a bulkier tetrakis(amido)uranium complex reported by Schelter and coworkers.[84 99]

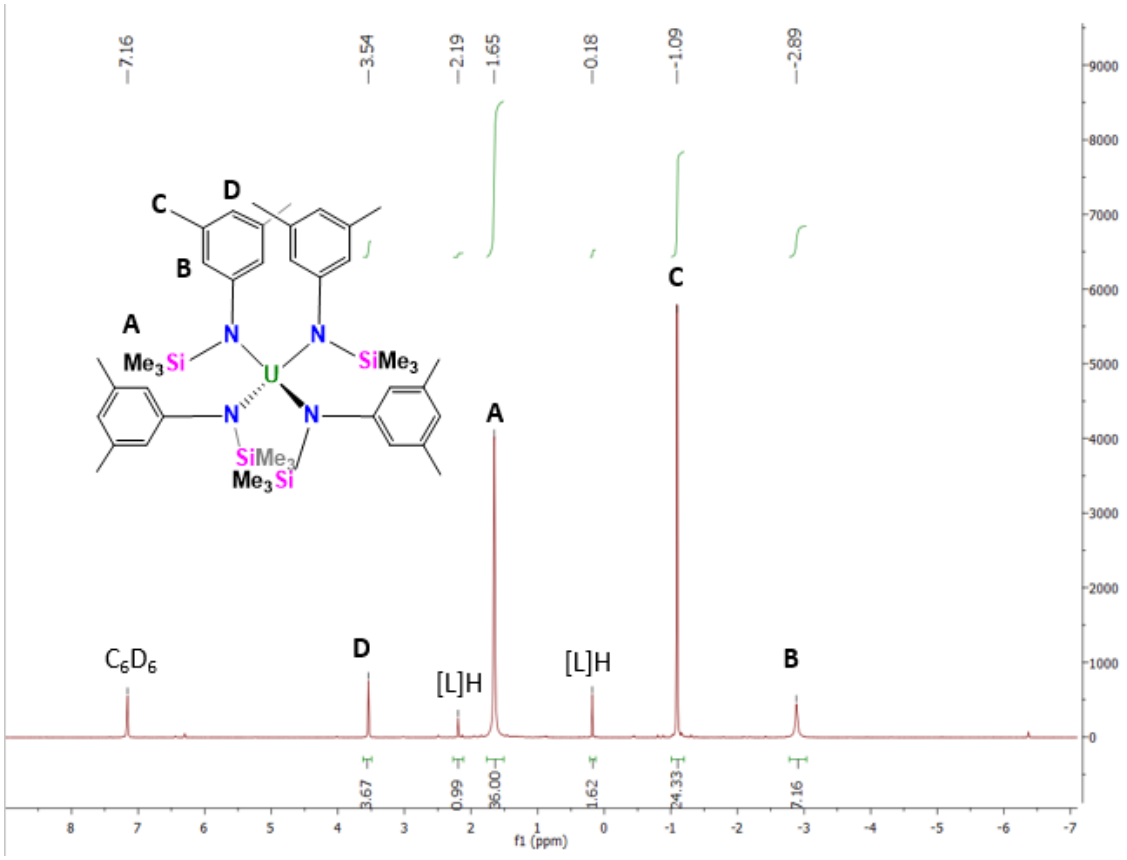
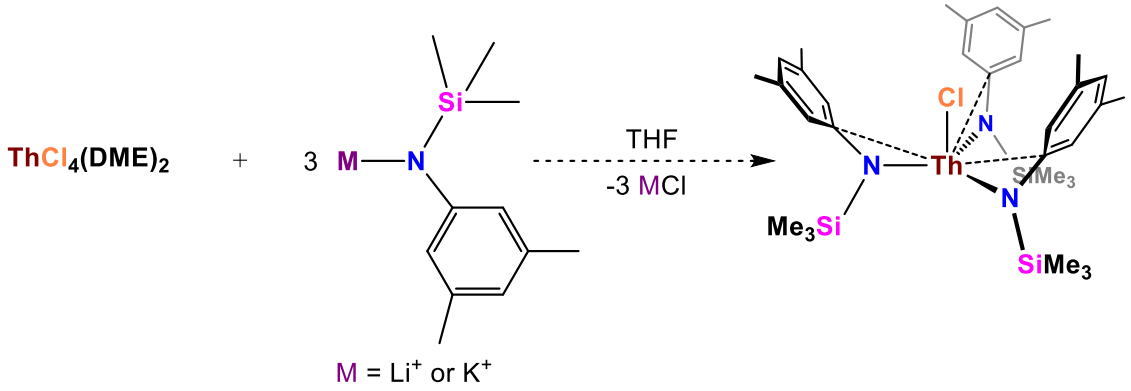


Figure 2-16: *300 MHz ^{1}H NMR spectrum of U[N(SiMe$_3$)(3,5-(CH$_3$)$_2$)(C$_6$H$_3$)]$_4$ (**2.6**) in C$_6$D$_6$*

2.6: Synthesis of Th[N(SiMe$_3$)(3,5-(CH$_3$)$_2$)(C$_6$H$_3$)]$_4$

Since the [N(SiMe$_3$)(3,5-(CH$_3$)$_2$)(C$_6$H$_3$)] ligand was able to support uranium tris(anilido) complexes of the type [L]$_3$U(X), it was determined that generating the analogous f^0 [L]$_3$Th(X) complexes would be beneficial. By generating these

thorium complexes, studies could be performed that examine the differences that exist in the bonding interactions between the analogous f^2 uranium and f^0 thorium complexes, including information regarding the role of *f*-electrons in bonding and covalency observed with early actinide complexes. There are very few easily accessible thorium halide starting materials suitable for generating analogous thorium tris(anilido) complexes. Given this limitation, $[L]_3Th(Cl)$ was targeted using the method shown in Scheme 2-11, as the necessary thorium halide starting material ($ThCl_4(DME)_2$) is easily prepared.[100]



Scheme 2-11: *Proposed synthesis of $[L]_3Th(Cl)$*

To our surprise, $[L]_3ThCl$ was not readily isolated using several permutations of analogous synthetic pathways that enabled the preparation of the LiCl ate salt (**2.2**) and $[L]_3UCl$ (**2.3**). Rather than generating the desired $[L]_3Th(Cl)$ anilido complex, the homoleptic $Th[L]_4$ complex was instead isolated in every attempt to generate the desired halo tris(anilido) thorium compound. This difference in reactivity between thorium and uranium is likely due to the difference in size of the ionic radii for Th(IV) and U(IV). It is well understood that low oxidation state uranium and thorium chemistry is governed primarily by steric considerations. This means that tetravalent uranium and thorium complexes are

more stable, and thus less likely to undergo side reactivity, when the metal center is protected by a large ligand or a ligand that creates a large cone angle around the metal center. As the [$N(SiMe_3)(3,5\text{-}(CH_3)_2(C_6H_3)$] ligand is less bulky than the previously studied [$N(SiMe_3)_2$] ligand, it stands to reason that a significant portion of the actinide metal center is exposed when the [$N(SiMe_3)(3,5\text{-}(CH_3)_2(C_6H_3)$] ligand is used for stabilization of an actinide metal center. Although having increased steric access to an actinide center with this ligand was chosen by design, it fails to adequately protect the actinide center from side reactivity like disproportionation, as demonstrated by bromo cluster **2.5**. Given that the ionic radius of Th(IV) is 0.08 Å larger than that of U(IV), greater steric access is available to the thorium center as compared to uranium, and the propensity for disproportionation greatly increases, resulting in the isolation of $Th[L]_4$ instead of the intended $[L]_3ThCl$ complex.[101] While the [$N(SiMe_3)(3,5\text{-}(CH_3)_2(C_6H_3)$] ligand has been shown to stabilize the U(IV) center from significant disproportionation with complexes **2.1**-**2.5**, it stands to reason that this ligand is too small to adequately stabilize a Th(IV) center from disproportionation when only 3 equiv. of the ligand are present.

Although [L]3ThCl could not be isolated, $Th[L]_4$ complex **2.7** can be isolated through recrystallization from either hydrocarbon or ethereal solvents, and the solid-state structure is shown in Figure 2-17.

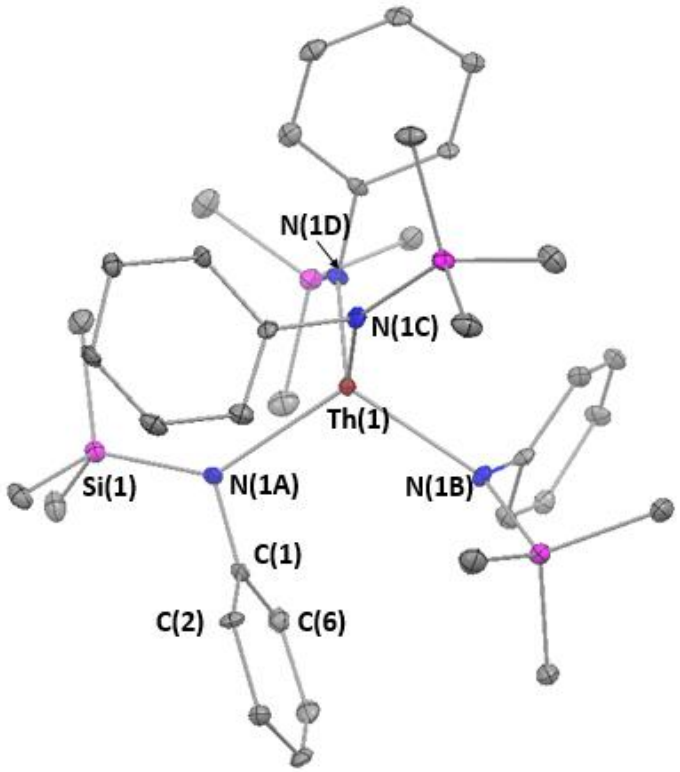


Figure 2-17: *ORTEP depiction of Th[N(SiMe$_3$)(3,5-(CH$_3$)$_2$)(C$_6$H$_3$)]$_4$ (**2.7**) with ellipsoids shown at 30% probability. Aryl-CH$_3$s and hydrogen atoms removed for clarity.*

Table 2-10*: Selected bond lengths (Å) and angles (°) for **2.7***

Bond	Distance (Å)	Bond Angle	Angle (°)
Th(1)-N(1)	2.309(5)	N(1A)-Th(1)-N(1B)	112.17
Th(1)-C(1)	3.058(8)	N(1A)-Th(1)-N(1C)	112.17
Th(1)-C(2)	3.846	N(1A)-Th(1)-N(1D)	104.20
Th(1)-C(6)	3.700	N(1B)-Th(1)-N(1C)	104.20
Si(1)-N(1)	1.734(3)	N(1B)-Th(1)-N(1D)	112.17
N(1)-C(1)	1.427(4)	N(1C)-Th(1)-N(1D)	112.17
		N(1)-Th(1)-C(1)	26.41(14)
		Si(1)-N(1)-Th(1)	135.19

Complex **2.7** displays a rare S_4 symmetry in the solid state and adopts a pseudo-tetrahedral coordination geometry. Structurally, this complex was nearly identical to complex **2.6**, with only a few minor differences noted in bond distances (Tables 2.8 and 2.9). As to be expected, the Th-N bond distances for

complex **2.7** were slightly longer than the corresponding U-N bond distances for complex **2.6**. The difference between the M-N bond distances for complexes **2.6** and **2.7** was about 0.062 Å, which is close to the expected difference of 0.08 Å.

Due to the structural similarities between complexes **2.6** and **2.7** it was determined that all of the anilido ligands in complex **2.7** are bound only κ^1 through the anilido nitrogen, as observed with the analogous $U[L]_4$ system. The ligands in complex **2.7** most likely do not engage in π-aryl donation. This claim can be further supported by the fact that the Th-C_{ipso}, Th-C_{ortho} and Th-C_{ortho}' bond distances are significantly longer than expected for ligands containing π-aryl donation.[74]

Like complex **2.6**, complex **2.7** displays high symmetry in solution, which can be seen in both the ^1H and ^{13}C NMR spectra for the complex. In the ^1H NMR spectrum, shown below in Figure 2-18, complex **2.7** displays only four prominent peaks. The aromatic protons of the ligands show up as singlet peaks at δ 6.80 and 6.68 and integrate for eight and four protons, respectively. The aryl-CH_3 protons show up as a singlet peak at δ 2.33 and integrate for 24 protons. The $SiMe_3$ protons show up as a singlet peak at δ 0.29 and integrate for 36 protons. These data are consistent with a structure for **2.7** where all the anilido ligands about the metal center are equivalent. The ^{13}C NMR spectrum of **2.7** is shown in Figure 2-19 and further supports the claim of high symmetry in solution. The spectrum has six peaks – one for each expected unique ^{13}C environment – where all four ligands are equivalent.

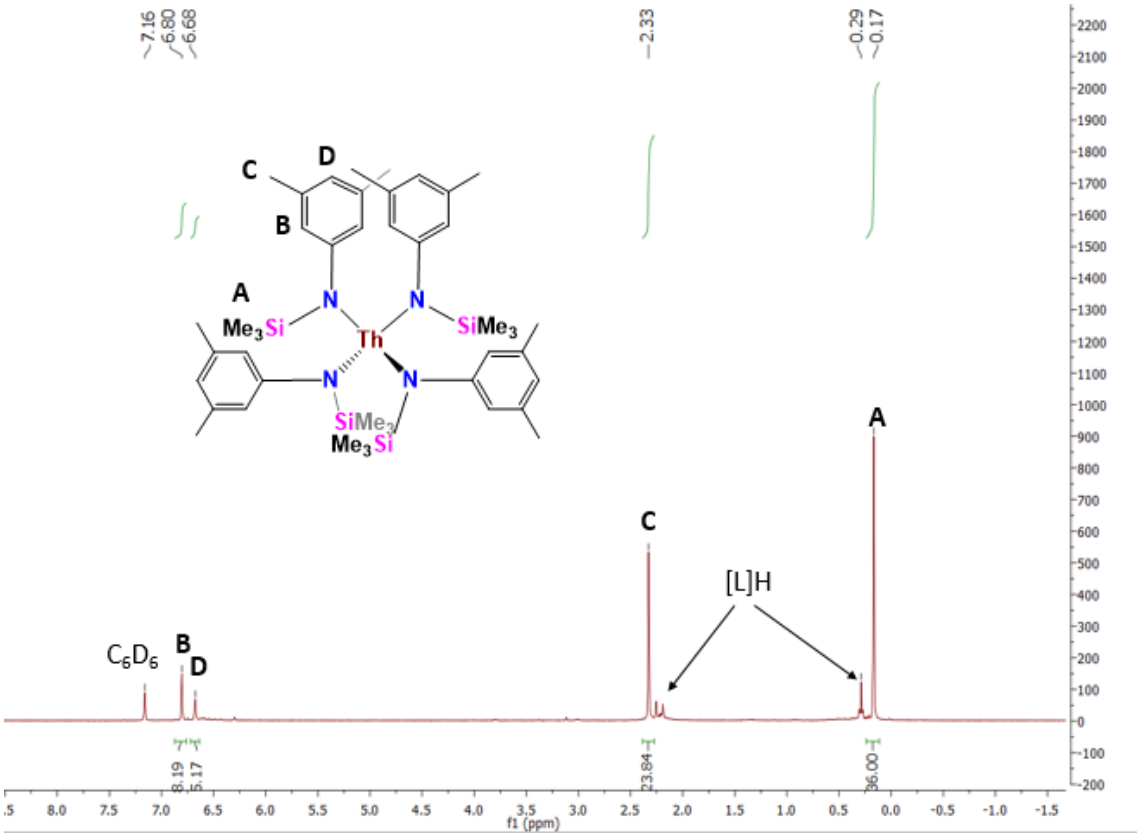


Figure 2-18: *400 MHz ^{1}H NMR spectrum of Th[N(SiMe$_3$)(3,5-(CH$_3$)$_2$)(C$_6$H$_3$)]$_4$ (**2.7**) in C$_6$D$_6$*

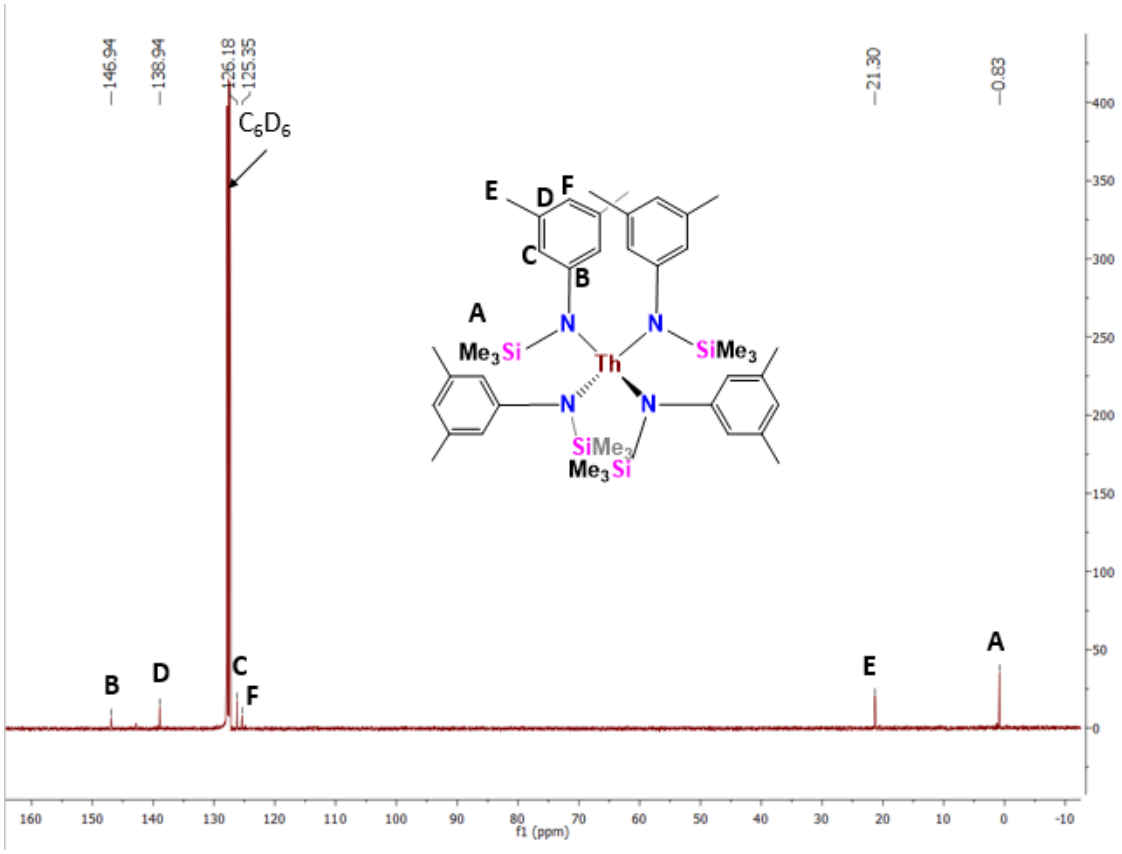


Figure 2-19: *400 MHz ^{13}C NMR spectrum of Th[N(SiMe$_3$)(3,5-(CH$_3$)$_2$)(C$_6$H$_3$)]$_4$ complex (**2.7**) in C$_6$D$_6$*

Although complexes **2.6** and **2.7** are nearly structurally identical, their ^{1}H NMR spectra differ greatly. This is the case because U[L]$_4$, (**2.6**) is paramagnetic, whereas Th[L]$_4$, (**2.7**) is diamagnetic. Thus, the U(IV) center of complex **2.6** contains unpaired electrons, whereas the Th(IV) center does not. These unpaired electrons affect the chemical shifts of the NMR active nuclei in the complex by either greatly shielding or deshielding them. This is why, for example, the aryl-CH$_3$ peak appears upfield at δ -1.09 in U complex **2.6** but appears downfield at δ 2.33 in Th complex **2.7**. Although we were unable to generate the intended [L]$_3$Th(X) series with this anilido ligand framework, we were able to see the structural differences that exist between the Th[L]$_4$ complex (**2.7**) and the uranium

analog (**2.6**) and how the unpaired electrons of the paramagnetic uranium complex influence the chemical shifts in the ^{1}H NMR spectrum.

2.7: Analysis of ^{1}H NMR chemical shift trends for the $[L]_3U(X)$ series

Currently, ^{1}H NMR spectroscopy is the most common and versatile form of characterization for low valent uranium complexes. Despite this, many challenges still exist with the interpretation of ^{1}H NMR spectra of complexes of this type. One of the main challenges associated with interpreting the ^{1}H NMR spectra of paramagnetic systems is the fact that it can often be difficult to accurately assign the peaks. This can arise from the fact that no information can be gained from peak splitting or coupling since the peaks are typically paramagnetically-broadened singlets. This leaves integration and chemical shift as the only other sources of spectral information useful in assigning peaks. To make matters worse, if the ligand contains many different sets of equivalent protons that all integrate for the same value, integration is useless for the correctly assigning the peaks. This leaves chemical shift as the only useful spectral useful for peak assignment. Although the coordination chemistry of low valent uranium has been studied for many years, little is known about where many common proton-containing functionalities show up in the ^{1}H NMR spectra of these complexes. Additionally, where certain functionalities show up in a ^{1}H NMR spectrum is highly dependent on the type of ancillary ligand used with the complex. Therefore, chemical shift is less useful for paramagnetic systems than for diamagnetic systems. Targeted studies that demonstrate how the chemical

shift of ligand functionalities change when the chemical environment is altered will greatly improve the value of chemical shift in peak assignments for paramagnetic U complexes. Subsequently, studies were initiated to examine how halogen identity effects anilido ligand ^{1}H NMR chemical shifts for the $[L]_3U(X)$ complexes **2.1**, **2.3**, **2.4** and **2.6**. Since amido and anilido ligands are becoming more common in low valent uranium chemistry, these studies could have broad applications for the actinide community.

In order to perform this study, the ^{1}H NMR spectra of complexes **2.1**, **2.3**, **2.4** and **2.6** were compared to see if a trend exists for the chemical shifts of the anilido ligand as the electronegativity of the halogen changes (Table 2-10 and Figure 2-20).

Table 2-11: *Comparison of ^{1}H NMR chemical shifts (ppm) for complexes **2.1**, **2.3**, **2.4** and **2.6***

Complex		δ $Si(CH_3)_3$	δ Ar-CH_3	δ *o*-Ar-H	δ *p*-Ar-H
$[L]_3U(Cl)$	**2.3**	10.34	-6.39	11.25	-1.81
$[L]_3U(Br)$	**2.4**	8.89	-5.92	11.18	-0.85
$[L]_3U(I)$	**2.1**	7.83	-5.57	-2.30	0.09
$U[L]_4$	**2.6**	1.65	-1.09	-2.89	3.54

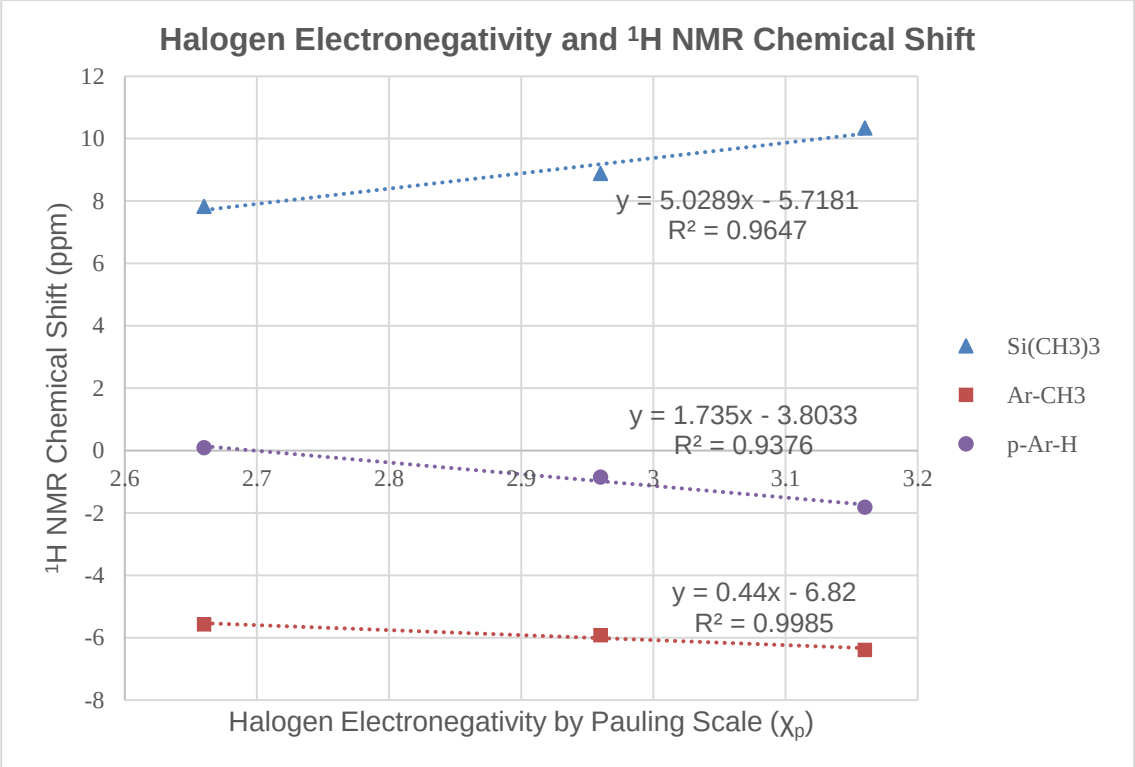


Figure 2-20: *Correlation between halogen electronegativity (X_p) and the ^{1}H NMR chemical shift (ppm) of selected protons.*

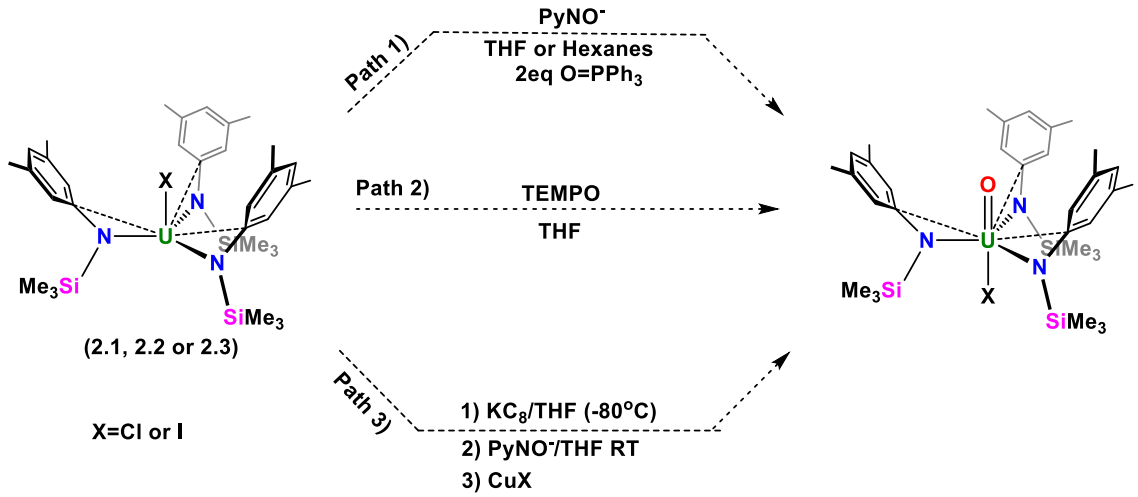
Figure 2-20 demonstrates a strong correlation between the electronegativity of the halogen atom and the chemical shift of the Ar-CH_3 protons (R^2 = 0.9985).[102] A moderately strong correlation exists between the halogen electronegativity and chemical shifts of the $SiMe_3$ protons and the *p*-Ar-H protons (R^2 = 0.9647 and R^2 = 0.9376, respectively). There appears to be no correlation between *o*-Ar-H proton chemical shift and halogen electronegativity (Table 2-10), so these data were not included in Figure 2-20. This may be due to the differing degrees of agostic/arene interactions of the *ortho* arene carbons to the uranium center, as discussed in Section 2.2. The chemical shifts of homoleptic complex **2.6** are also given in Table 2-11 to show how the presence of a halogen atom in the complex greatly changes the chemical shifts of all unique proton

environments in the system. From this comparison, we can generalize that ^{1}H NMR chemical shifts and halogen electronegativity are correlated. It is our hope that the information gained from this comparison can be used for predicting where ^{1}H NMR chemical shifts will show up for new paramagnetic uranium complexes that contain halogen functionalities.

2.8: Attempts to generate uranium-element multiple bonds using halo tris(anilido) uranium platform

It was shown through the generation of complexes **2.1**-**2.4** that the [N(SiMe$_3$)(3,5-(CH$_3$)$_2$(C$_6$H$_3$))] ligand framework is able to stabilize the U(IV) ion. Although many of the complexes that utilized this ligand framework were prone to disproportionation, the metal centers in these complexes remain more sterically accessible than their U(IV) counter parts that utilize the [N(SiMe$_3$)$_2$] ligand.[94] The increased steric accessibility to the U(IV) metal center makes these complexes suitable candidates reactivity to install U=ER functionalities with bulky groups. We thus attempted to explore one of the central aims of this research project: the generation of stable X-U=E functionalities for studies that examine the inverse *trans* influence and how U=E bond strength is changed as the identity of the *trans* π-donor X is altered. These studies are meant to provide insight into how to develop suitable sequestering agents for *f*-element extractions in nuclear waste reprocessing. Generation of the X-U=O functionality was attempted first; the U=O framework is the most relevant functionality for nuclear waste reprocessing as it is present in the waste as the uranyl ion, $[O=U=O]^{2+}$.[45, 46] In

order to accomplish this task, we decided to use a technique similar to that pioneered by Hayton and coworkers that successfully installed one U=O functionality on the $U[N(SiMe_3)_2]_3$ tris(amido) complex shown in Scheme 2-12.[52]



Scheme 2-12: *Synthetic pathways attempted to generate* $[L]_3U(O)(X)$

Path 1 of Scheme 2-12 employs the use of a pyridine N-oxide donor to transfer an oxygen atom to a uranium center via a two-electron oxidative process. As our $[L]_3U(X)$ framework is sterically more open than the $U[N(SiMe_3)_2]_3$ system (*vide infra*) and thus more prone to disproportionation, 2 equiv. of a bulky donor, $OPPh_3$, was added in hopes that it would coordinate to the uranium center and prevent unwanted disproportionation and dimerization from occurring. Unfortunately, upon characterization of the bulk material produced from this reaction by ^1H NMR spectroscopy, it was discovered that this pathway generated a mixture of products. Similarly, Path 2 (Scheme 2-12) employed the same strategy of donating an oxygen atom through the use of an N-oxide donor by using the bulkier TEMPO oxide donor, since it was reported by Hayton and coworkers that less bulky N-oxide donors may lead to the formation of a bridging

oxo species.[52, 103] Like Path 1, Path 2 was also unable to cleanly generate the desired $[L]_3U(O)(X)$ complex. It was found by ^1H NMR spectroscopy that this pathway exclusively generated the disproportionation byproduct $U[L]_4$ (**2.6**). It was rationalized that the U(IV) to U(VI) two-electron oxidative pathway was less favorable than disproportionation of the starting $[L]_3U(X)$ complex. This caused us to then explore the more favorable U(III) to U(V) transformation (Scheme 2-12, Path 3). Although more than one step, Path 3 directly utilizes the U(III) to U(V) oxidation used by Hayton and coworkers to install a U=O functionality.[52] This process first requires an *in situ* one-electron reduction of the $[L]_3U(X)$ starting material to generate a transient U(III) species. After reduction, the transient U(III) species is then rapidly oxidized to U(V) via an oxygen atom transfer from pyridine N-oxide. Finally, the U(V) $[L]_3U(O)$ species is oxidized to the desired U(VI) $[L]_3U(O)(X)$ complex with a copper halide salt. Unfortunately, this pathway was unsuccessful in generating the desired $[L]_3U(O)(X)$ complex. It was found through characterization by ^1H NMR spectroscopy that this pathway only produced the disproportionation byproduct $U[L]_4$ complex (**2.6**). To ensure that the first step of the process was working correctly, we decided to try and isolate the $U[L]_3$ species to see if reduction of the staring complex with KC_8 was occurring as intended. Isolation of the $U[L]_3$ species was accomplished by rapid workup of the reaction immediately after KC_8 was added to the reaction mixture. It was found that the $U[L]_3$ species can be isolated as a dark purple solid in moderate to high yields and can be recrystallized from hexanes at -30°C. While attempting to recrystallize this material, it was found that two products actually recrystallize from hexanes:

an amber material and a dark purple material. It was found that the amber material is the disproportionation byproduct $U[L]_4$, while the purple material is the desired $U[L]_3$ (**2.8**), which was characterized by XRD and is shown in Figure 2-21. Although these two products can be manually separated and characterized, the $U[L]_3$ complex decomposes within a few days in the solid state at low temperatures (-35°C). In solution, it was found the $U[L]_3$ complex completely disproportionates to $U[L]_4$ within a few hours at room temperature. If the reaction mixture is worked up within 15 min from the addition of the reactants, it is still found by ^1H NMR spectroscopy that approximately 50% of the bulk material is $U[L]_4$.

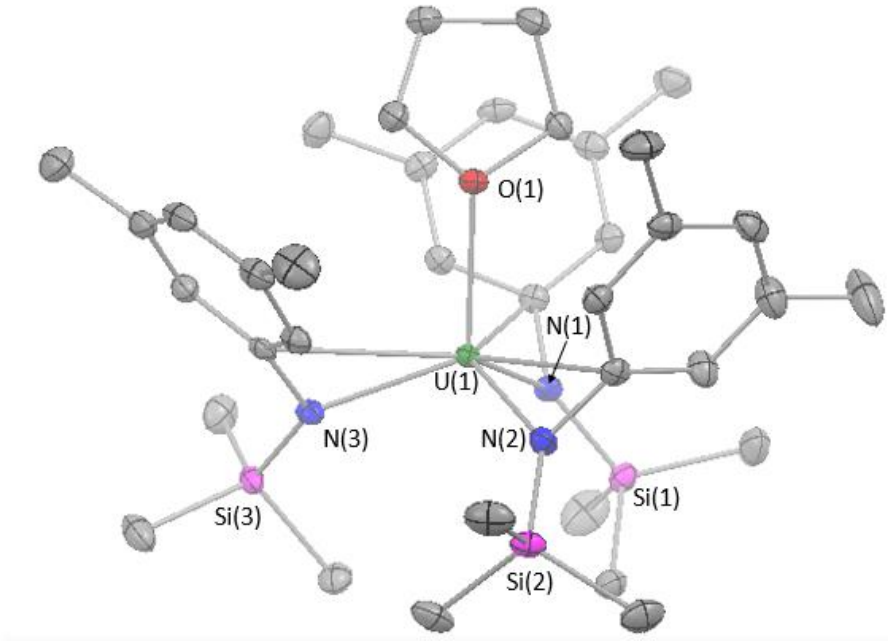


Figure 2-21: *ORTEP Depiction of (THF)U[N(SiMe$_3$)(3,5-(CH$_3$)$_2$)(C$_6$H$_3$)]$_3$ (**2.8**) with ellipsoids shown at 50% probability. Hydrogen atoms omitted for clarity.*

Table 2-12: *Selected bond distances (Å) and angles (°) for* ***2.8***

Bond	Distance (Å)	Bond Angle	Angle (°)
U(1)-N(1)	2.3445(17)	N(1)-U(1)-N(2)	108.59(6)
U(1)-N(2)	2.3112(17)	N(1)-U(1)-N(3)	105.51(6)
U(1)-N(3)	2.3445(17)	N(1)-U(1)-O(1)	110.73(5)
U(1)-O(1)	2.4811(14)	N(2)-U(1)-N(3)	110.49(6)
U(1)-C_{ipso}(1)	2.8879(12)	N(2)-U(1)-O(1)	109.22(5)
U(1)-C_{ipso}(2)	2.887(2)	N(3)-U(1)-O(1)	112.20(5)
U(1)-C_{ipso}(3)	2.912(2)	N(1)-U(1)-C_{ipso}(1)	28.77(6)
Si(1)-N(1)	1.7235(18)	N(2)-U(1)-C_{ipso}(2)	29.17(6)
Si(2)-N(2)	1.7151(18)	N(3)-U(1)-C_{ipso}(3)	28.40(6)
Si(3)-N(3)	1.7252(18)	Si(1)-N(1)-U(1)	136.52(9)
		Si(2)-N(2)-U(1)	139.98(10)
		Si(3)-N(3)-U(1)	135.13(9)

Table 2-13: *Selected bond distances (Å) for hapticity analysis for* ***2.8***

Ligand	U-N	U-C_{ipso}	U-C_{ortho}[a]	U-C_{ortho}'[b]	Δ[c]	Δ'[d]	Δ-Δ'[c,d]
L(N1)	2.3345	2.8879	2.997	4.008	0.1091	1.1201	1.011
L(N2)	2.3112	2.887	3.520	3.565	0.633	0.678	0.045
L(N3)	2.3444	2.912	3.048	4.048	0.136	1.136	1.000

[a]U-C_{ortho} denotes shorter U-C aromatic *ortho* carbon bond distance for each ligand (1, 2, 3)
[b]U-C_{ortho}' denotes longer U-C aromatic *ortho* carbon bond distance for each ligand (1, 2, 3)
[c]Δ=[(U-C_{ortho})-(U-N)]-[(U-C_{ipso})-(U-N)]
[d]Δ'=[(U-C_{ortho}')-(U-N)]-[(U-C_{ipso})-(U-N)]

Complex **2.8** displays C_s symmetry in the solid state and adopts a pseudo-tetrahedral geometry. The average U-N bond distance is ≥ ~0.1 Å than the average U-N bond distances of complexes **2.1**-**2.6**. This increase in U-N bond distance from the U(IV) tris(anilido) complexes to this U(III) complex is due to the higher ionic radius of the U(III) center as compared to the U(IV) center. This U(III) tris(anilido) complex is nearly identical to the (THF)U[N(C(CH_3)$_3$)(3,5-(CH_3)$_2$(C_6H_3)]$_3$ system generated by Cummins and coworkers.[81] The average U-N bond distance for complex **2.8** is about 0.01 Å longer than the average U-N bond distance for the analogous U(III) system generated by Cummins and coworkers, meaning that the two complexes have identical U-N bond lengths

within experimental error. The average U-C_{ipso} bond distance for complex **2.8**, however, is 0.022 Å shorter than the average U-C_{ipso} bond distance for the analogous U(III) complex produced by Cummins and coworkers.[81] By comparing the average U-N and U-C_{ipso} bond distances of complex **2.8** to the analogous bond distances in Cummins's U(III) tris(anilido) system, we can see that the two complexes are nearly identical. Interestingly, upon further bonding analysis, it can be seen that complex **2.8** showcases two anilido ligands that are bound η^3 and one that is bound η^1. By examining the U-C_{ipso} bond distances for ligands L(N1) and L(N3), we can see that there is a strong U-C_{ipso} interaction for these ligands. Additionally, we can see that there is a relatively short U-C_{ortho} distance, meaning that there is also a strong interaction between the ortho carbon of the aryl backbone. The bonding analysis shown in Table 2-12 indicates a large difference between Δ and Δ' suggesting that the ligand is bound η^3 through C_{ipso}, C_{ortho}, and C_{ortho}'.[74]

If we compare the space-filling model of complex **2.8** to the space-filling model of Andersen's tris(amido) complex U[$N(SiMe_3)_2$]$_3$ (Figure 2-22), it can be seen that the phenyl rings of **2.8** form a pocket in which the uranium center is accessible. Figure 2-22 also demonstrates that the metal center in complex **2.8** is more sterically accessible than the uranium center in Andersen's tris(amido) complex, meaning it may be possible for complex **2.8** to support a fairly bulky U=E functionality.[80]

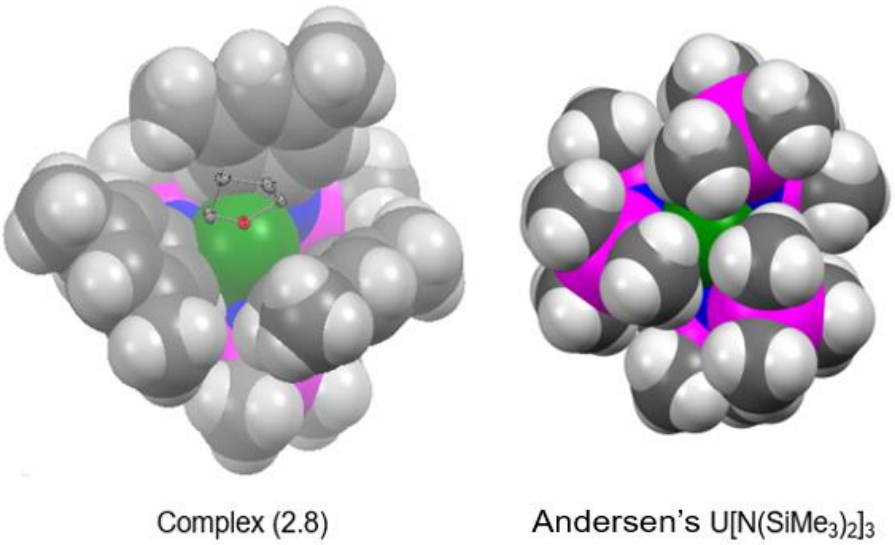


Figure 2-22: *Comparison of the space-filling models of complex **2.8** and Andersen's tris(amido) complex U[N(Si(Me$_3$)$_2$)]$_3$*

Due to our success in isolating **2.8** from a reduction pathway, we attempted to generate the complex using a less hazardous approach. This pathway involved adding 3 equivalents of K[N(SiMe$_3$)(3,5-(CH$_3$)$_2$)(C$_6$H$_3$)] to a solution of UI$_3$(1,4-dioxane)$_{1.5}$ in cold THF to try and isolate complex **2.8** in one step from the base uranium starting materials. Like the reduction pathway, this salt metathesis pathway was found to generate a mixture of complexes **2.6** and **2.8** by ^{1}H NMR spectroscopy (Figure 2-23).

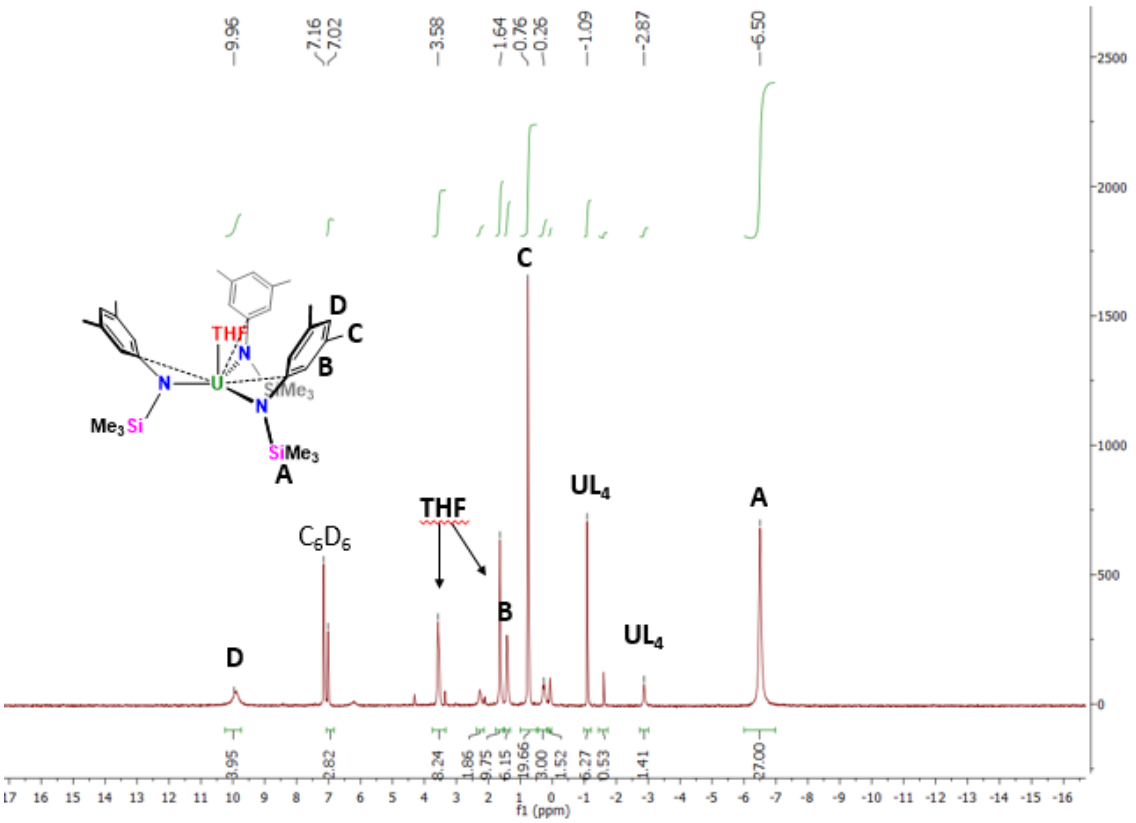
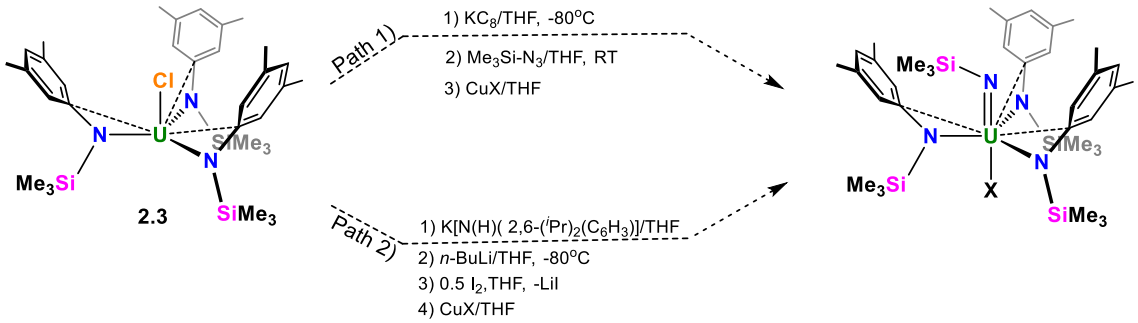


Figure 2-23: *300 MHz ^{1}H NMR spectrum of (THF)U[N(SiMe$_3$)(3,5-(CH$_3$)$_2$)(C$_6$H$_3$)]$_3$ (**2.8**) generated by salt metathesis from UI$_3$(dioxane)$_{1.5}$ in C$_6$D$_6$*

It should be noted that the Si(C*H*$_3$)$_3$ protons in complex **2.8** display a significant upfield shift from analogous Si(C*H*$_3$)$_3$ protons in complexes **2.1**-**2.6**, whereas the Ar-CH$_3$ protons in complex **2.8** experience a downfield shift relative to complexes **2.1**-**2.6**. The magnitude of these shifts may be explained by the additional unpaired electron of the U(III) center, where the additional unpaired electron may cause a shift in the shielding environments.

Although isolation of an [L]$_3$U(O)(X) complex was unsuccessful, additional strategies to generate X-U=E functionalities were explored. Recently, Schelter and coworkers demonstrated success in generating the U=N(R) functionality with the similar U[N(SiMe$_3$)$_2$]$_3$ system.[59] As a result, we attempted to employ a

modified version of Schelter's approach to installing the U=N(R) functionality with our own $[L]_3U(THF)$ system (Scheme 2-13, Path 1).



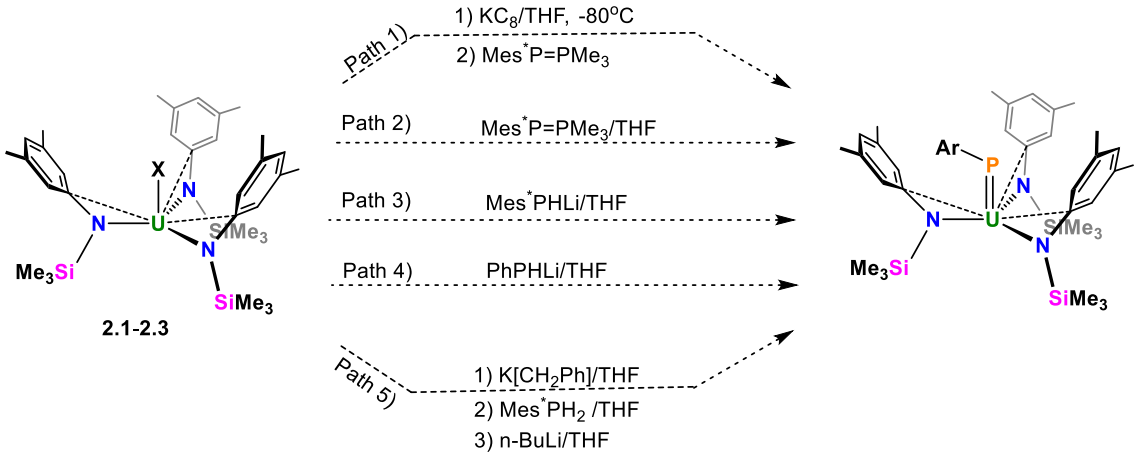
Scheme 2-13: *Synthetic approaches for generating the uranium imido (U=N) functionality*

Since Schelter's method to install the uranium imido functionality utilized a two-electron oxidation pathway from U(III) to U(V), we had to first generate the necessary U(III) tris(anilido) complex for the reaction. This was accomplished by reducing **2.3** with a strong one-electron reducing agent to generate $U[L]_3$ (**2.8**) *in situ*. This transient U(III) tris(anilido) complex was then treated with 1 equiv. of $Me_3Si\text{-}N_3$ to generate the desired U(V) imido complex $[L]_3U(=N(SiMe_3))$. Finally, this complex was to be treated with CuX to generate $[L]_3U(=N(SiMe_3))(X)$ and obtain the desired X-U=N(R) functionality. Unfortunately, this pathway did not work as intended, since a significant amount of $U[L]_4$ was generated during the reduction of **2.3** in the first step of Path 1 to generate complex **2.8**. Since the necessary U(III) tris(anilido) complex for the U(III) to U(V) two-electron oxidation process was unable to reliably be generated via reduction or salt metathesis methods as described earlier, it was determined that utilizing a synthetic pathway that made use of the U(III) to U(V) oxidation pathway was not suitable for this system. As a result, a salt metathesis approach to installing the imido functionality

was attempted (Scheme 2-13, Path 2). Salt metathesis followed by deprotonation was chosen since the necessary uranium starting material for the reaction, complex **2.3**, is stable and can be readily isolated. Additionally this pathway would aim to generate a $[L]_3U[L']$ type intermediate system where L' = $[N(H)(3,5\text{-}(CH_3)_2(C_6H_3)]$ which is similar to the stable easily isolable homoleptic complex **2.6**. This pathway uses $K[N(H)(3,5\text{-}(CH_3)_2(C_6H_3)]$ which reacts with **2.3**, eliminating an equivalent of KCl and generating the $[L]_3U[N(H)(3,5\text{-}(CH_3)_2(C_6H_3)$ intermediate. The N(H) proton on the intermediate complex is then deprotonated using *n*-BuLi to generate the lithium salt of the desired $[L]_3U{=}N(Ar)$ functionality. Once the imido functionality is generated, the lithium salt of the U(IV) imido tris(amido) complex would then be oxidized to the U(V) analog: $[L]_3U(=N(3,5\text{-}(CH_3)_2(C_6H_3))$ using 0.5 eq I_2 thereby eliminating an equivalent of LiI. Finally, the intended X-U=N(Ar) functionality would be installed by reacting $[L]_3U(=N(3,5\text{-}(CH_3)_2(C_6H_3))$ with one equivalent of CuX. This pathway unfortunately did not cleanly generate the desired U=N(Ar) functionality. It was noticed by ^1H NMR spectroscopy that multiple products were formed. As both methods failed to generate the desired U=N(Ar) functionality, it was decided to explore the possibility of generating different U=E moieties.

The last U=E functionality explored for the $[N(SiMe_3)(3,5\text{-}(CH_3)_2(C_6H_3)]$ tris(amido) uranium system was the generation of a uranium phosphinidene functionality, or U=P(R). Unlike the other U=E functionalities explored, the most naturally abundant isotope of phosphorus, ^{31}P, is NMR active. Thus, ^{31}P NMR spectroscopy could serve as an additional cost-effective tool to examine the

tuneability of the inverse *trans* influence. Information about the relative U=P(R) bond strength could be obtained from ^{31}P NMR spectroscopy by examining how the ^{31}P chemical shift tensor changes as the X group *trans* to the U=P(R) functionality is altered.[40] Generating this particular functionality posed the greatest synthetic challenge as this motif is highly reactive and unstable.[104, 105] The high reactivity of the U=P(R) functionality arises mainly from the poor hard-soft mismatch between U(IV), which is hard, and P, which is soft.[98] For these reasons, only a few examples of uranium phosphinidenes have been reported despite continued synthetic interest of the functionality within the actinide community.[50, 104-106] Due to the synthetic challenge posed by generating this U=P(R) functionality, we attempted a variety of synthetic pathways to try and access the U=P(R) functionality (Scheme 2-14).



Scheme 2-14: *Synthetic pathways used to attempt to generate the U=P(Ar) functionality*

Path 1 was the first approach used to generate a uranium phosphinidene and employed the use of a two-electron oxidation from U(III) to U(V). Although previously deemed synthetically non-feasible for this system, this pathway was

reexamined in hopes that a very bulky P^{2-} donor might react with the U(III) tris(amido) system to generate the U(V) phosphinidene and prevent ligand redistribution. This pathway made use of the phosphaylide $Mes^*P{=}PMe_3$ as the source of P^{2-} where Mes*=(2,4,6-tritertbutylphenyl).[107, 108] This particular pathway has been shown to generate the desired phosphinidene functionality with zirconium and vanadium.[107] Unfortunately, this pathway proved to be unsuccessful, with only the formation of $U[L]_4$ observed in the ^1H NMR spectrum. Path 2, like the first, makes use of a two-electron oxidation. This time, however, the uranium species would be oxidized from U(IV) to U(VI). As the U(IV) tris(anilido) complexes **2.1**-**2.3** are readily isolable and stable, this pathway seemed potentially lucrative. Unfortunately, this pathway did not result in the formation of a stable uranium phosphinidene complex. Instead, a highly stable Mes*P=PMes* diphosphene dimer was isolated (Figure 2-24).

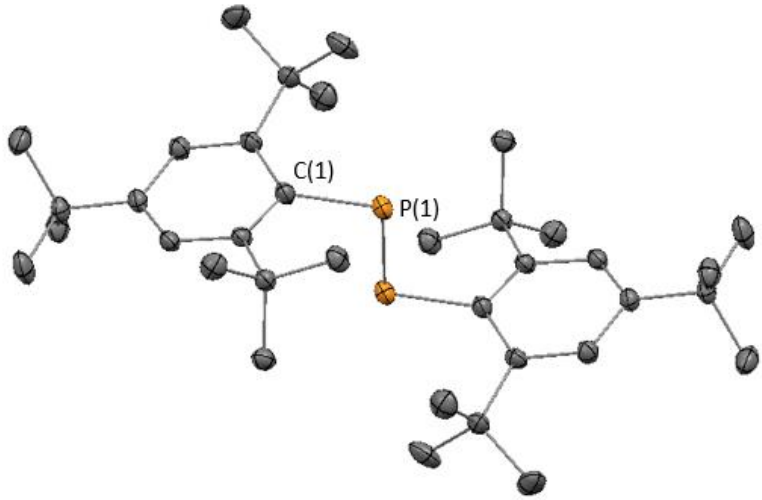


Figure 2-24: *ORTEP depiction of Mes*P=PMes* dimer isolated from Path 2 with ellipsoids shown at 30% probability. Hydrogen atoms omitted for clarity.*

This particular diphosphene species has been previously isolated and reported by Yoshifuji and coworkers; however, upon isolation from Path 2, it was found that the dimer crystallized in a different space group than previously reported, and metrical parameters vary slightly from the original report.[109] The generation of this dimeric species provides circumstantial evidence for the formation of a uranium phosphinidene that rapidly decomposed and dimerized.[108, 110-113] It is also possible that the phosphayilde did not react at all with the U(IV) tris(amido) species, but rather dimerized in solution; however, this particular decomposition pathway requires higher concentrations of Mes^*P^{2-} to be present in solution, which is unlikely.[112] As both oxidation pathways with the $Mes^*P{=}PMe_3$ phosphayilide proved to be unsuccessful in forming the desired uranium phosphinidene complex, alternative methods for the preparation and stabilization of the U=P(R) functionality were explored.

Paths 3 and 4 make use of a salt metathesis approach that aimed to generate the U=P(R) functionality in two steps, where Path 3 utilized the bulky Mes*PHLi proligand and Path 4 utilized the smaller lithium phenylphosphine salt. Isolation of a phosphinidene from a salt metathesis approach has been seen previously in the successful generation of a Zr=PMes* functionality.[108] In the case of Path 3, ^{31}P NMR spectroscopic analysis indicated that a phosphaindole byproduct was formed during the reaction (Figure 2-25). This particular byproduct was formed as a result of the insertion of the phosphorus atom into an *o*-^{t}Bu methyl C-H bond.[110, 112]

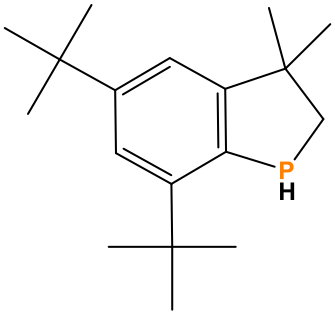
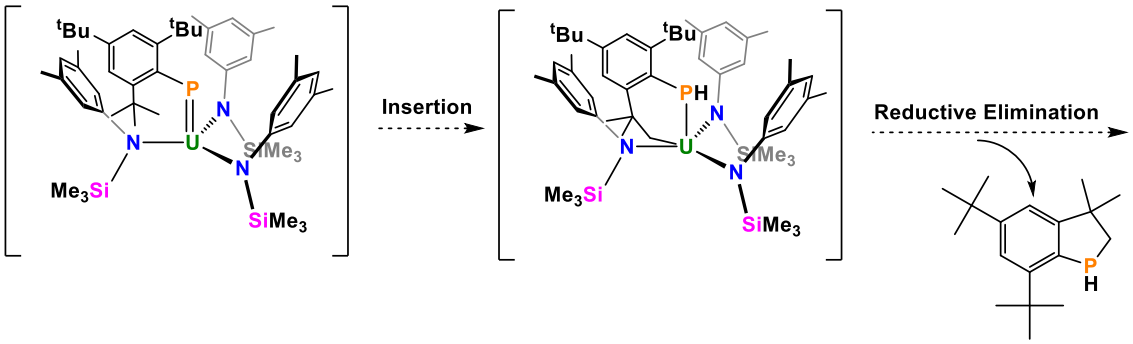


Figure 2-25: *Phosphaindole byproduct generated from Path 3 (Scheme 2-14)*

This particular phosphaindole has been observed in the literature while attempting to make terminal phosphinidene complexes with Ti[113], Fe[114], Co[114], Rh[112] and La[110]. It has been noted in each of these cases that the phosphaindole is formed as a direct result of decomposition of a transient phosphinidene complex, supporting the notion that the phosphaindole is generated as a result of transient U=PMes* decomposition (Scheme 2-15).



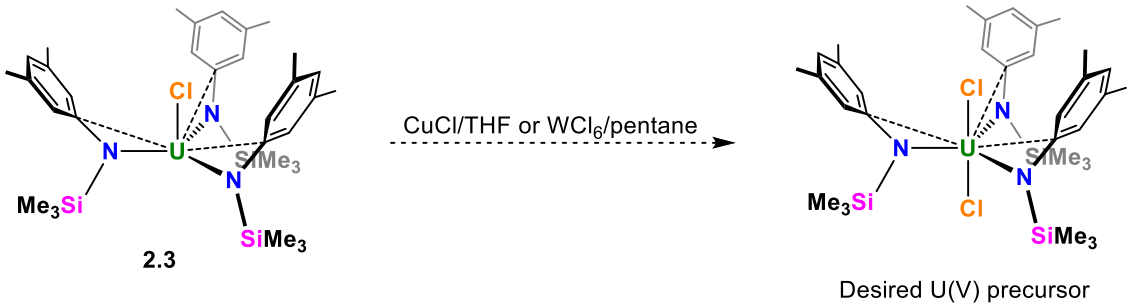
Scheme 2-15: *Possible mechanism for the formation of the phosphaindole*

Since the terminal phosphinidene complex $[L]_3U(=PMes^*)$ was not isolable via Paths 1-3, it was determined that the Mes* group may be too bulky to use as a steric protecting group for the phosphinidene moiety. Since all phosphorous-containing decomposition byproducts from Paths 1-3 suggest the formation of a transient terminal phosphinidene functionality *in situ*, it was determined that using a smaller aryl protecting group may allow for isolation of the desired U=P(Ar)

functionality. As a result, Path 4 utilizes a salt metathesis pathway with a sterically less-encumbering lithium phenylphosphine salt. This method was also unsuccessful in cleanly generating the desired terminal U=P(Ph) functionality, as determined by ^{1}H and ^{31}P NMR spectroscopy. Path 5, the last pathway attempted for the generation of the desired uranium phosphinidene, involved a protonolysis approach. This particular method would generate a transient uranium alkyl species that would then be exposed to Mes*PH_2. Treatment of the transient $[L]_3U(R)$ species with Mes*PH_2 would thus allow for the formation of $[L]_3U[P(H)(Mes*)]$ and the elimination of R-H (where R = $(CH_2(C_6H_5))$) in solution. The uranium phosphide complex $[L]_3U[P(H)(Mes*)]$ would then be treated with *n*-BuLi to generate the intended uranium phosphinidene functionality. Upon analysis of the bulk material isolated from Path 5 by ^{31}P NMR spectroscopy, it was found that LiHPMes* and the phosphaindole (*vida supra*) were the major phosphorus-containing products produced from the reaction. Additionally, it should be noted that a small peak or minor product was observed at δ 199.66 in the ^{31}P NMR spectrum. This peak may indicate formation of the precursor $[L]_3U[P(H)(Mes*)]$ phosphido complex. Unfortunately, since this uranium phosphido complex was not the major product produced from Path 5 it was determined that this protonolysis approach was not a viable method for producing the desired U=P(R) functionality. It was thus determined that the $U[N(SiMe_3)(3,5-(CH_3)_2(C_6H_5)]_3$ platform is unsuitable for stabilizing the highly reactive U=P(R) functionality.

In each of our previous attempts at stabilizing a U=E interaction, steric hindrance played a significant role in the inability to isolate this desired functionality. Many of the synthetic pathways used to generate this U=E functionality featured a uranium precursor complex that was often unable to sterically protect the resulting U=E functionality from subsequent reactivity. In the case of generating a uranium phosphinidene, however, the resulting transient $[L]_3U{=}P(R)$ complex was often too sterically encumbered, which lead to the degradation of the desired U=P functionality. We decided to further examine a way to modify the overall steric protection provided by the $[N(SiMe_3)(3,5\text{-}(CH_3)_2(C_6H_3)]$ ligand, such that a U=E functionality might be stabilized. After careful consideration, it was decided that using a U(V) tris(anilido) dihalo precursor complex may allow the ligand to provide additional steric support to the system and allow for isolation of a U=E interaction. This is the case since U(V) is about 0.10 Å smaller than U(IV), which in turn would result in possibly stronger M-L interactions for a U(V) complex as opposed to a U(IV) complex.[101] This would translate to having shorter bond distances between the nitrogen donors and the metal center. With the ligands closer to the uranium center, the anilido ligands would be able to provide additional steric support to the complex, making it less likely to undergo ligand redistribution. When determining which U(V) tris(anilido) complex would be the most suitable precursor for generating X-U=E functionality, it was rationalized that the precursor complex should have groups that can be easily activated for accessing the U=E framework. Since Schelter and coworkers have been able to install a U=O functionality on a *trans* dihalo U(V) tris(amido)

complex by means of salt metathesis with $NaNO_2$ followed by reductive cleavage of nitrite, we decided to design an analogous framework that would be best suited for similar reactivity.[48, 115] As we have been able to isolate $[L]_3U(Cl)$ (**2.3**) cleanly, we attempted to generate the desired U(V) precursor complex $[L]_3U(Cl)_2$ by means of oxidation of complex **2.3** with either CuCl or WCl_6 (Scheme 2-16).



Scheme 2-16: *Attempted synthetic pathway to access $(Cl)_2U(N(SiMe_3)(3,5\text{-}(CH_3)_2(C_6H_3))]_3$*

Unfortunately, both attempts at oxidizing complex **2.3** were unsuccessful. Upon analysis of the products from these reactions by ^1H NMR spectroscopy, it was found that only $U[L]_4$ was formed. It was ultimately decided that this particular ligand system is not suitable for stabilizing X-U=E functionalities due to the high proclivity for precursor complexes **2.1**-**2.5** and **2.8** to undergo ligand redistribution/disproportionation to generate $U[L]_4$.

2.9: Concluding remarks

The $[N(SiMe_3)(3,5\text{-}(CH_3)_2(C_6H_3)]$ anilido ligand framework is able to stabilize complexes of the type $[L]_3U(X)$ (where X = Cl, Br and I). These complexes can be readily accessed by reacting $UX_4(Solvent)_n$ (where X = Cl and I; n = 0 or 2) with 3 equiv. of the potassium salt of the proligand. Additionally, it

was discovered that the alkali counter ion identity of the proligand influenced the coordination chemistry and reactivity of the tris(anilido) system. This difference in coordination chemistry was showcased with the formation complexes **2.2** and **2.3**. If the Li salt of the proligand was used, [(THF)(Et_2O)LiCl][$(L)_3$U(Cl)] (**2.2**) was isolated; however, if the K salt of the proligand was used, $[L]_3$U(Cl) (**2.3**) was isolated. Interestingly, if both complexes **2.2** and **2.3** were exposed to excess Me_3Si-Br, two different bromo-containing products were formed: $[L]_3$U(Br) (**2.4**) and $[L]_2$U(Br)(μ-Br)$_3$U(Br)$[L]_2$ (**2.5**). While attempting to explore the reactivity of complexes **2.1**-**2.5** it was found that the tris(anilido) uranium complexes would often undergo ligand redistribution to generate the homoleptic complex $U[L]_4$ (**2.6**). Additionally, it was found that the analogous $[L]_3$Th(X) complexes could not be readily accessed through similar reactivity. Each attempt at generating the analogous $[L]_3$Th(X) complexes resulted in the formation of the homoleptic complex $Th[L]_4$ (**2.7**). A moderate to strong correlation exists between the chemical shifts of the Si(C*H*$_3$)$_3$, Ar-C*H*$_3$ and *p*-Ar protons and halogen electronegativity in this class of compounds, indicating that ^{1}H NMR spectroscopy can be a good measure of electron density at the U center.

While attempting to generate X-U=E functionalities for use in studying the inverse *trans* influence, it was found that the [N($SiMe_3$)(3,5-$(CH_3)_2(C_6H_3)$)] ligand is unable to support formation of X-U=O, X-U=N(R) and X-U=P(Ar) species. Precursor $[L]_3$U(X) complexes often underwent ligand redistribution to generate $U[L]_4$, which prevented isolation of the desired U=E functionalities. It was found that $[L]_3$U(THF) (**2.8**) could be co-isolated with $U[L]_4$ after reduction of $[L]_3$U(X)

with KC_8. Complex **2.8** was found to have poor stability at room temperature and readily disproportionated to form $U[L]_4$ in solution. Any reactivity explored with complex **2.8** lead to the direct formation of $U[L]_4$ via ligand redistribution.

Accessing the U=P(Ar) functionality also proved to be an unfruitful endeavor for this system. It was found that by reacting either **2.3** or **2.8** with the phosphayilde $Mes^*P{=}PMe_3$, the $Mes^*P{=}PMes^*$ diphosphene dimer was generated. This dimeric species is most likely formed by decomposition of a transient phosphinidene complex.[110, 113] Additionally, reactions of **2.3** with Mes^*PH_2 resulted in the formation of a phosphaindole byproduct. This particular byproduct supports the transient generation of a uranium phosphinidene complex, which then decomposes through a phosphorus insertion into an *ortho* ^{t}Bu methyl C-H bond followed by reductive elimination[111]. Unfortunately, the use of a smaller phosphine ligand did not allow for isolation of the desired uranium phosphinidene functionality.

As all reactivity with the $[L]_3U(X)$ complexes resulted in the formation of $U[L]_4$, it was determined that the $[N(SiMe_3)(3,5\text{-}(CH_3)_2(C_6H_3)]$ anilido ligand was unable to adequately protect the uranium center from undergoing ligand redistribution. Attempts at altering the steric properties of the system through use of a smaller U(V) tris(anildo) complex of the type $[L]_3U(Cl)_2$ were not possible, as the desired U(V) species could not be accessed through oxidation of $[L]_3U(Cl)$ (**2.3**) with either CuCl or WCl_6.

With most reactivity of the $[L]_3U(X)$ complexes resulting in the formation of $U[L]_4$, the $[N(SiMe_3)(3,5\text{-}(CH_3)_2(C_6H_3)]$ anilido ligand was deemed unsuitable for

stabilizing targeted X-U=E functionalities. With this in mind, other ancillary ligand frameworks that made use of chelating motifs were explored, as these systems are less likely to undergo unwanted ligand redistribution reactivity.

2.10: Experimental

2.10.1: General experimental procedures

All experiments were performed under an atmosphere of dry N_2 in a VAC Atmospheres dry box. Solvents were purified using the appropriate VAC Atmospheres solvent purifier or dried over sodium benzophenone ketyl and distilled under an atmosphere of dry N_2. Solvents purified by these methods were subsequently degassed using successive freeze-pump-thaw cycles, brought into the dry box without exposure to air, and stored over activated 4-Å molecular sieves. Celite and molecular sieves were activated and dried by heating under high vacuum (about 0.3 mmHg) at > 200°C overnight. Deuterated NMR solvents, C_6D_6 and $CDCl_3$, were purchased from Cambridge Isotope Laboratories, degassed using freeze-pump-thaw cycles and stored over 4-Å molecular sieves. The anilido ligand [Li][N((SiCH$_3$)$_3$)(3,5-dimethylphenyl)],[90] UI_3(1,4-dioxane)$_{1.5}$, UI_4(1,4-dioxane)$_2$,[88] UCl_4[93] and $ThCl_4$(DME)$_2$[100] were synthesized by reported methods. ^{1}H NMR spectra were recorded using Varian VNMRS spectrometers operating at 300 MHz or 400 MHz for ^{1}H at room temperature in C_6D_6 unless otherwise specified. All chemical shifts herein are reported with reference to residual solvent peaks for C_6D_6 at δ 7.16. Microanalyses were performed at Atlantic Microlabs in Norcross, GA.

2.10.2: Synthesis of [K][N(SiMe$_3$)(3,5-(CH$_3$)$_2$(C$_6$H$_3$)]

To a 20-mL scintillation vial charged with 15 mL of toluene and a small stir bar, (2.00 g, 10.35 mmol) of *N*-trimethylsilyl-3,5-dimethylaniline was added. The golden colored solution was allowed to mix thoroughly, where then (0.423 g, 10.55 mmol) of KH was added. The mixture was heated to 100°C and allowed to stir overnight (~15 hrs). The solid material was collected on a medium porosity frit and was washed with toluene. Volatiles were removed *in vacuo* to afford a pure product. **Yield: 2.23 g, 93%.** ^{1}H NMR (300 MHz, C$_6$D$_6$, 298K): δ = 6.14 (s, 1H, *p*-Ar-*H*), 6.06 (s, 2H, *o*-Ar-*H*), 2.29 (s, 6H, Ar-C*H*$_3$), 0.28 (s, 9H, Si(C*H*$_3$)$_3$).

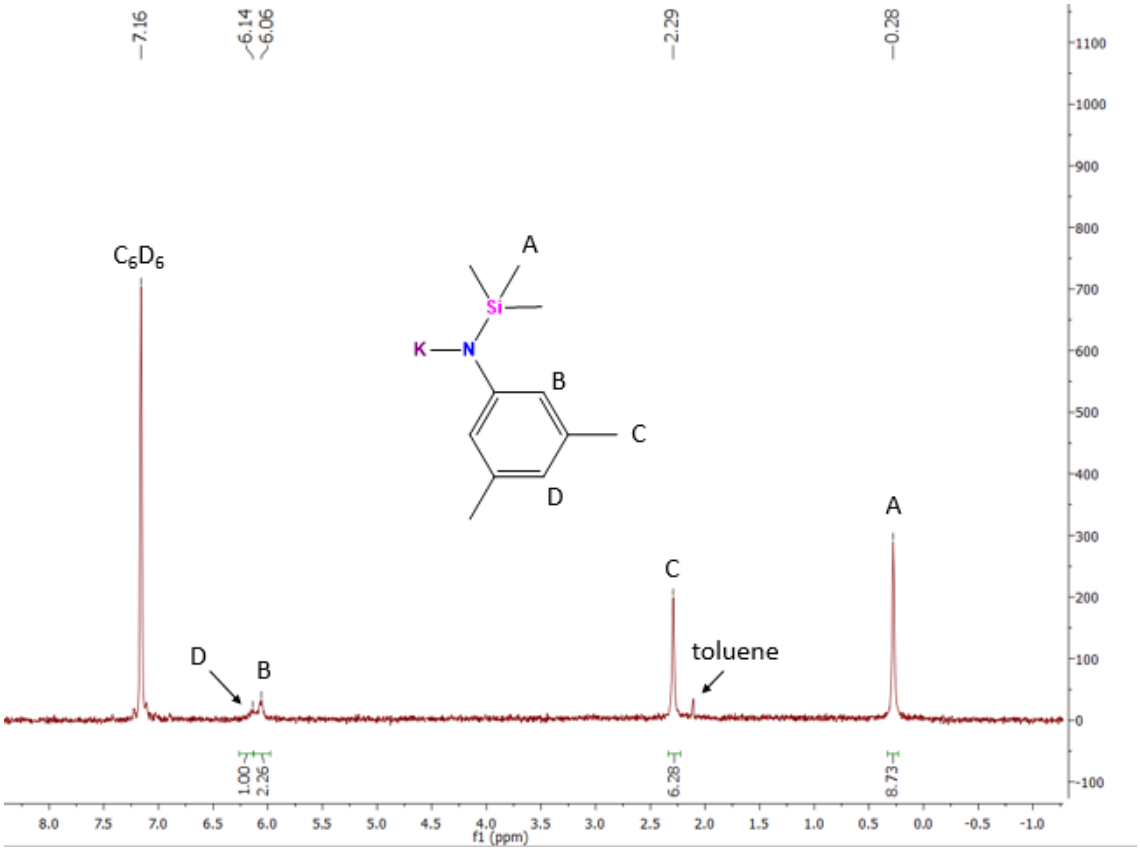


Figure 2-26: *300 MHz ^{1}H NMR spectrum of K[N(SiMe$_3$)(3,5-(CH$_3$)$_2$(C$_6$H$_3$)] in C$_6$D$_6$*

*2.10.3: Synthesis of $[L]_3U(I)$ (**2.1**) from [Li][N(Si(CH$_3$)$_3$)(3,5-dimethylphenyl)]*

To a 20-mL scintillation vial charged with 15 mL of diethyl ether and a small stir bar, (0.170 g, 0.185 mmol) of $UI_4(1,4\text{-dioxane})_2$ was added. The clear red solution was allowed to mix thoroughly, where then (0.150 g, 0.549 mmol) of $Li(Et_2O)[N(SiMe_3)((3,5\text{-dimethylphenyl})]$ was added as a powder. The solution became an opaque, red-orange color and was allowed to stir overnight (~18 h). Volatiles were removed *in vacuo*. The crude product was extracted with pentane and filtered over a bed of Celite in a Pasteur pipette to afford a clear red-orange solution. Volatiles were removed *in vacuo* to afford a red-orange solid. **Yield: 0.0928 g, 56%.** ^{1}H NMR (300 MHz, C_6D_6, 298 K): δ = 7.83 (27H, Si(C*H*$_3$)$_3$), 0.09 (3H, *p*-Ar-*H*), -2.30 (6H, *o*-Ar-*H*), -5.57 (18H, Ar-C*H*$_3$).

*2.10.4: Synthesis of $[Li(Cl)(THF)_2][[L]_3U(Cl)]$ (**2.2**)*

To a 20-mL scintillation vial charged with 10 mL of THF and a small stir bar, (0.282 g, 0.74 mmol) UCl_4 was added. The pale-green solution was allowed to mix thoroughly, where then (0.608 g, 2.22 mmol) of $Li(Et_2O)[N(SiMe_3)((3,5\text{-dimethylphenyl})]$ salt was added directly as a powder. The solution turned a darker green color and was allowed to stir overnight (~18 h). Volatiles were removed *in vacuo*. The crude product was extracted with diethyl ether and filtered over a bed of Celite in a Pasteur pipette. Volatiles were removed *in vacuo* to afford a green solid. **Yield: 0.663 g, 81%.** ^{1}H NMR (300 MHz, C_6D_6, 298K): δ = 9.99 (27H, Si(C*H*$_3$)$_3$), 4.02 (6H, THF), 1.65 (6H, THF), -1.74 (3H, Aryl-*H*), -6.30 (18H, Aryl-C*H*$_3$), -13.42 (6H, Aryl-*H*).

*2.10.5: Synthesis of $[L]_3U(Cl)$ (**2.3**)*

To a 20-mL scintillation vial charged with 10 mL of THF and a small stir bar, (0.075 g, 0.197 mmol) of UCl_4 was added. The green solution was allowed to mix thoroughly, where then a solution containing (0.133 g, 0.575 mmol) of K[N(Si(CH_3)$_3$)(3,5-dimethylphenyl) in 4 mL of THF was added dropwise over 5 min. The solution became darker green in color and was allowed to stir overnight (~18 h). Volatiles were removed *in vacuo* to afford a golden-brown powder. The crude product was extracted with ~10 mL of toluene and filtered over a bed of Celite in a Pasteur pipette. Volatiles were again removed *in vacuo*. Crude product was then extracted with pentane (~10mL) and filtered over a bed of Celite in a pasture pipette. Volatiles were removed in *vacuo* to afford a golden-brown powder. **Yield: 0.103 g, 68%.** ^{1}H NMR (300 MHz, C_6D_6): δ = 11.25 (6H, Aryl-*H*), 10.34 (27H, Si(C*H*$_3$)$_3$), -1.81 (3H, Aryl-*H*), -6.39 (18H, Aryl-C*H*$_3$), -13.78 (4H, THF).

*2.10.6: Synthesis of $[L]_3U(Br)$ (**2.4**)*

To a 20-mL scintillation vial charged with 10 mL of THF and a small stir bar, (0.060 g, 0.078 mmol) $[L]_3UCl$ (**2.3**) was added. The golden solution was allowed to mix thoroughly, where then (0.012 g, 0.078 mmol) of Me_3SiBr was added. The solution became yellow-green in color and was allowed to stir for 4 days. Volatiles were removed *in vacuo*. The crude product was extracted with ~10 mL of pentane and was then filtered over a bed of Celite in a Pasteur pipette. Volatiles were removed *in vacuo* at 40°C for 2 h to ensure excess Me_3SiBr was

removed. ^{1}H NMR (C_6D_6, 300 MHz, 298 K) : δ11.16 (6H, Ar-*H*), 8.89 (27H, Si(C*H*$_3$)$_3$, -0.85 (3H, Aryl-*H*), -5.92 (18H, Aryl-C*H*$_3$), -7.76 (4H, THF).

*2.10.7: Synthesis of [L]$_2$U(Br)(μ-Br)$_3$U(Br)[L]$_2$ (**2.5**)*

To a 20-mL scintillation vial charged with 10 mL of THF, 4 mL of 1,4-dioxane and a small stir bar, (0.100 g, 0.0964 mmol) of **2.2** was added. The yellow-green solution was allowed to mix thoroughly, where then a solution containing (0.086 g, 0.56 2mmol) of trimethylsilylbromide in 4 mL of THF was added dropwise over the course of 2 min. The resulting solution was allowed to stir for 6 days. Crystals suitable for X-ray diffraction were grown from THF at room temperature over the course of several days.

*2.10.8: Synthesis of [L]$_4$U from K[L] (**2.6**)*

To a 20-mL scintillation vial charged with 10 mL of THF and a small stir bar, (0.100 g, 0.108 mmol) of UI_4(dioxane)$_2$ was added. The clear red solution was allowed to mix thoroughly, where then (0.100 g, 0.434 mmol) of K[L] was added. The solution turned cloudy and a gold color and was allowed to stir overnight (~15 h). Volatiles were removed *in vacuo*. The crude product was extracted with pentane and filtered over Celite. Volatiles were again removed *in vacuo*. The crude product was extracted with pentane again and filtered over a bed of Celite. Volatiles were removed *in vacuo* to afford a golden powder. **Yield: 0.041 g, 38%.** ^{1}H NMR (300 MHz, C_6D_6, 298 K): δ = 3.54 (4H, Ar-*H*), 1.65 (36H, Si(C*H*$_3$)$_3$), -1.09 (24H, Ar-C*H*$_3$), -2.89 (8H, Ar-*H*).

*2.10.9: Synthesis of $[L]_4Th$ (**2.7**)*

To a 20-mL scintillation vial charged with 10 mL of THF and a small stir bar, (0.100 g,0.180 mmol) of $ThCl_4(DME)_2$ was added. The clear, colorless solution was allowed to mix thoroughly, where then (0.168 g, 0.726 mmol) of K[L] was added as a powder. The solution became cloudy and pale yellow upon addition of K[L]. The solution was allowed to stir overnight (~15 hrs). Volatiles were removed *in vacuo*. The crude product was then extracted with pentane and filtered over Celite. Volatiles were again removed *in vacuo*. The crude product was extracted with pentane again and filtered over a bed of Celite. Volatiles removed *in vacuo*. Crude product was recrystallized from diethyl ether at room temperature and formed golden-yellow hexagonal plate crystals. **Yield (recrystallized): 0.045 g, 25%.** ^{1}H NMR (400 MHz, C_6D_6, 298 K): δ = 6.80 (s, 8H, Ar-*H*), 6.68 (s, 4H, Ar-*H*), 2.33 (s, 24H, Ar-CH_3), 0.17 (s, 36H, Si(CH_3)$_3$). ^{13}C NMR (400 MHz, C_6D_6, 298 K) δ = 146.94 (Ar-*C*), 138.94 (Ar-*C*), 126.14 (Ar-*C*), 125.35 (Ar-*C*), 21.30 (Ar-*C*H_3), 0.83 (Si(*C*H_3)$_3$).

*2.10.10: Synthesis of $[L]_3U(THF)$ (**2.8**) via reduction pathway*

To a 20-mL scintillation vial charged with 10 mL of THF and a small stir bar, (0.073 g, 0.0953 mmol) $L_3U(Cl)$ (**2.3**) was added. The pale-green solution was allowed to mix thoroughly and was then chilled to -35°C for about 15 min. Once chilled, (0.013 g, 0.095 mmol) of KC_8 was added. The solution turned dark purple instantly and was allowed to stir for 45 min while warming to room temperature. Volatiles were removed *in vacuo*. The crude product was extracted

with hexanes and filtered over Celite. Volatiles were removed *in vacuo* to afford a dark purple solid. **Yield: 0.069 g, 90.2%.** Note: the complex is thermally unstable and decomposes after a few hours at room temperature. ^{1}H NMR (300 MHz, C_6D_6, 298 K): δ = 9.96 (3H, Ar-*H*), 0.76 (6H, Ar-*H*), 0.26 (18H, Ar-CH_3), -6.50 (27H, Si(CH_3)$_3$).

*2.10.11: Synthesis of [L]$_3$U(THF) (**2.8**) from K[L]*

To a 20-mL scintillation vial charged with 10 mL of THF and a small stir bar, (0.102 g, 0.136 mmol) of UI_3(dioxane)$_{1.5}$ was added. The purple solution was allowed to mix thoroughly, where then (0.047 g, 0.283 mmol) of KI was added. To this solution, 4 mL of a solution containing (0.092 g, 0.397mmol) of K[L] was added dropwise over 4 min. The solution turned a burgundy color instantly and was allowed to stir for 15 min. Volatiles were removed *in vacuo* to afford a dark-purple solid. **Yield: 0.077 g, 0.67%.**

2.11: References

1. World Nuclear Association. Radioactive Waste Management. 2017. http://www.world-nuclear.org/information-library/nuclear-fuel-cycle/nuclear-wastes/radioactive-waste-management.aspx (Accessed Apr 18, 2017).

2. Nuclear Energy Institute. On-Site Storage of Nuclear Waste. https://www.nei.org/Knowledge-Center/Nuclear-Statistics/On-Site-Storage-of-Nuclear-Waste (Accessed May 10, 2017).

3. World Nuclear Association. Processing of Used Nuclear Fuel. 2016. http://www.world-nuclear.org/information-library/nuclear-fuel-cycle/fuel-recycling/processing-of-used-nuclear-fuel.aspx (Accessed Apr 20, 2017).

4. Afsar, A.; Distler, P.; Harwood, L. M.; John, J.; Westwood, J., Extraction of minor actinides, lanthanides and other fission products by silica-immobilized BTBP/BTPhen ligands. *Chem. Commun.* **2017,** *53* (28), 4010-4013.

5. U.S. Department of Energy Office of Science. Heavy Element Chemistry. https://science.energy.gov/~/media/bes/pdf/brochures/bes-cras/2010-apr/cra_22_heavy_element_chemistry.pdf (Accessed Apr 18, 2017).

6. U.S. Department of Energy Office of Nuclear Energy. Mission. https://energy.gov/ne/mission (Accessed Apr 20, 2017).

7. Denecke, M. A., Synchrotron applications to f-element research in the nuclear fuel cycle. *Dalton Trans.* **2015,** *44* (6), 2606-2612.

8. Arnold, P. L.; Love, J. B.; Patel, D., Pentavalent uranyl complexes. *Coord. Chem. Rev.* **2009,** *253* (15-16), 1973-1978.

9. Thuery, P.; Villiers, C.; Jaud, J.; Ephritikhine, M.; Masci, B., Uranyl-based metallamacrocycles: Tri- and tetranuclear complexes with (2R,3R,4S,5S)-tetrahydrofurantetracarboxylic acid. *J. Am. Chem. Soc.* **2004,** *126* (22), 6838-6839.

10. Gregson, M.; Lu, E.; Mills, D. P.; Tuna, F.; McInnes, E. J. L.; Hennig, C.; Scheinost, A. C.; McMaster, J.; Lewis, W.; Blake, A. J.; Kerridge, A.; Liddle, S. T., The inverse-trans-influence in tetravalent lanthanide and actinide bis(carbene) complexes. *Nature Communications* **2017,** *8*.

11. La Pierre, H. S.; Rosenzweig, M.; Kosog, B.; Hauser, C.; Heinemann, F. W.; Liddle, S. T.; Meyer, K., Charge control of the inverse trans-influence. *Chem. Commun.* **2015,** *51* (93), 16671-16674.

12. Lam, O. P.; Franke, S. M.; Nakai, H.; Heinemann, F. W.; Hieringer, W.; Meyer, K., Observation of the Inverse Trans Influence (ITI) in a Uranium(V) Imide Coordination Complex: An Experimental Study and Theoretical Evaluation. *Inorg. Chem.* **2012,** *51* (11), 6190-6199.

13. La Pierre, H. S.; Meyer, K., Uranium-Ligand Multiple Bonding in Uranyl Analogues, L=U=L (n+), and the Inverse Trans Influence. *Inorg. Chem.* **2013,** *52* (2), 529-539.

14. Denning, R. G., Electronic-structure and bonding in actinyl ions. *Struct. Bond.* **1992,** *79*, 215-276.

15. Gong, Y.; Vallet, V.; Michelini, M. D.; Rios, D.; Gibson, J. K., Activation of Gas-Phase Uranyl: From an Oxo to a Nitrido Complex. *J. Phys. Chem. A* **2014,** *118* (1), 325-330.

16. Lewis, A. J.; Nakamaru-Ogiso, E.; Kikkawa, J. M.; Carroll, P. J.; Schelter, E. J., Pentavalent uranium trans-dihalides and -pseudohalides. *Chem. Commun.* **2012,** *48* (41), 4977-4979.

17. Lewis, A. J.; Carroll, P. J.; Schelter, E. J., Stable Uranium(VI) Methyl and Acetylide Complexes and the Elucidation of an Inverse Trans Influence Ligand Series. *J. Am. Chem. Soc.* **2013,** *135* (35), 13185-13192.

18. Burns, C. J.; Clark, D. L.; Donohoe, R. J.; Duval, P. B.; Scott, B. L.; Tait, C. D., A trigonal bipyramidal uranyl amido complex: Synthesis and structural characterization of $[Na(THF)_2][UO_2(N(SiMe_3)_2)_3]$. *Inorg. Chem.* **2000,** *39* (24), 5464-5468.

19. Arnold, P. L.; Turner, Z. R.; Kaltsoyannis, N.; Pelekanaki, P.; Bellabarba, R. M.; Tooze, R. P., Covalency in Ce-IV and U-IV Halide and N-Heterocyclic Carbene Bonds. *Chem. Eur. J.* **2010,** *16* (31), 9623-9629.

20. Fortier, S.; Brown, J. L.; Kaltsoyannis, N.; Wu, G.; Hayton, T. W., Synthesis, Molecular and Electronic Structure of $U^V(O)[N(SiMe_3)_2]_3$. *Inorg. Chem.* **2012,** *51* (3), 1625-1633.

21. Smiles, D. E.; Wu, G.; Hrobarik, P.; Hayton, T. W., Use of ^{77}Se and ^{125}Te NMR Spectroscopy to Probe Covalency of the Actinide-Chalcogen Bonding in $Th(E_n)\{N(SiMe_3)_2\}_3]^-$ (E = Se, Te; *n* = 1, 2) and Their Oxo-Uranium(VI) Congeners. *J. Am. Chem. Soc.* **2016,** *138* (3), 814-825.

22. Hayton, T. W., Recent developments in actinide-ligand multiple bonding. *Chem. Commun.* **2013,** *49* (29), 2956-2973.

23. Diaconescu, P. L.; Odom, A. L.; Agapie, T.; Cummins, C. C., Uranium-group 14 element single bonds: Isolation and characterization of a uranium(IV) silyl species. *Organometallics* **2001,** *20* (24), 4993-4995.

24. Cantat, T.; Graves, C. R.; Jantunen, K. C.; Burns, C. J.; Scott, B. L.; Schelter, E. J.; Morris, D. E.; Hay, P. J.; Kiplinger, J. L., Evidence for the Involvement of 5f Orbitals in the Bonding and Reactivity of Organometallic Actinide Compounds: Thorium(IV) and Uranium(IV) Bis(hydrazonato) Complexes. *J. Am. Chem. Soc.* **2008,** *130* (51), 17537-17551.

25. Cantat, T.; Graves, C. R.; Scott, B. L.; Kiplinger, J. L., Challenging the Metallocene Dominance in Actinide Chemistry with a Soft PNP Pincer Ligand: New Uranium Structures and Reactivity Patterns. *Angew. Chem. Int. Ed.* **2009,** *48* (20), 3681-3684.

26. Graves, C. R.; Scott, B. L.; Morris, D. E.; Kiplinger, J. L., Facile access to pentavalent uranium organometallics: One-electron oxidation of Uranium(IV) imido complexes with copper(I) salts. *J. Am. Chem. Soc.* **2007,** *129* (39), 11914-11915.

27. Graves, C. R.; Schelter, E. J.; Cantat, T.; Scott, B. L.; Kiplinger, J. L., A Mild Protocol To Generate Uranium(IV) Mixed-Ligand Metallocene Complexes using Copper(I) Iodide. *Organometallics* **2008,** *27* (20), 5371-5378.

28. Graves, C. R.; Yang, P.; Kozimor, S. A.; Vaughn, A. E.; Clark, D. L.; Conradson, S. D.; Schelter, E. J.; Scott, B. L.; Thompson, J. D.; Hay, P. J.; Morris, D. E.; Kiplinger, J. L., Organometallic uranium(V)-imido halide complexes: From synthesis to electronic structure and bonding. *J. Am. Chem. Soc.* **2008,** *130* (15), 5272-5285.

29. Graves, C. R.; Vaughn, A. E.; Schelter, E. J.; Scott, B. L.; Thompson, J. D.; Morris, D. E.; Kiplinger, J. L., Probing the Chemistry, Electronic Structure and Redox Energetics in Organometallic Pentavalent Uranium Complexes. *Inorg. Chem.* **2008,** *47* (24), 11879-11891.

30. Graves, C. R.; Scott, B. L.; Morris, D. E.; Kiplinger, J. L., Tetravalent and pentavalent uranium acetylide complexes prepared by oxidative functionalization with CuC CPh. *Organometallics* **2008,** *27* (14), 3335-3337.

31. Graves, C. R.; Kiplinger, J. L., Pentavalent uranium chemistry-synthetic pursuit of a rare oxidation state. *Chem. Commun.* **2009,** (26), 3831-3853.

32. Graves, C. R.; Scott, B. L.; Morris, D. E.; Kiplinger, J. L., Selenate and tellurate complexes of pentavalent uranium. *Chem. Commun.* **2009,** (7), 776-778.

33. Jantunen, K. C.; Burns, C. J.; Castro-Rodriguez, I.; Da Re, R. E.; Golden, J. T.; Morris, D. E.; Scott, B. L.; Taw, F. L.; Kiplinger, J. L., Thorium(IV) and uranium(IV) ketimide complexes prepared by nitrile insertion into actinide-alkyl and -aryl bonds. *Organometallics* **2004,** *23* (20), 4682-4692.

34. Kiplinger, J. L.; Pool, J. A.; Schelter, E. J.; Thompson, J. D.; Scott, B. L.; Morris, D. E., Actinide-mediated cyclization of 1,2,4,5-tetracyanobenzene: Synthesis and characterization of self-assembled trinuclear thorium and uranium macrocycles. *Angew. Chem. Int. Ed.* **2006,** *45* (13), 2036-2041.

35. Pool, J. A.; Scott, B. L.; Kiplinger, J. L., A new mode of reactivity for pyridine N-oxide: C-H activation with uranium(IV) and thorium(IV) bis(alkyl) complexes. *J. Am. Chem. Soc.* **2005,** *127* (5), 1338-1339.

36. Schelter, E. J.; Veauthier, J. M.; Thompson, J. D.; Scott, B. L.; John, K. D.; Morris, D. E.; Kiplinger, J. L., 4f-5f heterotrimetallic complexes exhibiting electrochemical and magnetic communication. *J. Am. Chem. Soc.* **2006,** *128* (7), 2198-2199.

37. Schelter, E. J.; Morris, D. E.; Scott, B. L.; Kiplinger, J. L., Actinide-mediated coupling of 4-fluorobenzonitrile: synthesis of an eight-membered thorium(IV) tetraazametallacycle. *Chem. Commun.* **2007,** (10), 1029-1031.

38. Schelter, E. J.; Yang, P.; Scott, B. L.; Da Re, R. E.; Jantunen, K. C.; Martin, R. L.; Hay, P. J.; Morris, D. E.; Kiplinger, J. L., Systematic studies of

early actinide complexes: Thorium(IV) fluoroketimides. *J. Am. Chem. Soc.* **2007,** *129* (16), 5139-5152.

39. Schelter, E. J.; Yang, P.; Scott, B. L.; Thompson, J. D.; Martin, R. L.; Hay, P. J.; Morris, D. E.; Kiplinger, J. L., Systematic studies of early actinide complexes: Uranium(IV) fluoroketimides. *Inorg. Chem.* **2007,** *46* (18), 7477-7488.

40. Schelter, E. J.; Wu, R. L.; Scott, B. L.; Thompson, J. D.; Morris, D. E.; Kiplinger, J. L., Mixed valency in a uranium multimetallic complex. *Angew. Chem. Int. Ed.* **2008,** *47* (16), 2993-2996.

41. Schelter, E. J.; Wu, R. L.; Scott, B. L.; Thompson, J. D.; Cantat, T.; John, K. D.; Batista, E. R.; Morris, D. E.; Kiplinger, J. L., Actinide Redox-Active Ligand Complexes: Reversible Intramolecular Electron-Transfer in U(dpp-BIAN)(2)/U(dpp-BIAN)(2)(THF). *Inorg. Chem.* **2010,** *49* (3), 924-933.

42. Thomson, R. K.; Graves, C. R.; Scott, B. L.; Kiplinger, J. L., Organometallic uranium(IV) fluoride complexes: preparation using protonolysis chemistry and reactivity with trimethylsilyl reagents. *Dalton Trans.* **2010,** *39* (29), 6826-6831.

43. Thomson, R. K.; Scott, B. L.; Morris, D. E.; Kiplinger, J. L., Synthesis, structure, spectroscopy and redox energetics of a series of uranium(IV) mixed-ligand metallocene complexes. *C. R. Chimie* **2010,** *13* (6-7), 790-802.

44. Thomson, R. K.; Graves, C. R.; Scott, B. L.; Kiplinger, J. L., Synthesis and Molecular Structure of (C5Me5)(2)U((OBu)-Bu-t)(SePh): A Mixed-Ligand Alkoxide-Selenide Uranium(IV) Metallocene Complex Resulting from tert-Butoxy-Trimethylsilane Elimination. *J. Chem. Crystallog.* **2011,** *41* (8), 1241-1244.

45. Thomson, R. K.; Graves, C. R.; Scott, B. L.; Kiplinger, J. L., Uncovering alternate reaction pathways to access uranium(IV) mixed-ligand aryloxide-chloride and alkoxide-chloride metallocene complexes: Synthesis and molecular structures of (C5Me5)(2)U(O-2,6-(Pr2C6H3)-Pr-i)(Cl) and (C5Me5)(2)U(O-Bu-t)(Cl). *Inorg. Chim. Acta* **2011,** *369* (1), 270-273.

46. Haskel, A.; Straub, T.; Eisen, M. S., Organoactinide-catalyzed intermolecular hydroamination of terminal alkynes. *Organometallics* **1996,** *15* (18), 3773-3775.

47. Benaud, O.; Berthet, J. C.; Thuery, P.; Ephritikhine, M., The Bis Metallacyclic Anion $[U(N\{SiMe_3\}_2)(CH_2SiMe_2N\{SiMe_3\})_2]^-$. *Inorg. Chem.* **2010,** *49* (17), 8117-8130.

48. Andersen, R. A., chloro (hexamethyldidilyl)amido zirconium(IV) and methyltris (hexamethyldisilyl)amido zirconium(IV) and chloro

(hexamethyldisilyl)amido hafnium(IV) and methyltris (hexamethldisilyl)amido hafnium(IV). *Inorg. Chem.* **1979,** *18* (6), 1724-1725.

49. Andersen, R. A., Tris((hexamethyldisilyl)amido)uranium(III) - Preparation and coordination chemistry. *Inorg. Chem.* **1979,** *18* (6), 1507-1509.

50. Odom, A. L.; Arnold, P. L.; Cummins, C. C., Heterodinuclear uranium/molybdenum dinitrogen complexes. *J. Am. Chem. Soc.* **1998,** *120* (23), 5836-5837.

51. Fox, A. R.; Creutz, S. E.; Cummins, C. C., A bimetallic uranium mu-dicarbide complex: synthesis, X-ray crystal structure, and bonding. *Dalton Trans.* **2010,** *39* (29), 6632-6634.

52. Smiles, D. E.; Wu, G.; Hayton, T. W., Reactivity of $[U(CH_2SiMe_2NSiMe_3)(NR_2)_2]$ (R = $SiMe_3$) with elemental chalcogens: towards a better understanding of chalcogen atom transfer in the actinides. *New J. Chem.* **2015,** *39* (10), 7563-7566.

53. Lewis, A. J.; Williams, U. J.; Carroll, P. J.; Schelter, E. J., Tetrakis(bis(trimethylsilyl)amido)uranium(IV): Synthesis and Reactivity. *Inorg. Chem.* **2013,** *52* (13), 7326-7328.

54. Brown, J. L.; Fortier, S.; Lewis, R. A.; Wu, G.; Hayton, T. W., A Complete Family of Terminal Uranium Chalcogenides, U(E)(N{SiMe3}(2))(3) (-) (E = O, S, Se, Te). *J. Am. Chem. Soc.* **2012,** *134* (37), 15468-15475.

55. Mullane, K. C.; Lewis, A. J.; Yin, H. L.; Carroll, P. J.; Schelter, E. J., Anomalous One-Electron Processes in the Chemistry of Uranium Nitrogen Multiple Bonds. *Inorg. Chem.* **2014,** *53* (17), 9129-9139.

56. Smiles, D. E.; Wu, G.; Hayton, T. W., Reversible Chalcogen-Atom Transfer to a Terminal Uranium Sulfide. *Inorg. Chem.* **2014,** *53* (24), 12683-12685.

57. Monreal, M. J.; Thomson, R. K.; Cantat, T.; Travia, N. E.; Scott, B. L.; Kiplinger, J. L., UI4(1,4-dioxane)(2), UCl4(1,4-dioxane) (2), and UI3(1,4-dioxane)(1.5): Stable and Versatile Starting Materials for Low- and High-Valent Uranium Chemistry. *Organometallics* **2011,** *30* (7), 2031-2038.

58. Dormond, A.; El Bouadili, A.; Aaliti, A.; Moise, C., Insertion of carbonyl compounds into actinide—carbon σ bonds: Reactivity of [(Me3Si)2)2N]2M・Ch2Si(Me)2NSiMe3. *J. Organomet. Chem.* **1985,** *288* (1), C1-C5.

59. Nagae, H.; Hato, W.; Kawakita, K.; Tsurugi, H.; Mashima, K., Arylimido-Bridged Dinuclear Ti(mu-NAr)(2)Ti Scaffold for Alkyne Insertion into the ortho-C-H Bond of Arylimido Ligands. *Chem. Eur. J.* **2017,** *23* (3), 586-596.

60. Berthet, J. C.; Thuery, P.; Ephritikhine, M., Polyimido Clusters of Neodymium and Uranium, Including a Cluster with an M-6(mu(3)-N)(8) Core. *Eur. J. Inorg. Chem.* **2008,** *2008* (35), 5455-5459.

61. Day, B. M.; Coles, M. P., Assigning Hapticity to Cyclopentadienyl Derivatives of Antimony and Bismuth. *Organometallics* **2013,** *32* (15), 4270-4278.

62. Kiplinger, J. L.; Morris, D. E.; Scott, B. L.; Burns, C. J., Convenient synthesis, structure, and reactivity of (C5Me5)U(CH2C6H5)(3): a simple strategy for the preparation of monopentamethylcyclopentadienyl uranium(IV) complexes. *Organometallics* **2002,** *21* (26), 5978-5982.

63. Herve, A.; Bouzidi, Y.; Berthet, J. C.; Belkhiri, L.; Thuery, P.; Boucekkine, A.; Ephritikhine, M., U-III-CN versus U-IV-NC Coordination in Tris(silylamide) Complexes. *Inorg. Chem.* **2015,** *54* (5), 2474-2490.

64. Thomson, R. K.; Graves, C. R.; Scott, B. L.; Kiplinger, J. L., Straightforward and efficient oxidation of tris(aryloxide) and tris(amide) uranium(III) complexes using copper(I) halide reagents. *Inorg. Chem. Communications* **2011,** *14* (11), 1742-1744.

65. Lichtscheidl, A. G.; Pagano, J. K.; Scott, B. L.; Nelson, A. T.; Kiplinger, J. L., Expanding the Chemistry of Actinide Metallocene Bromides. Synthesis, Properties and Molecular Structures of the Tetravalent and Trivalent Uranium Bromide Complexes: (C5Me4R)(2)UBr2, (C5Me4R)(2)U(O-2,6-(Pr2C6H3)-Pr-i)(Br), and K(THF) (C5Me4R)(2)UBr2 (R = Me, Et). *Inorganics* **2016,** *4* (1), 1-17.

66. Secaur, C. A.; Day, V. W.; Ernst, R. D.; Kennelly, W. J.; Marks, T. J., Ring-bridged biscyclopentadienyluranium(IV) halides. *J. Am. Chem. Soc.* **1976,** *98* (12), 3713-3715.

67. Pearson, R. G., Hard and soft acids and bases—the evolution of a chemical concept. *Coord. Chem. Rev.* **1990,** *100*, 403-425.

68. Vandersluys, W. G.; Sattelberger, A. P., Tetrakis(2,6-di-*tert*-butylphenoxy)uranium(IV) - The 1st structurally characterized neutral homoleptic aryloxide complex of uranium(IV). *Polyhedron* **1989,** *8* (9), 1247-1249.

69. Monreal, M. J.; Thomson, R. K.; Scott, B. L.; Kiplinger, J. L., Enhancing the synthetic efficacy of thorium tetrachloride bis(1,2-dimethoxyethane) with added 1,2-dimethoxyethane: Preparation of metallocene thorium dichlorides. *Inorg. Chem. Commun.* **2014,** *46*, 51-53.

70. Materials Department of Imperial College London Atomistic Simulation Group. Database of Ionic Radii. http://abulafia.mt.ic.ac.uk/shannon/ptable.php (Accessed May 31, 2017).

71. Winter, M. Electronegativity (Pauling): Periodicity. https://www.webelements.com/periodicity/electronegativity_pauling/ (Accessed May 31, 2017).

72. Fortier, S.; Kaltsoyannis, N.; Wu, G.; Hayton, T. W., Probing the Reactivity and Electronic Structure of a Uranium(V) Terminal Oxo Complex. *J. Am. Chem. Soc.* **2011,** *133* (36), 14224-14227.

73. Gardner, B. M.; Balazs, G.; Scheer, M.; Tuna, F.; McInnes, E. J. L.; McMaster, J.; Lewis, W.; Blake, A. J.; Liddle, S. T., Triamidoamine-Uranium(IV)-Stabilized Terminal Parent Phosphide and Phosphinidene Complexes. *Angew. Chem. Int. Ed.* **2014,** *53* (17), 4484-4488.

74. Arney, D. S. J.; Schnabel, R. C.; Scott, B. C.; Burns, C. J., Preparation of actinide phosphinidene complexes: Steric control of reactivity. *J. Am. Chem. Soc.* **1996,** *118* (28), 6780-6781.

75. Duttera, M. R.; Day, V. W.; Marks, T. J., Organoactinide phosphine phosphite coordination chemistry - Facile hydride-induced dealkoxylation and the formation of actinide phosphinidene complexes. *J. Am. Chem. Soc.* **1984,** *106* (10), 2907-2912.

76. Kilgore, U. J.; Fan, H.; Pink, M.; Urnezius, E.; Protasiewicz, J. D.; Mindiola, D. J., Phosphinidene group-transfer with a phospha-Wittig reagent: a new entry to transition metal phosphorus multiple bonds. *Chem. Commun.* **2009,** (30), 4521-4523.

77. Weber, L., Phospha- and arsaalkenes RE=C(NMe2)(2) (E = p, as) as novel phosphinidene- and arsinidene-transfer reagents. *Eur. J. Inorg. Chem.* **2007,** *2007* (26), 4095-4117.

78. Yoshifuji, M.; Shima, I.; Inamoto, N.; Hirotsu, K.; Higuchi, T., Synthesis and structure of bis(2,4,6-tri-*tert*-butylphenyl)diphosphene - Isolation of a true phosphobenzene. *J. Am. Chem. Soc.* **1981,** *103* (15), 4587-4589.

79. Masuda, J. D.; Jantunen, K. C.; Ozerov, O. V.; Noonan, K. J. T.; Gates, D. P.; Scott, B. L.; Kiplinger, J. L., A lanthanide phosphinidene complex: Synthesis, structure, and phospha-Wittig reactivity. *J. Am. Chem. Soc.* **2008,** *130* (8), 2408-2409.

80. Bohm, V. P. W.; Brookhart, M., Dehydrocoupling of phosphanes catalyzed by a rhodium(I) complex. *Angew. Chem. Int. Ed.* **2001,** *40* (24), 4694-4695.

81. Stradiotto, M.; Fujdala, K. L.; Tilley, T. D., Generation and reactivity of {(ethane-1,2-diyl)bis diisopropylphosphine-kappa P }-{ 2,4,6-tri(tert-butyl)phenyl phosphino-kappa P}rhodium (Rh PH((Bu3C6H2)-Bu-t) ((Pr2PCH2CH2PPr2)-

Pr-i-Pr-i)): Catalytic C-P bond formation via intramolecular C-H/P-H dehydrogenative cross-coupling. *Helv. Chim. Acta* **2001,** *84* (10), 2958-2970.

82. Masuda, J. D.; Hoskin, A. J.; Graham, T. W.; Beddie, C.; Fermin, M. C.; Etkin, N.; Stephan, D. W., Catalytic P-H activation by Ti and Zr catalysts. *Chem. Eur. J.* **2006,** *12* (34), 8696-8707.

83. Danopoulos, A. A.; Braunstein, P.; Monakhov, K. Y.; van Leusen, J.; Kogerler, P.; Clemancey, M.; Latour, J. M.; Benayad, A.; Tromp, M.; Rezabal, E.; Frison, G., Heteroleptic, two-coordinate M(NHC){N(SiMe3)(2)} (M = Co, Fe) complexes: synthesis, reactivity and magnetism rationalized by an unexpected metal oxidation state. *Dalton Trans.* **2017,** *46* (4), 1163-1171.

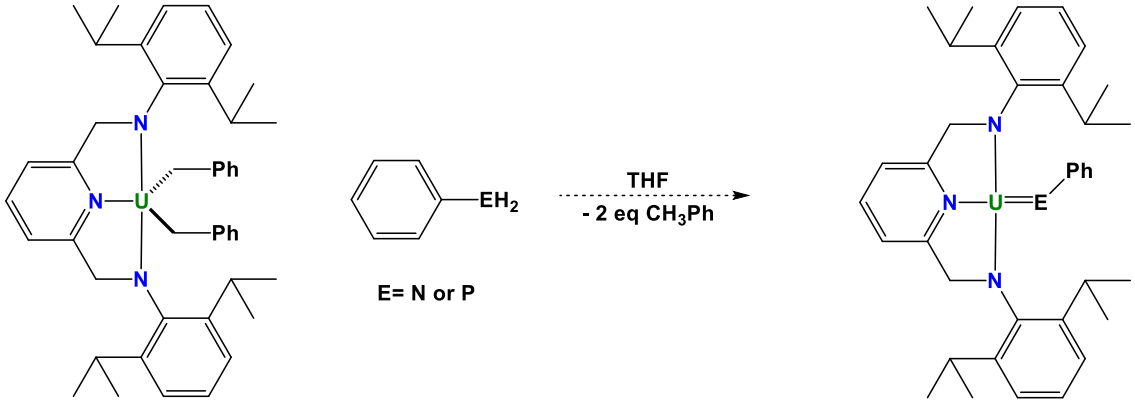
84. Lewis, A. J.; Carroll, P. J.; Schelter, E. J., Reductive Cleavage of Nitrite to Form Terminal Uranium Mono-Oxo Complexes. *J. Am. Chem. Soc.* **2013,** *135* (1), 511-518.

Chapter 3 ~~III~~

An unexpected alkylation: Redox non-innocent ligand reactivity of a bis(amido)pyridine uranium complex

3.1: Exploring the use of a new ligand framework

With the inability to isolate An=E functionalities using monodentate (κ^1) amido ligands, a different ancillary ligand platform was sought to support the desired X-An=E fragments. In order to avoid the complications faced while using the monodentate amido ligands, the new ancillary ligand platform needed to be resistant to ligand redistribution. As low valent actinide chemistry is often dictated by steric properties, the new platform must also provide sufficient steric protection to stabilize the potentially reactive An=E group and allow for inverse trans influence studies of the X-An=E fragment.[45] Multidentate ligand platforms were thus pursued as a means of mitigating unwanted side reactivity, like ligand redistribution, due to their stronger affinity for the metal center. The κ^3 2,6-bis(2,6-diisopropylanilidomethyl)pyridine (BDPP) ligand framework was chosen due to its documented use with thorium[116-119] and uranium[120, 121] to give access to bis(alkyl), alkyl halide and dihalide actinide complexes, which are suitable precursor complexes for generating An=E functionalities. It was hoped that these bis(alkyl) BDPP uranium complexes could be used as suitable building blocks to generate An=E groups (E = N, P) as outlined in Scheme 3-1.



Scheme 3-1: *Proposed protonolysis pathway to BDPP stabilized U=E functionalities (E = N, P).*

In addition to actinide complex formation, bis(amido)pyridine ligands have seen widespread use with many different metals including metals from groups 3,[120, 122-124] 4,[125-130] 5,[131, 132] 7,[133-135] 8,[136-138] 10[139] and 11,[140] as well as some lanthanides.[120, 122-124] With the exception of a Sn complex that exhibits unusual redox reactivity to generate a bis(imino)pyridine complex (BIP),[141] the BDPP ligand framework has proven to be a robust structural motif that is largely innocent during metal based reactivity. This behavior is in stark contrast to the redox-promiscuous behavior seen with the structurally-similar BIP ligand framework (Figure 3-1) on a wide array of metals.[142] Due to its redox innocence, widespread use with many different metals and robust nature, the BDPP ligand framework is a prime candidate for use in stabilizing actinide complexes that contain potentially unstable An=E functionalities.

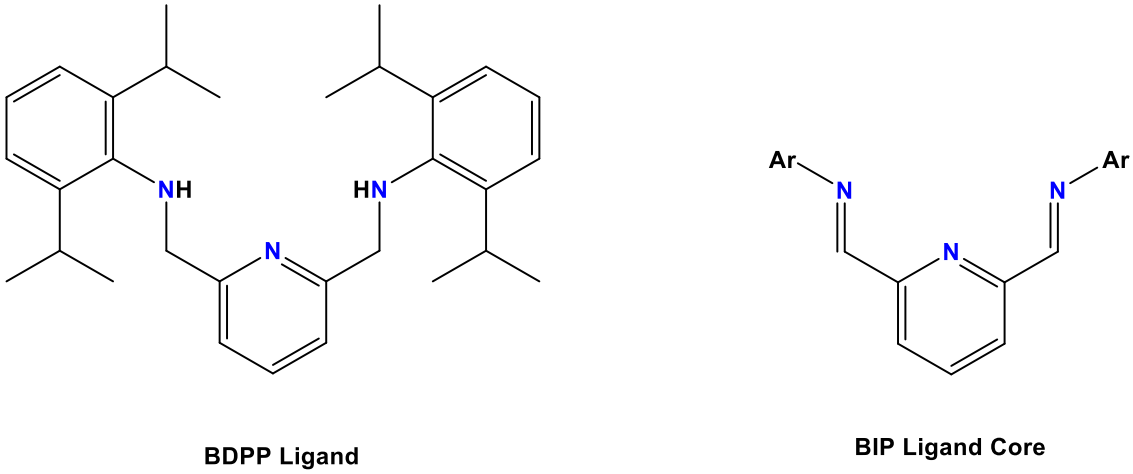


Figure 3-1: *Structural comparison between the BDPP ligand framework and the core of the structurally-similar BIP ligand.*

3.2: An unexpected alkylation resulting in [BDPP']U($CH_2Ph)_2$

It has been reported that salt metathesis reactivity to install the BDPP ligand framework on uranium can be problematic, leading to the formation of

[BDPP]$_2$U.[121] Issues with installing only 1 equiv. of the BDPP ligand on uranium by this method are due in part to the instability of the Li_2[BDPP] salt.[118] As such, we pursued the synthesis of [BDPP]U($CH_2Ph)_2$ by means of a reported protonolysis route.[121] This particular pathway, developed by Diaconescu and coworkers, involves the *in situ* generation of a U(III) alkyl species "U($CH_2Ph)_3$" from $UI_3(THF)_4$, which then undergoes a proposed redox disproportionation to generate the desired [BDPP]U($CH_2Ph)_2$ complex and an uncharacterized U(0) byproduct.[121] As disproportionation is essential to generate the bis(alkyl) BDPP uranium complex, the yield of the desired complex is inherently low; after the disproportionation occurs, roughly 50% of the uranium is lost as an uncharacterized low valent uranium species. With the recent development and characterization of U($CH_2Ph)_4$ by Bart and coworkers,[143-145] a similar, more direct protonolysis route that does not require a disproportionation reaction was envisioned. This pathway would require the reaction between 1 equiv. of Bart and coworkers U($CH_2Ph)_4$ precursor and 1 equiv. of the proligand [BDPP]H_2.[127, 143] If successful, this reaction would install the BDPP ligand and eliminate 2 equiv. of $PhCH_3$.

Upon attempting to generate [BDPP]U($CH_2Ph)_2$ by this new method, it was found that an unexpected alkylation occurred at the 4-position of the pyridine ring, generating [K]([BDPP']U($CH_2Ph)_2$) (**3.1**) (Figure 3-2), where BDPP′ = 2,6-bis(2,6-diisopropylanilidomethyl)-4-(benzyl)dihydropyridonate.

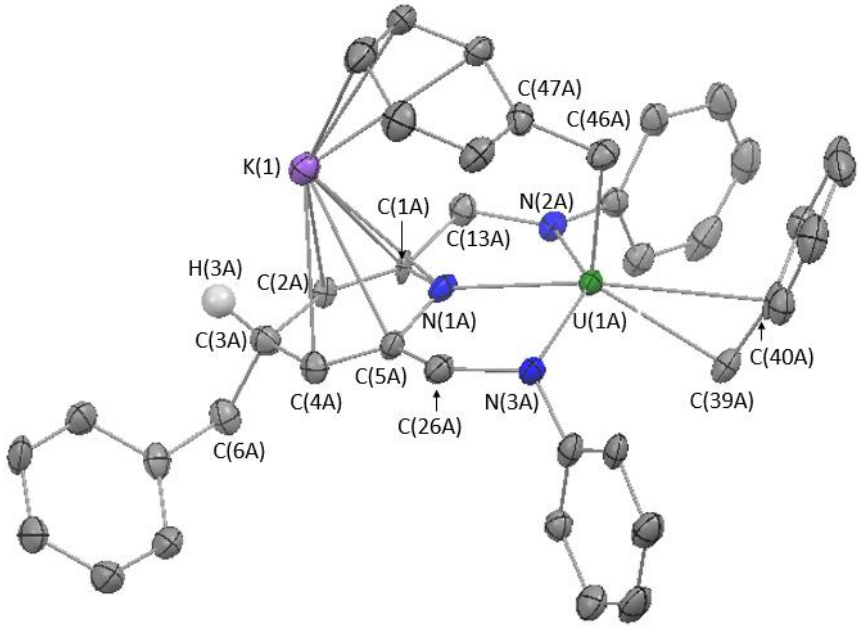


Figure 3-2: *ORTEP depiction of [K]([BDPP']U($CH_2Ph)_2$) (**3.1**) with ellipsoids shown at 30% probability. 2,6-diisopropyl groups and most hydrogen atoms removed for clarity.*

Table 3-1: *Selected bond distances (Å) and angles (°) for **3.1***

Bond	Distance (Å)	Bond Angle	Angle (°)
U(1A)-N(1A)	2.347(5)	N(1A)-U(1A)-N(2A)	67.79(18)
U(1A)-N(2A)	2.239(5)	N(1A)-U(1A)-N(3A)	70.57(18)
U(1A)-N(3A)	2.242(5)	N(1A)-U(1A)-C(39A)	139.3(2)
U(1A)-C(39A)	2.572(6)	N(1A)-U(1A)-C(46A)	101.16(19)
U(1A)-C(40A)	2.851(5)	N(2A)-U(1A)-N(3A)	136.27(17)
U(1A)-C(46A)	2.490(6)	N(2A)-U(1A)-C(39A)	101.2(2)
U(1A)-C(47A)	3.403	N(2A)-U(1A)-C(46A)	103.1(2)
N(1A)-C(1A)	1.404(7)	N(3A)-U(1A)-C(39A)	101.6(2)
C(1A)-C(2A)	1.356(8)	N(3A)-U(1A)-C(46A)	97.3(2)
C(2A)-C(3A)	1.471(8)	C(39A)-U(1A)-C(46A)	119.6(2)
C(3A)-C(4A)	1.517(8)	C(40A)-U(1A)-C(39A)	30.43
C(4A)-C(5A)	1.299(8)	C(47A)-U(1A)-C(46A)	23.44
C(5A)-N(1A)	1.427(8)	U(1A)-C(39A)-C(40A)	85.49
C(13A)-N(2A)	1.483(7)	U(1A)-C(46A)-C(47A)	115.03
C(26A)-N(3A)	1.468(7)		

Complex **3.1** adopts a pseudo-trigonal bipyramidal geometry with approximate C_s symmetry in the solid state. Additionally, the alkylated ligand, BDPP', binds in a meridonal fashion to the uranium center with N(1A)-U(1A)-

N(2A), N(1A)-U(1A)-N(3A) and N(2A)-U(1A)-N(3A) bond angles of 67.79(18)°, 70.57(18)° and 139.3(2)°, respectively. These angles deviate from ideal meridonal binding angles of 90°, 90° and 180°, respectively, in order to accommodate 2 equiv. of CH_2Ph about the uranium center and allow for higher hapticity interactions of one of these CH_2Ph ligands with the uranium center. The binding geometry of the pincer ligand also deviates from ideality due to the short length of the methylene bridges between the Py ring and the amido donors, which do not accommodate ideal meridonal bond angles. Complex **3.1** is structurally very similar to the [BDPP]U$(CH_2Ph)_2$ complex characterized by Diaconescu and coworkers.[121] For example, the U(1A)-N(2A) and U(1A)-N(3A) bond distances of 2.239(5) and 2.242(5) Å, respectively, are nearly identical to the analogous distances observed by Diaconescu and coworkers for their BDPP uranium complex.[121] A major difference between **3.1** and Diaconescu's [BDPP]U$(CH_2Ph)_2$ complex is the U(1A)-N(1A) bond distance. For complex **3.1**, this bond distance is 2.347(5) Å and is about 0.15 Å shorter than the analogous bond for the non-alkylated BDPP complex reported by Diaconescu and coworkers.[121] The shorter U(1A)-N(1A) bond distance for **3.1** is consistent with the formation of an anionic amido donor through the dearomatization of the pyridine ring to form a dihydropyridonate species.[146] Dearomatization of the pyridine ring was confirmed crystallographically through the bond distances within the dihydropyridonate ring: N(1A)-C(1A) 1.404(7) Å, C(1A)-C(2A) 1.356(8) Å, C(2A)-C(3A) 1.471(8) Å, C(3A)-C(4A) 1.517(8)Å, C(4A)-C(5A) 1.299(8) Å and N(1A)-C(5A) 1.427(8)Å. The C(1A)-C(2A) and C(4A)-C(5A) bond distances are consistent with C=C

double, and the C(2A)-C(3A) and C(3A)-C(4A) bond distances are consistent with C-C single bonds. This pattern of bond distances is supportive of broken aromaticity of the BDPP pyridine backbone after alkylation.

The benzyl ligands are best described as η^1 and η^4, with the η^1-benzyl ligand having a U(1A)-C(46A) bond distance of 2.490(6) Å and the η^4-benzyl ligand having a U(1A)-C(39A) bond distance of 2.572(6) Å and a U(1A)-C(40A) bond distance of 2.851(5) Å to the *ipso* carbon of the phenyl ring. Additionally, the η^4-benzyl ligand displays a very acute U(1A)-C(39A)-C(40A) bond angle of 85.5(4)º, in comparison to the U(1A)-C(46A)-C(47A) bond angle of 115.03° for the η^1-benzyl ligand. This acute bond angle seen with the η^4-benzyl ligand is characteristic of similar η^4-benzyl interactions, including that seen with [BDPP]U($CH_2Ph)_2$ characterized by Diaconescu and coworkers.[121, 144] The K^+ ion seen in complex **3.1** is involved in intramolecular π-interactions with both the dihydropyridonate ring and the phenyl ring of the η^1-benzyl ligand. In addition, the K^+ ion also experiences intermolecular π-interactions with the η^4-benzyl ligand of a neighboring molecule of complex **3.1** (Figure 3-3).

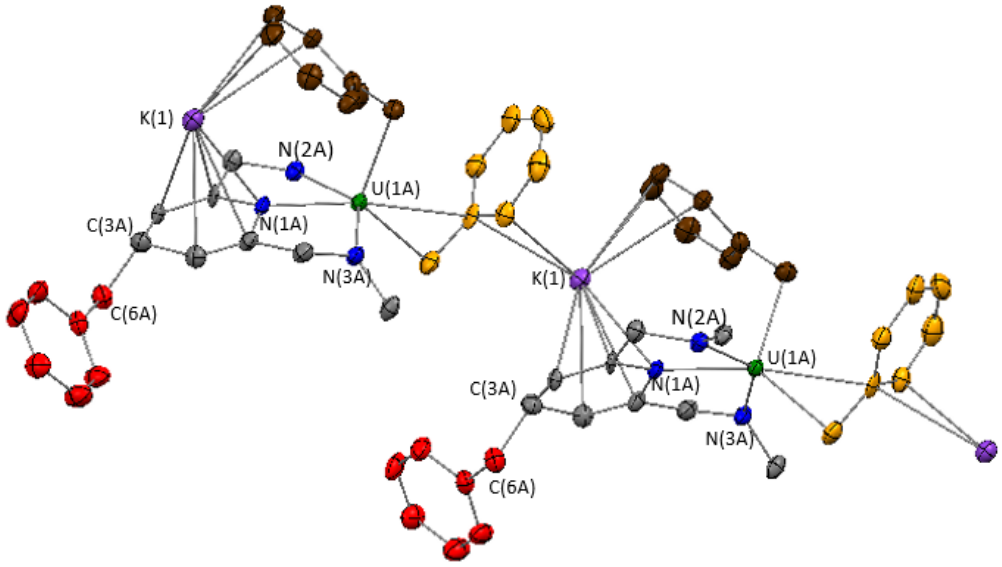


Figure 3-3: *Crystal packing depiction of* ***3.1*** *illustrating intermolecular interactions between K^+ ions and benzyl ligands.* η^4*-benzyl ligands displayed in orange,* η^1*-benzyl ligands displayed in brown and pyridine alkylated benzyl groups shown in red. Hydrogen atoms and BDPP aryl groups omitted for clarity.*

In solution, complex **3.1** displays evidence of low symmetry, which is contrary to what is observed in the solid-state structure. It is possible that **3.1** could display low symmetry in solution due to complex intermolecular interactions brought on by the *π*-donation of the benzyl ligands to the K^+ ions. Unfortunately, due to the complicated nature of the ^{1}H NMR spectrum for a crystalline sample of complex **3.1** (Figure 3-4), peak assignments could not be made with any certainty. Interestingly, the expected U-C*H*$_2$Ph protons are not observed in ^{1}H NMR spectrum at the expected upfield-shifted region of the spectrum near -100 ppm;[121] however, metal-alkyl protons can sometimes be broadened into the baseline with U(IV) alkyl species.[143]

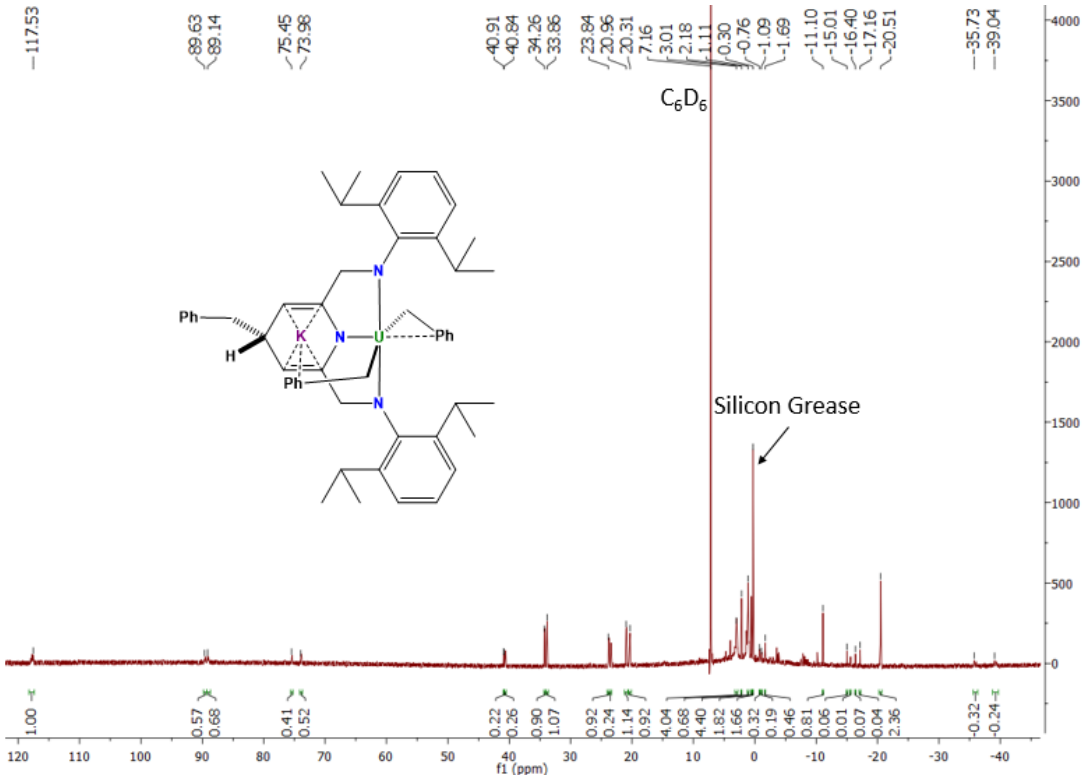


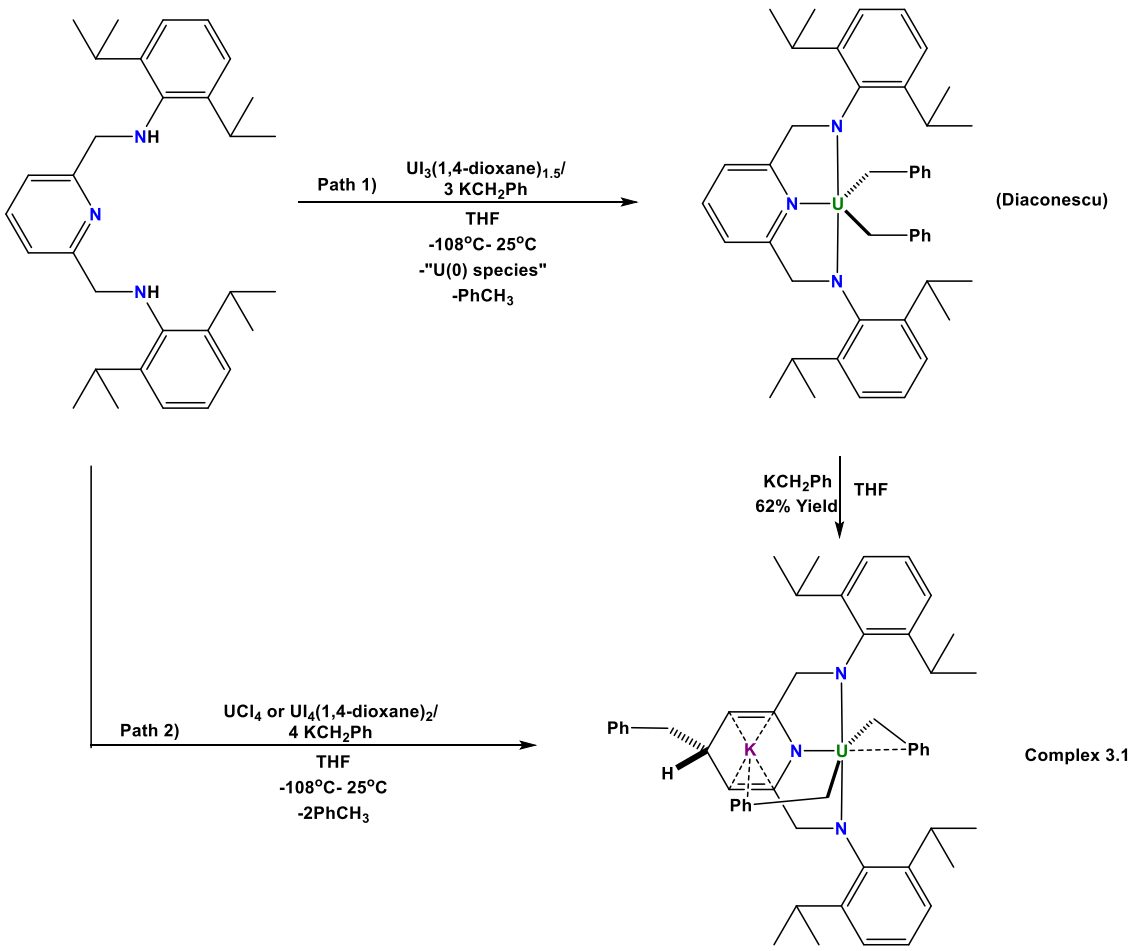
Figure 3-4: *300 MHz ^{1}H NMR spectrum of complex* ***3.1*** *in C_6D_6 at 298 K*

Although proton assignments could not be conclusively made for the ^{1}H NMR spectrum of **3.1**, it was possible to conclude from the NMR data that the main species present in solution is not [BDPP]U($CH_2Ph)_2$, as this spectrum differs greatly from that of the ^{1}H NMR spectrum reported for the non-alkylated BDPP complex by Diaconescu and coworkers.[121] This suggests that complex **3.1** is the prevalent species in solution and that the crystal obtained from this sample is representative of the bulk material.

3.3: Rational synthesis of [K][BDPP′]U($CH_2Ph)_2$ from [BDPP]U($CH_2Ph)_2$

Although solution phase data do not definitively confirm formation of complex **3.1**, elucidation of the structure of **3.1** by X-ray diffraction begs the

question: how does this non-innocent ligand based reactivity occur during the intended preparation of [BDPP]U($CH_2Ph)_2$? Considering that U($CH_2Ph)_4$ was generated *in situ* during the synthesis of **3.1**, it is plausible that residual KCH_2Ph in solution is responsible for the alkylation of the BDPP ligand framework.[143] Alkylation of the electron-deficient pyridine ring was most likely made possible through coordination of the BDPP ligand to the uranium center, where the uranium center acts as a strong Lewis acid, activating the pyridine for reactivity. The residual KCH_2Ph could then attack the activated ring causing the observed dearomatization of the pyridine moiety and formation of the anionic donor nitrogen atom N(1A). In order to validate whether the presence of excess KCH_2Ph caused the formation of complex **3.1**, [BDPP]U($CH_2Ph)_2$ by prepared independently by established methods[121] and reacted with one equiv. of KCH_2Ph (Scheme, 3-2 Path 1).

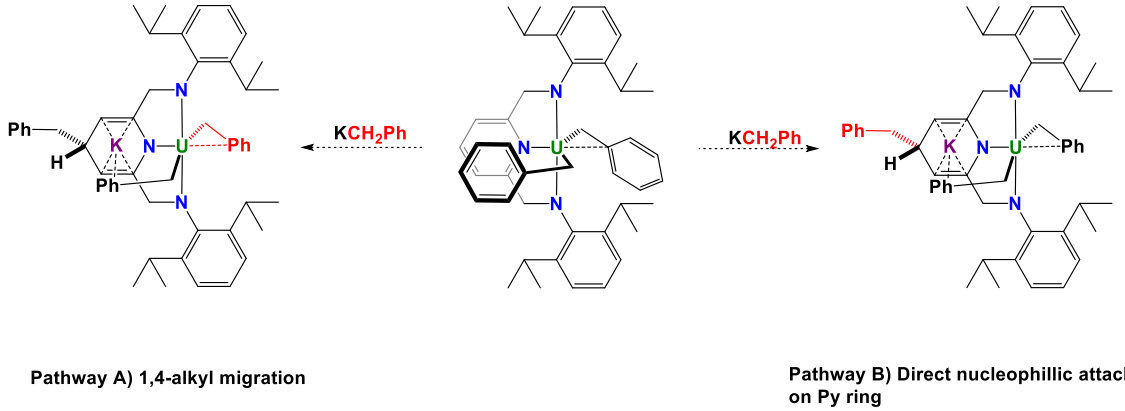


Scheme 3-2: *Direct and multistep procedures used to generate complex* ***3.1***

Upon addition of 1 equiv. of KCH_2Ph to $[BDPP]U(CH_2Ph)_2$, the material isolated in modest yield was characterized by ^1H NMR spectroscopy. It was found that the spectrum for the isolated material matches the ^1H NMR spectrum of the crystalline material first isolated for complex **3.1**, supporting the intermediacy of $[BDPP]U(CH_2Ph)_2$ in the synthesis of **3.1**. The isolation of complex **3.1** was rather surprising given the lack of reactivity observed at the BDPP ligand for lanthanide[120, 122-124], actinide[116-121] and transition metal complexes.[120, 122-140]

3.4: Attempts at elucidating a mechanism for the observed alkylation

Two reasonable mechanistic possibilities are envisioned to explain the formation of complex **3.1** (Scheme 3-3).

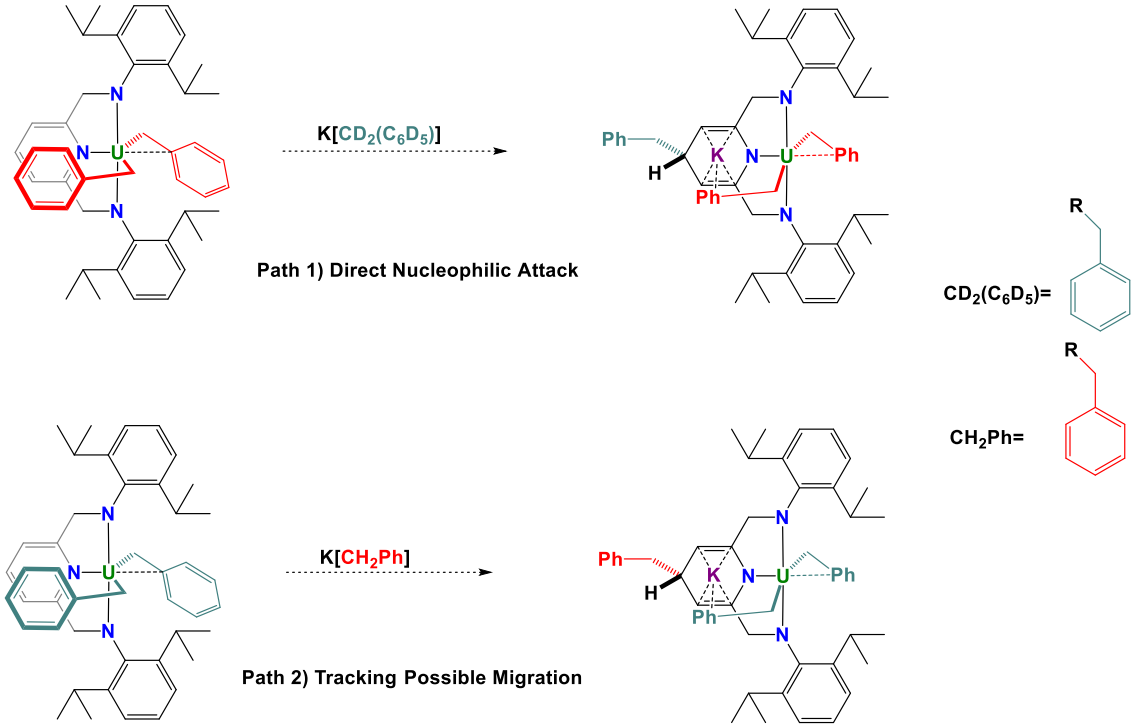


Scheme 3-3: *Possible mechanisms for the formation of [BDPP´]U(CH$_2$Ph)$_2$ (**3.1**)*

Path A illustrates a mechanism where 1,4-migration of the benzyl ligand from the uranium center to the 4-position of the pyridine ring occurs. At first glance, this mechanistic pathway seems to be a viable candidate to explain the formation of complex **3.1,** as similar migrations have been observed with structurally-similar BIP complexes of Zn(CH$_2$Ph)$_2$ and Mn(CH$_2$Ph)$_2$.[147, 148] In these BIP complexes, the migration occurs via two successive 1,3-migrations around the periphery of the ligand. This step-wise mechanism of migration is not possible with the BDPP ligand, as it does not have an unsaturated imine ligand backbone to facilitate this type of migration.[142, 147, 148] A more plausible mechanism can be envisioned to explain the formation of **3.1** involving the direct nucleophilic attack of KCH$_2$Ph on the Py ring of the BDPP ligand (Scheme 3-3, Path B). In this case, the highly electrophilic U(IV) center polarizes the electron density in the pyridine ring, activating it for nucleophilic attack by KCH$_2$Ph. Recent

work has shown that uranium is capable of activating C-H bonds of N-heterocycles for protonolysis chemistry and coupling reactions, indicating that uranium can act as a very powerful Lewis acid activator.[66, 149]

In an effort to elucidate how the 4-benzyl group is actually added to the pyridine backbone of the BDPP ligand framework, isotopic labeling studies were performed. These used $KCD_2(C_6D_5)$ as an alkylating agent for direct nucleophilic attack and $[BDPP]U(CD_2(C_6D_5))_2$ to trace benzyl ligand migration from the uranium center to the 4-position of the Py moiety (Scheme 3-4).



Scheme 3-4: *Isotopic labeling studies probing the mechanism of formation of [BDPP´]U(CH₂Ph)₂ (**3.1**)*

To test if direct nucleophilic attack is the favored mechanistic pathway to generate $[BDPP´]U(CH_2Ph)_2$, 1 equiv. of $K[CD_2(C_6D_5)]$ was added to $[BDPP]U(CH_2Ph)_2$ (Scheme 3-4, Path 1). If the deuterated benzyl ligand added only to the 4-position of the pyridine ring, then it could be assumed that

nucleophilic attack of the pyridine ring by the extra equivalent of $KCD_2(C_6D_5)$ was the most likely mechanism to form the alkylated BDPP complex **3.1**. Conversely, if it was found that the most prevalent species in solution contained a protonated form of the benzyl ligand at the 4-position of the benzene ring, then it could be assumed that either some sort of ligand exchange followed by a nucleophilic attack was occurring, or a migration was occurring.

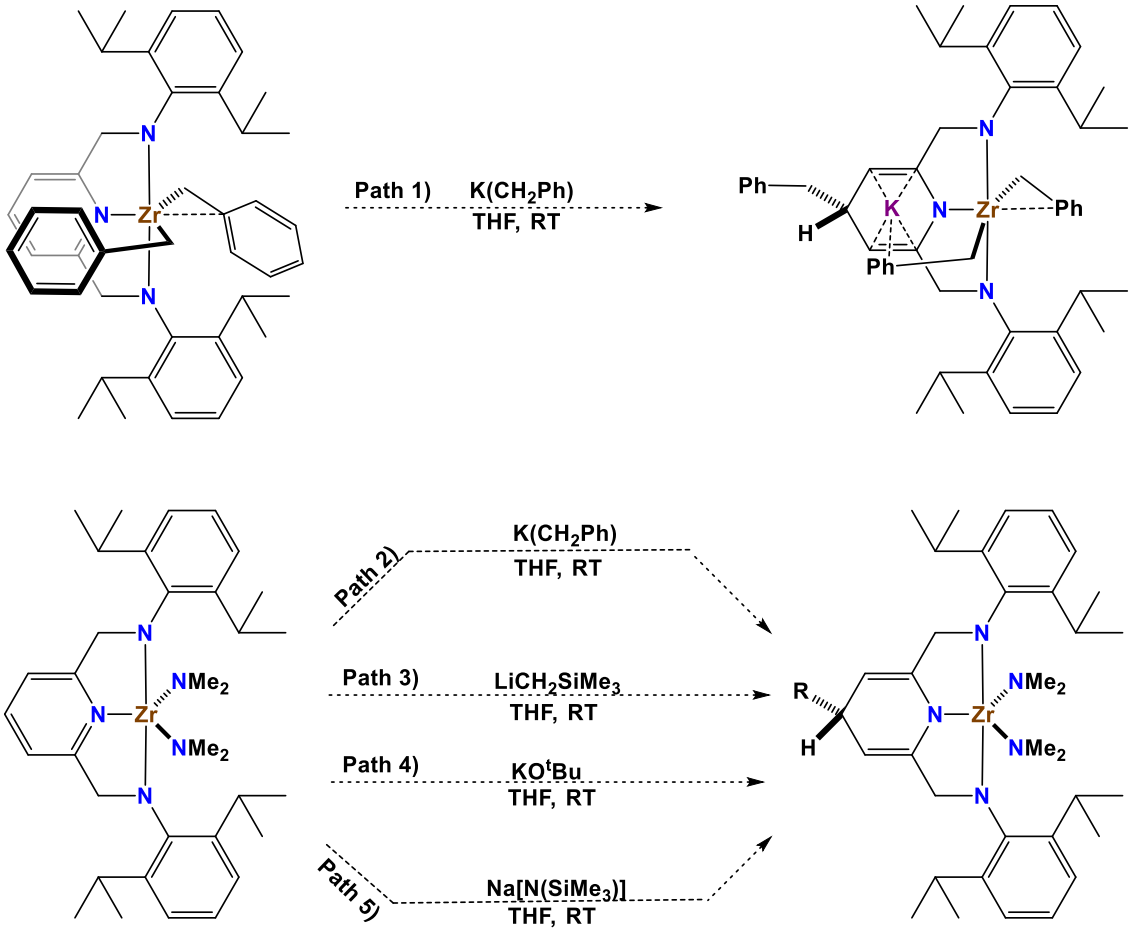
A second isotopic labeling experiment was also performed where 1 equiv. of $K(CH_2Ph)$ was added to $[BDPP]U(CD_2(C_6D_5))_2$ (Scheme 3-4, Path 2). Similar to the first isotopic labeling experiment, if the CH_2Ph ligand added directly to the pyridine ring, then it could be assumed nucleophilic attack was the favored mechanistic pathway. Conversely, if a deuterated benzyl ligand were to add to the pyridine ring, then either benzyl ligand exchange was occurring or a migration was occurring. Although the experiment from Path 2 was not designed to add any new insight into the elucidation of the mechanism, it was run as a means to deconvolute the ^1H NMR spectrum obtained for the non-deuterated analog of complex **3.1**. ^1H NMR data from this experiment was particularly desirable as it would illustrate where the peaks show up for the coordinated alkylated BDPP ligand only, as the deuterated η^1 and η^4-benzyl ligands coordinated to the metal center would not show up in the ^1H NMR spectrum. Unfortunately, these isotopic labeling experiments were unable to help us identify which peaks belonged to the benzyl groups in the ^1H NMR spectrum of the crystalline material of complex **3.1**, as the ^1H NMR spectra from these isotopic labeling experiments were also very complicated.

Since minimal information was gained through the analysis of the ^{1}H NMR spectra from these isotopic labeling experiments, we decided to hydrolyze off the alkylated BDPP' ligands from these experiments and analyze them by mass spectrometry to see which benzyl ligand isotopomer added to the BDPP ligand framework. Unfortunately, in each case it was noted that both deuterated and non-deuterated benzyl ligands added to the BDPP ligand framework in roughly equal proportions, suggesting that isotopic scrambling may have occurred in the mass spectrometer.[150] While a migration mechanism cannot be ruled out, given the lack of unsaturation in the ligand backbone for BDPP and the absence of evidence for benzyl migration with the reported synthesis of [BDPP]U(CH_2Ph)$_2$ and related thorium and transition metal BDPP complexes, we believe that a direct nucleophilic attack mechanism is the most likely pathway to generate the alkylated BDPP complex **3.1**.

3.5: Scope of nucleophilicity

Given this observed non-innocent ligand based reactivity and the difficulties faced with deciphering the paramagnetic ^{1}H NMR spectrum of complex **3.1**, it was determined that the BDPP ligand framework was not a suitable candidate for use in generating An=E functionalities for further study. Although we no longer intended to pursue generating An=E functionalities for use in studying the ITI with this ligand framework, many questions still remained about the nature of the alkylation observed to generate complex **3.1**. For example, we desired to know if this type of alkylation could occur with additional nucleophiles

and whether alkylation of the BDPP ligand framework was specific to uranium, or if it was more general. Due to the widespread use of this ligand with transition metals, lanthanides and actinides, answering these questions would be of general interest to the organometallic community at large. In an effort to answer these questions, we generated the analogous [BDPP]Zr(CH_2Ph)$_2$ complex by established methods,[129] and added 1 equiv. of K(CH_2Ph) to [BDPP]Zr(CH_2Ph)$_2$ (Scheme 3-5, Path 1).



Scheme 3-5: *Scope of nucleophilicity for alkylation of [BDPP]Zr(X)$_2$ complexes (X = (CH_2Ph) or N(Me_2))*

Unfortunately, all attempts at characterizing the product from this reaction by ^{1}H NMR spectroscopy proved to be inconclusive. Likewise, several attempts

at growing crystals suitable for X-ray diffraction analysis were made but proved to be unsuccessful. Due to the difficulty faced with characterizing the product from Path 1, we tested possible alkylation reactivity with a simpler [BDPP]Zr(NMe_2)$_2$ system. Although electronically different than [BDPP]Zr(CH_2Ph)$_2$, it was hoped that the [BDPP]Zr(NMe_2)$_2$ complex would be unable to π-donate to both the Zr metal center and the resultant alkali metal counterion like the previously used benzyl ligands could for **3.1**.[127] This inability to interact with the alkali metal counter ion was important to our choice in using this bis(amido) zirconium scaffold, since the inter- and intramolecular π-interactions observed with the benzyl ligands to the potassium counterion in **3.1** most likely contributed to the complicated ^{1}H NMR spectrum observed with attempted alkylation of the [BDPP]Zr(CH_2Ph)$_2$ complex. Aside from not being able to engage in unwanted inter- and intramolecular interactions that could further convolute solution phase analysis, alkylation of the [BDPP]Zr(NMe_2)$_2$ complex would demonstrate that the non-innocent behavior of the BDPP ligand is not specific to use of the BDPP ligand with uranium. Additionally, alkylation of the [BDPP]Zr(NMe_2)$_2$ complex would also show that this non-innocent ligand behavior can occur under a variety of different electronic conditions. We thus decided to test for possible alkylation reactivity of the BDPP backbone of this system using a variety of different nucleophiles (Scheme 3-5, Paths 2-5).

We first attempted to induce non-innocent behavior of the pyridine moiety by adding 1 equiv. of K(CH_2Ph) to the [BDPP]Zr(NMe_2)$_2$ complex (Scheme 3-5, Path 2). This particular reaction was performed as a means to determine if the

same alkylation reactivity would occur at the pyridine backbone if the BDPP ligand was coordinated to a more electron-rich metal center. Upon analysis of the product of this reaction by ^{1}H NMR spectroscopy, it could be seen that alkylation of some kind most likely occurred (Figure 3-5). The ^{1}H NMR spectrum of the product (bottom panel (red) of Figure 3-5) differs greatly from ^{1}H NMR spectrum of the starting material [BDPP]Zr(NMe$_2$)$_2$ (top panel (blue) of Figure 3-5). In particular, the spectrum shows signs of the dihydropyridinate moiety (labeled F), along with further signs of proton inequivalence brought on by the addition of a benzyl group to the pyridine backbone of the BDPP ligand. Although the product spectrum differs significantly from the ^{1}H NMR spectrum of the [BDPP]Zr(NMe$_2$)$_2$ starting material, it is still difficult to conclude if the alkylation reactivity occurred as intended. This is further complicated by the fact that there appears to be at least one other species present in solution, evidenced by the peak labeled ^{i}Pr in the product spectrum.

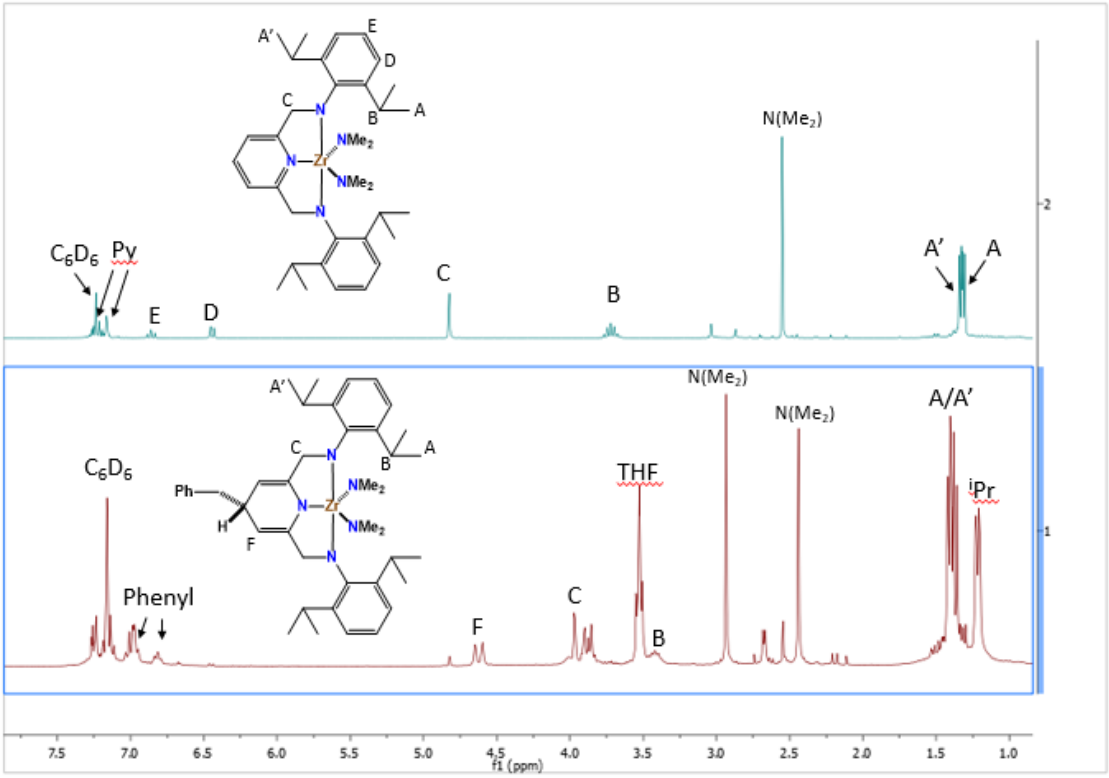


Figure 3-5: *Stacked 300 MHz ^{1}H NMR spectra of [BDPP]Zr(NMe$_2$)$_2$ (top, blue) and possible alkylation product [BDPP´]Zr(NMe$_2$)$_2$ (bottom, red) in C$_6$D$_6$ at 298 K*

Unfortunately, all attempts to generate crystalline material of sufficient quality for X-ray diffraction analysis of this material were unsuccessful. Due to the difficulty in characterizing the alkylation products from reactions involving the use of K(CH$_2$Ph), alkylation based reactivity of [BDPP]Zr(NMe$_2$)$_2$ was attempted with a nucleophile that would potentially result in a simpler ^{1}H NMR spectrum. LiCH$_2$SiMe$_3$ was used as a nucleophile as it is a similar carbon based nucleophile to the previously used K(CH$_2$Ph) nucleophile and it contains an easy to follow ^{1}H NMR handle in the Si(C*H*$_3$)$_3$ protons that would help in analyzing if alkylation occurs. If the ^{1}H NMR chemical shift for the Si(C*H*$_3$)$_3$ protons changes significantly, then we could assume that most likely the nucleophile attacked the pyridine moiety of the BDPP ligand as intended. To this end, 1 equiv. of

$LiCH_2SiMe_3$ was added to $[BDPP]Zr(NMe_2)_2$ (Scheme 3-5, Path 3). Unfortunately, analysis of the product from this reaction by ^1H NMR spectroscopy provided data (not shown) that were also inconclusive for determining if alkylation reactivity occurred at the BDPP ligand. Ironically, despite choosing $LiCH_2SiMe_3$ as a nucleophile for its potentially simpler ^1H NMR spectral characteristics, the ^1H NMR spectrum for this reaction was the most complicated observed yet. The reason for this complication could be that multiple products may have been formed in solution. Unfortunately, all attempts to generate suitable crystals for X-ray analysis were also unsuccessful.

Although we were unable to conclusively characterize the alkylation products from reactions of strong carbon nucleophiles with $[BDPP]Zr(NMe_2)_2$, we did learn through ^1H NMR spectroscopy that some form of alkylation reactivity is likely occurring with this system at the BDPP ligand. It thus appears that non-innocent behavior of the BDPP ligand is not limited to the ligands use with uranium, and can in fact occur when the ligand is coordinated to other metals. In an effort to determine whether or not similar alkylation reactivity could be observed with non-carbon containing nucleophiles, 1 equiv. of potassium *tert*-butoxide (KO^tBu) was added to the $[BDPP]Zr(NMe_2)_2$ starting material (Scheme 3-5, Path 4). Unfortunately, after isolation of the product and analysis by ^1H NMR spectroscopy, the results of the alkylation experiment were inconclusive. From the ^1H NMR spectrum (Figure 3-6), it can be seen that a reaction occurred, but what exactly happened is too difficult to tell from these data. Again, attempts at growing crystals suitable for X-ray diffraction were unsuccessful.

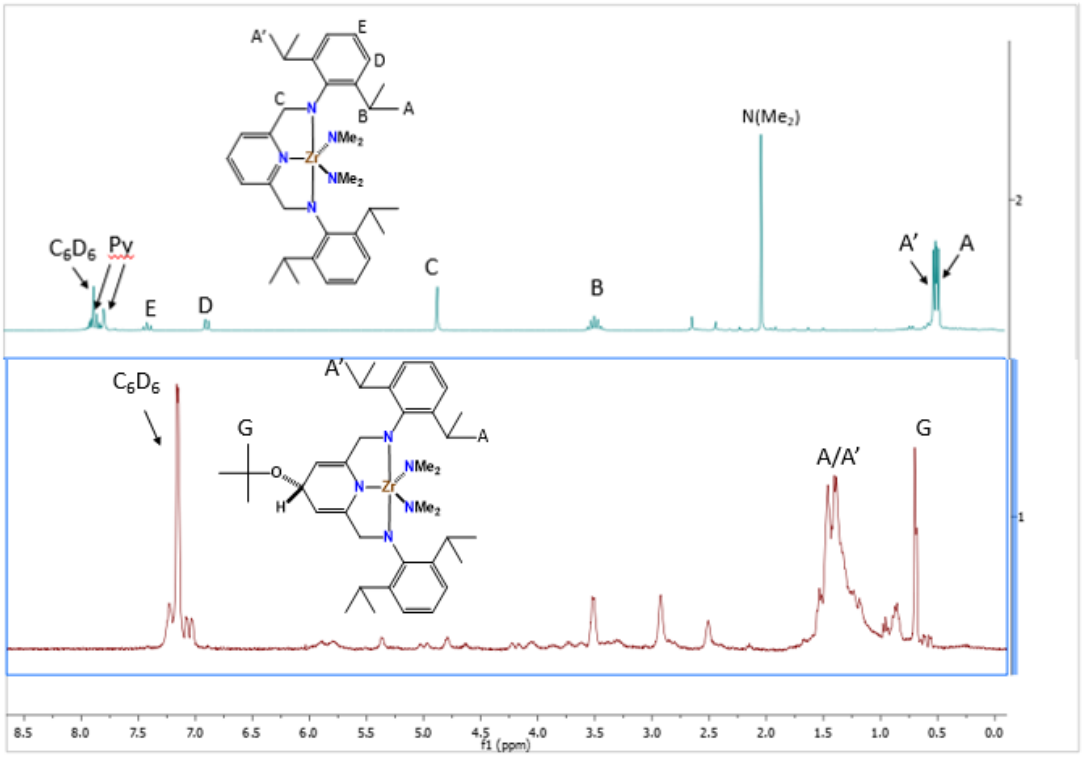


Figure 3-6: *Stacked 300 MHz ^{1}H NMR spectra of [BDPP]Zr(NMe$_2$)$_2$ (top, blue) and the attempted alkylation product [BDPP-O^{t}Bu]Zr(NMe$_2$)$_2$ (bottom, red) in C$_6$D$_6$ at 298 K*

With the inability to isolate the product of the reaction between [BDPP]Zr(NMe$_2$)$_2$ and 1 equiv. of KO^{t}Bu, we attempted nucleophilic attack at the BDPP ligand using a stronger nitrogen based nucleophile. When 1 equiv. of Na[N(SiMe$_3$)$_2$] was added to [BDPP]Zr(NMe$_2$)$_2$, however, no apparent reaction occurred.

3.6: Concluding Remarks

Although our initial goal was to utilize the BDPP ligand scaffold to access complexes that contain X-U=E functionalities, we ultimately determined that this ligand framework was unsuitable for use due to unwanted ligand based side reactivity. Additionally, due to the difficulty in characterizing the alkylation

products using both the BDPP uranium and zirconium systems, it was decided that further investigation into the nature of the non-innocent behavior of the BDPP ligand would futile. Despite this limitation, we did establish that the non-innocent behavior exhibited by the BDPP ligand is not specific to its use with uranium. Additionally, from the ^{1}H NMR data obtained for the attempted reactions of the [BDPP]Zr(NMe_2)$_2$ system, we were able to determine that nucleophilic attack is likely occurring with non-carbon based as well. Unfortunately, as we were not able to fully characterize the products from the reactions with non-carbon based nucleophiles, this non-innocent alkylation of the BDPP backbone by these nucleophiles is likely but not conclusive. Although the BDPP ancillary ligand system proved not to be a suitable candidate for stabilizing desired An=E functionalities as originally intended, we discovered that the multidentate system did not engage in unwanted ligand redistribution side reactivity as previously seen with the [$N(SiMe_3)(3,5\text{-}(Me_2C_6H_3)$] amido ligand in Chapter 2.

3.7: Experimental

3.7.1: General experimental procedures

All experiments were performed under a dry nitrogen atmosphere in a VAC Atmospheres inert-gas glove box under an atmosphere of dry N_2. Solvents were purified using the appropriate VAC Atmospheres solvent purifier or dried using sodium benzophenone ketyl and distilled under nitrogen. Solvents purified by these methods were subsequently degassed and brought into the glove box without exposure to air and stored over activated molecular sieves. Celite was

activated and dried by heating at > 200°C overnight under high vacuum (about 0.3 mmHg). Deuterated NMR solvents, C_6D_6 and D_8-toluene were purchased from Cambridge Isotope Laboratories, degassed and stored over molecular sieves. KCH_2Ph,[143] $KCD_2(C_6D_5)$, $UI_3(1,4\text{-dioxane})_{1.5}$, [88] $U(CH_2Ph)_4$,[144] $[BDPP]H_2$ [121] and $[BDPP]U(CH_2Ph)_2$[121] were produced by literature methods. ^1H NMR spectra were recorded using Varian VNMRS spectrometers operating at 300 MHz or 400 MHz for ^1H at room temperature in C_6D_6 unless otherwise specified. All chemical shifts herein are reported in reference to residual solvent peaks for C_6D_6 at δ 7.16. Mass spectrometry measurements were collected by the University of Oklahoma Mass Spectrometry facility.

*3.7.2: Synthesis of K[BDPP']U(CH$_2$(C$_6$H$_5$))$_2$ (**3.1**) from U(CH$_2$Ph)$_4$*

Synthesis of $U(CH_2Ph)_4$ generated for *in situ* use

To a 20-mL scintillation vial charged with 4 mL of THF and a small stir bar, (250 mg, 0.655 mmol) of UCl_4 was added. To a separate 20-mL scintillation vial charged with 13 mL of THF and a small stir bar, (343 mg, 2.63 mmol) of $K(CH_2Ph)$ was added. Both solutions were allowed to cool in the glove box freezer at -10°C for 1 hour. After cooling, the solution containing the $K(CH_2Ph)$ was added dropwise to the solution containing the UCl_4 while stirring. The resultant solution turned dark red and was allowed to stir for 2 min to generate $U(CH_2Ph)_4$. The formation of $U(CH_2Ph)_4$ was confirmed by ^1H NMR spectroscopy.

Synthesis of **3.1**

To the solution containing $U(CH_2Ph)_4$, (298 mg, 0.658 mmol) of $[BDPP]H_2$ was added. The dark red solution was allowed to stir for 15 min, after which the solution volume was concentrated to a total volume of 8 mL *in vacuo*. The crude product was allowed to recrystallize in the glove box freezer at -10°C for several weeks.

*3.7.3: Synthesis of [K][BDPP']U(CH$_2$Ph)$_2$ (**3.1**) from [BDPP]U(CH$_2$Ph)$_2$*

To a 20-mL scintillation vial charged with 10 mL of THF and a small stir bar, (51 mg, 0.0586 mmol) of $[BDPP]U(CH_2Ph)_2$ (**3.2**) was added. The dark red solution was allowed to stir for 1 min to dissolve and mix thoroughly. To this solution, (7.6 mg, 0.0586 mmol) of $K(CH_2Ph)$ was added. The resulting dark brown solution was allowed to stir overnight. The solution was concentrated to dryness *in vacuo*. **Yield: 36.4 mg, 62%.**

3.7.4: Synthesis of [BDPP]U(CD$_2$C$_6$D$_5$)$_2$

To a 20-mL scintillation vial charged with 10 mL of THF and a small stir bar, (250 mg, 0.333 mmol) of $UI_3(1,4\text{-dioxane})_{1.5}$ was added. The dark blue solution was allowed to stir for 1 minute, where it was then allowed to cool in the cold well (approx. -108°C) for 75 min. Once chilled, (0.137 g, 0.999 mmol) of $K(CD_2C_6D_5)$ was added. Upon addition of the $K(CD_2C_6D_5)$ the solution color changed from dark blue-purple to a dark red-brown. The resulting solution was allowed to stir for about 2 min, where then a cold solution (about -108°C)

containing (152 mg, 0.333 mmol) of [BDPP]H_2 in 5 mL of diethyl ether was added dropwise over 5 min. The resulting solution was allowed to stir for 30 min, after which the crude product solution was filtered over a pad of activated Celite in a Pasteur pipette to afford a transparent, dark-red solution. Volatiles were removed in vacuo and the crude product was extracted with toluene and filtered over a pad of activated Celite in a Pasteur pipette to afford a red solution. Toluene was removed in vacuo. Crude product was extracted with hexanes and filtered over a pad of activated Celite in a Pasteur pipette. Volatiles were removed in vacuo and the product was recrystallized from diethyl ether at -10°C. **Yield: 124 mg, 42%.**

3.7.5: Synthesis of K[BDPP']U($CD_2C_6D_5$)$_2$

To a 20-mL scintillation vial charged with 10 mL of THF and a small stir bar, (51.3 mg, 0.0579 mmol) of [BDPP]U(CD2C6D5)2 was added. The dark-red solution was allowed to stir for 1 min to dissolve and mix thoroughly. To this solution, (7.5 mg, 0.0579 mmol) of K(CH2Ph) was added. The resulting dark-brown solution was allowed to stir overnight. Volatiles were removed in vacuo to afford a dark-brown powder. **Yield: 35.0 mg, 59%.**

3.8: References

1. Arnold, P. L.; Love, J. B.; Patel, D., Pentavalent uranyl complexes. *Coord. Chem. Rev.* **2009,** *253* (15-16), 1973-1978.

2. Cruz, C. A.; Chu, T.; Emslie, D. J. H.; Jenkins, H. A.; Harrington, L. E.; Britten, J. F., Divergent reactivity of (kappa(3)-L)ThCl2(dme) with Grignard reagents: Alkylation, ancillary ligand transfer to magnesium, and halide exchange caught in the act. *J. Organomet. Chem.* **2010,** *695* (25-26), 2798-2803.

3. Cruz, C. A.; Emslie, D. J. H.; Jenkins, H. A.; Britten, J. F., A thermally robust di-n-butyl thorium complex with an unstable dimethyl analogue. *Dalton Trans.* **2010,** *39* (29), 6626-6628.

4. Cruz, C. A.; Emslie, D. J. H.; Harrington, L. E.; Britten, J. F.; Robertson, C. M., Extremely stable thorium(IV) dialkyl complexes supported by rigid tridentate 4,5-bis(anilido)xanthene and 2,6-bis(anilidomethyl)pyridine ligands. *Organometallics* **2007,** *26* (3), 692-701.

5. Cruz, C. A.; Emslie, D. J. H.; Robertson, C. M.; Harrington, L. E.; Jenkins, H. A.; Britten, J. F., Cationic Thorium Alkyl Complexes of Rigid NON- and NNN-Donor Ligands: pi-Arene Coordination as a Persistent Structural Motif. *Organometallics* **2009,** *28* (6), 1891-1899.

6. Diaconescu, P. L., Reactions of Aromatic N-Heterocycles with d(0)f(n)-Metal Alkyl Complexes Supported by Chelating Diamide Ligands. *Acc. Res. Chem.* **2010,** *43* (10), 1352-1363.

7. Duhovic, S.; Khan, S.; Diaconescu, P. L., In situ generation of uranium alkyl complexes. *Chem. Commun.* **2010,** *46* (19), 3390-3392.

8. Jie, S.; Diaconescu, P. L., Reactions of Aromatic N-Heterocycles with Yttrium and Lutetium Benzyl Complexes Supported by a Pyridine-Diamide Ligand. *Organometallics* **2010,** *29* (5), 1222-1230.

9. Estler, F.; Eickerling, G.; Herdtweck, E.; Anwander, R., Organo-rare-earth complexes supported by chelating diamide ligands. *Organometallics* **2003,** *22* (6), 1212-1222.

10. Zimmermann, M.; Estler, F.; Herdtweck, E.; Tornroos, K. W.; Anwander, R., Distinct C-H bond activation pathways in diamido-pyridine-supported rare-earth metal hydrocarbyl complexes. *Organometallics* **2007,** *26* (24), 6029-6041.

11. Guerin, F.; McConville, D. H.; Payne, N. C., Conformationally rigid diamide complexes: Synthesis and structure of titanium(IV) alkyl derivatives. *Organometallics* **1996,** *15* (24), 5085-5089.

12. Guerin, F.; Del Vecchio, O.; McConville, D. H., Ortho-substituted aryl diamido complexes of zirconium: observation of rotameric isomers. *Polyhedron* **1998,** *17* (5-6), 917-923.

13. Guerin, F.; McConville, D. H.; Vittal, J. J., Conformationally rigid diamide complexes of zirconium: Electron deficient analogues of Cp(2)Zr. *Organometallics* **1996,** *15* (26), 5586-5590.

14. Guerin, F.; McConville, D. H.; Vittal, J. J., Synthesis, structure, and reactivity of titanacyclopentadiene complexes bearing ancillary pyridine diamide ligands. *Organometallics* **1997,** *16* (7), 1491-1496.

15. Guerin, F.; McConville, D. H.; Vittal, J. J.; Yap, G. A. P., Synthesis, structure, and reactivity of zirconium alkyl complexes bearing ancillary pyridine diamide ligands. *Organometallics* **1998,** *17* (23), 5172-5177.

16. Kang, K. K.; Hong, S. P.; Jeong, Y. T.; Shiono, T.; Ikeda, T., The synthesis and polymerization behavior of bimetallic pyridine diamide complexes containing transition metal (Ti, Zr). *J. Polym. Sci. A Polym. Chem.* **1999,** *37* (20), 3756-3762.

17. Guerin, F.; McConville, D. H.; Vittal, J. J., Conformationally rigid diamide complexes - Synthesis and structure of tantalum(III) alkyne derivatives. *Organometallics* **1995,** *14* (7), 3154-3156.

18. Guerin, F.; McConville, D. H.; Vittal, J. J.; Yap, G. A. P., Successive insertion of alkynes into a tantalum-alkynyl bond: Implications for the coordination polymerization of alkynes. *Organometallics* **1998,** *17* (7), 1290-1296.

19. Lilly, C. P.; Boyle, P. D.; Ison, E. A., Synthesis and characterization of oxorhenium(V) diamido pyridine complexes that catalyze oxygen atom transfer reactions. *Dalton Trans.* **2011,** *40* (44), 11815-11821.

20. Smeltz, J. L.; Lilly, C. P.; Boyle, P. D.; Ison, E. A., The Electronic Nature of Terminal Oxo Ligands in Transition-Metal Complexes: Ambiphilic Reactivity of Oxorhenium Species. *J. Am. Chem. Soc.* **2013,** *135* (25), 9433-9441.

21. Lilly, C. P.; Boyle, P. D.; Ison, E. A., Synthesis of Oxorhenium Acetyl and Benzoyl Complexes Incorporating Diamidopyridine Ligands: Implications for the Mechanism of CO Insertion. *Organometallics* **2012,** *31* (11), 4295-4301.

22. Britovsek, G. J. P.; Gibson, V. C.; Mastroianni, S.; Oakes, D. C. H.; Redshaw, C.; Solan, G. A.; White, A. J. P.; Williams, D. J., Imine versus amine donors in iron-based ethylene polymerisation catalysts. *Eur. J. Inorg. Chem.* **2001,** *2001* (2), 431-437.

23. Sellmann, D.; Shaban, S. Y.; Rosler, A.; Heinemann, F. W., Substitution and redox reactions of mono- and dinuclear ruthenium complexes containing the pyN(2)H(2)S(2)(2-) ligand pyN(2)H(2)S(2) (2-)=2, 6-bis(2-mercaptophenylaminomethyl)pyridine(2-). *Inorg. Chim. Acta* **2005,** *358* (6), 1798-1806.

24. Gemel, C.; Folting, K.; Caulton, K. G., New approach to Ru(II) pincer ligand chemistry. Bis(tert-butylaminomethyl)pyridine coordinated to ruthenium(II). *Inorg. Chem.* **2000,** *39* (7), 1593-1597.

25. Suffert, J.; Ziessel, R., Design, synthesis and heterotrimetallic complexes od functionalized tweezer ligands. *J. Organomet. Chem.* **1989,** *359* (2), C45-C49.

26. Zhong, Z. L.; Postnikova, B. J.; Hanes, R. E.; Lynch, V. M.; Anslyn, E. V., Large pK(a) shifts of alpha-carbon acids induced by copper(II) complexes. *Chem. Eur. J.* **2005,** *11* (8), 2385-2394.

27. Flock, J.; Suljanovic, A.; Torvisco, A.; Schoefberger, W.; Gerke, B.; Pottgen, R.; Fischer, R. C.; Flock, M., The Role of 2,6-Diaminopyridine Ligands in the Isolation of an Unprecedented, Low-Valent Tin Complex. *Chem. Eur. J.* **2013,** *19* (46), 15504-15517.

28. Gibson, V. C.; Redshaw, C.; Solan, G. A., Bis(imino)pyridines: Surprisingly reactive ligands and a gateway to new families of catalysts. *Chem. Rev.* **2007,** *107* (5), 1745-1776.

29. Kraft, S. J.; Fanwick, P. E.; Bart, S. C., Carbon-Carbon Reductive Elimination from Homoleptic Uranium(IV) Alkyls Induced by Redox-Active Ligands. *J. Am. Chem. Soc.* **2012,** *134* (14), 6160-6168.

30. Kraft, S. J.; Fanwick, P. E.; Bart, S. C., Exploring the Insertion Chemistry of Tetrabenzyluranium Using Carbonyls and Organoazides. *Organometallics* **2013,** *32* (11), 3279-3285.

31. Matson, E. M.; Franke, S. M.; Anderson, N. H.; Cook, T. D.; Fanwick, P. E.; Bart, S. C., Radical Reductive Elimination from Tetrabenzyluranium Mediated by an Iminoquinone Ligand. *Organometallics* **2014,** *33* (8), 1964-1971.

32. Wan, J. P.; Liu, Y. Y., Recent advances in new multicomponent synthesis of structurally diversified 1,4-dihydropyridines. *RSC Adv.* **2012,** *2* (26), 9763-9777.

33. Sandoval, J. J.; Palma, P.; Alvarez, E.; Rodriguez-Delgado, A.; Campora, J., Dibenzyl and diallyl 2,6-bisiminopyridinezinc(ii) complexes: selective alkyl migration to the pyridine ring leads to remarkably stable dihydropyridinates. *Chem. Commun.* **2013,** *49* (60), 6791-6793.

34. Perez, C. M.; Rodriguez-Delgado, A.; Palma, P.; Alvarez, E.; Gutierrez-Puebla, E.; Campora, J., Neutral and Cationic Alkylmanganese(II) Complexes Containing 2,6-Bisiminopyridine Ligands. *Chem. Eur. J.* **2010,** *16* (46), 13834-13842.

35. Pool, J. A.; Scott, B. L.; Kiplinger, J. L., A new mode of reactivity for pyridine N-oxide: C-H activation with uranium(IV) and thorium(IV) bis(alkyl) complexes. *J. Am. Chem. Soc.* **2005,** *127* (5), 1338-1339.

36. Pool, J. A.; Scott, B. L.; Kiplinger, J. L., Synthesis of actinide eta(2)-pyridyl and eta(2)-alpha-picolyl complexes by carbon-hydrogen bond activation. *J. Alloy. Compd.* **2006,** *418* (1-2), 178-183.

37. Kuck, D., Half a century of scrambling in organic ions: Complete, incomplete, progressive and composite atom interchange. *Int. J. Mass Spectrom.* **2002,** *213* (2-3), 101-144.

38. Monreal, M. J.; Thomson, R. K.; Cantat, T.; Travia, N. E.; Scott, B. L.; Kiplinger, J. L., UI4(1,4-dioxane)(2), UCl4(1,4-dioxane) (2), and UI3(1,4-dioxane)(1.5): Stable and Versatile Starting Materials for Low- and High-Valent Uranium Chemistry. *Organometallics* **2011,** *30* (7), 2031-2038.

Chapter 4

A new hope for generating An=E functionalities: Synthesis, characterization and reactivity of Th(IV) and U(IV) dichloro Schiff base complexes

4.1: Background

The generation of An=E functionalities has thus far proven to be a difficult synthetic challenge. Through previous studies exploring the stabilization of this motif, it was found that low valent uranium precursor complexes are prone to decomposition through unwanted side reactivity.[33] Typically, if a low valent uranium center is inadequately sterically protected, it can readily undergo unwanted side reactivity, such as ligand redistribution, disproportionation and C-H activation.[33, 151] These unwanted decomposition pathways usually occur to provide the metal center with optimal steric protection. Thus, it is essential to choose an ancillary ligand support system that can provide adequate steric protection for low valent actinide metal centers, while still allowing desirable chemistry to occur.[152] Additionally, it is important for this ancillary ligand to be resistant to decomposition pathways such as ligand redistribution or C-H activation. After carefully considering common decomposition pathways for low valent uranium complexes it was determined that utilizing an ancillary ligand that binds to the actinide metal center in multiple locations is optimal. The ancillary ligand framework must therefore have more than one donor bound to the actinide center at once, increasing the ligand's affinity for the metal center through the chelate effect and preventing decomposition pathways like ligand redistribution from occurring.[153] In order to best prevent unwanted C-H activation events from occurring, it is imperative to make sure that the ancillary ligand does not overly crowd the uranium center.[151] In many cases, C-H activation occurs when a C-H bond is in close proximity to a uranium center due to excess steric encumbrance

imparted by the ancillary ligands.[151] Typically, C-H activation will relieve steric pressure about the metal center, creating a lower energy system. We thus targeted a ligand framework that reduced the number of bulky substituents on the ligand, which could overly crowd the metal center. This left us with an interesting challenge; how could we develop a ligand system that is resistant to decomposition through ligand redistribution or C-H activation while still being able adequately protect the metal center? With this question in mind, we decided to investigate a multi-dentate ligand framework that binds solely across the equatorial plane of the metal center. This type of ligand system would theoretically be resistant to ligand redistribution while still allowing for chemistry to occur at the axial positions of the metal center, assuming the metal adopts a pseudo-octahedral geometry. We decided to investigate the use of a κ^4-salen type Schiff base ligand as the ancillary support system for use in our An=E precursor, complexes as they can be prepared in high yields through a simple, modular synthesis.[154]

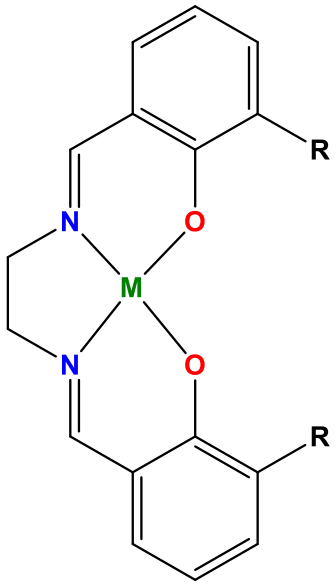
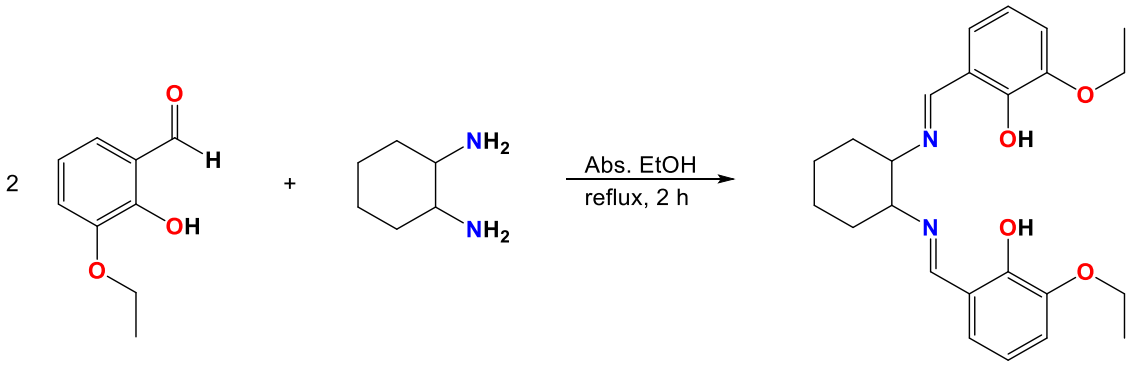


Figure 4-1: *Highlighted κ⁴ bonding motif of the Schiff base ligand (salen)*

Schiff base ancillary ligands are ubiquitous in transition metal chemistry.[155-158] Transition metal Schiff base complexes have been used to catalyze a variety of different transformations, including: asymmetric α-addition reactions,[159] enantioselective epoxidation reactions,[160] asymmetric nitro-Mannich reactions,[161] enantioselective ring opening reactions of meso aziridenes[162] and other enantioselective transformations.[163, 164] Transition metal Schiff base complexes have been shown to stabilize M=O[165] and M=N(R)[166] functionalities, making these ligands ideal candidates for use in stabilizing An=E bonds (E = O, NR, etc.). Additionally, κ^4-Schiff base ligands of the type shown in Figure 4-1 have been shown to stabilize uranyl ($[UO_2]^{2+}$) complexes.[53, 167-169] Despite this, these ligands have not been widely used to study other X-An=E motifs, making this ligand type suitable for our use in studying the "tuneability" of the inverse *trans* influence (ITI) as discussed in Chapter 1. Interestingly, while widely utilized with uranyl derivatives, very few examples exist of κ^4-Schiff base ligands stabilizing low valent uranium complexes or their thorium counterparts.[170-174] In light of this, we decided to explore the following Schiff base ligand for use in accessing An=E precursor complexes (Scheme 4-1).



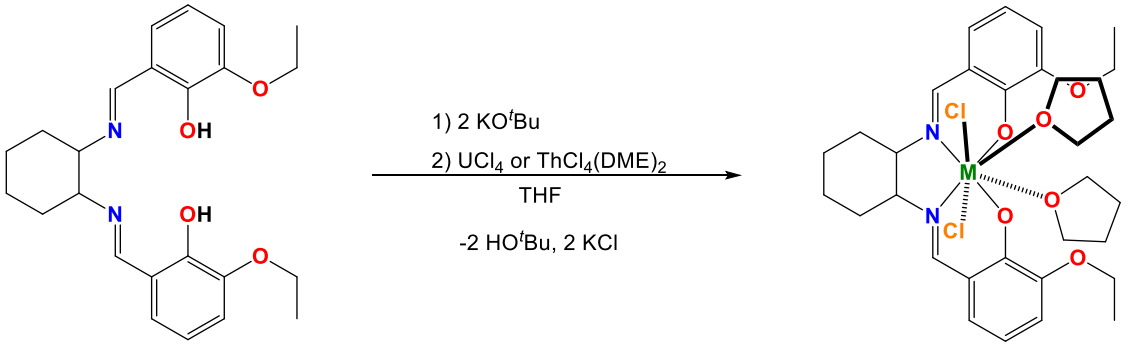
Scheme 4-1: *Synthesis of Schiff base proligand* $[L]H_2$

We targeted the racemate (±)-*trans*-6,6′-diethoxy-2,2′-[cyclohexane-1,2-diylbis(nitrilomethanylylidene)]diphenol for a proligand ([L]H_2) for stabilizing An=E precursor complexes for a variety of reasons.[154] The cyclohexyl backbone of this Schiff-base ligand provides additional steric protection along the equatorial plane of the metal center not offered by traditional salen type Schiff base ligands or Schiff base ligands that have a planar backbone. This element of ligand design was appealing since it is well established that inadequately protected actinide metal centers are prone to ligand redistribution (see Chapter 2). The steric protection afforded by the cyclohexyl backbone was more appealing than the use of traditional bulky functionalities in our ligand design, since it avoided incorporation of functional groups prone to C-H activation. The ethoxy groups were incorporated into our ligand design as a potential platform for generating actinide-metal bonds. The two pendent ether groups have been shown to coordinate to other metal centers when this ligand was used to stabilize transition metal complexes.[159, 161] As such, it is our hope that the pendent ether groups will datively coordinate to other metal centers to allow for the generation of potential actinide-metal bonds to form.

4.2: Synthesis and characterization of [L]An$(Cl)_2(Solv)_2$ complexes

After carefully considering our ligand design, we then focused on suitable precursor complexes for generating the desired X-U=E functionalities. Precursor complexes bearing *trans* or pseudo-*trans* dihalo X-U-X functionalities could be readily used to access X-U=E motifs through salt metathesis.[60] The

[L]U(Cl)$_2$(THF)$_2$ complex was thus targeted, as the necessary UCl$_4$ starting material is more readily accessed than other uranium tetrahalide starting materials. To the best of our knowledge, κ^4-Schiff base ligands have not been used to stabilize Th(IV). Consequently, we extended this approach to the analogous [L]Th(Cl)$_2$(THF)$_2$ complex using ThCl$_4$(DME)$_2$ as the starting material. This provided an interesting opportunity to compare the basic coordination chemistry of an f^0 thorium system to that of an isostructural f^2 uranium system. Currently, the role f-electrons play in the bonding of actinide complexes is still poorly understood.[38] By comparing and contrasting the coordination chemistry of these two complexes, inferences can be drawn regarding the role *f*-electrons play in the bonding of actinide complexes. We were able to access both Th and U Schiff base complexes in good yields by the method shown in Scheme 4-2.[175]



Scheme 4-2: *Synthesis of Th(IV) and U(IV) dichloro Schiff base complexes*

As illustrated in Scheme 4-2, deprotonation of the proligand [L]H$_2$ was accomplished through addition of 2 equiv. of potassium tertbutoxide *in situ*. Formation of the dipotassium salt is signaled by a solution color change from yellow to yellow-green. The solution of the dipotassium salt of the Schiff base

proligand is then slowly added to a THF solution of either UCl_4 or $ThCl_4(DME)_2$. $[L]U(Cl)_2(THF)_2$ (**4.1**) and $[L]Th(Cl)_2(THF)_2$ (**4.2**) can be purified and isolated in moderate yields through extraction with dichlorometane and filtration over Celite. Complexes **4.1** and **4.2** have poor solubility in common ethereal solvents and, as such, could only be slowly recrystallized from pyridine. For both complexes, THF is displaced by pyridine to generate complexes **4.1-(Py)** and **4.2-(Py)** (Figure 4-2).[175]

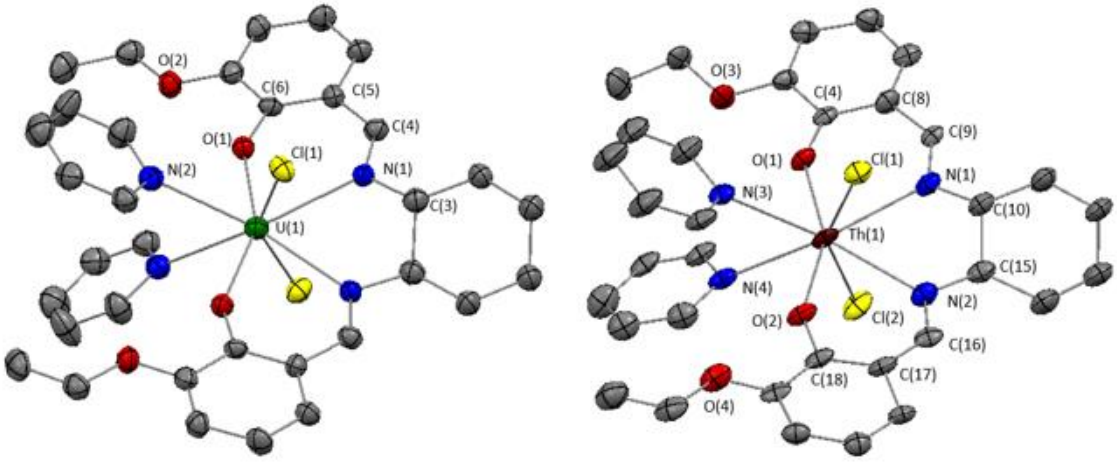


Figure 4-2: *ORTEP depiction of $[L]U(Cl)_2(Py)_2$ (**4.1-(Py)**) (left) and $[L]Th(Cl)_2(Py)_2$ (**4.2-(Py)**, right) with ellipsoids shown at 50% probability. Hydrogen atoms omitted for clarity.*

Table 4-1: *Selected bond distances (Å) for **4.1-(Py)** and **4.2-(Py)***

Complex 4.1-(Py)		Complex 4.2-(Py)	
Bond	**Distance (Å)**	**Bond**	**Distance (Å)**
U(1)-Cl(1)	2.7112(17)	Th(1)-Cl(1)	2.764(7)
U(1)-N(1)	2.614(5)	Th(1)-Cl(2)	2.744(7)
U(1)-O(1)	2.190(4)	Th(1)-N(1)	2.62(2)
U(1)-N_{py}(2)	2.666(6)	Th(1)-N(2)	2.60(2)
N(1)-C(4)	1.283(8)	Th(1)-O(1)	2.20(8)
		Th(1)-O(2)	2.212(16)
		Th(1)-N(3)	2.69(2)
		Th(1)-N(4)	2.62(2)
		N(1)-C(9)	1.28(3)
		N(2)-C(16)	1.29(3)

Table 4-2: *Selected bond angles (°) for* ***4.1-(Py)*** *and* ***4.2-(Py)***

Complex 4.1-(Py)		Complex 4.2-(Py)	
Bond Angle	**Angle (°)**	**Bond Angle**	**Angle (°)**
O(1)-U(1)-O(1)	151.2(2)	O(1)-Th(1)-O(2)	154.1(6)
N(1)-U(1)-N(1)	65.7(2)	N(1)-Th(1)-N(2)	64.3(6)
N(2)-U(1)-N(2)	66.7(2)	N(3)-Th(1)-N(4)	64.5(6)
Cl(1)-U(1)-Cl(1)	148.36(7)	Cl(1)-Th(1)-Cl(2)	150.0(2)
O(1)-U(1)-N(1)	71.41(16)	O(1)-Th(1)-N(1)	72.0(6)
O(1)-U(1)-N(2)	80.95(16)	O(1)-Th(1)-N(4)	80.9(7)

In both complexes **4.1-(Py)** and **4.2-(Py)**, the Schiff base ligand adopts a nearly planar configuration, where the *trans* cyclohexyl backbone creates a slight distortion of the N_2O_2 plane of the ligand. In each complex, the chlorido ligands are pseudo-*trans* to one another with Cl-M-Cl bond angles of 148.36(7)° for complex **4.1-(Py)** and 150.0(2)° for complex **4.2-(Py)**. Both complexes adopt pseudo-dodecahedral geometries and display approximate C_{2v} symmetry in the solid state. In each complex, the chlorido ligands are bent away from the open face of the metal center to best accommodate coordination of the pyridine moieties and round out the 8-fold coordination sphere of the complexes. Both complexes exhibit similar M-O bond distances, which are consistent with single bonds at 2.190(4) Å for complex **4.1-(Py)** and 2.208(16)/2.212(16) Å for complex **4.2-(Py)**. The dative imino M-N bond distances of the Schiff base ligand are also similar for complexes **4.1-(Py)** and **4.2-(Py)** at 2.614(5) Å and 2.62(2)/2.60(2) Å, respectively. These bond distances are on the long side and are consistent with weak M-N interactions.[176] This slight difference between the M-L bond distances of the Th(IV) and U(IV) Schiff base complexes can be accounted for primarily by the slightly larger ionic radius of Th(IV) vs. U(IV). The M-L bond distances, however, are slightly shorter than expected by this argument alone. It is likely that

the observed M-L bond distances strike a compromise between optimizing M-L distances and minimizing ligand distortion, which can be severe (*vide supra)*. This rationalization is supported by the fact that the U(1)-Cl(1) bond distance of complex **4.1-(Py)** is about 0.05 Å shorter than the Th(1)-Cl bond distances in complex **4.2-(Py)**, which is consistent with the approximate 0.05 Å longer ionic radius of 8-coordinate Th(IV) vs U(IV).[177] It should be noted, however, that the U(1)-Cl(1) bond distance of complex **4.1-(Py)** is slightly longer than a typical U-Cl bond for a U(IV) complex.[80, 94, 152, 176] In both complexes **4.1-(Py)** and **4.2-(Py)**, the ligand imine C=N bond distances are between 1.28-1.29 Å and are consistent with typical C=N bond distances, suggesting that the C=N bond is not activated or reduced.

In solution, complexes **4.1, 4.1-(Py)** and **4.2-(Py)** display high symmetry, which can be seen through the simplicity of the ^{1}H NMR spectra for these complexes. Complex **4.2**, however, displays dynamic behavior in solution in the absence of a strong donor solvent, partially due to aggregation. This is supported by the broadness of each peak in the ^{1}H NMR spectrum for this complex and further supported by the fact that addition of a strong donor greatly simplifies the ^{1}H NMR spectrum for complex **4.2**. In addition, when exposed to D_5-Py, each peak in the ^{1}H NMR spectrum for complex **4.2** becomes sharp and is readily assignable to the pyridine adduct of **4.2**, complex **4.2-(Py)**.

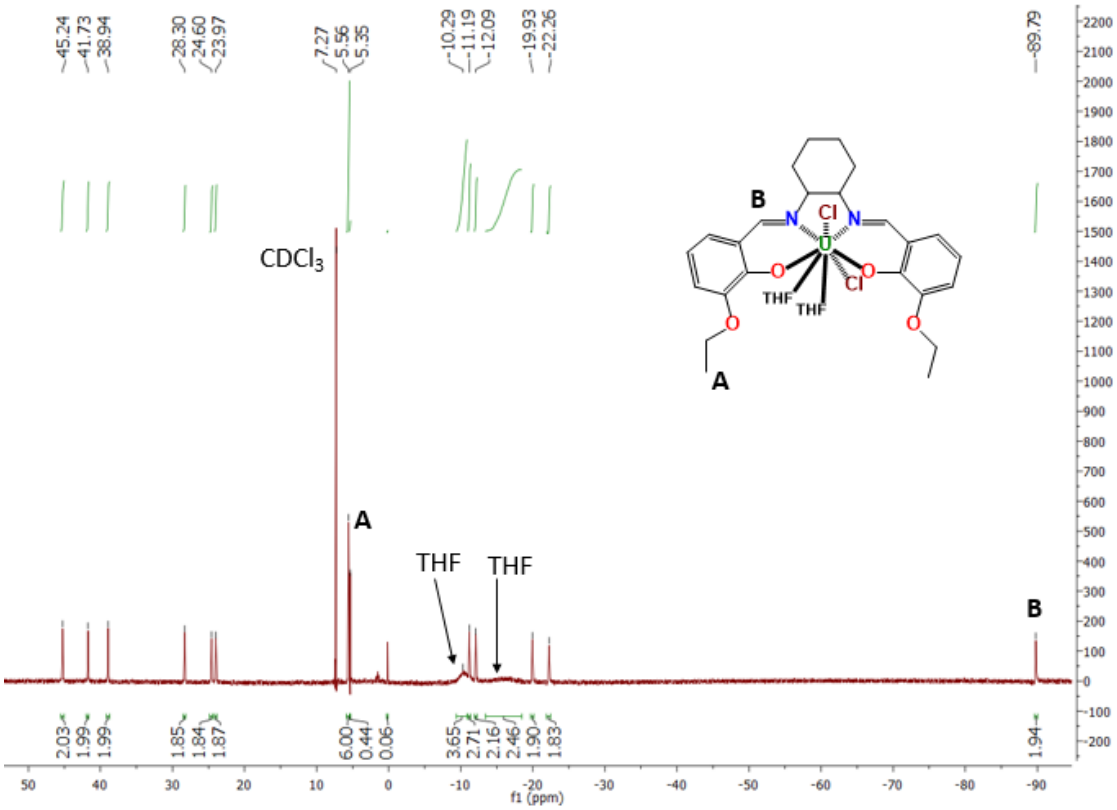


Figure 4-3: *300 MHz ^{1}H NMR spectrum of [L]U(Cl)$_2$(THF)$_2$ (**4.1**) in $CDCl_3$ at 298 K*

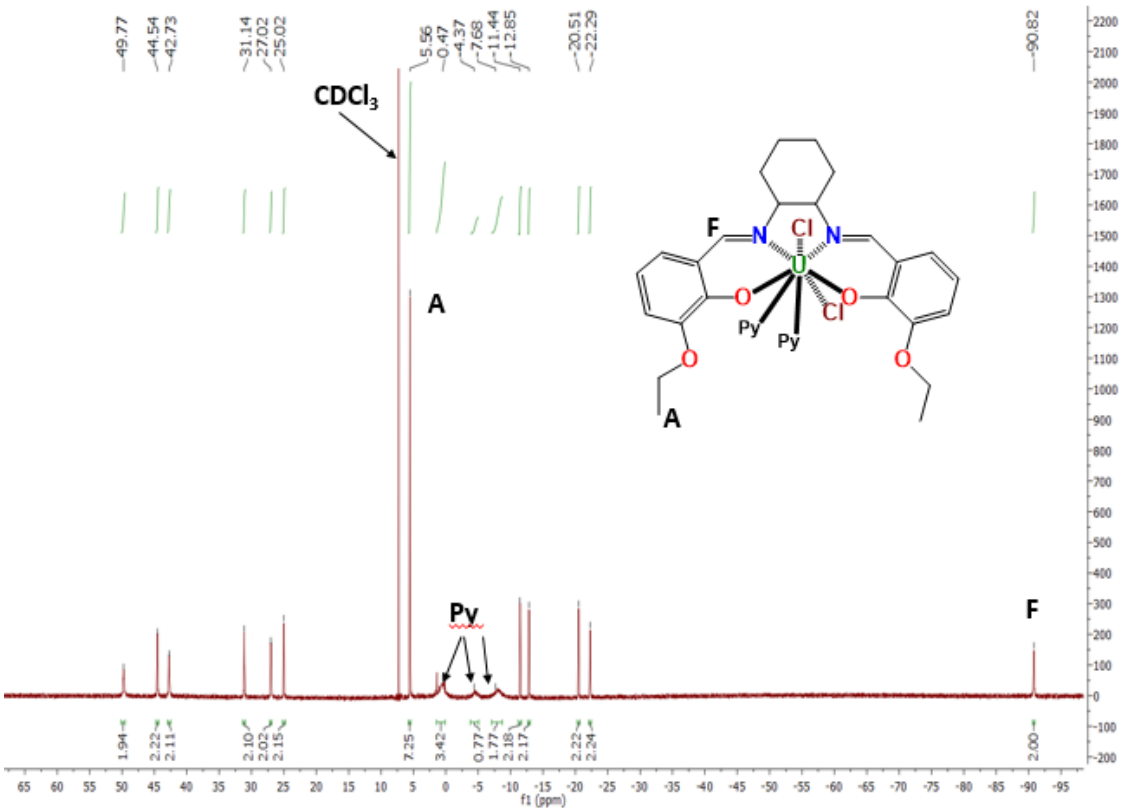


Figure 4-4: *400 MHz ^{1}H NMR spectrum of $[L]U(Cl)_2(Py)_2$* ***4.1-(Py)*** *in $CDCl_3$ at 298 K*

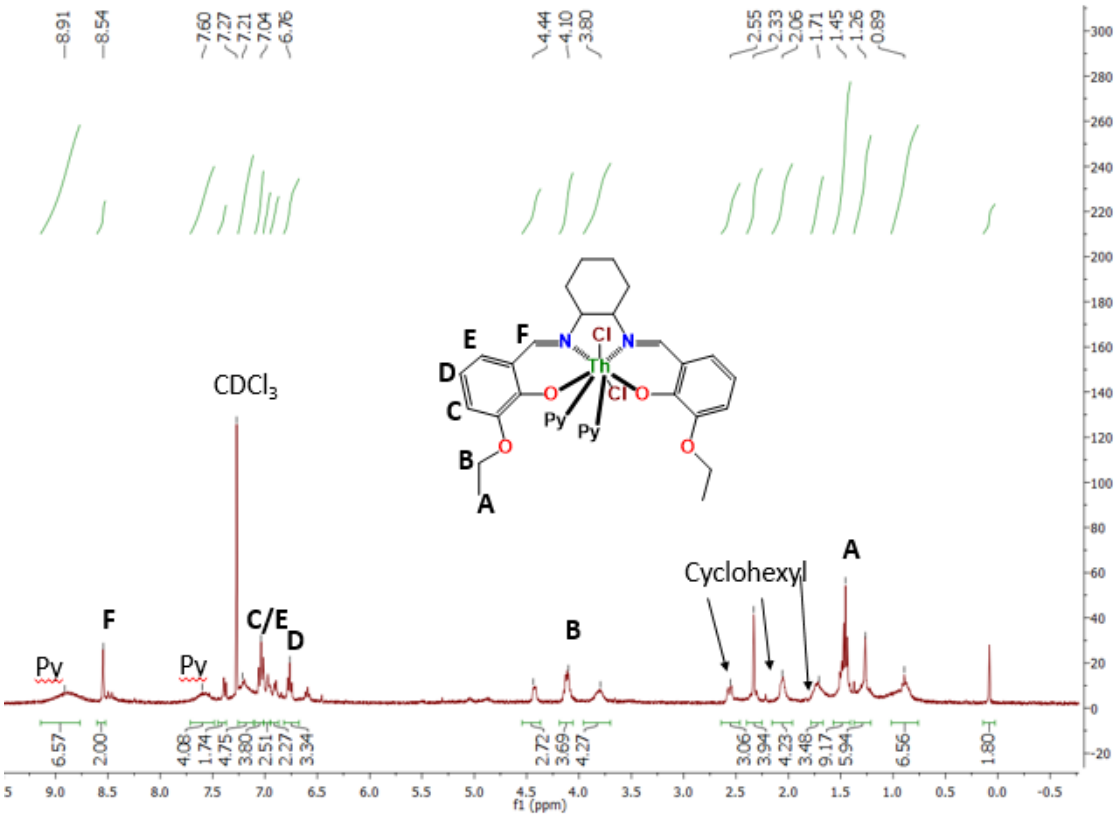


Figure 4-5: *300 MHz ^{1}H NMR spectrum of complex* ***4.2-(Py)*** *in $CDCl_3$ at 298 K*

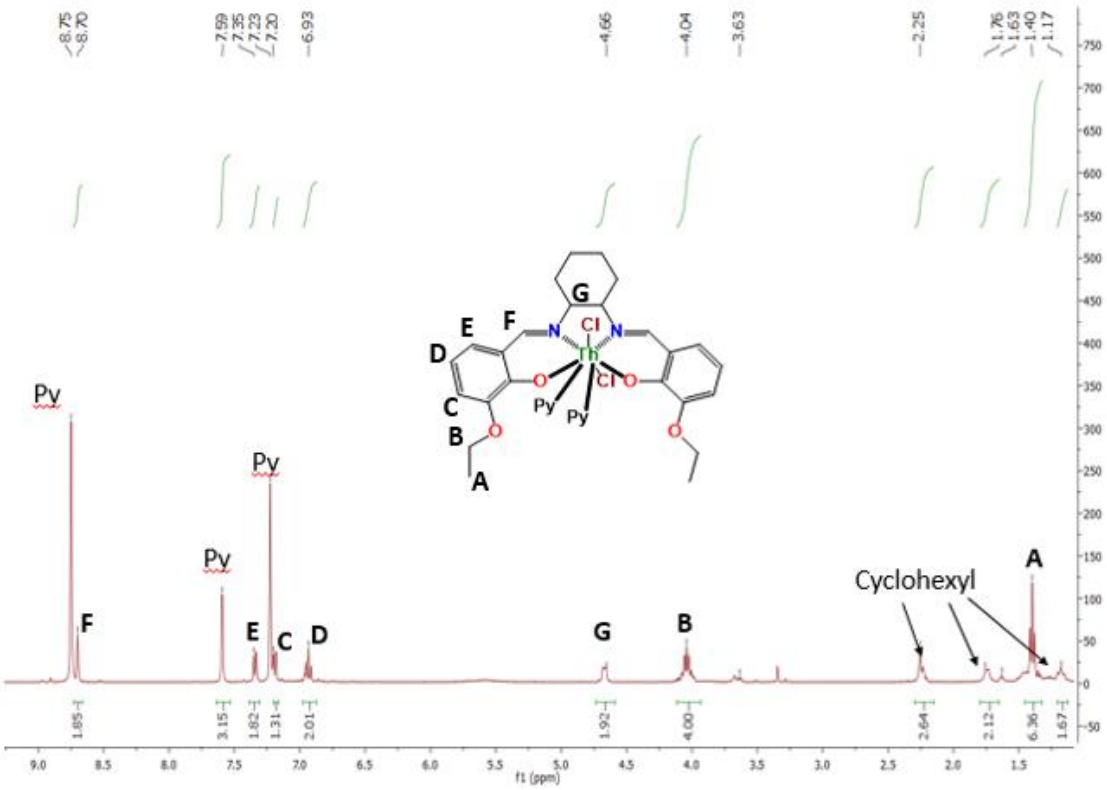


Figure 4-6: *400 MHz ^{1}H NMR spectrum of [L]Th(Cl)$_2$(Py)$_2$* ***4.2-(Py)*** *in D_5-pyridine at 298 K*

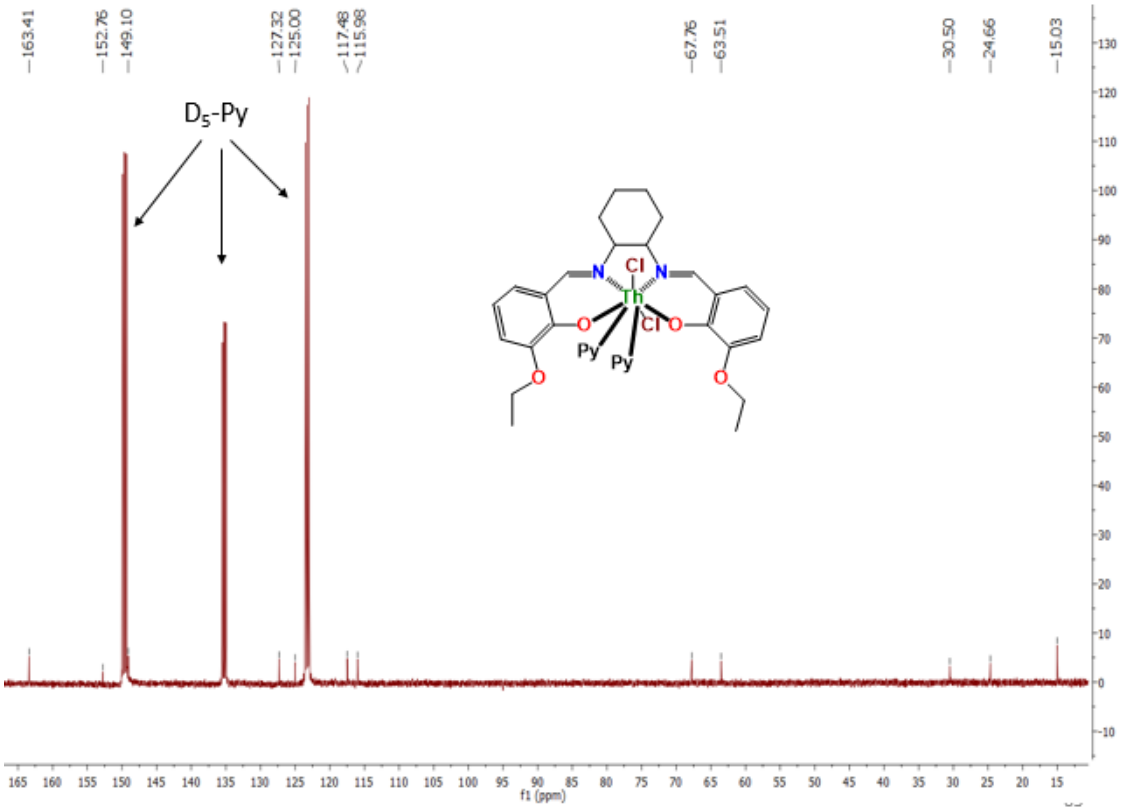
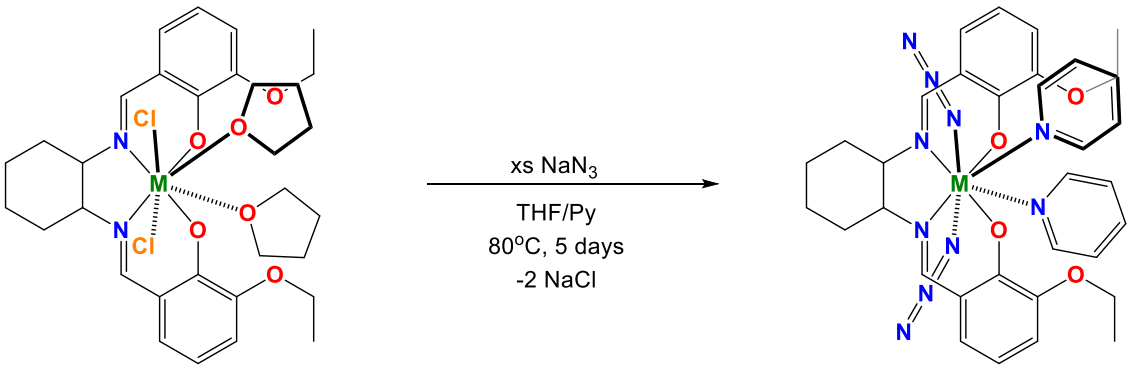


Figure 4-7: *100 MHz ^{13}C NMR spectrum of [L]Th(Cl)$_2$(Py)$_2$ (**4.2-(Py)**) in D$_5$-pyridine at 298 K*

4.3: Salt metathesis reactivity of the [L]An(Cl)$_2$(Solv)$_2$ complexes with NaN$_3$

Unlike our previous attempts to access *trans* X-An-X functionalities, the ^{1}H NMR spectroscopic data for complexes **4.1** and **4.2** and their pyridine adducts do not show evidence of complex decomposition nor the formation of ligand redistribution byproducts in solution. The κ^4-Schiff base ligand is able to support pseudo-*trans* dihalo actinide species. We next sought to ensure that the Schiff base ligand was not prone to non-innocent redox behavior observed with the BDPP ligand (described in Chapter 3). Potential non-innocent ligand behavior was a concern since many ligands with imine linkages have been shown to

participate in redox activity.[143, 167, 171, 178-188] In order to demonstrate ancillary ligand innocence, we decided to test the degree of electrophilicity with this system by investigating whether the ligand exhibited non-innocent nucleophilic substitution reactivity with complexes **4.1** and **4.2**. In order to avoid potential nucleophilic activation of the imine bond of the Schiff base ligand, we first targeted weaker nucleophilies for ligand substitution reactivity. Imine C=N bond activation was evaluated during our reactivity studies by monitoring changes of the C=N bond by IR spectroscopy. For complexes **4.1** and **4.2**, the imine C=N stretch appears at 1614 cm^{-1} and 1611 cm^{-1}, respectively, which is shifted from the free ligand C=N stretch of 1626 cm^{-1}.[175] The C=N stretches for **4.1** and **4.2** are similar to other Schiff base complexes.[176] During initial reactivity screening, complexes **4.1** and **4.2** reacted cleanly with sodium azide in THF/pyridine to generate the diazide species **4.3** in 61% yield and **4.4** in 82% yield, respectively (Scheme 4-3).[175]

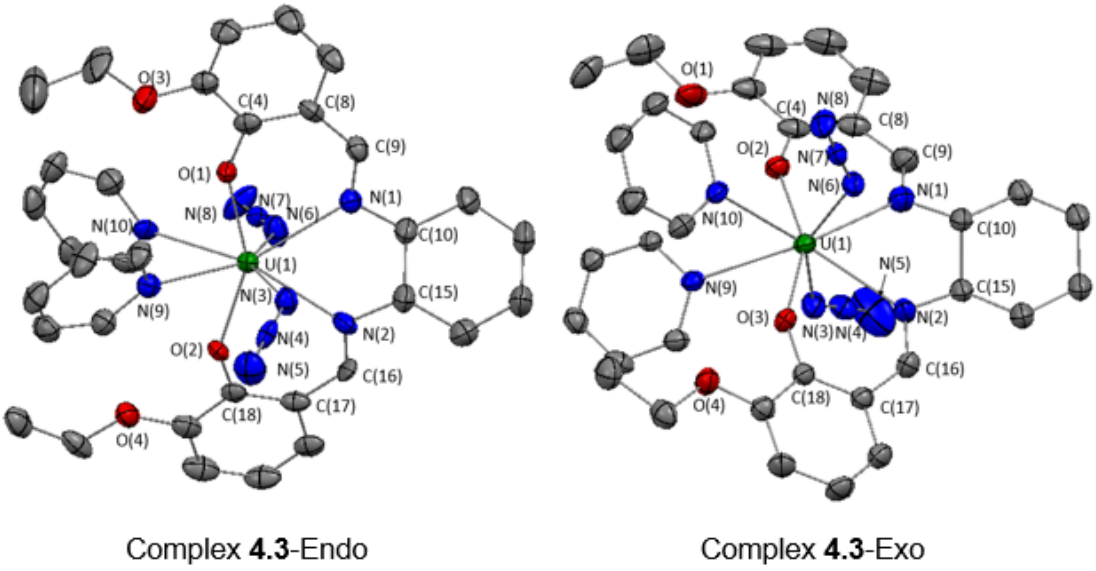


M = U (**4.1**)
M = Th (**4.2**)

M = U (**4.3**), 61% yield
M = Th (**4.4**), 82% yield

Scheme 4-3: *Synthesis of [L]An(N$_3$)$_2$(Py)$_2$ complexes from [L]An(Cl)$_2$(THF)$_2$ where An = U, Th*

Diazido actinide complexes **4.3** and **4.4** are readily isolated by means of extraction from dichloromethane and filtration over Celite. [L]U$(N_3)_2(Py)_2$ (**4.3**) can be recrystallized by slow evaporation of a solution of either dichloromethane or toluene. Interestingly, depending on the solvent used for crystallization, two conformers of complex **4.3** were isolated and characterized by single crystal x-ray diffraction (Figure 4-8). The *endo* conformation of complex **4.3** was the major product of the reaction, as indicated by mass, while the *exo* conformation constituted less than 5% of the bulk material by mass. The *endo* conformation was isolated as brown crystals from dichloromethane and was the only conformer isolated when recrystallized from dichloromethane; the *exo* conformation was isolated as green crystals and was the only conformer isolated when recrystallized from toluene. Unfortunately, suitable crystals for [L]Th$(N_3)_2(Py)_2$ (**4.4**) could not be obtained.



Complex **4.3**-Endo Complex **4.3**-Exo

Figure 4-8: *Solid-state structures of endo and exo conformers of complex **4.3**, with ellipsoids shown at 50% probability. Hydrogen atoms omitted for clarity.*

Table 4-3: *Selected bond lengths (Å) for* ***4.3*****-Endo** *and* ***4.3*****-Exo**

Complex 4.3-*Endo*		**Complex 4.3-*Exo***	
Bond	**Distance (Å)**	**Bond**	**Distance (Å)**
U(1)-N(1)	2.609(5)	U(1)-N(1)	2.561(4)
U(1)-N(2)	2.567(6)	U(1)-N(2)	2.610(3)
U(1)-N(3)	2.440(7)	U(1)-N(3)	2.404(4)
U(1)-N(6)	2.425(8)	U(1)-N(6)	2.407(4)
U(1)-N(9)	2.632(6)	U(1)-N(9)	2.6551(3)
U(1)-N(10)	2.652(6)	U(1)-N(10)	2.615(3)
U(1)-O(1)	2.157(4)	U(1)-O(2)	2.160(3)
U(1)-O(2)	2.170(4)	U(1)-O(3)	2.161(3)
N(3)-N(4)	1.147(8)	N(3)-N(4)	1.126(5)
N(4)-N(5)	1.165(9)	N(4)-N(5)	1.167(6)
N(6)-N(7)	1.138(9)	N(6)-N(7)	1.175(5)
N(7)-N(8)	1.176(9)	N(7)-N(8)	1.153(4)
N(1)-C(9)	1.290(7)	N(1)-C(9)	1.281(5)
N(2)-C(16)	1.283(9)	N(2)-C(16)	1.273(5)

Table 4-4: *Selected bond angles (°) for* ***4.3*****-Endo** *and* ***4.3*****-Exo**

Complex 4.3-*Endo*		**Complex 4.3-*Exo***	
Bond Angle	**Angle (°)**	**Bond Angle**	**Angle (°)**
O(1)-U(1)-O(2)	150.73(16)	O(2)-U(1)-O(3)	152.86(11)
N(3)-U(1)-N(6)	145.2(2)	N(3)-U(1)-N(6)	149.65(12)
N(1)-U(1)-N(2)	66.08(16)	N(1)-U(1)-N(2)	65.36(11)
N(9)-U(1)-N(10)	68.54(18)	N(9)-U(1)-N(10)	67.52(10)
U(1)-N(3)-N(4)	134.5(5)	U(1)-N(3)-N(4)	138.5(3)
U(1)-N(6)-N(7)	144.7(5)	U(1)-N(6)-N(7)	137.0(3)
N(3)-N(4)-N(5)	177.7(8)	N(3)-N(4)-N(5)	177.0(3)
N(6)-N(7)-N(8)	177.0(7)	N(6)-N(7)-N(8)	178.0(4)

Both structures of [L]U$(N_3)_2(Py)_2$ complexes **4.3-*Endo*** and **4.3-*Exo*** are nearly identical and are largely similar to that of [L]U$(Cl)_2(Py)_2$ (**4.1-(Py)**), with all adopting 8-coordinate pseudo-dodecahedral geometries. Like complex **4.1-(Py)**, complexes **4.3-*Endo*** and **4.3-*Exo*** contain pseudo-*trans* X-U-X functionalities (X = N_3), with N(3)-U(1)-N(6) bond angles of 145.2(2)° and 149.65(12)°, respectively. The N(3)-U(1)-N(6) bond angle of complex **4.3-*Endo*** is slightly contracted compared to the 148.36(7)° Cl(1)-U-Cl(1) bond angle of complex **4.1-**

(Py). In contrast, complex **4.3-*Exo*** displays a slightly more obtuse N(3)-U(1)-N(6) bond angle compared to the Cl(1)-U(1)-Cl(1) bond angle in **4.1-(Py)**. In both complexes **4.3-Endo** and **4.3-Exo**, the azido ligands are essentially linear with N=N=N bond angles between 177-178°. The U-N azido bond distances are similar to those seen for other non-Cp uranium(IV) azide complexes at 2.440(7) Å and 2.425(8) Å for **4.3-*Endo*** and 2.404(4) Å and 2.407(4) Å for **4.3-*Exo***.[78, 176, 189-193] These bond distances are slightly longer than the U-N azido bond distances reported by Walensky and coworkers for a related 8-coordinate bis(salicyladiminato) diazido complex ($U\text{-}N_{azide}$ = 2.362(10) Å), where the azide ligands are in a *cis* arrangement.[176] The presence of the azide functionality for these complexes can also be confirmed through IR spectroscopy, with a strong azide stretch for the bulk material of **4.3** at 2056 cm^{-1}. This stretch is red shifted from the N_3 stretch of NaN_3 at 2104 cm^{-1}, signaling ligand π-donation to the uranium center.[175] Additionally, the ligand imine C=N functionality is maintained in both conformers of **4.3**, with C=N bond distances between 1.27 and 1.29 Å and an IR C=N stretch at 1611 cm^{-1} for the bulk material. Importantly, this means that the ancillary ligand remains innocent and allows nucleophilic substitution reactivity to cleanly occur at the actinide metal center.

Although a crystal structure was not obtained for complex **4.4**, the complex was analyzed by IR and NMR spectroscopy. Similar to complex **4.3**, complex **4.4** displayed a strong, red shifted azide stretch at 2061 cm^{-1} and a red shifted C=N stretch at 1603 cm^{-1} in the IR spectrum, confirming that the Schiff base ancillary ligand remains innocent during reactivity at both U and Th centers. In solution,

both complexes **4.3** and **4.4** display high symmetry, with diagnostic imine *H*C=N peaks. Like complex **4.1**, complex **4.3** has an upfield *H*C=N resonance at δ -86.8, whereas the diamagnetic Th complex **4.4** displays this imine C-H peak downfield at δ 8.81. Like [L]Th$(Cl)_2(THF)_2$ (**4.2**), [L]Th$(N_3)_2(Py)_2$ (**4.4**) displays aggregation behavior in solution in the absence of a strong donor solvent.[175] This is supported by the broadness of the peaks in the ^{1}H NMR spectrum of this complex in $CDCl_3$ and by the fact that the resonances become sharp and easy to assign when the NMR solvent is changed to D_5-pyridine. Successful isolation of **4.4** is also supported by elemental analysis data obtained for the complex.[175] Combustion analysis indicated complex **4.4** was comprised of 43.46% C, 4.42% H, and 13.69% N, which correlates well with the calculated values (C: 43.48, H: 4.18, N: 14.01).

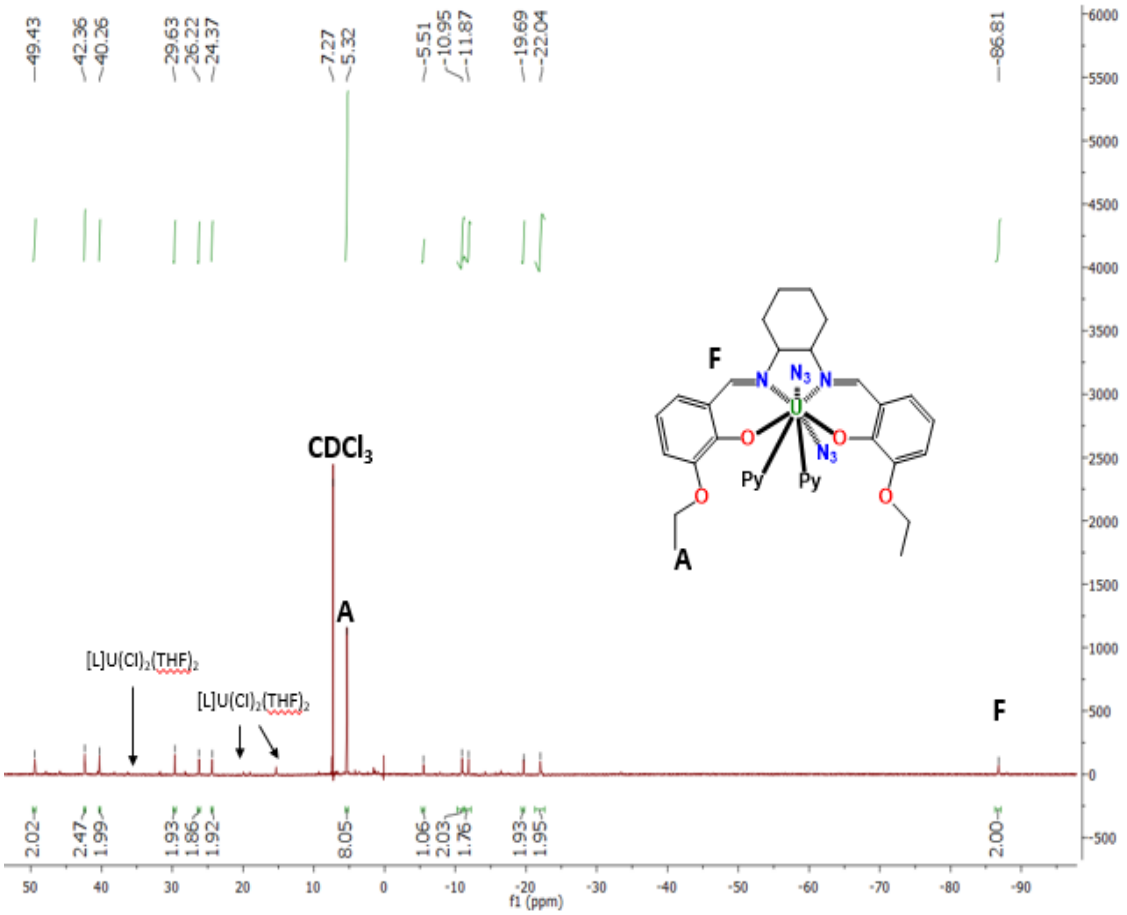


Figure 4-9: *300 MHz ^{1}H NMR spectrum of [L]U(N$_3$)$_2$(Py)$_2$* ***(4.3)*** *(bulk material) in CDCl$_3$ at 298 K*

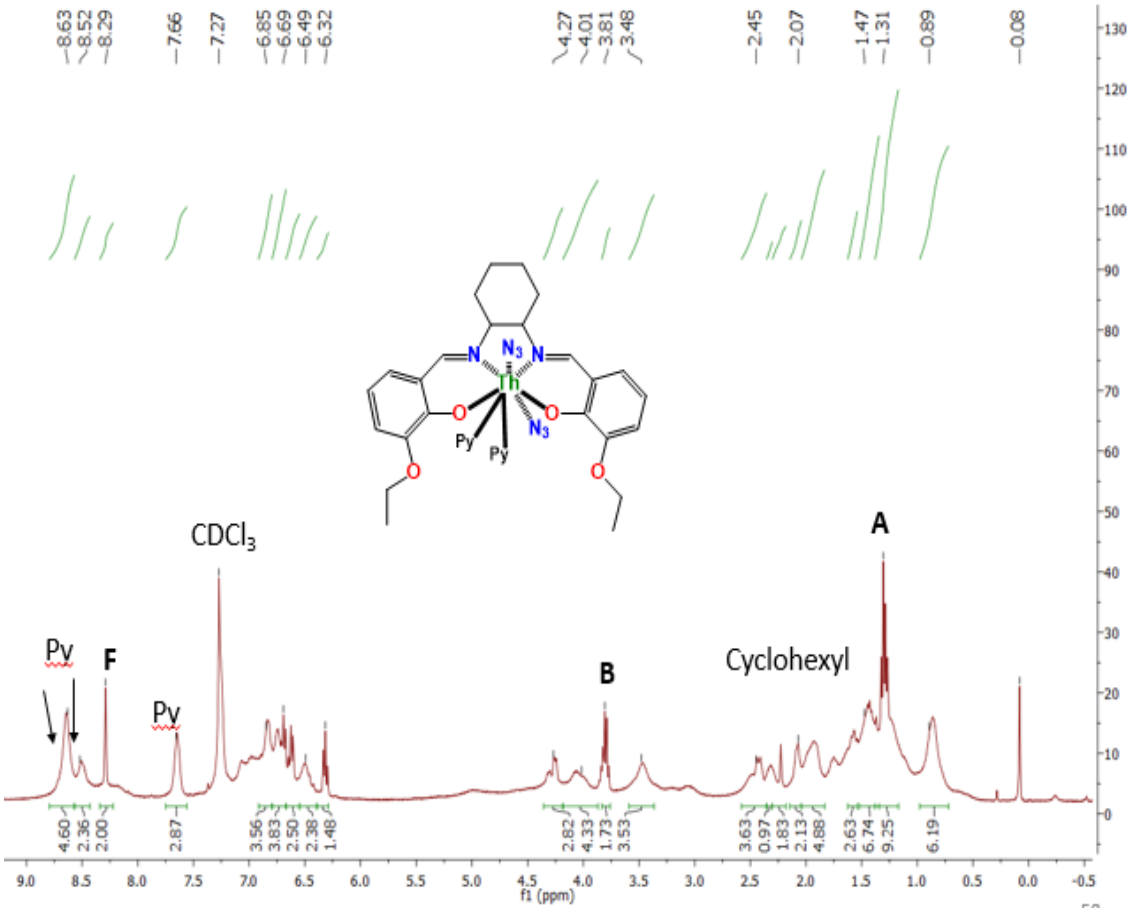


Figure 4-10: *400 MHz ^{1}H NMR spectrum of [L]Th$(N_3)_2(Py)_2$ (**4.4**) in $CDCl_3$ at 298 K*

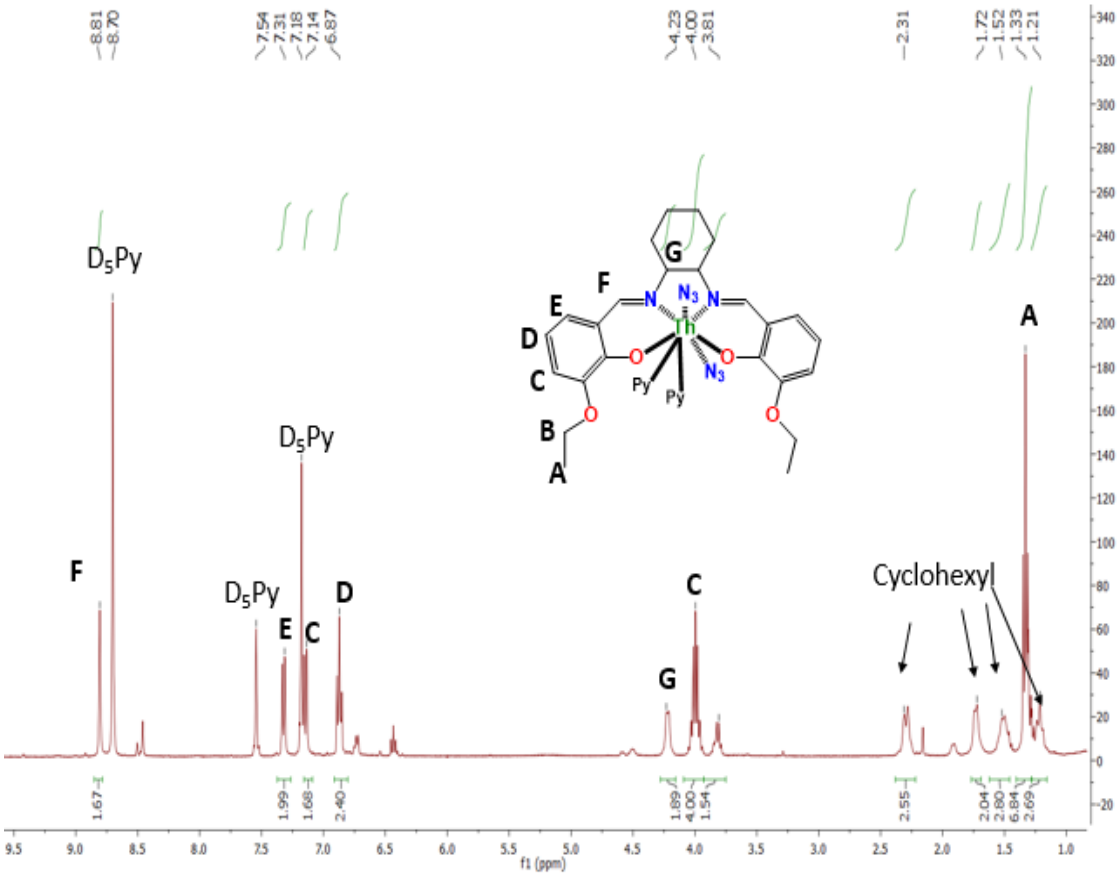


Figure 4-11: *400 MHz ^{1}H NMR spectrum of [L]Th$(N_3)_2(Py)_2$ (**4.4**) in D_5-pyridine at 298 K*

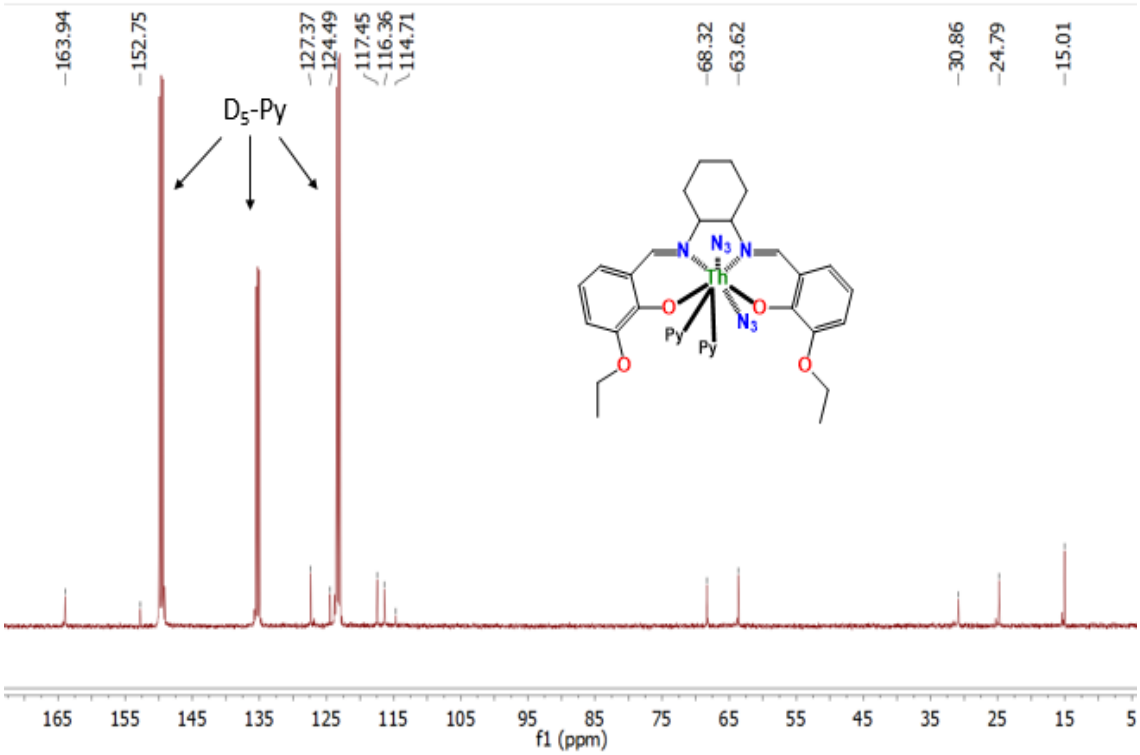
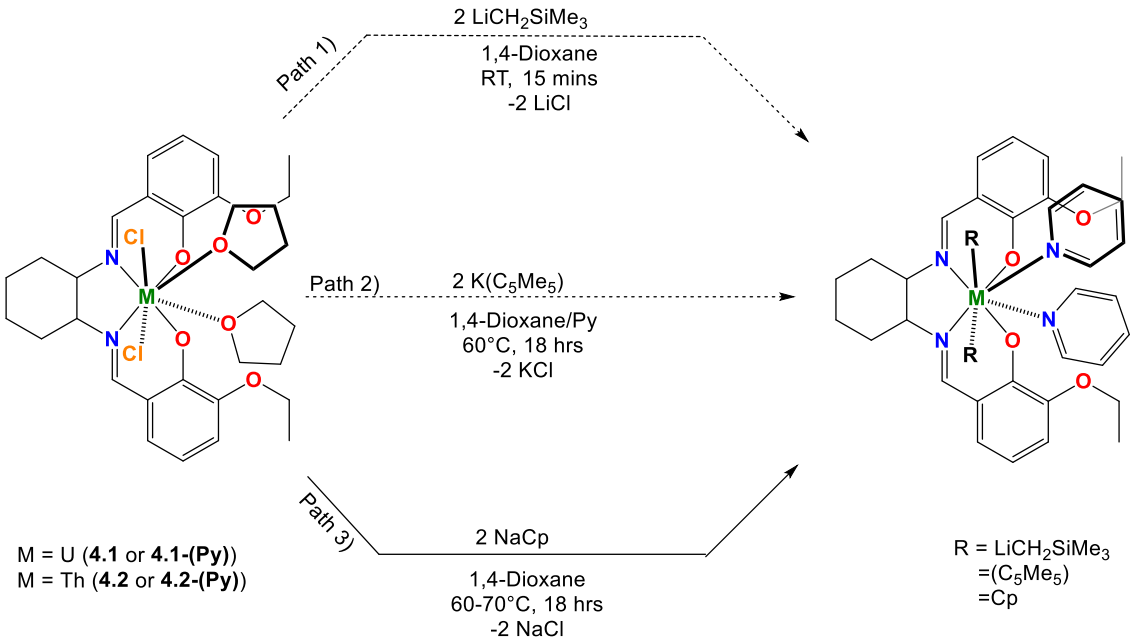


Figure 4-12: *100 MHz ^{13}C NMR spectrum of [L]Th(N$_3$)$_2$(Py)$_2$ (**4.4**) in D$_5$-pyridine at 298 K*

4.4: Salt metathesis reactivity of [L]An(Cl)$_2$(Solv)$_2$ complexes with carbon nucleophiles

Through solution-phase NMR spectroscopic, IR spectroscopic and X-ray diffraction data, it was determined that complexes **4.1** and **4.2** cleanly undergo salt metathesis reactivity with NaN_3 to form pseudo-*trans* diazido uranium and thorium Schiff base complexes (**4.3** and **4.4**, respectively) with no observed non-innocent redox behavior of the ligand system. In order to ensure the Schiff base ancillary ligand will maintain its innocence complexes **4.1** and **4.2** were reacted with stronger, carbon-based nucleophiles. Reactivity with carbon nucleophiles was chosen specifically since these reagents have been known to induce non-innocent ligand redox behavior for a variety of metal complexes – including our

uranium BDPP system (Chapter 3) – and is a better test for redox non-innocence. If the Schiff base ligand is able to support clean salt metathesis reactivity with carbon nucleophiles, then it is a suitable candidate for testing oxidation chemistry and stabilizing the desired An=E functionalities. If the Schiff base ligand is able to support reactivity to form the typically-sensitive actinide alkyl species, then it may also be a suitable candidate for supporting sensitive An=E(R) functionalities as well. To this end, complexes **4.1** and **4.2** were reacted with a variety of carbon-based nucleophiles (Figure 4-13), with nucleophiles ranging in size from small to large to probe the steric limits that can be accommodated by the ancillary ligand system.



Scheme 4-4: *Synthetic approaches for generating dialkyl Schiff base actinide complexes*

The first attempt at preparing a Schiff base bis(alkyl) complex involved the addition of 2 equiv. of $LiCH_2SiMe_3$ to **4.1** or **4.1-(Py)**. In theory, this salt metathesis pathway would eliminate 2 equiv. of LiCl and generate a pseudo-*trans* dialkyl

uranium complex of the type [L]U(CH_2SiMe_3)$_2$(Solv)$_2$. Unfortunately, ^{1}H NMR spectroscopy of the isolated products was inconclusive, and all attempts to recrystallize the product from Path 1 were unsuccessful. The inability to cleanly isolate a bis(alkyl) uranium species could be due to instability brought about by the poor steric protection afforded by the Schiff base ligand. Although uncommon for uranium complexes, it is also possible that upon generation of the bis(alkyl) complex *in situ*, the alkyl groups undergo reductive elimination to form $Me_3SiCH_2CH_2SiMe_3$ and a transient U(II) species that undergoes further decomposition. We were ultimately unable to isolate the Schiff base bis(alkyl) uranium complex via Path 1, and we decided to use bulkier cyclopentadiene functionalities to see if the added steric protection would allow for isolation of a bis(alkyl) actinide complex.

Although cyclopentadienyl uranium and thorium complexes have been widely studied, we decided to use these frameworks to potentially access rare linear actinide metallocenes. To date, almost all known uranium metallocenes bearing cyclopentadienyl type ligands are bent, with a few exceptions reported recently by Berthart, Ephritikhine and coworkers.[194, 195] Furthermore, prior to our investigations, there were no reported cases of linear thorium metallocence species, despite the fact that these complexes have been computationally predicted to be stable.[196] Since complexes **4.1** and **4.2** contain pseudo-*trans* dihalo functionalities, they are useful platforms for accessing linear actinide metallocenes. To test the limits of steric bulk that could be accommodated by the

ancillary Schiff base ligand framework, complex **4.1** was reacted with 2 equiv. of K(Cp*) (Cp*= C_5Me_5).

The reaction mixture was heated to 60°C for 24 hours in an effort to overcome a potentially high activation energy barrier associated with accommodating two equivalents of the bulky Cp* ligand. Upon isolation and recrystallization of the uranium product from Path 2, it was determined through X-ray diffraction that an open-faced metallocene [L]U(Cp*)(Cl)(1,4-dioxane) (**4.5**, Figure 4-13) was generated rather than the desired linear uranium metallocene.

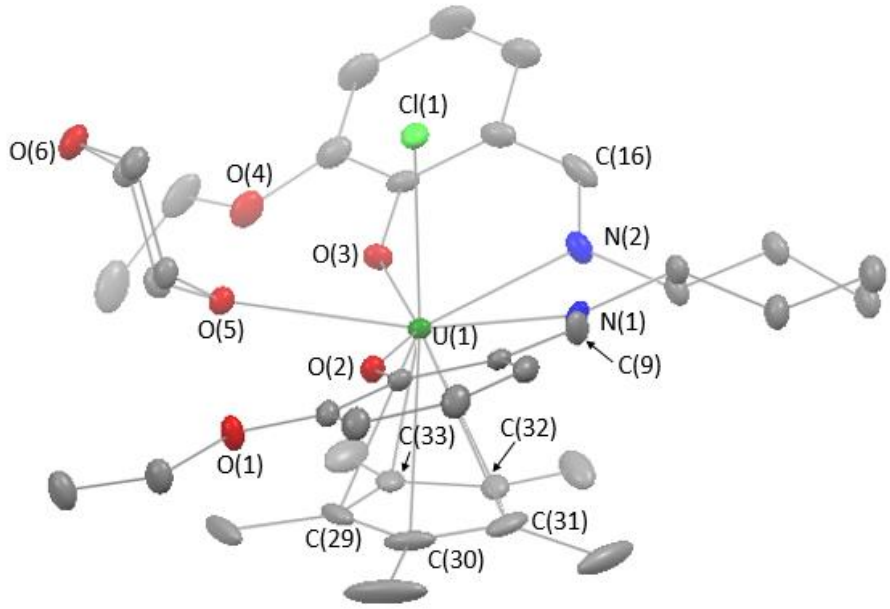


Figure 4-13: *ORTEP depiction of [L]U(Cp*)(Cl)(1,4-dioxane) (**4.5**) with ellipsoids shown at 50% probability. Hydrogen atoms omitted for clarity.*

Table 4-5: *Selected bond lengths (Å) and angles (°) for* ***4.5***

Bond	Distance (Å)	Bond Angle[a]	Angle (°)
U(1)-Cl(1)	2.6874(8)	O(2)-U(1)-O(3)	147.30(8)
U(1)-N(1)	2.592(2)	O(2)-U(1)-O(5)	73.55(7)
U(1)-N(2)	2.571(2)	O(3)-U(1)-O(5)	74.42(7)
U(1)-O(2)	2.1936(19)	O(2)-U(1)-N(1)	71.60(8)
U(1)-O(3)	2.210(2)	O(2)-U(1)-N(2)	134.89(8)
U(1)-O(5)	2.629(2)	O(3)-U(1)-N(1)	133.73(10)
U(1)-C(29)	2.772(3)	O(3)-U(1)-N(2)	70.98(8)
U(1)-C(30)	2.795(3)	N(1)-U(1)-N(2)	64.18(9)
U(1)-C(31)	2.830(3)	Cl(1)-U-O(2)	84.44(6)
U(1)-C(32)	2.822(3)	Cl(1)-U(1)-O(3)	83.81(6)
U(1)-C(33)	2.786(3)	Cl(1)-U(1)-O(5)	80.23(5)
N(1)-C(9)	1.298(4)	Cl(1)-U(1)-N(1)	75.66(11)
N(2)-C(16)	1.294(3)	Cl(1)-U(1)-N(2)	76.73(6)
		Cl(1)-U(1)- $Cp^*_{centroid}$	178.94

[a] $Cp^*_{centroid}$ is the calculated center of the ring containing C(29), C(30), C(31), C(32) and C(33)

Complex **4.5** is heptacoordinate and displays a pseudo-pentagonal bipyramidal geometry in the solid state. As anticipated, the N_2O_2 plane of the Schiff base ligand is puckered compared to complex **4.1** to accommodate the bulky Cp* ligand. From the extent of puckering caused by the Cp* ligand, it can be inferred that the system more than likely cannot support the addition of a second Cp* ligand. Comparatively, the U(1)-Cl(1) bond distance in complex **4.5** is slightly shorter than in complex **4.1** but is similar to other Cp*-containing U(IV) complexes. Additionally, the U-N bond distances for complex **4.5** are slightly shorter than reported in complex **4.1**.[175] This is likely due to the fact that complex **4.5** is heptacoordinate while complex **4.1** is octacoordinate. Reduced donation to the metal center in heptacoordinate complex 4.5 is compensated by strengthening the dative U-N bond interactions. Although the N(1)-C(9) and N(2)-C(16) bond distances of 1.298(4) Å and 1.294(3) Å are slightly longer than the C=N bond distances of complex **4.1**, they are within acceptable parameters for

C=N double bonds. This indicates that the Schiff base ligand remains innocent during salt metathesis with the strong carbon nucleophile, Cp*. Interestingly, the Cl(1)-U(1)-Cp*$_{centroid}$ (Cp*$_{centroid}$ = center of cyclopentadienyl ring) bond angle is nearly linear at 178.94°, suggesting that it could be possible to generate a linear uranium metallocene with this Schiff base ligand framework utilizing a less bulky cyclopentadienyl ligand variant.

In solution, complex **4.5** does not display C_s symmetry, illustrating that there is inequivalence within the ancillary Schiff base framework. This can be seen from the complexity of the ^{1}H NMR spectrum for this complex (Figure 4-14).

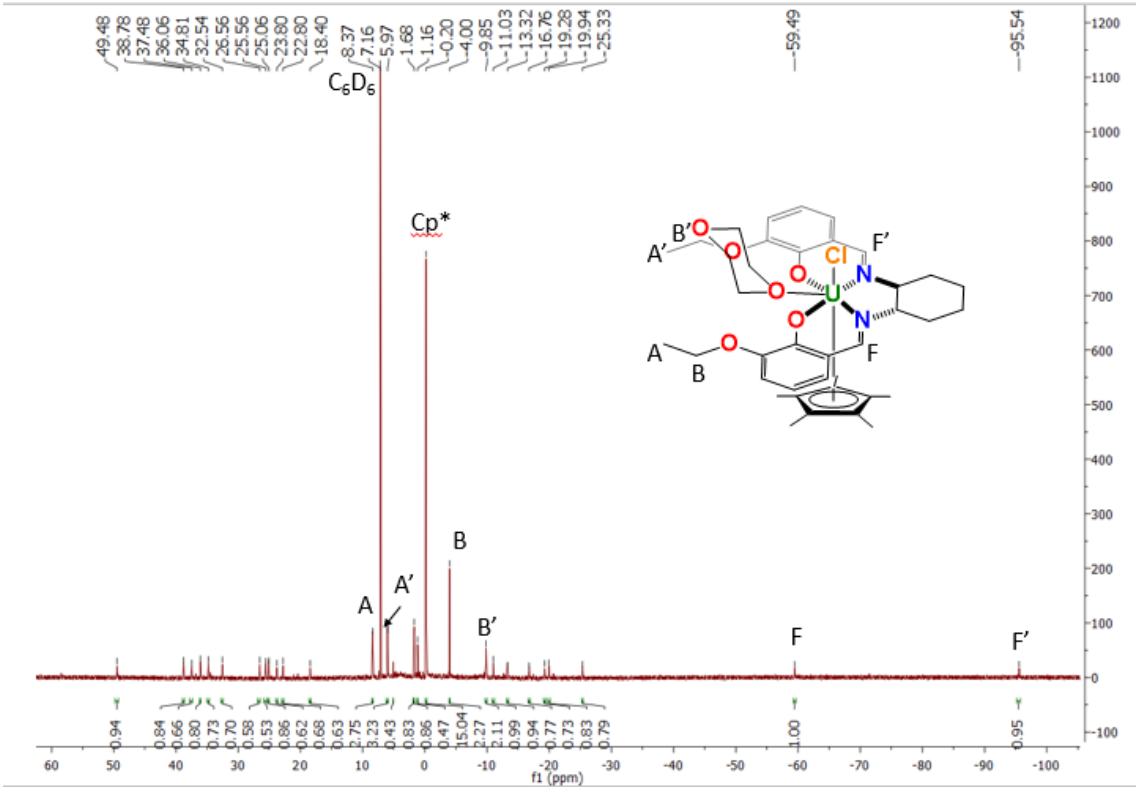


Figure 4-14: *300 MHz ^{1}H NMR spectrum of complex* ***4.5*** *in C_6D_6 at 298 K*

Due to the puckering of the Schiff base ligand caused by the Cp* moiety, complex **4.5** contains two diagnostic imine *H*C=N peaks at δ -59.46 and δ -95.58.

The more upfield peak at -95.58 ppm is likely due to the imine that is closer to the Cl ligand, since the imine peaks of complex **4.1** come in near this value. This is further supported by the Cl-H interaction distances in the solid state for complex **4.5** (Figure 4-13), where the distance between Cl(1) and the C(16) imine proton (3.551 Å) is significantly shorter than the distance between Cl(1) and the C(9) imine proton (3.817 Å). Assuming that ligand puckering does not fluctuate readily on the NMR time scale, it is possible for two very different imine proton peaks to be present in the ^{1}H NMR spectrum. An analogous reaction of 2 equiv. of KCp* with complex **4.2** was attempted as a means of accessing the linear thorium metallocene [L]Th(Cp*)$_2$(Solv). Unfortunately, despite several attempts, a pure product could not be isolated from this reaction mixture.

In an effort to mitigate the issue of excess steric encumbrance seen with Cp*, linear actinide metallocenes were pursued utilizing 2 equiv. of the less bulky sodium cyclopentadienyl proligand (Scheme 4-4, Path 3). The reaction mixtures of **4.1** and **4.2** with NaCp were heated between 65-75° for at least 24 hours. Gratifyingly, the reaction of **4.1** and 2 equiv. of NaCp resulted in generation of the linear uranium metallocene [L]U(Cp)$_2$(1,4-dioxane) (**4.6**) (Figure 4-15).

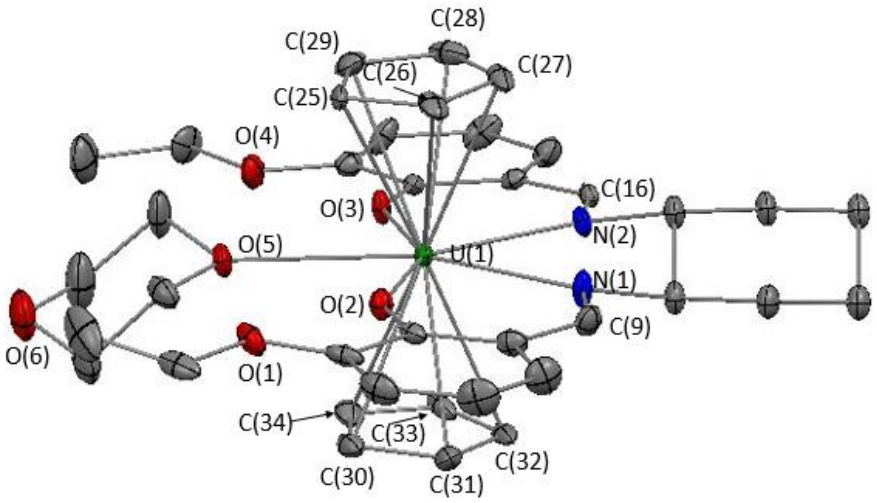


Figure 4-15: *ORTEP depiction of [L]U(Cp)$_2$(1,4-dioxane) (**4.6**) with ellipsoids shown at 30% probability. Hydrogen atoms and cocrystallized 1,4-dioxane removed for clarity.*

Table 4-6: *Selected bond lengths (Å) and angles (°) for **4.6***

Bond Distance[a,b]	Distance (Å)	Bond Angle[a,b]	Angle (°)
U(1)-O(2)	2.234(5)	O(2)-U(1)-O(3)	149.66(18)
U(1)-O(3)	2.240(5)	O(2)-U(1)-O(5)	75.4(2)
U(1)-O(5)	2.781(4)	O(2)-U(1)-N(1)	72.49(18)
U(1)-N(1)	2.605(6)	O(2)-U(1)-N(2)	137.42(18)
U(1)-N(2)	2.584(5)	O(2)-U(1)-Cp$_{cent}$(1)	88.88
U(1)-C(25)	2.829(13)	O(2)-U(1)-Cp$_{cent}$(2)	89.95
U(1)-C(26)	2.826(12)	O(3)-U(1)-O(5)	74.2(2)
U(1)-C(27)	2.827(8)	O(3)-U(1)-N(1)	137.84(17)
U(1)-C(28)	2.823(9)	O(3)-U(1)-N(2)	72.92(17)
U(1)-C(29)	2.825(8)	O(3)-U(1)-Cp$_{cent}$(1)	89.99
U(1)-C(30)	2.812(16)	O(3)-U(1)-Cp$_{cent}$(2)	88.98
U(1)-C(31)	2.832	O(5)-U(1)-N(1)	147.83(19)
U(1)-C(32)	2.855	O(5)-U(1)-N(2)	147.2(2)
U(1)-C(33)	2.844	O(5)-U(1)-Cp$_{cent}$(1)	88.89
U(1)-C(34)	2.796(13)	O(5)-U(1)-Cp$_{cent}$(2)	88.04
U(1)-Cp$_{cent}$(1)	2.562	N(1)-U(1)-N(2)	64.94(18)
U(1)-Cp$_{cent}$(2)	2.568	N(1)-U(1)-Cp$_{cent}$(1)	92.69
N(1)-C(9)	1.283(9)	N(1)-U(1)-Cp$_{cent}$(2)	90.89
N(2)-C(16)	1.282(9)	N(2)-U(1)-Cp$_{cent}$(1)	91.88
		N(2)-U(1)-Cp$_{cent}$(2)	91.72
		Cp$_{cent}$(1)-U(1)-Cp$_{cent}$(2)	175.80

[a]Cp$_{cent}$(1) is the calculated centroid for Cp carbons 25-29.
[b]Cp$_{cent}$(2) is the calculated centroid for Cp carbons 30-34.

Complex **4.6** is 7-coordinate (with Cp ligands considered to be monodentate in the apical positions) and adopts a pseudo-pentagonal bipyramidal geometry in the solid state, with approximate C_s symmetry. Although bis(cyclopentadienyl) uranium complexes have been widely studied, almost all of these species have featured the Cp rings in a bent conformation, where Cp-U-Cp bond angle is ≥ 145°.[58, 74, 151, 195] As this is the case, the isolation of complex **4.6** presents a rare opportunity to examine the bonding interactions of a bis(cyclopentadienyl) uranium complex with the Cp rings in a different conformation. Although complex **4.6** is not the first linear uranium metallocene, it is – to the best of our knowledge – the first neutral uranium(IV) linear metallocene species. Like the series of anionic 7-coordinate linear uranium metallocenes of the general type $[X][(Cp^*)_2U(CN)_5]$ (X = cation) reported by Berthet, Ephritikhine and coworkers[53], the two Cp rings in complex **4.6** are virtually eclipsed, with a slight torsion of -7.8°. The average Cp carbon-uranium bond distance for **4.6** is 2.82 Å, which is only slightly longer than the average $U\text{-}C_{Cp}$ bond distances of 2.81(1) Å for the anionic linear metallocene series.[53] Notably, the average $U\text{-}C_{Cp}$ bond distance for **4.6** is slightly longer than other reported average $U\text{-}C_{Cp}$ bond distances for bent uranium metallocene species.[2, 52, 55, 57] Like the series of anionic linear metallocenes, **4.6** displays strong Cp-U interactions, with short $Cp_{centroid}$-U distances of 2.562 and 2.568 Å. The nearly linear arrangement of the Cp rings is manifested by a $Cp_{cent}(1)\text{-}U(1)\text{-}Cp_{cent}(2)$ bond angle of 175.80°. This bond angle is slightly more acute than the analogous $Cp^*_{centroid}(1)\text{-}U(1)\text{-}Cp^*_{centroid}(2)$ bond angles of 177.5-179.5° for the anionic linear uranium

metallocene series, which can be explained in part by the steric properties of the system.[53] Given the size of the ancillary Schiff base ligand, it is possible that the Cp rings move closer to the smaller, more labile 1,4-dioxane ligand to reduce the possible ligand-ligand repulsion with the cyclohexyl backbone of the Schiff base ligand. This is supported by the weak coordination of the 1,4-dioxane ligand to the uranium center, which has a very long U(1)-O(5) bond distance of 2.781(4) Å. Interestingly, N(1), N(2), (O2), O(3) and O(5) are coplanar, creating an equatorial motif reminiscent of the ancillary cyano ligands in the series of anionic linear metallocenes.[53] The Schiff base U-O bond distances are longer than the analogous bond distances for starting complex **4.1** by about 0.044-0.05 Å, while the U(1)-N(1) and U(1)-N(2) bond distances are shorter than analogous distances for **4.1** by about 0.01 and 0.03 Å, respectively. Finally, it should be noted that the N(1)-C(9) and N(2)-C(16) Schiff base C=N imine bond distances of 1.283(9) and 1.282(9) Å, respectively, are within expected parameters for a C=N bond, indicating that the Schiff base ligand remained a non-participant in salt metathesis reactivity at the metal center with a strong carbon nucleophile.

In solution, complex **4.6** appears to display high symmetry, as demonstrated by ^{1}H NMR spectroscopy (Figure 4-17). There are 15 peaks with an appreciable integration, each correlating to a unique hydrogen environment for the complex, as expected for a C_s symmetric species. Additionally, it should be noted that there are no diagnostic upfield peaks around -90 ppm as seen with the dichloro starting material (**4.1**), indicating a change in shielding environment around the imine protons due to the presence of the Cp rings.

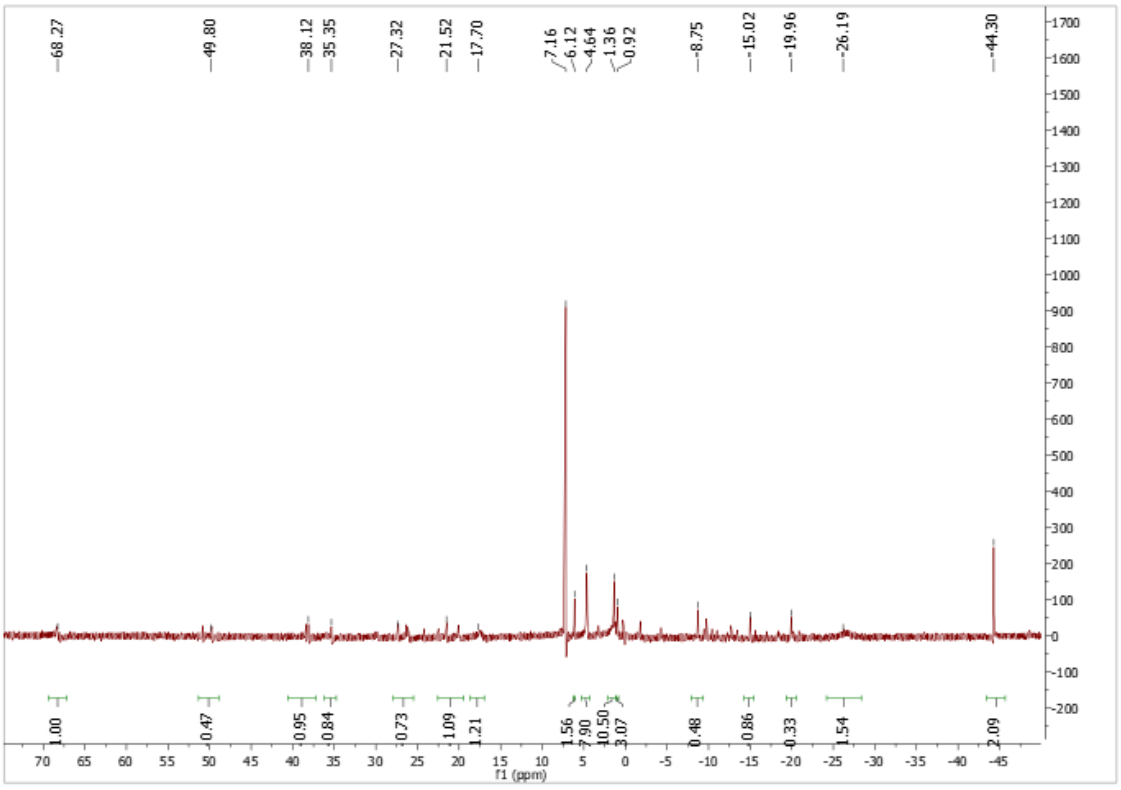


Figure 4-16: *300 MHz ^{1}H NMR spectrum of the linear uranium metallocene (**4.6**) in C_6D_6 at 298 K*

This is further supported by the fact that there is a diagnostic imine *H*C=N peak at -44.30 ppm, which is in a similar location to one of the *H*C=N peaks (-59.46 ppm) for the confirmed Cp*-containing complex **4.5**. The approximate 15 ppm difference between the imine *H*C=N peaks of complexes **4.5** and **4.6** could be accounted for by the fact that complex **4.5** has a chlorido ligand that could significantly shield the second imine proton on its Schiff base ligand. As mentioned earlier, the Schiff base imine hydrogens of complex **4.5** differ significantly in location relative to the ancillary chlorido ligand of the complex. The imine proton that is further away from the chlorido ligand would be expected to be less shielded than the imine proton that is closer to the chlorido ligand.

Inspired by the isolation of the linear uranium metallocene **4.6**, the analogous reaction to generate the linear thorium metallocene was also attempted. Upon reacting two equivalents of NaCp with complex **4.2**, the linear thorium metallocene [L]Th(Cp)$_2$(1,4-dioxane) (**4.7**) was formed in 88% recrystallized yield. Surprisingly, crystals suitable for X-ray diffraction were only obtainable if the complex was not isolated from the NaCl byproduct. A structure of the linear thorium metallocene was confirmed through X-ray diffraction (Figure 4-17).

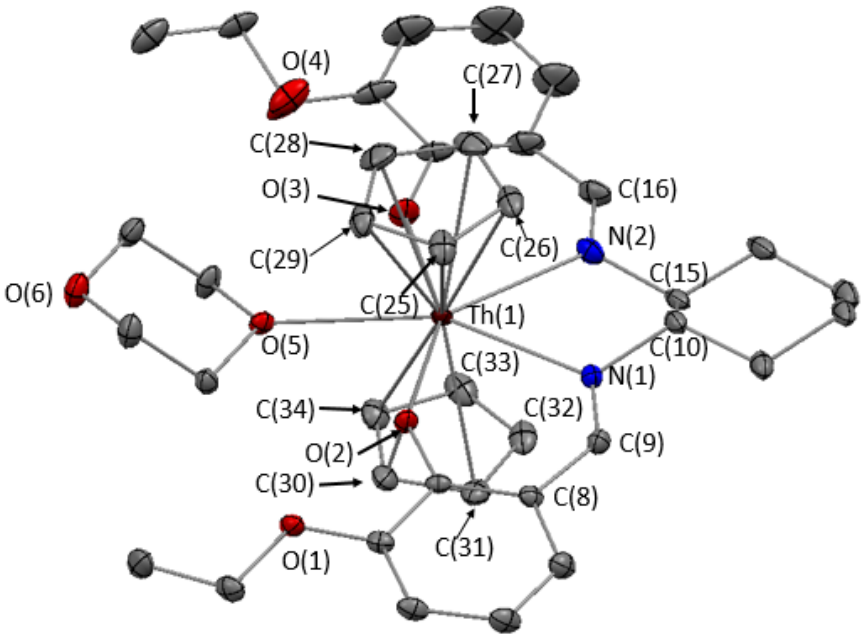


Figure 4-17: *ORTEP depiction of [L]Th(Cp)$_2$(1,4-dioxane) (**4.7**) with ellipsoids shown at 30% probability. Hydrogen atoms and 2 cocrystallized 1,4-dioxane molecules removed for clarity.*

Table 4-7: *Selected bond lengths (Å) and angles (°) for* ***4.7***

Bond[a,b]	Distance (Å)	Bond Angle[a,b]	Angle (°)
Th(1)-O(2)	2.287(3)	O(2)-Th(1)-O(3)	151.97(11)
Th(1)-O(3)	2.295(3)	O(2)-Th(1)-O(5)	77.51(13)
Th(1)-O(5)	2.719(3)	O(3)-Th(1)-O(5)	74.49(13)
Th(1)-N(1)	2.642(3)	O(2)-Th(1)-N(1)	72.25(9)
Th(1)-N(2)	2.645(3)	O(2)-Th(1)-N(2)	136.03(10)
Th(1)-C(25)	2.911	O(3)-Th(1)-N(1)	135.78(10)
Th(1)-C(26)	2.898(4)	O(3)-Th(1)-N(2)	71.98(11)
Th(1)-C(27)	2.872(4)	N(1)-Th(1)-N(2)	63.85(10)
Th(1)-C(28)	2.849(4)	N(1)-Th(1)-O(5)	149.70(12)
Th(1)-C(29)	2.876(4)	N(2)-Th(1)-O(5)	146.16(14)
Th(1)-C(30)	2.872(4)	Cp_{cent}(1)-Th(1)-Cp_{cent}(2)	177.47
Th(1)-C(31)	2.897(4)	Cp_{cent}(1)-Th(1)-O(2)	89.04
Th(1)-C(32)	2.923	Cp_{cent}(1)-Th(1)-O(3)	90.27
Th(1)-C(33)	2.930	Cp_{cent}(1)-Th(1)-O(5)	91.23
Th(1)-C(34)	2.904	Cp_{cent}(1)-Th(1)-N(1)	90.14
Th(1)-Cp_{cent}(1)	2.624	Cp_{cent}(1)-Th(1)-N(2)	93.37
Th(1)-Cp_{cent}(2)	2.648	Cp_{cent}(2)-Th(1)-O(2)	89.28
N(1)-C(9)	1.292(5)	Cp_{cent}(2)-Th(1)-O(3)	90.34
N(2)-C(16)	1.287(5)	Cp_{cent}(2)-Th(1)-O(5)	86.57
		Cp_{cent}(2)-Th(1)-N(1)	91.13
		Cp_{cent}(2)-Th(1)-N(2)	89.15

[a]Cp_{cent}(1) is the calculated center of cyclopentadienyl ring: C(25), C(26), C(27), C(28), C(29)
[b]Cp_{cent}(2) is the calculated center of cyclopentadienyl ring: C(30), C(31), C(32), C(33), C(34)

In the solid state, the Th complex **4.7** is structurally similar to its U analog (**4.6**), being heptacoordinate with pentagonal bipyramidal geometry exhibiting pseudo C_s symmetry. As this is the first linear bis(cyclopentadienyl) thorium metallocene complex, there is no structural information available to compare the Cp C-Th bond distances to gauge if they are within expected parameters for a complex of this type. Consequently, only structural comparisons between **4.7** and known bent bis(cyclopentadienyl) thorium metallocene complexes were possible. Notably, the Th-O and Th-N bond distances for complex **4.7** are slightly longer than the analogous bonds in complex **4.2**. The Th-O and Th-N bond elongation observed with complex **4.7** can be explained in part due to the steric demands of

the system. As complex **4.7** accommodates two fairly bulky cyclopentadienyl ligands along with the Schiff base ligand and an equivalent of 1,4-dioxane, it is reasonable that these ligands adopt positions further from the thorium center to minimize ligand repulsion. Additionally, the Th-O and Th-N bond elongation observed with complex **4.7** can be rationalized using an electronic argument as well. Since the cyclopentadienyl ligands are both strong π-donors and contribute more electron density to the metal center than the chlorido ligands of complex **4.2**, the Th center of complex **4.7** does not require as much electron density from the Schiff base ligand to stabilize the metal center, resulting in weaker Th-O and Th-N interactions. The average cyclopentadienyl Th-C bond distance for complex **4.7** is approximately 2.897 Å. Although on the long side, this average cyclopentadienyl Th-C bond distance is similar to a variety of bis(cyclopentadienyl) thorium complexes reported by Walter and coworkers, which contain a range of average metallocene Th-C bond distances between 2.835 and 2.936 Å.[58, 59] Additionally, the Cp_{cent}(1)-Th(1)-Cp_{cent}(2) bond angle in **4.7** is nearly linear at 177.47°. This bond angle differs significantly from the Cp_{cent}(1)-Th(1)-Cp_{cent}(2) bond angles of the bent thorium metallocenes, which span a range of 118.6-144.9°.[58, 59] It should also be noted that the Schiff base C=N imine bond distances of 1.292(5) Å and 1.287(5) Å for N(1)-C(9) and N(2)-C(16), respectively, are in good agreement with other reported imine C=N bond distances, illustrating that this ligand does not engage in non-innocent behavior.[30]

In solution, complex **4.7** displays high symmetry, which can be observed through the simplicity of the ^{1}H NMR spectrum for this complex (Figure 4-18), with a single peak for the ten cyclopentadienyl hydrogens.

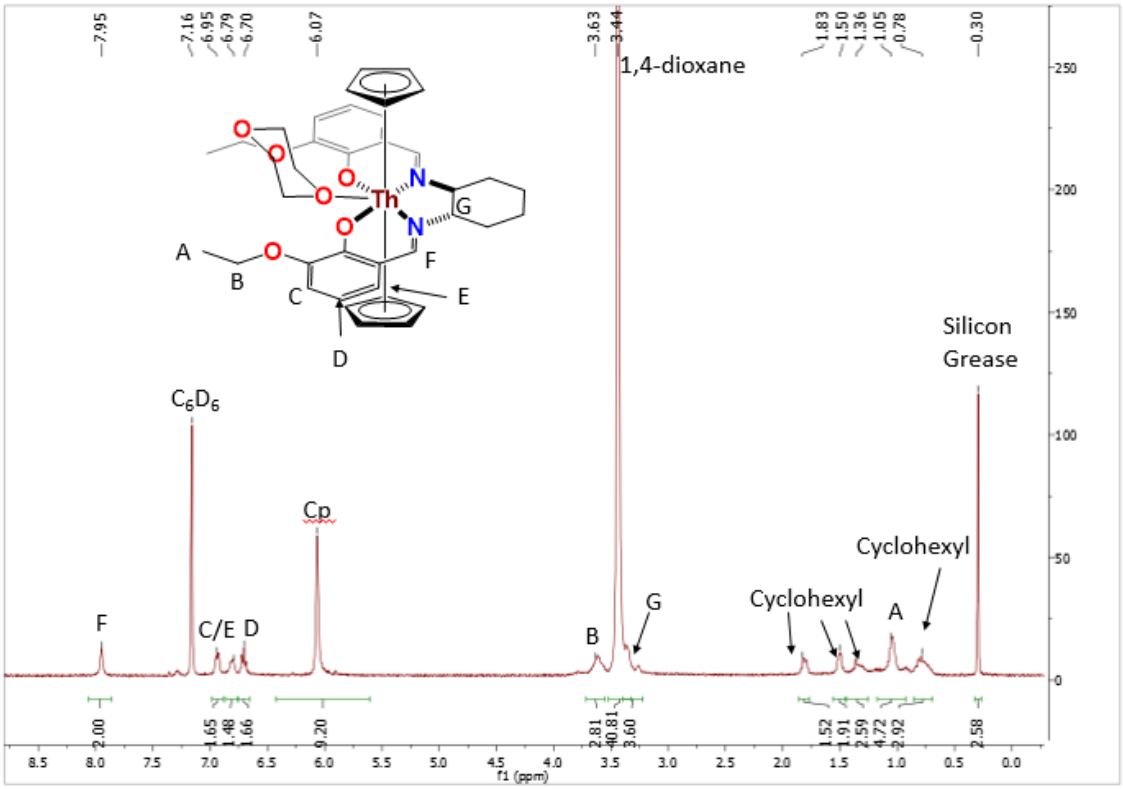


Figure 4-18: *400 MHz ^{1}H NMR spectrum of [L]Th(Cp)$_2$(1,4-dioxane) (**4.7**) spiked with excess 1,4-dioxane in C_6D_6 at 298 K*

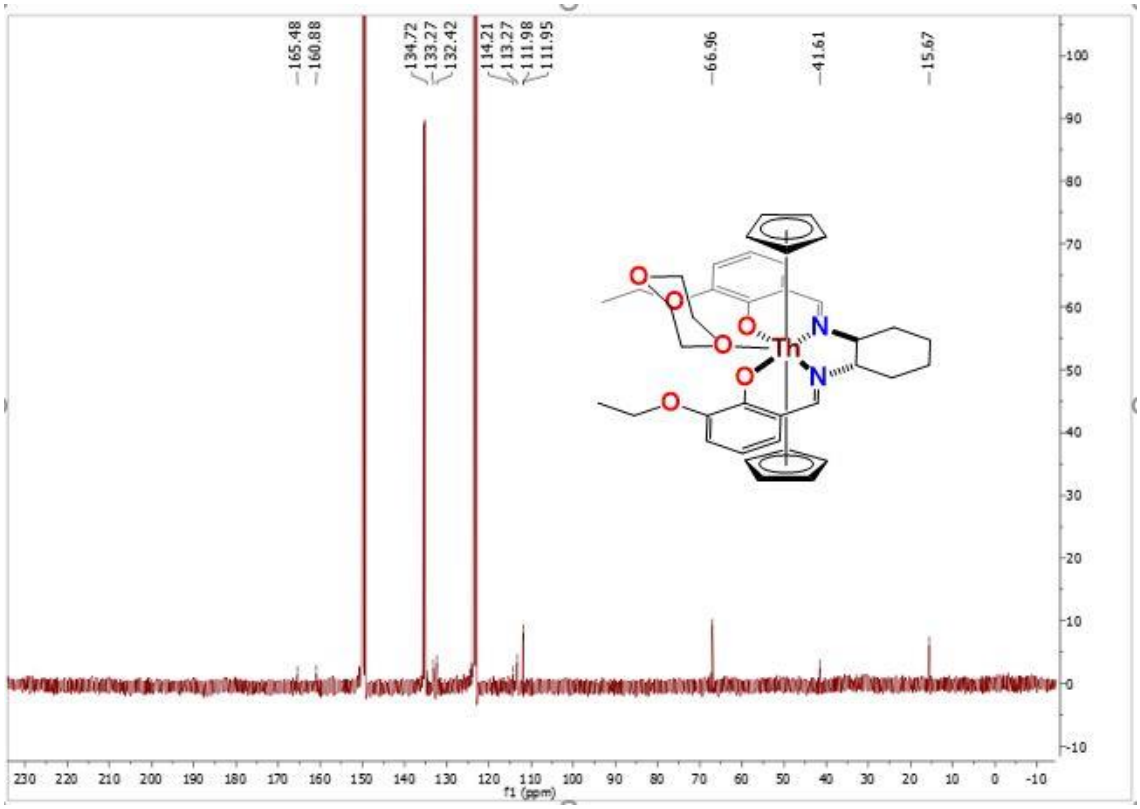
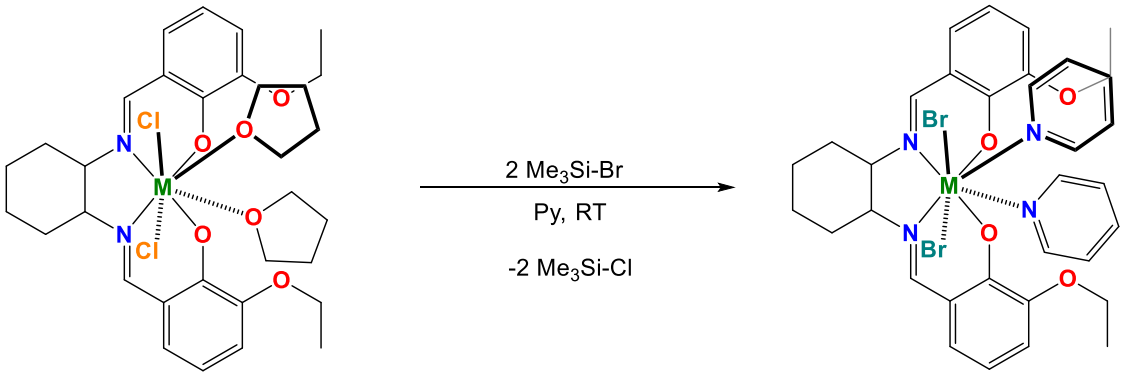


Figure 4-19: *100 MHz ^{13}C NMR spectrum of [L]Th(Cp)$_2$(1,4-dioxane) (**4.7**) in D$_5$-pyridine at 298 K*

Prior to the isolation of complex **4.7**, linear bis(cyclopentadienyl) thorium metallocenes were calculated to be stable,[54] but only bent metallocenes have been reported. Upon generating the first bis(Cp*) linear uranium metallocene, Ephritikhine, Maron and coworkers calculated that an f^0 actinide metal center, like Th(IV), should exhibit greater stability with a linear metallocene geometry as compared to a bent conformation.[54] In fact, from their calculations, it was determined that a linear actinide metallocene geometry is more favored for actinide complexes that contain fewer *f*-electrons.[54] Complex **4.7** provides the first experimental evidence supporting the calculations performed by Ephritikhine and coworkers.

4.5: σ-Bond metathesis reactivity of [L]An(Cl)$_2$(Solv)$_2$ complexes with Me$_3$Si-Br

In addition to examining the reactivity of complexes **4.1** and **4.2** with nitrogen and carbon based nucleophiles, we explored σ-bond metathesis reactivity using Me$_3$Si-Br with these complexes. This reactivity was explored as a means for comparing the activation of the chlorido ligands with the tris(anilido) system discussed in Chapter 2. Aside from accessing an additional dihalo Schiff base complex, it was hoped that exploring σ-bond metathesis reactivity would shed light on whether this type of reactivity could be used to install different An=E functionalities. To this end, 2 equiv. of Me$_3$Si-Br were added to a solution of either complex **4.1** or **4.2** in pyridine (Scheme 4-5).



M = U
4.1 or **4.1-(Py)**

M = Th
4.2 or **4.2-(Py)**

M = U (**4.8**), 79% yield

M = Th (**4.9**), 69% yield

Scheme 4-5: *σ-Bond metathesis reactivity used to generate [L]An(Br)$_2$(Py)$_2$, complexes **4.6** (An = U) and **4.7** (An = Th)*

Complexes **4.1** and **4.2** readily undergo σ-bond metathesis with an excess of Me$_3$Si-Br to generate [L]U(Br)$_2$(Py)$_2$ (**4.8**) and [L]Th(Br)$_2$(Py)$_2$ (**4.9**) in good yields. The dibromo Schiff base actinide complexes are less soluble in

chlorinated solvents than their dichloro counterparts, which made isolation and purification of these complexes difficult; however, single crystals were obtained for both complexes by means of slow evaporation from chloro benzene (Figure 4-20).

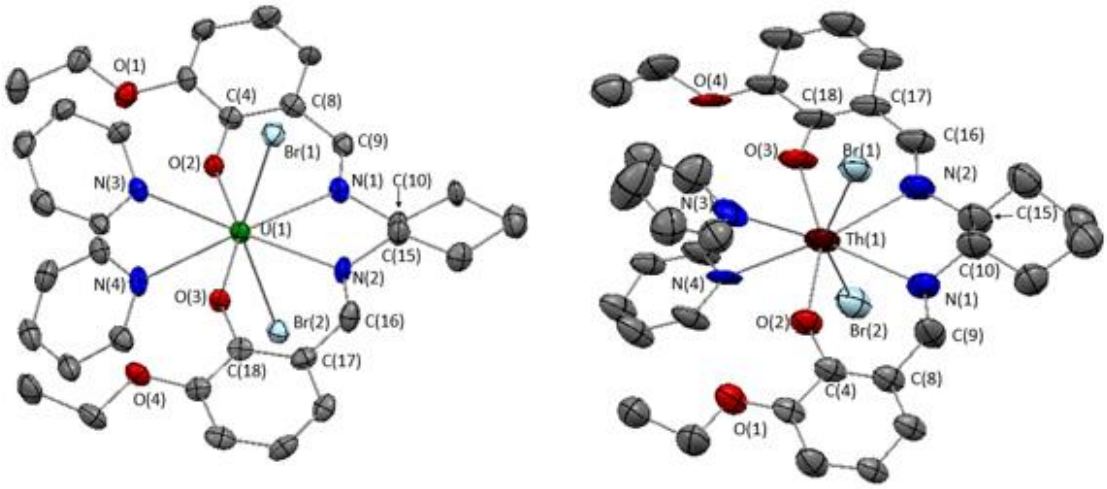


Figure 4-20: *ORTEP depiction of [L]U(Br)$_2$(Py)$_2$ (**4.8**) and [L]Th(Br)$_2$(Py)$_2$ (**4.9**) with ellipsoids shown at 50% probability. Hydrogen atoms omitted for clarity.*

Table 4-8: *Selected bond lengths (Å) and angles (°) for **4.8***

Bond	Distance (Å)	Bond Angle	Angle (°)
U(1)-Br(1)	2.9015(10)	Br(1)-U(1)-Br(2)	149.16(3)
U(1)-Br(2)	2.9026(10)	O(2)-U(1)-O(3)	152.5(2)
U(1)-O(2)	2.160(6)	O(2)-U(1)-N(1)	71.1(2)
U(1)-O(3)	2.143(6)	O(2)-U(1)-Br(1)	90.89(16)
U(1)-N(1)	2.605(7)	O(3)-U(1)-N(2)	71.4(2)
U(1)-N(2)	2.597(7)	O(3)-U(1)-Br(2)	87.65(15)
U(1)-N(3)	2.623(7)	N(1)-U(1)-N(2)	65.3(2)
U(1)-N(4)	2.659(7)	N(3)-U(1)-N(4)	66.0(2)
N(1)-C(9)	1.286(10)		
N(2)-C(16)	1.265(12)		

Complexes **4.8** and **4.9**, like their dichloro counterparts, are 8-coordinate and display pseudo-dodecahedral geometry in the solid state. Although a structure was solved for complex **4.9**, the X-ray diffraction data for this complex

is not of sufficient quality to reliably determine metrical parameters but can be used to establish symmetry. As this is the case, a detailed structural analysis is only provided for complex **4.8**. Structurally, complex **4.8** is very similar to its dichloro precursor (**4.1**). The Br(1)-U(1)-Br(2) bond angle is 149.16(3)°, whereas the Cl(1)-U(1)-Cl(1) bond angle of **4.1** is 148.36(7)°. This subtle difference in the X-U-X bond angle is likely due to the larger size of the bromido ligands, which move further apart to minimize repulsion of the bromido ligands' lone pairs. Interestingly, the O(2)-U(1) and O(3)-U(1) bond distances of 2.160(6) Å and 2.143(6) Å, respectively, are slightly shorter than the U(1)-O(1) bond distance of 2.190(4) Å for **4.1**. Additionally, all of the U-N bond distances for complex **4.8** are slightly shorter than the U-N bond distances of complex **4.1**. These stronger U-L interactions observed for complex **4.8** could be due in part to the weaker σ-donating ability of the bromido ligands compared to the chlorido ligands of complex **4.1**, where the shorter U-L bond distances in **4.8** arise as a means to compensate for the reduced donation to the metal center. The U(1)-Br(1) and U(2)-Br(2) bond distances of 2.9015(10) Å and 2.9026(10) Å, respectively, are in good agreement with other U(IV)-Br bond distances previously reported.[57] Additionally the N(1)-C(9) and N(2)-C(16) bond distances of 1.286(10) and 1.265(10) Å are consistent with the C=N bond distances and are similar to the C=N distances for **4.1** and **4.3**.

In solution, complexes **4.8** and **4.9** display high symmetry in their ^{1}H NMR spectra. Similar complex **4.1** the ^{1}H NMR spectrum of **4.8** displays a diagnostic

upfield peak for the imine protons of the Schiff base ligand at δ -92.23 (Figure 4-21).

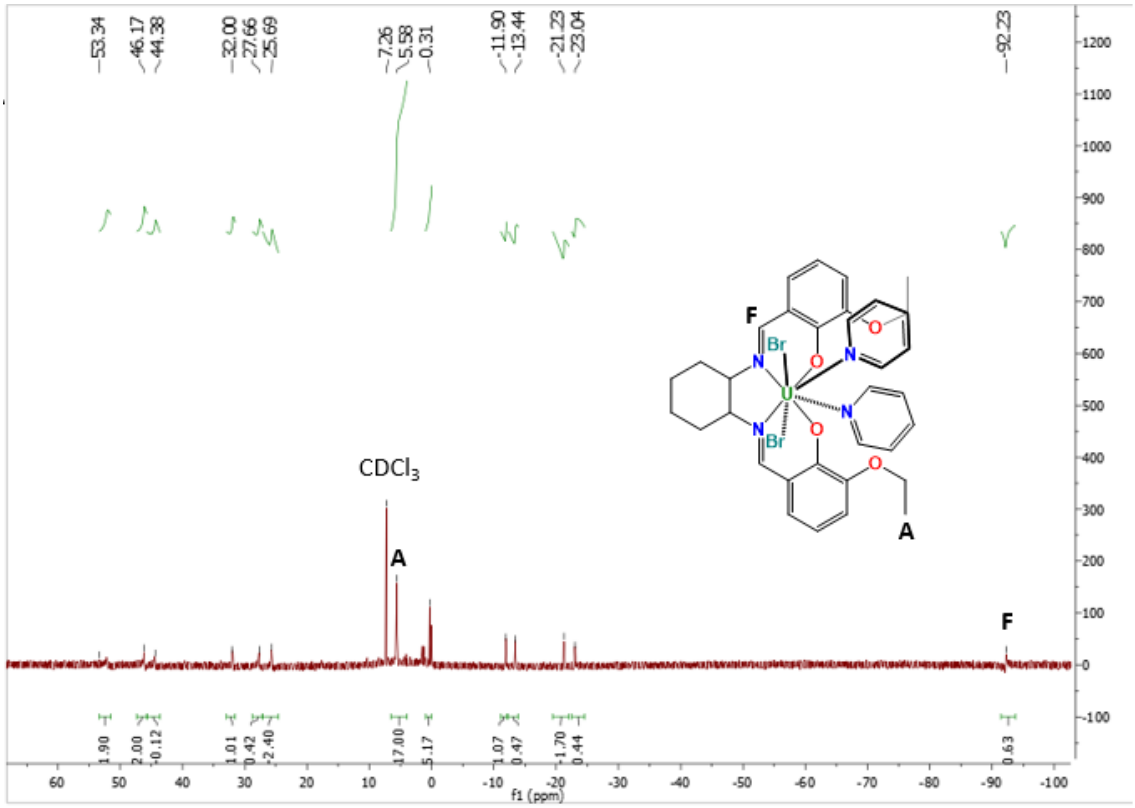


Figure 4-21: *300 MHz ^{1}H NMR spectrum of [L]U(Br)$_2$(Py)$_2$ (**4.8**) in CDCl$_3$ at 298 K*

Due to the poor solubility of complex **4.8** in most common organic solvents, a ^{1}H NMR spectrum that accurately depicts the integrations of each peak could not be obtained. Like complex **4.8**, complex **4.9** also displays poor solubility in most common organic solvents, including pyridine. The Th dibromo complex (**4.9**) displays high symmetry in solution by ^{1}H NMR spectroscopy (Figure 4-22), and, unlike the Th dichloro complex (**4.2**), does not display signs of aggregation in the absence of a strong donor solvent. we can see that the complex displays high symmetry in solution. Due to poor solubility of this complex in most organic

solvents, a suitable ^{13}C NMR spectrum could not be obtained, despite several hours of data acquisition.

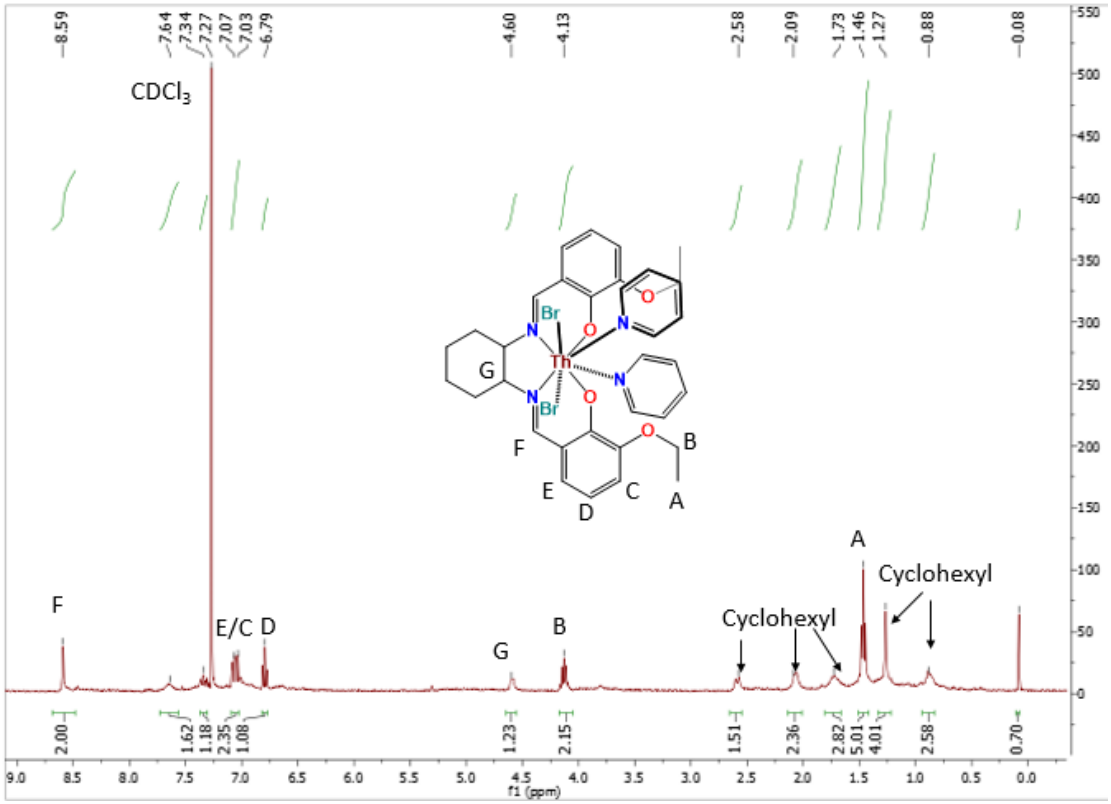


Figure 4-22: *400 MHz ^{1}H NMR spectrum of [L]Th(Br)$_2$(Py)$_2$ (**4.9**) in $CDCl_3$ at 298 K*

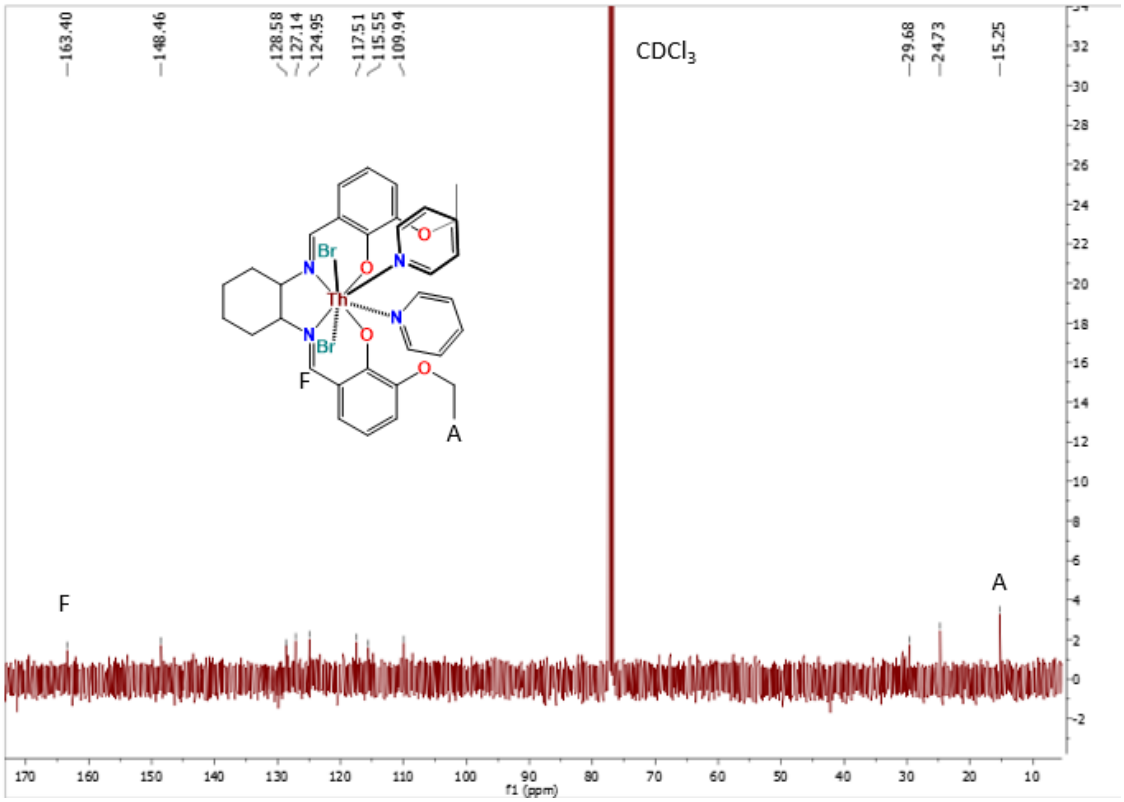
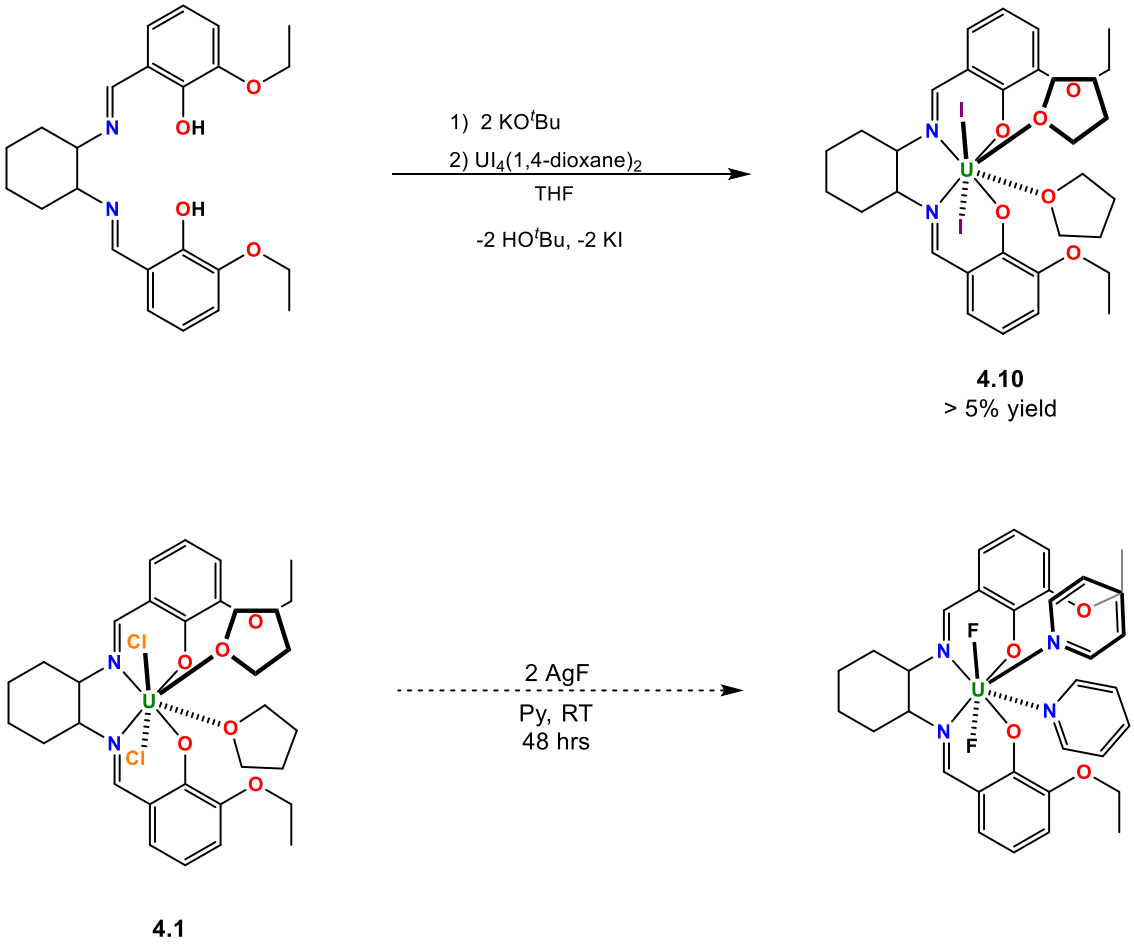


Figure 4-23: *100 MHz ^{13}C NMR spectrum of [L]Th(Br)$_2$(Py)$_2$ (**4.9**) in $CDCl_3$ at 298 K*

The solution phase and solid state data show that complexes **4.1** and **4.2** readily undergo σ-bond metathesis with Me_3Si-Br. The Schiff base C=N bonds remain intact, indicating that the Schiff base backbone is robust enough to attempt oxidation chemistry to generate desired An=E functionalities.

Before attempting oxidation chemistry, we sought to study the effect halide electronegativity has on ^1H NMR chemical shift of the Schiff base ligand. In order to generate the remaining dihalo Schiff base complexes for this study, the reactions outlined in Scheme 4-6 were attempted.



Scheme 4-6: *Synthetic approaches to generate the diiodo and difluoro Schiff base complexes of the type [L]U(X)$_2$(Solv)$_2$*

In an effort to generate [L]U(I)$_2$(Py)$_2$ (**4.10**), the same method used to generate complex **4.1** was utilized due to its success in accessing the dichloro Schiff base complex. Unfortunately, this method was far less successful for accessing the diiodo complex. While complex **4.10** could be isolated, the reaction yielded less than 5% of the desired product. This is mainly due to the poor solubility of complex **4.10** in most common organic solvents. It was qualitatively determined that the solubility of the dihalo Schiff base complexes in chlorinated solvents was: [L]U(Cl)$_2$(Py)$_2$ > [L]U(Br)$_2$(Py)$_2$ > [L]U(I)$_2$(THF)$_2$. For this reason, all

attempts to recrystallize complex **4.10** were unsuccessful. Despite this, solution phase data were obtained by ^{1}H NMR spectroscopy (Figure 4-24).

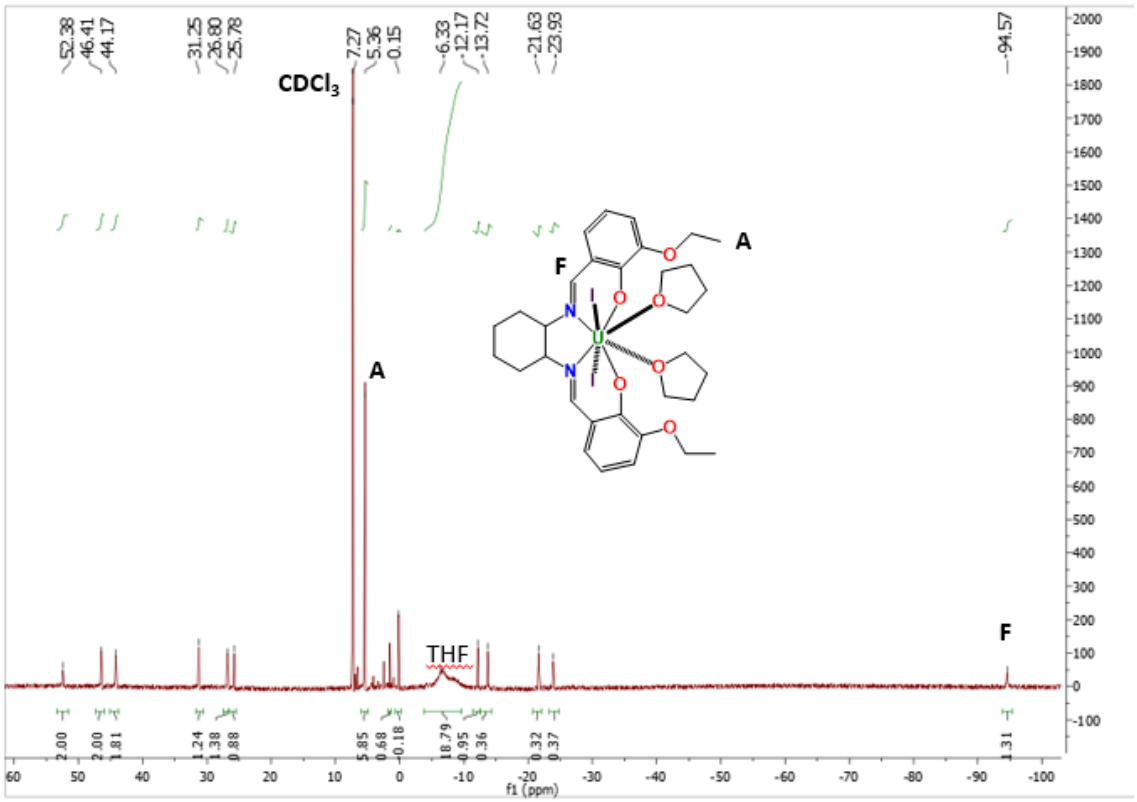


Figure 4-24: *300 MHz ^{1}H NMR spectrum of [L]U(I)$_2$(THF)$_2$ (**4.10**) in CDCl$_3$ at 298 K*

As demonstrated by the ^{1}H NMR spectrum, complex **4.10** exhibits high symmetry in solution like the other dihalo Schiff base uranium complexes in the series. Like complexes **4.1** and **4.8**, complex **4.10** also displays a diagnostic upfield *H*C=N imine peak at δ -94.57. Although a crystal structure could not be obtained for this complex, it is still possible to safely conclude that the desired [L]U(I)$_2$(THF)$_2$ species was generated. The ^{1}H NMR spectrum for this complex contains the appropriate number of peaks that account for all of the protons for the intended bis(iodido) species. Additionally, the ^{1}H NMR spectrum for complex

4.10 closely resembles the ^{1}H NMR spectra of the other dihalo Schiff base uranium complexes that have been fully characterized in the series.

In an effort to generate [L]U(F)$_2$(Py)$_2$, the final dihalo uranium Schiff base complex of the series, we attempted to utilize a transmetallation reaction to install the flourido ligands on the uranium center by means of ligand exchange with silver fluoride. Unfortunately, although a red-orange powder was isolated from the reaction, all attempts at characterizing the product from this reaction pathway were inconclusive.

Despite being unable to conclusively access the difluoro uranium Schiff base complex, we decided to go ahead and analyze the ^{1}H NMR chemical shift data to see if there is a strong correlation that exists between ^{1}H NMR chemical shift and halide electronegativity for this series of dihalo uranium Schiff base complexes. In an effort to best observe this correlation, we decided to examine the diagnostic upfield *H*C=N peaks and plot this data against the Pauling electronegativity values for the corresponding halides of the series (Figure 4-25).

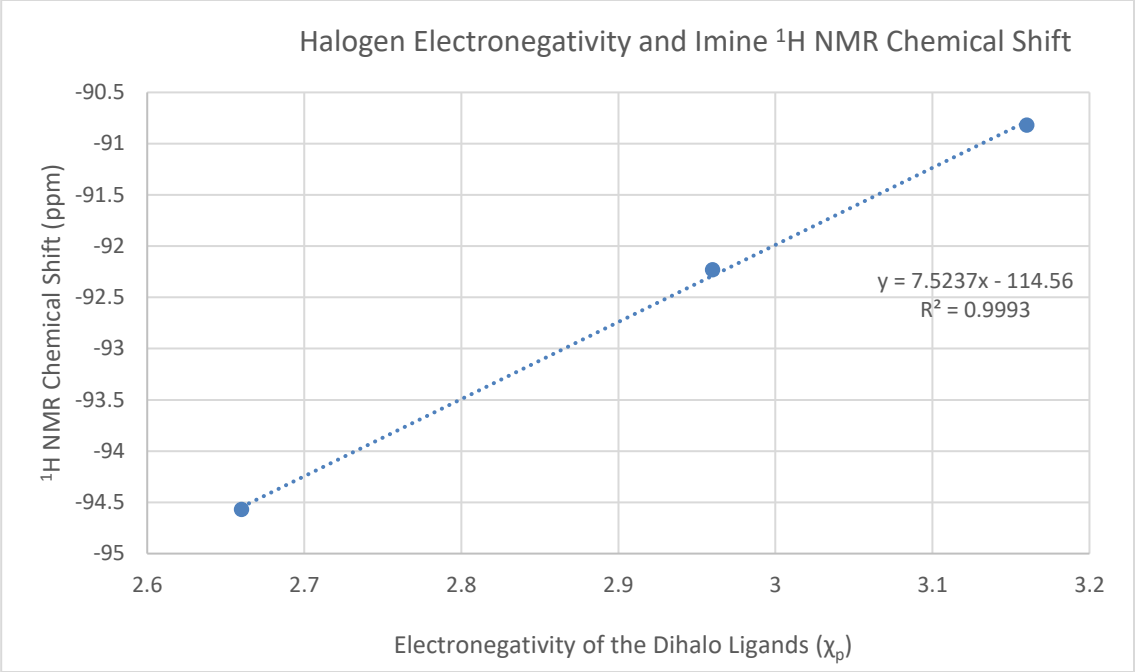


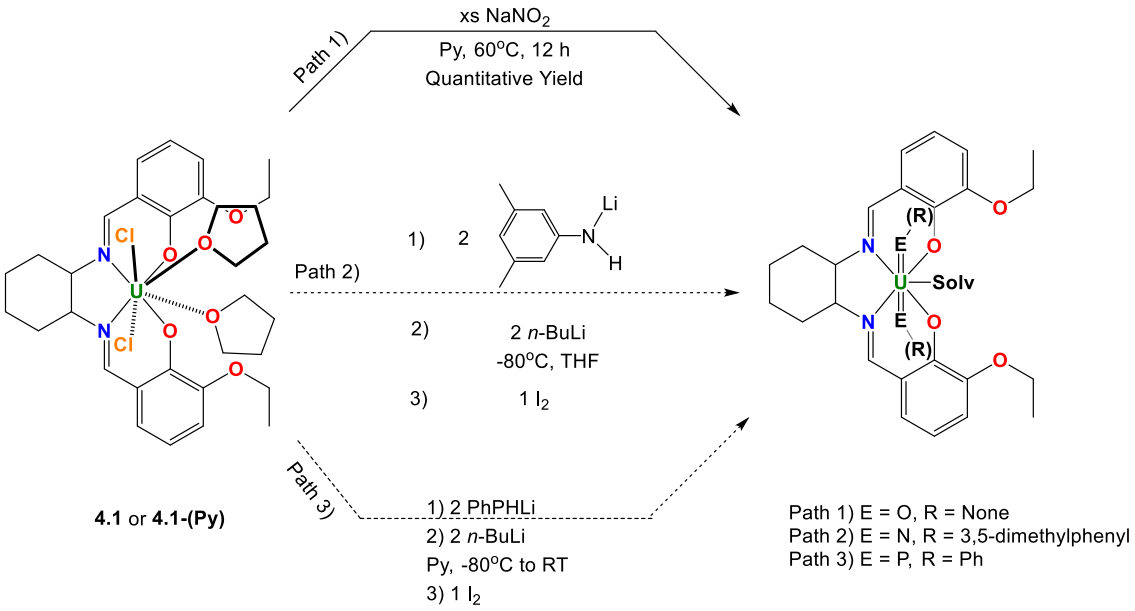
Figure 4-25: *^{1}H NMR chemical shifts of the diagnostic imine peaks in **4.1**, **4.8**, and **4.10** compared to the Pauling electronegativity value of the halides*

By plotting the ^{1}H NMR chemical shift data of the diagnostic Schiff base *H*C=N imine protons against the electronegativity values of the corresponding halides, we were able to see that there is a very strong correlation (R^2=0.9993) that exists between ^{1}H NMR chemical shift and halide electronegativity (Figure 4-25). The information gained from this study may prove useful in helping to predict the expected ^{1}H NMR chemical shifts for uranium complexes containing *trans* pseudo-halide ligands.

4.6: Attempts at generating [L]An=E functionalities via oxidative pathways

Through the isolation and characterization of complexes **4.3**-**4.9**, we were able to demonstrate the innocent behavior of the ancillary Schiff base ligand under a variety of different reaction conditions. In each of these cases, we were

able to show crystallographically and spectroscopically that the Schiff base C=N imine fragment remains intact and does not undergo reactivity at this site seen in some related systems. As a result, we sought to explore the generation of An=E functionalities through oxidative pathways with this ligand framework. as outlined in Scheme 4-7.



Scheme 4-7: *Oxidative pathways used to generate (R)E=U=E(R) functionalities*

As uranyl complexes supported by Schiff base ligands are well known,[60, 61] our first oxidation pathway targeted the isolation of a Schiff base uranyl species for ease of comparison. Recently, Schelter and coworkers disclosed that the nitrite anion (NO_2^-) can act as a one-electron oxidant to install the uranium oxo functionality through the elimination of NO (g).[62] Path 1 makes use of this transformation through the addition of excess $NaNO_2$ to a solution of compound **4.1** or **4.1-(Py)** in THF/Py. The resultant reaction mixture was heated to 60°C over the course of about 12 h. Upon isolation, it was found that $[L]U(O)_2(Py)$ (**4.11**) was generated in quantitative yield.[29] Red-orange crystals suitable for X-

ray diffraction were grown by means of slow evaporation from $CDCl_3$. To the best of our knowledge, this is the first reported conversion of a dichloro uranium(IV) complex to a uranyl species utilizing oxidation with $NaNO_2$. In the solid state, complex **4.11** is 7-coordinate and adopts a pseudo-pentagonal bipyramidal geometry and displays pseudo C_s symmetry in the solid state (Figure 4-26).

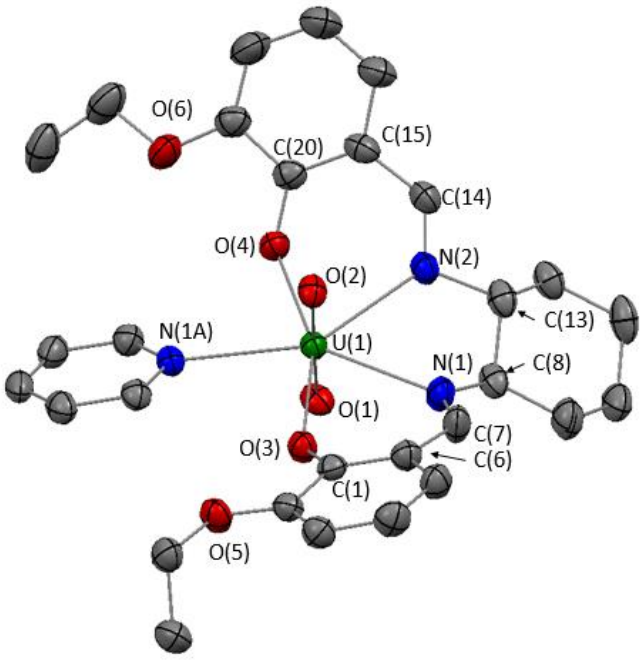


Figure 4-26: *ORTEP depiction of $[L]U(O)_2(Py)$ (**4.11**) with ellipsoids shown at 30% probability. Hydrogen atoms omitted for clarity.*

Table 4-9: *Selected bond lengths (Å) and angles (°) for* ***4.11***

Bond	Distance (Å)	Bond Angle	Angle (°)
U(1)-O(1)	1.786(3)	O(1)-U(1)-O(2)	178.67(14)
U(1)-O(2)	1.775(3)	O(1)-U(1)-O(3)	92.12(15)
U(1)-O(3)	2.259(3)	O(1)-U(1)-O(4)	90.89(15)
U(1)-O(4)	2.262(3)	O(1)-U(1)-N(1)	89.92(16)
U(1)-N(1)	2.549(4)	O(1)-U(1)-N(2)	91.81(14)
U(1)-N(2)	2.557(4)	O(1)-U(1)-N(1A)	89.70(14)
U(1)-N(1A)	2.609(4)	O(2)-U(1)-O(3)	88.14(14)
N(1)-C(7)	1.269(7)	O(2)-U(1)-O(4)	89.39(14)
N(2)-C(14)	1.284(7)	O(2)-U(1)-N(1)	88.96(15)
		O(2)-U(1)-N(2)	87.06(14)
		O(2)-U(1)-N(1A)	91.62(13)
		O(3)-U(1)-O(4)	156.39(12)
		O(3)-U(1)-N(1)	69.46(12)
		O(3)-U(1)-N(2)	132.90(12)
		O(3)-U(1)-N(1A)	79.03(12)
		O(4)-U(1)-N(1)	133.97(12)
		O(4)-U(1)-N(2)	70.35(12)
		O(4)-U(1)-N(1A)	77.58(12)
		N(1)-U(1)-N(2)	63.63(13)
		N(1)-U(1)-N(1A)	148.45(13)
		N(2)-U(1)-N(1A)	147.91(13)

Interestingly, the Schiff base U(1)-N(1) and U(1)-N(2) interactions (2.549(4) and 2.557(4) Å, respectively, are considerably shorter in complex **4.11** than in complex **4.1-(Py)**. Conversely, the U(1)-O(3) and U(1)-O(4) U-L bond distances of (2.259(3) and 2.262(3) Å, respectively, are substantially longer in complex **4.11** than the analogous bonds in complex **4.1-(Py)**. This can be largely attributed to the size difference of 8-coordinate U(IV) and the smaller 7-coordinate U(VI). As nitrogen is a better donor than oxygen, the more electron-deficient U(VI) center tries to maximize the U-N interaction, resulting in shorter the U-N bond distances for **4.11** than previously observed for complex **4.1-(Py)**. Additionally, as the U(VI) center is smaller than U(IV), the N_2O_2 binding environment of the Schiff base ligand deviates significantly from planarity in order

to find a suitable equilibrium geometry that optimizes electron donation from the nitrogen and oxygen atoms of the Schiff base ligand. This deviation from planarity of the N_2O_2 bonding environment causes the Schiff base ligand to create a “bowl” like shape that encompasses O(2) and leaves O(1) relatively exposed. As seen with all discrete uranyl complexes, the O(1)-U(1)-O(2) bond angle is effectively linear with a bond angle of 178.67(14)°.[20, 63, 64] The U=O bond distances for the uranyl complex (**4.11**) are 1.786(3) Å for U(1)-O(1) and 1.775(3) Å for U(1)-O(2), which are in good agreement with other reported uranyl U=O bond distances and – as expected due to the bond strengthening attributed to the inverse trans influence (ITI) – shorter than non-uranyl U=O bond distances.[20, 63, 64] Importantly, the Schiff base imine N(1)-C(7) and N(2)-C(14) bond distances of 1.269(7) and 1.284(7) Å, respectively, are in good agreement with other reported imine C=N distances, indicating that the Schiff base ligand remains innocent during metal based redox reactivity. In solution, complex **4.11** is unremarkable and displays a diamagnetic ^{1}H NMR spectrum as expected for a U(VI) complex with approximate C_{2v} symmetry in solution, as demonstrated by the simplicity of the ^{1}H NMR spectrum for this compound (Figure 4-27).

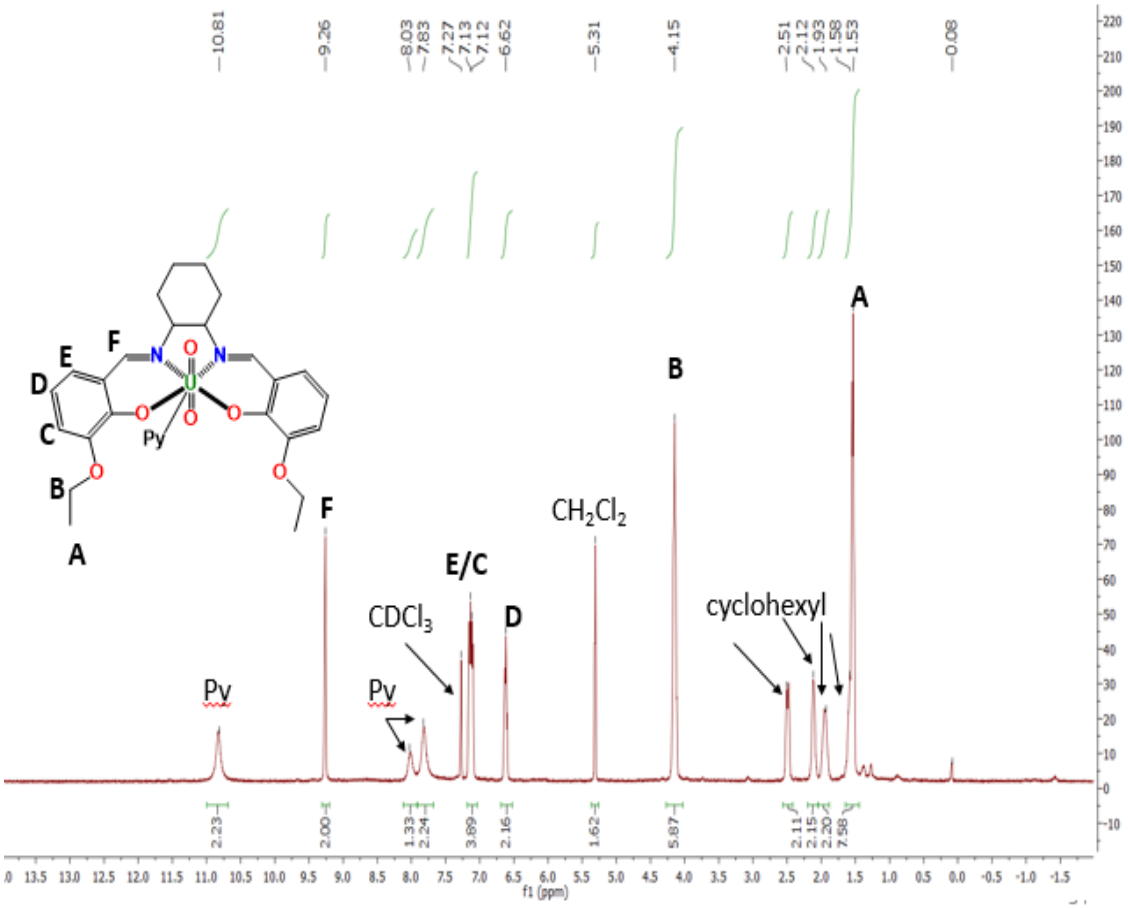


Figure 4-27: *300 MHz ^{1}H NMR spectrum for [L]U(O)$_2$(Py) (**4.11**) in $CDCl_3$ at 298 K*

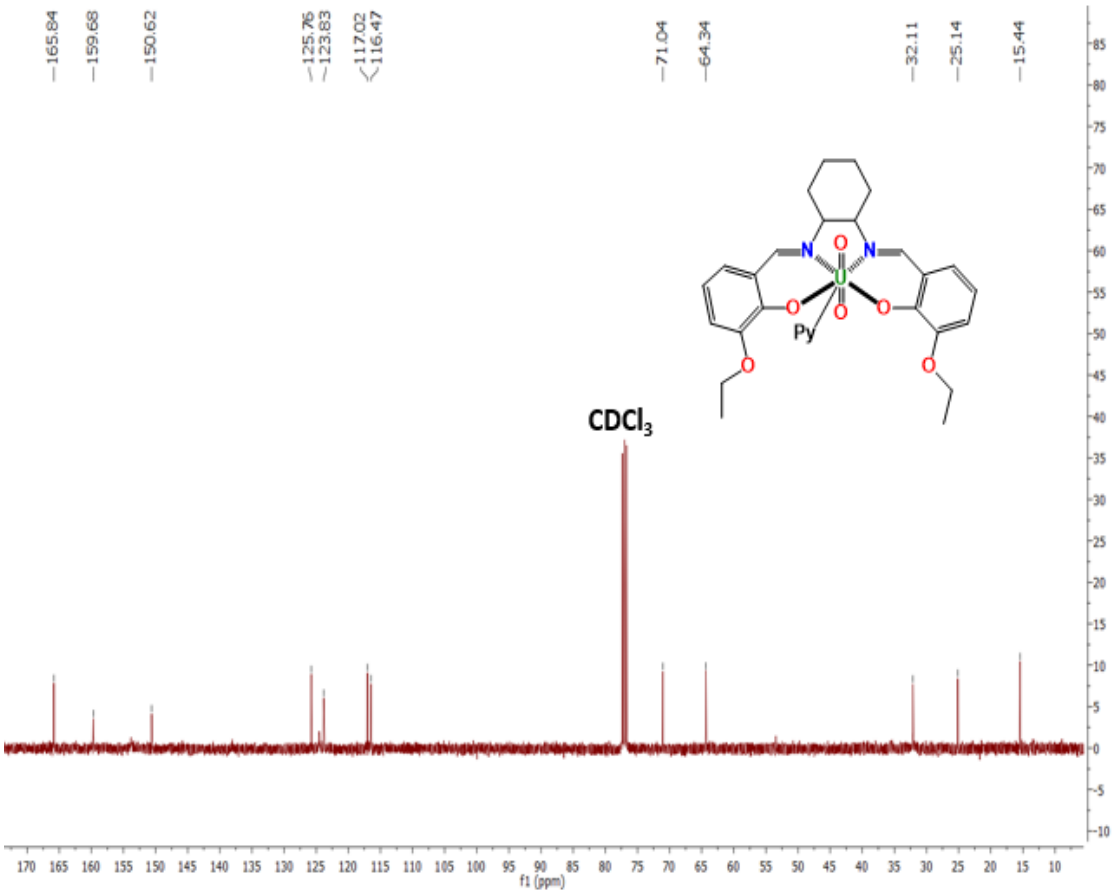


Figure 4-28: *100 MHz ^{13}C NMR spectrum of [L]U(O)$_2$(Py) (**4.11**) in $CDCl_3$ at 298 K*

The number of peaks in the ^{13}C NMR spectrum for complex **4.11** (Figure 4-28) is matches the number of unique carbon environments for a C_{2v} symmetric uranyl complex. The ^{1}H and ^{13}C NMR spectroscopic and X-ray diffraction data verify that complex **4.1-(Py)** is able to react with an excess of $NaNO_2$ to generate the uranyl species [L]U(O)$_2$(Py) (**4.11**) in high yields and high purity.[29] In an effort to generate additional X-U=O functionalities suitable for studying the inverse trans influence (ITI), we modified the reaction from Path 1 (Scheme 4-7) by adding only 1 equiv. of $NaNO_2$ in hopes of generating the *trans* Cl-U=O functionality. Unfortunately, the product from this reaction disproportionated to

generate an equivalent of complex **4.11** and complex **4.1-(Py)**. It should also be noted that the generation of the analogous [L]Th$(O)_2$(Py) species from complex **4.2** was not attempted, as thorium, unlike uranium, can only access a maximum oxidation state of +4.

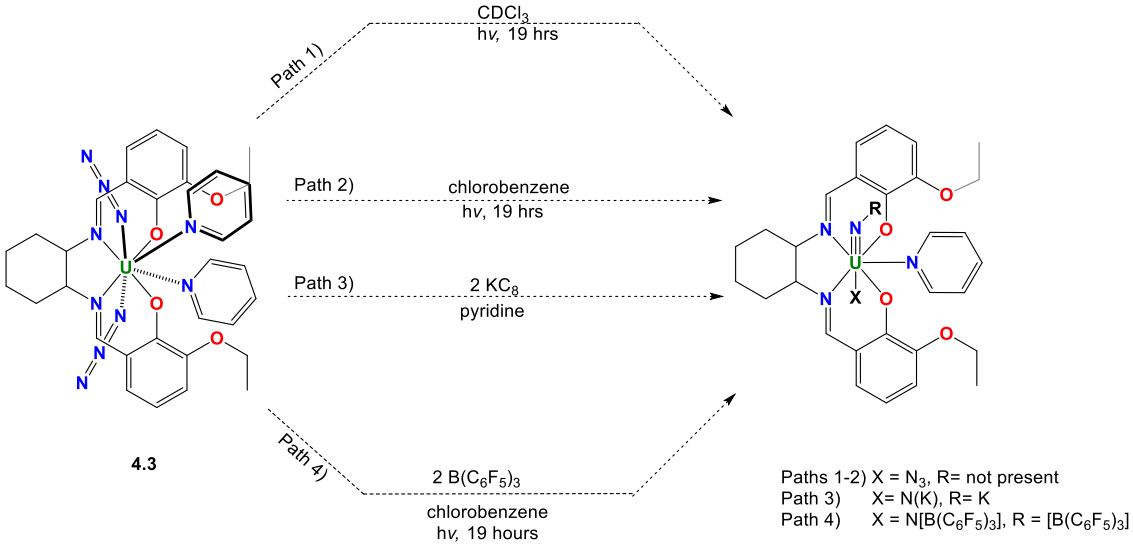
As the oxidation pathway to generate the U=O functionality was successful, we decided to explore the generation of additional U=E functionalities for use in studying the ITI. The next two oxidation pathways examined aimed to install either U=N(Ar) or U=P(Ar) functionalities, Paths 2 and 3, respectively. Each of these pathways utilized an identical three-step process for generating the desired U=E(Ar) functionality. The first step in this process was a salt metathesis reaction with complex **4.1** to install the U-E(H)(Ar) oxidation precursor functionality. This step involved the addition of either 2 equiv. of [Li][N(H)(3,5-$(CH_3)_2(C_6H_3)$] (Path 2) or [Li][P(H)(C_6H_5)] (Path 3) to generate the U-$(E(H)(Ar))_2$ oxidation precursor species. The second step of this process attempted to generate the desired U=E(Ar) functionality by deprotonating the U-E(H)(Ar) moieties with a strong base. Finally the third step of this process oxidized the desired U=E(R) containing complexes via a formal two electron oxidation using I_2. This would in turn remove any excess Li^+ from the complexes as LiI. Path 2 aimed to generate the bis(imido) Schiff base complex [L]U[=N(3,5-$(CH_3)_2(C_6H_3)$)]$_2$(Solv), which is a N=U=N uranyl analog for use in studying the inverse trans influence (ITI). We hoped that accessing this complex would help us understand how the magnitude of bond strengthening observed with strong *trans* U=E π-donors changes as the identity of E changes. Unfortunately, all

attempts to isolate and characterize the desired bis(imido) species were unsuccessful. Like Path 2, Path 3 aimed to access a similar P=U=P uranyl analog. This species was targeted for a number of reasons, the first of which was the fact that a uranium trans bis(phosphinidene) complex has never been accessed before. Aside from the synthetic novelty of the species, this moiety could provide additional information relevant to the ITI that would help us understand how the magnitude of bond strengthening observed with strong *trans* U=E π-donors changes as E changes. Additionally, accessing this P=U=P functionality affords the opportunity to inexpensively monitor changes to the U=P bond strength spectroscopically using ^{31}P NMR spectroscopy as changes are made to the system. This technique can be used to monitor the U=P bond strength by taking into account the correlation between phosphorous bond strength and the ^{31}P chemical shift tensor. Once an initial ^{31}P chemical shift is obtained for the P=U=P fragment, relative bond strength information can be obtained from any changes to the ^{31}P chemical shift tensor that occur after chemical perturbations are made to the P=U=P system. This information coupled with DFT calculations can provide insight into the magnitude of any changes in U=P bond strength that occur after a chemical perturbation is made to the P=U=P system. Unlike with U=O and U=N fragments, this spectroscopic technique to monitor U=E bond strength is only readily available for the U=P fragment, since ^{31}P is NMR active and 100% naturally abundant, unlike the most abundant isotopes of O and N. Despite repeated attempts to access this U=P functionality, all attempts to isolate and characterize a *trans* bis(phosphinidene) species of the

type [L]U[=P(Ph)]$_2$(Solv) were unsuccessful. Isolation of the desired *trans* bis(phosphinidene) species could have eluded us in part due to the poor hard-soft acid/base match of the hard U(VI) metal center and the softer RP^{2-} phosphinidene species, making the U=P bonds highly reactive and unstable. This is reflected by the low number of known uranium phosphinidene species and may be why each of these species have been observed with softer U(IV) centers.[65-67] Due to the possible stability problems with accessing the U(VI) U=P functionality, we abandoned our attempts to isolate the Schiff base supported *trans* bis(phosphinidene) species.

Since the technique of salt metathesis followed by deprotonation and oxidation to generate U=N and U=P functionalities (Scheme 4-7, Paths 2-3) were unsuccessful, we shifted our focus to complexes that contain the uranium nitride functionality (U≡N) and decided to explore their generation through alternate means (Scheme 4-8). This particular moiety was targeted as species containing this type of functionality have been strongly considered for use as Gen II, III and IV nuclear fuel sources, and, as such, are coveted industrial targets in the field of nuclear energy[68]. Uranium nitride species are desirable since they have been postulated to be a more accident-tolerant nuclear fuel source due to their higher thermal conductivity, melting point and fissile density than traditional MOX fuel sources.[69] Despite the interest in these uranium nitride materials as nuclear fuel sources, very little experimental data characterizing the U≡N fragment is currently available.[2, 70-72] In an effort to provide critical experimental data to the actinide

community, we attempted to isolate the U≡N fragment using a variety of methods, focusing on reduction and photochemical pathways. (Scheme 4-8).



Scheme 4-8: *Methods attempted to generate the uranium nitride functionality*

We first attempted to access the U≡N fragment by means of photochemical cleavage of the azido ligands of complex **4.3** in either $CDCl_3$ or chlorobenzene (Scheme 4-8, Paths 1 and 2, respectively). By exposing the azido ligands of complex **4.3** to UV light, we hoped that we could induce homolytic cleavage of an N-N bond within the azido ligand to give off N_2 gas and an generate the desired U≡N moiety as seen previously with an azido complex generated by Kiplinger and coworkers.[2] As complex **4.3** is readily soluble in chlorinated solvents, we decided to explore the photolysis of this complex in $CDCl_3$ and chlorobenzene. Although $CDCl_3$ can readily generate chlorine radicals under photolytic conditions that could potentially cause complex **4.3** to undergo unwanted side reactivity, this solvent was still chosen for Path 1 to enable monitoring by ^{1}H NMR spectroscopy. Interestingly, after running the reaction for 19 hours, the ^{1}H NMR spectrum for this reaction showed evidence of the

formation multiple products in solution. In an effort to better characterize these products, separation of these complexes was attempted through selective recrystallization by means of slow evaporation from $CDCl_3$ at room temperature. Upon analysis of the crystals by X-ray diffraction, three different species were found to be cocrystallized in roughly a 75:24:1 ratio. The chloro azido species $[L]U(Cl)(N_3)(Py)_2$ (**4.12**) was formed as the major product, making up roughly 75% of the material analyzed. The starting material (**4.3**) comprised more than 24% of the sample analyzed, and the desired nitride complex made up a negligible portion of the sample (about 1%). This result suggests that chlorine radicals were generated in $CDCl_3$ under photolytic conditions, which then reacted with complex **4.3** to generate $[L]U(Cl)(N_3)(Py)_2$ as the major product (Figure 4-29).

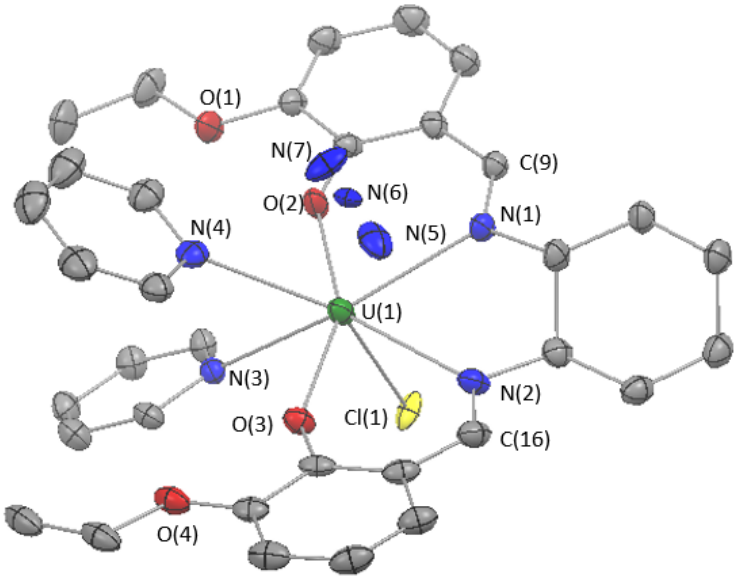


Figure 4-29: *ORTEP depiction of $[L]U(Cl)(N_3)(Py)_2$ (**4.12**), the major product of Path 1 (Scheme 4-8) with ellipsoids shown at 30% probability. Hydrogen atoms omitted for clarity.*

While solving the structure for complex **4.12**, it was found that the chlorido and azido ligands exhibited positional disorder. As a result, restraints on the positional and displacement parameters for these groups were required. A discussion related to the bond lengths and angles for this system will be omitted since the metrical data for this system is unreliable. Although this is the case, it can still be seen that 8-coordinate complex **4.12** is similar to both complexes **4.1** ($[L]U(Cl)_2(Py)_2$ and **4.3** $[L]U(N_3)_2(Py)_2$ and adopts a pseudo dodecahedral geometry in the solid state, with pseudo-C_s symmetry.

Since the desired uranium nitride product could not be isolated in any appreciable yield in Path 1, we altered our photochemical approach by using a solvent that is far less susceptible to forming chlorine radicals under photolytic conditions. Since formation of a phenyl radical is unfavorable, we used chlorobenzene as our solvent of choice for Path 2. Unfortunately, all attempts to isolate and characterize a uranium nitride product by this method proved unsuccessful.

Since photochemical cleavage methods proved to be unsuccessful for the isolation of a terminal uranium nitride complex, we determined that the Schiff base ancillary framework could not stabilize an unprotected terminal U≡N fragment. This is supported by Kiplinger and coworkers' finding that upon generating a terminal uranium nitride species, the nitride fragment rapidly underwent decomposition through C-H bond activation.[2] In an effort to prevent possible insertion behavior of the nitride with our system, we employed strategies to generate the U≡N fragment in a sterically and electronically protected way. In

an effort to protect the nitride fragment, we attempted to reduce the azido ligands of complex **4.3** with 1 equiv. of KC_8, a strong 1-electron reducing agent (Scheme 4-8, Path 3). It was anticipated that KC_8 would induce cleavage of an N-N bond of the azido ligand to generate the U≡N-K fragment, giving off N_2 gas as a byproduct. Through coordination of the nitride to the potassium counterion, it was hoped that the U≡N bond would not participate in unwanted side reactivity. Unfortunately, all attempts to isolate and characterize a Schiff base supported uranium nitride species was unsuccessful. As this was the case, we determined that it was possible that either KC_8 was not inducing N-N bond cleavage to form the uranium nitride species as intended or the potassium counterion is not suitably protecting the nitride fragment, as found for a terminal uranium nitride species generated by Liddle and coworkers.[70]

Due to the inability to access a uranium nitride species through reductive methods, we decided to try to access the uranium nitride functionality again through photochemical methods. This time, however, we added a borane to the reaction mixture in hopes of generating a nitrido-borane adduct species that could form through coordination of the nitride nitrogen lone pair to the neutral borane species. Forming such a nitride-borane adduct species would sterically protect the U≡N fragment and prevent it from engaging in unwanted side reactivity. In order to ensure a strong interaction between the nitride nitrogen lone pair and the borane species, we utilized a borane that contained strong electron withdrawing groups, $B(C_6F_5)_3$. The electron withdrawing groups of the borane would strengthen the nitride-borane interaction, as these groups would strengthen lone

pair donation to the borane through induction. Unfortunately, even with the inclusion of a borane species during photolysis, isolation of a Schiff-base-supported terminal nitride complex was unsuccessful. With this method failing to yield the desired functionality, we concluded that the Schiff base ligand framework is unable to sterically protect a nitride species.

4.7: Concluding remarks

The Schiff base compound (±)-*trans*-6,6′-diethoxy-2,2′-[cyclohexane-1,2-diylbis(nitrilomethanylylidene)]diphenol was used as an ancillary ligand to support low and high oxidation state actinide metal centers.[29] This particular framework was used in an effort to find a redox-innocent ancillary ligand framework that was also resistant to undergoing unwanted side reactivity like disproportionation, ligand exchange and C-H activation such that chemistry could be performed at the actinide metal centers to generate An=E multiple bond functionalities. Through our initial investigations with this ancillary ligand framework we determined that the Schiff base framework could support pseudo-*trans* dichloro U(IV) and Th(IV) species of the general type [L]An$(Cl)_2(Solv)_2$, complexes **4.1**, **4.2**, **4.1-(Py)** and **4.2-(Py)**. In an effort to establish the redox innocent behavior of the Schiff base ligand framework before generating the desired An=E functionalities, these dichloro Schiff base actinide species were exposed to different nucleophiles to see if desired salt metathesis reactivity would occur as intended. It was found that the dichloro Schiff base complexes [L]An$(Cl)_2(Solv)_2$ reacted cleanly with an excess of NaN_3 at 80°C for several days

to generate bis(azido) actinide complexes of the type [L]An$(N_3)_2(Py)_2$ (complexes **4.3** and **4.4**). Additionally, when dichloro Schiff base complexes **4.1** and **4.2** were exposed to stronger carbon nucleophiles like NaCp, salt metathesis reactivity occurred as intended to generate the first neutral uranium linear metallocene [L]U$(Cp)_2$(1,4-dioxane) (**4.6**) and the first ever linear thorium metallocene [L]Th$(Cp)_2$(1,4-dioxane) (**4.7**). Even in the presence of these strong carbon nucleophiles, the Schiff base ligand framework remains redox innocent and allows desired chemistry to occur at the actinide centers. It was also found that complexes **4.1** and **4.2** readily undergo σ-bond metathesis with Me_3Si-Br to generate complexes of the type [L]An$(Br)_2(Py)_2$ (**4.8** and **4.9**) in good yields. Attempts at isolating the analogous [L]U$(F)_2(Py)_2$ complex were unsuccessful; however, the diiodo complex [L]U$(I)_2(THF)_2$ (**4.10**) was isolated and characterized spectroscopically. Upon comparing the ^{1}H NMR spectra of the series of dihalo Schiff base uranium complexes, it was determined that a very strong correlation exists between ^{1}H NMR chemical shift of the imine protons and the electronegativity of the halide ligands (R^2= 0.9993). Additionally, the solubility of the dihalo uranium complexes in chlorinated solvents was found to decrease as the size of the halogen atom increased: ([L]U$(Cl)_2(THF)_2$ > ([L]U$(Br)_2(THF)_2$ > ([L]U$(I)_2(THF)_2$).

Generation of uranium-element multiple bond functionalities was also explored. During these investigations, it was found that complex **4.1** can be readily oxidized to the uranyl complex [L]U$(O)_2$(Py) (**4.11**) upon reaction with excess $NaNO_2$. To the best of our knowledge, this is the first reported example

where a dichloro uranium complex was converted to a uranyl species in one step using $NaNO_2$ as an oxidant. Attempts at generating U=N(Ar) and U=P(Ar) functionalities for use in studying the ITI was also attempted. Unfortunately, all attempts to isolate Schiff base complexes that bared these functionalities were unsuccessful. Investigations into the generation of a U≡N terminal nitride moiety were also explored in an effort to better understand the main functionality proposed for next-generation ceramic nuclear fuel. Photochemical cleavage of the azido ligands from complex **4.3** was investigated, and upon exposure of complex **4.3** to UV light for 19 hours in $CDCl_3$, an unwanted side product, $[L]U(Cl)(N_3)(Py)_2$ (**4.12**), was isolated as the major product from the reaction instead of generating the desired U≡N functionality. Isolation of **4.12** showed that complex **4.3** was susceptible to unwanted side reactivity, where a chloride radical is generated and substitutes an azido ligand from complex **4.3**. Further investigations into photochemically generating the U≡N functionality using solvents that are less likely to form chlorine radicals proved to be unfruitful, and a Schiff-base-supported terminal uranium nitride complex could not be isolated. Similarly, attempts to isolate the actinide nitride functionality, using methods to sterically protect the resultant terminal nitride fragment were employed, but we were unsuccessful.

Although isolation of U=N, U=P and U≡N functionalities was unsuccessful, we demonstrated that the ancillary Schiff base ligand framework is readily able to support oxidation chemistry, salt metathesis and σ-bond metathesis reactivity at the actinide metal centers. Additionally, we were able to confirm

crystallographically and spectroscopically that this ancillary ligand framework remains innocent under a variety of different reaction conditions, thereby allowing for desired reactivity to occur at the actinide metal centers. The behavior of this Schiff base framework differs significantly from our previously studied κ^1-anilido and κ^3-BDPP ligand frameworks. Since this Schiff base ligand framework remained innocent in the presence of strong carbon nucleophiles and complexes that made use of this scaffold did not generally undergo unwanted side reactivity, we believe that this κ^4-framework is a viable candidate for the continued exploration of the generation of An=E functionalities.

4.8: Experimental

4.8.1: General Experimental Procedures

All experiments were performed under an atmosphere of dry N_2 in a VAC Atmospheres dry box. Solvents were purified using the appropriate VAC Atmospheres solvent purifier or dried over sodium benzophenone ketyl and distilled under an atmosphere of dry N_2. Solvents purified by these methods were subsequently degassed using successive freeze-pump-thaw methods, brought into the dry box without exposure to air, and stored over activated 4 Å molecular sieves. Celite was activated and dried by heating under high vacuum (approx. 0.3 mmHg) at > 200°C overnight. Deuterated NMR solvents, C_6D_6 and $CDCl_3$, were purchased from Cambridge Isotope Laboratories, degassed using freeze-pump-thaw cycles and stored over 4 Å molecular sieves. The Schiff base ligand $[L]H_2$,[5] UCl_4[73] and $ThCl_4(DME)_2$[74] were synthesized by reported methods. ^1H

NMR spectra were recorded using Varian VNMRS spectrometers operating at 300 MHz or 400 MHz for ^{1}H at room temperature in $CDCl_3$ unless otherwise specified. All chemical shifts herein are reported with reference to residual solvent peaks: δ 7.27 for $CDCl_3$ or δ 7.16 for C_6D_6. All infrared spectra were collected using an ATR adapter on a Thermo Scientific Nicolet 6700 FT-IR instrument at room temperature. Microanalyses were performed by Atlantic Microlabs in Norcross, GA.

*4.8.2: Synthesis of (L)$UCl_2(THF)_2$ (**4.1**)*

Synthesis of K_2(L) generated for *in situ* use

To a 20 mL scintillation vial charged with 14 mL of THF and a small stir bar, (0.250 g, 0.609 mmol) of the racemate of (±)-*trans*-6,6′-Diethoxy-2,2′-[cyclohexane-1,2-diylbis(nitrilomethanylylidene)]diphenol, [L]H_2 was added. The resulting clear yellow solution was allowed to mix thoroughly, after which 2 equiv of KO^tBu (0.136 g, 1.21 mmol) was added to the solution as a solid. The solution immediately became opaque, and a color change to a yellow-green was noted. The resulting solution was allowed to stir for 1.5 h prior to use in subsequent chemistry.

Synthesis of (L)$UCl_2(THF)_2$ (**4.1**)

To a 20-mL scintillation vial charged with 4 mL of THF and a small stir bar, (0.231 g, 0.608 mmol) of UCl_4 was added. The clear green solution was allowed to mix thoroughly, after which the solution of K_2[L] (*vide infra*) was added

dropwise over 5 min. The resulting solution turned dark brown and then became a cloudy, golden-yellow suspension during the addition of the dipotassium salt solution. The cloudy, golden-yellow suspension was allowed to stir overnight (approx. 12 h). Volatiles were then removed under vacuum, and the crude product was extracted with dichloromethane (about 75 mL). The extraction products were then filtered over a bed of Celite on a 30-mL medium porosity frit under vacuum. The filtrate was then concentrated to dryness *in vacuo* and the product was isolated as a yellow powder. **Yield: 0.423 g, 81%**. The product was recrystallized from pyridine over the course of 2 weeks at room temperature. ^{1}H NMR (300 MHz, $CDCl_3$, 298 K): δ = 45.23 (2H), 41.73 (2H), 38.94 (2H), 28.30 (2H), 24.59 (2H), 23.97 (2H), 5.56 (6H, $OCH_2C\mathit{H_3}$), -10.29 (4H, THF), -11.19 (2H), -12.11 (2H), -15.58 (4H, THF), -19.93 (2H), -22.27 (2H), -89.80 (2H, *H*C=N). IR (cm^{-1}): 2973 (C-H), 2927 (C-H), 1614 (C=N), 1598 (C=C). Elemental analysis of $(L)UCl_2(THF)_2 \bullet CH_2Cl_2$: Theoretical C: 41.87, H: 4.90, N: 2.96; Actual: C: 42.30, H: 5.01, N: 3.17.

*4.8.3: Synthesis of $(L)UCl_2(Py)_2$ (**4.1-(Py)**)*

To a 20-mL scintillation vial charged with 8 mL of pyridine and a small stir bar, (0.250 g, 0.608 mmol) of $[L]H_2$ was added. The clear yellow solution was allowed to mix thoroughly, after which 2 equiv. of KO^{t}Bu powder was added. The solution became cloudy upon addition of the KO^{t}Bu, and was allowed to stir for 1 h. To a separate 20-mL scintillation vial charged with 3 mL of THF, 4 mL of Py and a small stir bar, (0.231 g, 0.608 mmol) of UCl_4 was added. The green solution

was allowed to mix thoroughly, after which the solution of K_2[L] prepared separately was added dropwise over 5 min. During the addition of K_2[L], the solution turned cloudy yellow-green, and the resulting mixture was allowed to stir overnight (approx. 18 h). Volatiles were removed *in vacuo* to afford a yellow-green powder. The crude product was then extracted with dichloromethane (~50 mL) and filtered over a bed of Celite on a medium porosity frit. The resulting yellow solution was collected in a 125-mL side arm flask and the volatiles were removed *in vacuo*, providing a yellow-green powder. **Yield: 0.423 g, 79%**. ^{1}H NMR (400 MHz, $CDCl_3$, 298 K) : δ 49.77 (2H), 44.54 (2H), 42.73 (2H), 31.14 (2H), 27.02 (2H), 25.02 (2H), 5.56 (6H, $OCH_2C\mathit{H_3}$), 0.47 (4H, Py), -4.37 (1H, Py), -7.68 (2H, Py), -11.44 (2H), -12.85 (2H), -20.51 (2H), -22.29 (2H), -90.82 (2H, *H*C=N).

*4.8.4: Synthesis of (L)$ThCl_2(THF)_2$ (**4.2**)*

A solution of K_2(L) was generated *in situ* by the method above using (0.200 g, 0.487 mmol) of the racemate of (L)H_2 and (0.109 g, 0.971 mmol) of KO^{t}Bu. To a 20-mL scintillation vial charged with 5 mL of THF and a small stir bar, (0.270 g, 0.487 mmol) of $ThCl_4(DME)_2$ was added. The clear, colorless solution was allowed to mix thoroughly, after which the solution of K_2(L) was added dropwise over 5 min. The combined solution instantly turned cloudy and yellow upon addition of the dipotassium salt. The resulting suspension was allowed to stir overnight (approx. 12 h), after which volatiles were removed *in vacuo*. The crude product was extracted with dicholormethane (~75 mL) and filtered over a bed of Celite on a 30-mL medium-porosity frit. Volatiles were removed *in vacuo* to afford

a yellow powder. **Yield: 0.302 g, 72%**. The yellow powder was recrystallized from pyridine over 2 weeks at room temperature. ^{1}H NMR (400 MHz, D_5-Py, 298 K): δ = 8.70 (s, 2H, *H*C=N), 7.35 (d, 2H, $^{3}J_{HH}$ = 8 Hz, Ar-*H*), 7.20 (d, 2H, $^{3}J_{HH}$ = 8 Hz, Ar-*H*), 6.93 (t, 2H, $^{3}J_{HH}$ = 8 Hz, Ar-*H*), 4.66 (2H, m, cyclohexyl), 4.04 (4H, q, ^{3}J = 7 Hz, OC*H*$_2$CH$_3$), 2.25 (2H, m, cyclohexyl), 1.76 (2H, m, cyclohexyl), 1.40 (t, 6H, $^{3}J_{HH}$ = 8Hz, OCH$_2$C*H*$_3$), 1.17 (2H, m, cyclohexyl). ^{13}C NMR (100 MHz, D_5-Py, 298 K): δ = 163.41 (*C*=N), 152.76 (Ar-*C*), 149.10 (Ar-*C*), 127.32 (Ar-*C*), 125.00 (Ar-*C*), 117.48 (Ar-*C*), 115.98 (Ar-*C*), 67.76 (cyclohexyl), 63.51 (O*C*H$_2$CH$_3$), 30.50 (cyclohexyl), 24.66 (cyclohexyl), 15.03 (OCH$_2$*C*H$_3$). IR (cm^{-1}): 2973 (C-H), 2928 (C-H), 1611 (C=N), 1561 (C=C). Elemental analysis of (L)ThCl$_2$(THF)$_2$•(1.5 CH$_2$Cl$_2$): Theoretical: C: 41.29, H: 4.79, N: 2.83; Actual: C: 41.21, H:4.80, N: 3.27.

*4.8.5: Synthesis of (L)U(N$_3$)$_2$(Py)$_2$ (**4.3**)*

To a 20-mL scintillation vial charged with 8 mL of pyridine and a small stir bar, (0.115 g, 0.133 mmol) of (L)UCl$_2$(THF)$_2$ (**4.1**) was added. The resulting clear yellow-green solution was allowed to mix thoroughly and was heated to 70 °C, after which 6 equiv. of NaN$_3$ (0.053 g, 0.800 mmol) was added. No immediate color changed was observed, but after 24 h the solution changed color from yellow-green to dark amber. The resulting solution was allowed to stir for 4 days, after which volatiles were removed under vacuum. The crude product was extracted with dichloromethane and filtered over a bed of Celite in a Pasteur pipette to afford a clear, amber solution. Volatiles were removed under vacuum to yield a pale-brown solid. The resulting solid was recrystallized slowly from

dichloromethane, and dark brown crystals were afforded within 24 h. **Yield 0.072 g, 61%**. ^{1}H NMR (300 MHz, $CDCl_3$, 298 K): δ = 49.43 (2H), 42.37 (2H) ,40.25 (2H), 29.63 (2H), 26.20 (2H), 24.35 (2H), 5.32 (6H, $OCH_2C\mathit{H_3}$), -5.51 (1H), -10.95 (2H), -11.87 (2H), -19.66 (2H), -22.04 (2H), -86.81 (2H, *H*CN). IR (cm^{-1}): 2973 (C-H), 2055 (N_3), 1611 (C=N), 1599 (C=C). Elemental analysis of $(L)U(N_3)_2(Py)_2$•(1.5 Py, 1 CH_2Cl_2): Theoretical C: 46.73, H: 4.38, N: 14.75; Actual: C: 46.93, H: 4.64, N: 14.27.

*4.8.6 Synthesis of $(L)Th(N_3)_2(Py)_2$ (**4.4**)*

To a 20-mL scintillation vial charged with 10 mL of pyridine and 4 mL of THF, (0.075 g, 0.088 mmol) of $(L)ThCl_2(THF)_2$ (**4.2**) was added. The yellow, translucent solution was allowed to mix thoroughly, after which approximately 8 equiv. of NaN_3 (0.046 g, 0.701 mmol) was added. The solution was heated to 80°C and stirred for 4 days. The cloudy, yellow suspension was filtered over Celite to give a pale-yellow solution and volatiles were removed *in vacuo* to afford a yellow solid. The crude product was then extracted with dichloromethane and filtered over Celite a second time, and volatiles were removed *in vacuo*. **Yield: 0.063 g, 82%**. ^{1}H NMR (400 MHz, D_5-Py, 298 K): δ = 8.85 (s, 2H, *H*C=N), 7.36 (d, 2H, $^{3}J_{HH}$ = 8Hz, Ar-*H*), 7.18 (d, 2H, $^{3}J_{HH}$ = 8Hz, Ar-*H*), 6.92 (t, 2H, $^{3}J_{HH}$ = 8 Hz, Ar-*H*), 4.28 (m, 2H, cyclohexyl), 4.04 (q, 4H, $^{3}J_{HH}$ = 8Hz, $OC\mathit{H_2}CH_3$), 2.36 (m, 2H, cyclohexyl), 1.77 (2H, m, cyclohexyl), 1.38 (m, 2H, cyclohexyl), 1.33 (t, 6H, $^{3}J_{HH}$ = 7 Hz, $OCH_2C\mathit{H_3}$). ^{13}C NMR (100 MHz, D_5-Py, 298 K): δ = 163.94 (*C*=N), 152.75 (Ar-*C*), 127.37 (Ar-*C*), 124.49 (Ar-*C*), 117.45 (Ar-*C*), 116.36 (Ar-*C*), 114.71 (Ar-

C), 68.32 (cyclohexyl), 63.62 (O*C*H_2CH_3), 30.86 (cyclohexyl), 24.79 (cyclohexyl), 15.01 (OCH_2*C*H_3). IR (cm^{-1}): 2930 (C-H), 2061 (N_3), 1603 (C=N), 1558 (C=C). Elemental analysis of (L)Th$(N_3)_2(Py)_2$•(1.5 CH_2Cl_2, 0.5 Py): Theoretical: C: 43.48, H: 4.18, N: 14.01; Actual: C: 43.46, H: 4.42, N: 13.69.

4.8.7: Synthesis of [L]U(Cp)(Cl)(1,4-dioxane) (**4.5**)*

To a 20-mL scintillation vial charged with 10 mL of 1,4-dioxane, 4 mL of pyridine and a small stir bar, (0.101 g, 0.115 mmol) [L]U$(Cl)_2(Py)_2$ (**4.1-(Py)**) was added. The yellow-brown mixture was allowed to mix thoroughly, where then (0.040 g, 0.231 mmol) of K[Cp*] was added. The reaction mixture was then heated to 60°C and allowed to stir at this temperature overnight (approx. 18 h), during which the resulting solution became dark red in color. Volatiles were then removed under vacuum, and the crude product was extracted with benzene. The extraction products were then filtered over a bed of Celite in a Pasteur pipette. Volatiles were removed under vacuum at 65°C to afford a red-brown powder. **Yield: 0.043 g, 36%.** Crystals suitable for X-ray diffraction were afforded through slow evaporation from 1,4-dioxane at room temperature. ^{1}H NMR (300 MHz, C_6D_6, 298 K): δ = 49.48 (1H), 38.78 (1H), 37.48 (1H), 36.06 (1H), 34.81 (1H), 32.54 (1H), 26.56 (1H), 25.56 (1H), 25.06 (1H), 23.80 (1H), 22.80 (1H), 18.40 (1H), 8.37 (3H, OCH_2C*H*$_3$), 5.97 (3H, OCH_2C*H*$_3$), 1.68 (1H), 1.16 (1H), -0.20 (15H, $C_5(C$*H*$_3)_5$), -4.00 (2H, O*C*H_2CH_3), -9.85 (2H, O*C*H_2CH_3), -11.03 (1H), -13.32 (1H), -16.76 (1H), -19.28 (1H), -19.94 (1H), -25.33 (1H), -59.49 (1H, *H*C=N), -

95.54 (1H, *H*C=N). Elemental analysis of (L)U(Cp)$_2$(1,4-dioxane)•2(1,4-dioxane): Theoretical: C: 51.09, H: 6.24, N: 2.60; Actual: C:51.03, H:5.96, N: 3.01

*4.8.8: Synthesis of [L]U(Cp)$_2$(1,4-dioxane) (**4.6**)*

To a 20-mL scintillation vial charged with 8 of mL 1,4-dioxane and a small stir bar, (0.075 g, 0.087 mmol) [L]U(Cl)$_2$(THF)$_2$ (**4.1**) was added. The yellow-brown reaction mixture was allowed to mix thoroughly, where then (0.10 mL, 0.174 mmol) of a 2.25 M NaCp solution in THF was added. The reaction mixture turned transparent and red instantly upon addition of the NaCp solution. The resulting reaction mixture was heated to 70°C and allowed to stir overnight (approx. 18 h). [L]U(Cp)$_2$(1,4-dioxane) was selectively recrystallized from the reaction mixture through slow evaporation. **Yield: 0.059 g, 78%**. Elemental analysis of [L]U(Cp)$_2$(1,4-dioxane)$_2$•1.5(KCl): Theoretical: C: 46.73, H: 4.75, N: 2.87; Actual: C: 47.16, H: 4.87, N: 3.11.

*4.8.9: Synthesis of [L]Th(Cp)$_2$(1,4-dioxane) (**4.7**)*

To a 20-mL scintillation vial charged with 10 mL of 1,4-dioxane and a small stir bar, (0.150 g, 0.175 mmol) [L]Th(Cl)$_2$(THF)$_2$ (**4.2**) was added. The opaque, yellow reaction mixture was allowed to mix thoroughly, where then (0.18 mL, 0.405 mmol) of a 2.25 M NaCp solution in THF was added. Upon addition of the NaCp solution, the reaction mixture became translucent but remained yellow. The resulting solution was heated to 70°C and allowed to stir for 6 days. [L]Th(Cp)$_2$(1,4-dioxane) was selectively recrystallized from the reaction mixture

through slow evaporation. **Yield: 0.132 g, 88%**. ^{1}H NMR (400 MHz, C_6D_6, 298 K): δ = 7.95 (s, 2H, *H*C=N), 6.94 (d, $^{3}J_{HH}$ = 8 Hz, 2H, Ar-*H*), 6.80 (d, $^{3}J_{HH}$ = 8 Hz, 2H, Ar-*H*), 6.71 (t, $^{3}J_{HH}$ = 8 Hz, 2H, Ar-*H*), 6.07 (s, 10H, Cp-*H*), 3.62 (m, 4H, OC*H*$_2$CH$_3$), 3.38 (m, 2H, cyclohexyl), 1.83 (m, 2H, cyclohexyl), 1.49 (m, 2H, cyclohexyl), 1.36 (m, 2H, cyclohexyl), 1.05 (t, $^{3}J_{HH}$ = 8 Hz, OCH$_2$C*H*$_3$), 0.81 (m, 2H, cyclohexyl). ^{13}C NMR (100 MHz, D_5-pyridine, 298 K): δ = 165.46 (H*C*=N), 160.87 (Ar-*C*), 157.17 (Ar-*C*), 133.27 (Ar-*C*), 132.42 (Ar-*C*), 127.66 (Ar-*C*), 125.93 (Ar-*C*), 114.21 (cyclohexyl), 113.27 (cyclohexyl), 111.98 (Cp-*C*), 63.61 (cyclohexyl), 41.61 (O*C*H$_2$CH$_3$), 15.67 (OCH$_2$*C*H$_3$). Elemental analysis of [L]Th(Cp)$_2$(1,4-dioxane)•1.5(KCl): Theoretical: C: 47.02, H: 4.78, N: 2.89; Actual: C: 46.88, H: 4.88, N: 3.30.

*4.8.10: Synthesis of [L]U(Br)$_2$(Py)$_2$ (**4.8**)*

To a 20-mL scintillation vial charged with 10 mL of pyridine and a small stir bar, (0.105 g, 0.126 mmol of [L]U(Cl)$_2$(THF)$_2$ (**4.1**) was added. The yellow slurry was allowed to mix thoroughly, where then (0.076 g, 0.487 mmol) of Me$_3$Si-Br was added dropwise via syringe. The resultant reaction mixture was allowed to stir overnight. Volatiles were removed under vacuum to afford a green solid. **Yield: 0.092 g, 79%**. Crystals suitable for X-ray diffraction were afforded through slow evaporation from chlorobenzene at room temperature over several days. ^{1}H NMR (300 MHz, $CDCl_3$, 298 K): δ = 53.34 (2H), 46.17 (2H), 44.38 (2H), 32.00 (2H), 27.66 (2H), 25.69 (2H), 0.31 (6H, OCH$_2$C*H*$_3$), -11.90 (2H), -13.44 (2H), -21.23 (2H), -23.04 (2H), -92.23 (2H, *H*C=N).

*4.8.11: Synthesis of [L]Th(Br)$_2$(Py)$_2$ (**4.9**)*

To a 20-mL scintillation vial charged with 8 mL of pyridine and small stir bar, (0.085g, 0.0977 mmol) [L]Th(Cl)$_2$(Py)$_2$ (**4.2-(Py)**) was added. The yellow slurry was allowed to mix thoroughly, where then (0.060g, 0.391 mmol) of Me$_3$Si-Br was added dropwise via syringe. The resultant reaction mixture was then heated to 60°C and allowed to stir for 3 days, and the reaction mixture then became an opaque yellow color. Volatiles were removed under vacuum at 65°C and a pale-yellow powder was afforded. **Yield: 0.065 g, 69%**. ^{1}H NMR (400 MHz, CDCl$_3$, 298 K): δ = 8.59 (s, 2H, *H*C=N), 7.07 (d, 2H, $^3J_{HH}$ = 8 Hz, Ar-*H*), 7.03 (d, 2H, $^3J_{HH}$ = 8 Hz, Ar-*H*), 6.79 (t, 2H, $^3J_{HH}$ = 8 Hz, Ar-*H*), 4.60 (m, 2H, cyclohexyl), 4.13 (q, 4H, $^3J_{HH}$ = 8 Hz, OC*H$_2$*CH$_3$), 2.58 (m, 2H, cyclohexyl), 2.09 (m, 2H, cyclohexyl), 1.73 (m, 2H, cyclohexyl), 1.46 (t, 6H, $^3J_{HH}$ = 8 Hz, OCH$_2$C*H$_3$*), 0.88 (m, 2H, cyclohexyl). ^{13}C NMR (100 MHz, CDCl$_3$, 298 K) δ = 163.40 (H*C*=N), 148.46 (Ar-*C*), 128.58 (Ar-*C*), 127.14 (Ar-*C*), 124.95 (Ar-*C*), 117.51 (Ar-*C*), 115.55 (Ar-*C*), 109.94 (cyclohexyl), 29.68 (cyclohexyl), 24.73 (O*C*H$_2$CH$_3$), 15.25 (OCH$_2$*C*H$_3$).

*4.8.12: Synthesis of [L]U(I)$_2$(THF)$_2$ (**4.10**)*

To a 20-mL scintillation vial charged with 6 mL of THF and a small stir bar, (0.564 g, 0.617 mmol) of UI$_4$(1,4-dioxane)$_2$ was added. The clear, red solution was allowed to mix thoroughly, where then a solution containing 1 equiv. (0.298 g, 0.617 mmol) of the [K]$_2$[L] proligand in 12 mL of THF was added slowly over the course of 5 min. For preparation, of [K]$_2$[L] see above in preparation of

complex **4.1**. The resultant solution became cloudy and yellow upon addition of the proligand solution. The reaction mixture was allowed to stir for 48 h at room temperature. Volatiles were removed under vacuum. The crude product was extracted with dicholormethane (~50 mL) and filtered over a bed of Celite in a medium-porosity frit. Volatiles were again removed under vacuum to afford a yellow-orange powder. **Yield: 0.015 g, 2%**. ^{1}H NMR (300 MHz, $CDCl_3$, 298 K): δ = 52.38 (2H), 46.41 (2H), 44.17 (2H), 31.25 (2H), 26.80 (2H), 25.78 (2H), 5.36 (6H, $OCH_2C\mathit{H_3}$), -6.23 (16H, THF), -12.17 (2H), -13.72 (2H), -21.63 (2H), -23.93 (2H), -94.57 (2H, *H*C=N).

*4.8.13: Synthesis of (L)UO_2(Py) (**4.11**)*

To a 20-mL scintillation vial charged with 8 mL of pyridine and a small stir bar, (0.100 g, 0.114 mmol) of (L)$UCl_2(Py)_2$ (**4.1-(Py)**) was added. The opaque yellow suspension was allowed to mix thoroughly, after which approximately 11 equiv (0.088 g, 1.26 mmol) of $NaNO_2$ were added to the solution. After approximately 1 h of stirring, the color of the solution changed from yellow to orange. The resulting solution was allowed to stir overnight (~12 h) at 60°C. Volatiles were removed *in vacuo* to afford an orange solid. The crude product was then extracted with dichloromethane (~14 mL) and filtered over a bed of Celite on a frit and volatiles were removed *in vacuo* to afford a bright-orange solid. **Yield: 0.087 g, quantitative yield**. The product was recrystallized slowly from $CDCl_3$ at room temperature as orange plate crystals. ^{1}H NMR (300 MHz, $CDCl_3$, 298 K): δ = 10.81 (2H, Py), 9.26 (s, 2H, *H*C=N), 8.03 (1H, Py), 7.83 (2H, Py), 7.13

(d, 2H, $^{3}J_{HH}$ = 8 Hz, Ar-*H*), 7.11 (d, 2H, $^{3}J_{HH}$ = 8 Hz, Ar-*H*) 6.62 (t, 2H, $^{3}J_{HH}$ = 8 Hz, Ar-*H*), 4.15 (q, 4H, $^{3}J_{HH}$ = 7 Hz, OC*H*$_2$CH$_3$), 2.51 (m, 2H, cyclohexyl), 2.12 (m, 2H, cyclohexyl), 1.93 (m, 2H, cyclohexyl), 1.58 (m, 2H, cyclohexyl) 1.53 (t, 6H, $^{3}J_{HH}$ = 8 Hz, OCH$_2$C*H*$_3$). ^{13}C NMR (100 MHz, $CDCl_3$, 298 K): δ = 165.84 (*C*=N), 159.68 (Ar-*C*), 150.62 (Ar-*C*), 125.76 (Ar-*C*), 123.83 (Ar-*C*), 117.02 (Ar-*C*), 116.47 (Ar-*C*), 71.04 (cyclohexyl), 64.34 (O*C*H$_2$CH$_3$), 32.11 (cyclohexyl), 25.14 (cyclohexyl), 15.44 (OCH$_2$*C*H$_3$). Elemental analysis of (L)UO_2(Py)•(2 $CDCl_3$): Theoretical: C: 37.33, H: 3.64, N: 4.21; Actual: C: 36.88, H: 3.64, N: 4.18.

4.9: References

1. La Pierre, H. S.; Meyer, K., Uranium-Ligand Multiple Bonding in Uranyl Analogues, L=U=L (n+), and the Inverse Trans Influence. *Inorg. Chem.* **2013,** *52* (2), 529-539.

2. Thomson, R. K.; Cantat, T.; Scott, B. L.; Morris, D. E.; Batista, E. R.; Kiplinger, J. L., Uranium azide photolysis results in C-H bond activation and provides evidence for a terminal uranium nitride. *Nat. Chem.* **2010,** *2* (9), 723-729.

3. King, D. M.; Gardner, B. M.; Lewis, W.; Liddle, S. T., Uranium halide complexes stabilized by a new sterically demanding tripodal tris(N-adamantylamidodimethylsilyl)methane ligand. *J. Coord. Chem.* **2016,** *69* (11-13), 1893-1903.

4. Blackman, A. G., Overcoming the chelate effect: hypodentate coordination of common multidentate amine ligands. *C. R. Chim.* **2005,** *8* (2), 107-119.

5. Constable, E. C.; Zhang, G.; Housecroft, C. E.; Neuburger, M.; Schaffner, S., Hierarchical multicomponent assembly utilizing sequential metal-ligand and hydrogen-bonding interactions. *CrystEngComm* **2009,** *11* (4), 657-662.

6. Cozzi, P. G., Metal-Salen Schiff base complexes in catalysis: practical aspects. *Chem. Soc. Rev.* **2004,** *33* (7), 410-421.

7. Gupta, K. C.; Sutar, A. K., Catalytic activities of Schiff base transition metal complexes. *Coordin. Chem. Rev.* **2008,** *252* (12-14), 1420-1450.

8. Leung, A. C. W.; MacLachlan, M. J., Schiff base complexes in macromolecules. *J. Inorg. Organomet. Polym. Mater.* **2007,** *17* (1), 57-89.

9. Clarke, R. M.; Storr, T., The chemistry and applications of multimetallic salen complexes. *Dalton Trans.* **2014,** *43* (25), 9380-9391.

10. Mihara, H.; Xu, Y. J.; Shepherd, N. E.; Matsunaga, S.; Shibasaki, M., A Heterobimetallic Ga/Yb-Schiff Base Complex for Catalytic Asymmetric alpha-Addition of Isocyanides to Aldehydes. *J. Am. Chem. Soc.* **2009,** *131* (24), 8384-8385.

11. Bernardo, K.; Leppard, S.; Robert, A.; Commenges, G.; Dahan, F.; Meunier, B., Synthesis and characterization of new chiral Schiff base complexes with diiminobinaphthyl or diiminocyclohexyl moieties as potential enantioselective epoxidation catalysts. *Inorg. Chem.* **1996,** *35* (2), 387-396.

12. Handa, S.; Gnanadesikan, V.; Matsunaga, S.; Shibasaki, M., syn-selective catalytic asymmetric nitro-Mannich reactions using a heterobimetallic Cu-Sm-Schiff base complex. *J. Am. Chem. Soc.* **2007,** *129* (16), 4900-4901.

13. Li, Z.; Fernandez, M.; Jacobsen, E. N., Enantioselective ring opening of meso aziridines catalyzed by tridentate Schiff base chromium(III) complexes. *Org. Lett.* **1999,** *1* (10), 1611-1613.

14. Handa, S.; Nagawa, K.; Sohtome, Y.; Matsunaga, S.; Shibasaki, M., A heterobimetallic Pd/La/Schiff base complex for anti-selective catalytic asymmetric nitroaldol reactions and applications to short syntheses of beta-adrenoceptor agonists. *Angew. Chem. Int. Ed.* **2008,** *47* (17), 3230-3233.

15. Handa, S.; Gnanadesikan, V.; Matsunaga, S.; Shibasaki, M., Heterobimetallic Transition Metal/Rare Earth Metal Bifunctional Catalysis: A Cu/Sm/Schiff Base Complex for Syn-Selective Catalytic Asymmetric Nitro-Mannich Reaction. *J. Am. Chem. Soc.* **2010,** *132* (13), 4925-4934.

16. Ismail, M. B.; Booysen, I. N.; Akerman, M. P., Oxorhenium(V) complexes with bidentate carbohydrazide Schiff bases: synthesis, characterization and DNA interaction studies. *Transit. Metal Chem.* **2017,** *42* (5), 405-412.

17. McInnes, J. M.; Swallow, D.; Blake, A. J.; Mountford, P., Titanium imido complexes with tetradentate Schiff base ligands. *Inorg. Chem.* **1998,** *37* (23), 5970-5977.

18. Hayton, T. W., Recent developments in actinide-ligand multiple bonding. *Chem. Commun.* **2013,** *49* (29), 2956-2973.

19. Herasymchuk, K.; Chiang, L.; Hayes, C. E.; Brown, M. L.; Ovens, J. S.; Patrick, B. O.; Leznoff, D. B.; Storr, T., Synthesis and electronic structure determination of uranium(VI) ligand radical complexes. *Dalton Trans.* **2016,** *45* (31), 12576-12586.

20. Love, J. B., A macrocyclic approach to transition metal and uranyl Pacman complexes. *Chem. Commun.* **2009,** (22), 3154-3165.

21. Dalla Cort, A.; Pasquini, C.; Schiaffino, L., Nonsymmetrically substituted uranyl-salophen receptors: New opportunities for molecular recognition and catalysis. *Supramol. Chem.* **2007,** *19* (1-2), 79-87.

22. Calderazzo, F.; Floriani, C.; Pasquali, M.; Cesari, M.; Perego, G., Bis-*N*,*N*'-ethylenebis(salicylideneiminato) complexes of titanium(IV), thorium(IV) and uranium(IV), their redistribution reactions and structures of some of mixed compounds. *Gazz. Chim. Ital.* **1976,** *106* (1-2), 127-137.

23. Camp, C.; Andrez, J.; Pecaut, J.; Mazzanti, M., Synthesis of Electron-Rich Uranium(IV) Complexes Supported by Tridentate Schiff Base Ligands and Their Multi-Electron Redox Chemistry. *Inorg. Chem.* **2013,** *52* (12), 7078-7086.

24. Le Borgne, T.; Riviere, E.; Marrot, J.; Thuery, P.; Girerd, J. J.; Ephritikhine, M., Syntheses, X-ray crystal structures, and magnetic properties of novel linear (M2UIV)-U-II complexes (M = Co, Ni, Cu, Zn). *Chem. Eur. J.* **2002,** *8* (4), 774-783.

25. Salmon, L.; Thuery, P.; Ephritikhine, M., Synthesis and crystal structure of tetra-and hexanuclear uranium(IV) complexes with hexadentate compartmental Schiff-base ligands. *Dalton Trans.* **2004,** (24), 4139-4145.

26. Salmon, L.; Thuery, P.; Ephritikhine, M., Strictly heterodinuclear compounds containing U4+ and Cu2+ or Ni2+ ions. *Polyhedron* **2007,** *26* (3), 645-652.

27. Graves, C. R.; Vaughn, A. E.; Schelter, E. J.; Scott, B. L.; Thompson, J. D.; Morris, D. E.; Kiplinger, J. L., Probing the Chemistry, Electronic Structure and Redox Energetics in Organometallic Pentavalent Uranium Complexes. *Inorg. Chem.* **2008,** *47* (24), 11879-11891.

28. Kozimor, S. A.; Yang, P.; Batista, E. R.; Boland, K. S.; Burns, C. J.; Clark, D. L.; Conradson, S. D.; Martin, R. L.; Wilkerson, M. P.; Wolfsberg, L. E., Trends in Covalency for d- and f-Element Metallocene Dichlorides Identified Using Chlorine K-Edge X-ray Absorption Spectroscopy and Time-Dependent Density Functional Theory. *J. Am. Chem. Soc.* **2009,** *131* (34), 12125-12136.

29. Stobbe, B. C.; Powell, D. R.; Thomson, R. K., Schiff base thorium(IV) and uranium(IV) chloro complexes: synthesis, substitution and oxidation chemistry. *Dalton Trans.* **2017,** *46* (15), 4888-4892.

30. Dame, A. N.; Bharara, M. S.; Barnes, C. L.; Walensky, J. R., Synthesis of Thorium(IV) and Uranium(IV) Salicylaldiminate Pseudo-Halide Complexes. *Eur. J. Inorg. Chem.* **2015,** *2015* (18), 2996-3005.

31. *CRC Handbook of Chemistry and Physics*, 94th ed.; Haynes, W. CRC Press: Boca Raton, FL, 2013.

32. Andersen, R. A., Tris((hexamethyldisilyl)amido)uranium(III) - Preparation and coordination chemistry. *Inorg. Chem.* **1979,** *18* (6), 1507-1509.

33. Herve, A.; Bouzidi, Y.; Berthet, J. C.; Belkhiri, L.; Thuery, P.; Boucekkine, A.; Ephritikhine, M., U-III-CN versus U-IV-NC Coordination in Tris(silylamide) Complexes. *Inorg. Chem.* **2015,** *54* (5), 2474-2490.

34. Kawai, M.; Yamaguchi, T.; Masaoka, S.; Tani, F.; Kohzuma, T.; Chiang, L.; Storr, T.; Mieda, K.; Ogura, T.; Szilagyi, R. K.; Shimazaki, Y., Influence of Ligand Flexibility on the Electronic Structure of Oxidized Ni-III-Phenoxide Complexes. *Inorg. Chem.* **2014,** *53* (19), 10195-10202.

35. Dunn, T. J.; Ramogida, C. F.; Simmonds, C.; Paterson, A.; Wong, E. W. Y.; Chiang, L.; Shimazaki, Y.; Storr, T., Non-Innocent Ligand Behavior of a Bimetallic Ni Schiff-Base Complex Containing a Bridging Catecholate. *Inorg. Chem.* **2011,** *50* (14), 6746-6755.

36. Storr, T.; Verma, P.; Pratt, R. C.; Wasinger, E. C.; Shimazaki, Y.; Stack, T. D. P., Defining the Electronic and Geometric Structure of One-Electron Oxidized Copper-Bis-phenoxide Complexes. *J. Am. Chem. Soc.* **2008,** *130* (46), 15448-15459.

37. Storr, T.; Wasinger, E. C.; Pratt, R. C.; Stack, T. D. P., The geometric and electronic structure of a one-electron-oxidized nickel(II) bis(salicylidene)diamine complex. *Angew. Chem. Int. Ed.* **2007,** *46* (27), 5198-5201.

38. Pankhurst, J. R.; Bell, N. L.; Zegke, M.; Platts, L. N.; Lamfsus, C. A.; Maron, L.; Natrajan, L. S.; Sproules, S.; Arnold, P. L.; Love, J. B., Inner-sphere vs. outer-sphere reduction of uranyl supported by a redox-active, donor-expanded dipyrrin. *Chem. Sci.* **2017,** *8* (1), 108-116.

39. Kiernicki, J. J.; Cladis, D. P.; Fanwick, P. E.; Zeller, M.; Bart, S. C., Synthesis, Characterization, and Stoichiometric U-O Bond Scission in Uranyl Species Supported by Pyridine(diimine) Ligand Radicals. *J. Am. Chem. Soc.* **2015,** *137* (34), 11115-11125.

40. Kiernicki, J. J.; Ferrier, M. G.; Pacheco, J. S. L.; La Pierre, H. S.; Stein, B. W.; Zeller, M.; Kozimor, S. A.; Bart, S. C., Examining the Effects of Ligand Variation on the Electronic Structure of Uranium Bis(imido) Species. *J. Am. Chem. Soc.* **2016,** *138* (42), 13941-13951.

41. Anderson, N. H.; Odoh, S. O.; Williams, U. J.; Lewis, A. J.; Wagner, G. L.; Pacheco, J. L.; Kozimor, S. A.; Gagliardi, L.; Schelter, E. J.; Bart, S. C., Investigation of the Electronic Ground States for a Reduced Pyridine(diimine) Uranium Series: Evidence for a Ligand Tetraanion Stabilized by a Uranium Dimer. *J. Am. Chem. Soc.* **2015,** *137* (14), 4690-4700.

42. Kiernicki, J. J.; Newell, B. S.; Matson, E. M.; Anderson, N. H.; Fanwick, P. E.; Shores, M. P.; Bart, S. C., Multielectron C-O Bond Activation Mediated by a Family of Reduced Uranium Complexes. *Inorg. Chem.* **2014,** *53* (7), 3730-3741.

43. Anderson, N. H.; Odoh, S. O.; Yao, Y.; Williams, U. J.; Schaefer, B. A.; Kiernicki, J. J.; Lewis, A. J.; Goshert, M. D.; Fanwick, P. E.; Schelter, E. J.; Walensky, J. R.; Gagliardi, L.; Bart, S. C., Harnessing redox activity for the formation of uranium tris(imido) compounds. *Nat. Chem.* **2014,** *6* (10), 919-926.

44. Cladis, D. P.; Kiernicki, J. J.; Fanwick, P. E.; Bart, S. C., Multi-electron reduction facilitated by a trianionic pyridine(diimine) ligand. *Chem. Commun.* **2013,** *49* (39), 4169-4171.

45. Kraft, S. J.; Fanwick, P. E.; Bart, S. C., Carbon-Carbon Reductive Elimination from Homoleptic Uranium(IV) Alkyls Induced by Redox-Active Ligands. *J. Am. Chem. Soc.* **2012,** *134* (14), 6160-6168.

46. Fortier, S.; Wu, G.; Hayton, T. W., U(IV) and U(V) azide complexes supported by amide or aryloxide ligands. *Dalton Trans.* **2010,** *39* (2), 352-354.

47. Nocton, G.; Pecaut, J.; Mazzanti, M., A nitrido-centered uranium azido cluster obtained from a uranium azide. *Angew. Chem. Int. Ed.* **2008,** *47* (16), 3040-3042.

48. Evans, W. J.; Kozimor, S. A.; Ziller, J. W., Molecular octa-uranium rings with alternating nitride and azide bridges. *Science* **2005,** *309* (5742), 1835-1838.

49. Crawford, M. J.; Ellern, A.; Mayer, P., UN213-: A structurally characterized binary actinide heptaazide anion. *Angew. Chem. Int. Ed.* **2005,** *44* (48), 7874-7878.

50. Maria, L.; Santos, I. C.; Sousa, V. R.; Marcalo, J., Uranium(III) Redox Chemistry Assisted by a Hemilabile Bis(phenolate) Cyclam Ligand: Uranium-Nitrogen Multiple Bond Formation Comprising a trans-{RN=U(VI)=NR}(2+) Complex. *Inorg. Chem.* **2015,** *54* (18), 9115-9126.

51. Benaud, O.; Berthet, J. C.; Thuery, P.; Ephritikhine, M., The Bis Metallacyclic Anion $[U(N\{SiMe_3\}_2)(CH_2SiMe_2N\{SiMe_3\})_2]^-$. *Inorg. Chem.* **2010,** *49* (17), 8117-8130.

52. Maynadie, J.; Berthet, J. C.; Thuery, P.; Ephritikhine, M., An unprecedented type of linear metallocene with an f-element. *J. Am. Chem. Soc.* **2006,** *128* (4), 1082-1083.

53. Maynadie, J.; Berthet, J. C.; Thuery, P.; Ephritikhine, M., Bent and linear Uranium(IV) metallocenes with terminal and bridging cyanide ligands. *Organometallics* **2007,** *26* (18), 4585-4591.

54. Maynadie, J.; Barros, N.; Berthet, J. C.; Thuery, P.; Maron, L.; Ephritikhine, M., The crucial role of the f electrons in the bent or linear configuration of uranium cyanido metallocenes. *Angew. Chem Int. Edit.* **2007,** *46* (12), 2010-2012.

55. Thomson, R. K.; Scott, B. L.; Morris, D. E.; Kiplinger, J. L., Synthesis, structure, spectroscopy and redox energetics of a series of uranium(IV) mixed-ligand metallocene complexes. *C. R. Chimie* **2010,** *13* (6-7), 790-802.

56. Graves, C. R.; Schelter, E. J.; Cantat, T.; Scott, B. L.; Kiplinger, J. L., A Mild Protocol To Generate Uranium(IV) Mixed-Ligand Metallocene Complexes using Copper(I) Iodide. *Organometallics* **2008,** *27* (20), 5371-5378.

57. Lichtscheidl, A. G.; Pagano, J. K.; Scott, B. L.; Nelson, A. T.; Kiplinger, J. L., Expanding the Chemistry of Actinide Metallocene Bromides. Synthesis, Properties and Molecular Structures of the Tetravalent and Trivalent Uranium Bromide Complexes: (C5Me4R)(2)UBr2, (C5Me4R)(2)U(O-2,6-(Pr2C6H3)-Pr-i)(Br), and K(THF) (C5Me4R)(2)UBr2 (R = Me, Et). *Inorganics* **2016,** *4* (1), 1-17.

58. Ren, W. S.; Zi, G. F.; Fang, D. C.; Walter, M. D., Thorium Oxo and Sulfido Metallocenes: Synthesis, Structure, Reactivity, and Computational Studies. *J. Am. Chem. Soc.* **2011,** *133* (33), 13183-13196.

59. Ren, W. S.; Zi, G. F.; Walter, M. D., Synthesis, Structure, and Reactivity of a Thorium Metallocene Containing a 2,2 '-Bipyridyl Ligand. *Organometallics* **2012,** *31* (2), 672-679.

60. Bharara, M. S.; Heflin, K.; Tonks, S.; Strawbridge, K. L.; Gorden, A. E. V., Hydroxy- and alkoxy-bridged dinuclear uranyl-Schiff base complexes: hydrolysis, transamination and extraction studies. *Dalton Trans.* **2008,** (22), 2966-2973.

61. Mougel, V.; Horeglad, P.; Nocton, G.; Pecaut, J.; Mazzanti, M., Cation-Cation Complexes of Pentavalent Uranyl: From Disproportionation Intermediates to Stable Clusters. *Chem. Eur. J.* **2010,** *16* (48), 14365-14377.

62. Lewis, A. J.; Carroll, P. J.; Schelter, E. J., Reductive Cleavage of Nitrite to Form Terminal Uranium Mono-Oxo Complexes. *J. Am. Chem. Soc.* **2013,** *135* (1), 511-518.

63. Arnold, P. L.; Love, J. B.; Patel, D., Pentavalent uranyl complexes. *Coordin. Chem. Rev.* **2009,** *253* (15-16), 1973-1978.

64. Fortier, S.; Hayton, T. W., Oxo ligand functionalization in the uranyl ion (UO22+). *Coordin. Chem. Rev.* **2010,** *254* (3-4), 197-214.

65. Arney, D. S. J.; Schnabel, R. C.; Scott, B. C.; Burns, C. J., Preparation of actinide phosphinidene complexes: Steric control of reactivity. *J. Am. Chem. Soc.* **1996,** *118* (28), 6780-6781.

66. Gardner, B. M.; Balazs, G.; Scheer, M.; Tuna, F.; McInnes, E. J. L.; McMaster, J.; Lewis, W.; Blake, A. J.; Liddle, S. T., Triamidoamine-Uranium(IV)-Stabilized Terminal Parent Phosphide and Phosphinidene Complexes. *Angew. Chem Int. Edit.* **2014,** *53* (17), 4484-4488.

67. Duttera, M. R.; Day, V. W.; Marks, T. J., Organoactinide phosphine phosphite coordination chemistry - Facile hydride-induced dealkoxylation and the formation of actinide phosphinidene complexes. *J. Am. Chem. Soc.* **1984,** *106* (10), 2907-2912.

68. World Nuclear Association. Advanced Nuclear Power Reactors. 2017. http://www.world-nuclear.org/information-library/nuclear-fuel-cycle/nuclear-power-reactors/advanced-nuclear-power-reactors.aspx (Accessed June 12, 2017).

69. World Nuclear Association. Nuclear Fuel and Its Fabrication. 2017. http://www.world-nuclear.org/information-library/nuclear-fuel-cycle/conversion-enrichment-and-fabrication/fuel-fabrication.aspx (Accessed June 12, 2017).

70. King, D. M.; Tuna, F.; McInnes, E. J. L.; McMaster, J.; Lewis, W.; Blake, A. J.; Liddle, S. T., Synthesis and Structure of a Terminal Uranium Nitride Complex. *Science* **2012,** *337* (6095), 717-720.

71. King, D. M.; Tuna, F.; McInnes, E. J. L.; McMaster, J.; Lewis, W.; Blake, A. J.; Liddle, S. T., Isolation and characterization of a uranium(VI)-nitride triple bond. *Nat. Chem.* **2013,** *5* (6), 482-488.

72. King, D. M.; Liddle, S. T., Progress in molecular uranium-nitride chemistry. *Coord. Chem. Rev.* **2014,** *266*, 2-15.

73. Kiplinger, J. L.; Morris, D. E.; Scott, B. L.; Burns, C. J., Convenient synthesis, structure, and reactivity of (C5Me5)U(CH2C6H5)(3): a simple strategy for the preparation of monopentamethylcyclopentadienyl uranium(IV) complexes. *Organometallics* **2002,** *21* (26), 5978-5982.

74. Cantat, T.; Scott, B. L.; Kiplinger, J. L., Convenient access to the anhydrous thorium tetrachloride complexes ThCl4(DME)(2), ThCl4(1,4-

dioxane)(2) and ThCl4(THF)(3.5) using commercially available and inexpensive starting materials. *Chem. Commun.* **2010,** *46* (6), 919-921.

Appendix A

X-ray diffraction data for complexes described in Chapter 2

Table A-1: *X-ray diffraction data for $L_3U(I)$ (**2.1**)*

Empirical formula	$C_{33}\ H_{54}\ I\ N_3\ Si_3\ U$	
Formula weight	941.99	
Crystal system	monoclinic	
Space group	$P2_1/n$	
Unit cell dimensions	a = 11.5338(7) Å	α= 90°
	b = 17.3628(11) Å	β= 95.9269(8)°
	c = 20.1160(13) Å	γ= 90°
Volume	4006.9(4) $Å^3$	
Z, Z'	4, 1	
Density (calculated)	1.562 Mg/m^3	
Wavelength	0.71073 Å	
Temperature	100(2) K	
F(000)	1840	
Absorption coefficient	4.935 mm^{-1}	
Absorption correction	semi-empirical from equivalents	
Max. and min. transmission	0.360 and 0.169	
Theta range for data collection	1.553 to 25.809°	
Reflections collected	40798	
Independent reflections	7289 [R(int) = 0.0259]	
Data / restraints / parameters	7289 / 0 / 370	
$wR(F^2$ all data)	$wR2$ = 0.0424	
$R(F$ obsd data)	$R1$ = 0.0177	
Goodness-of-fit on F^2	0.994	
Observed data [I > 2σ(I)]	6485	
Largest and mean shift / s.u.	0.003and 0.000	
Largest diff. peak and hole	0.663 and -0.370 e/$Å^3$	

$wR2 = \{ \Sigma [w(F_o^2 - F_c^2)^2] / \Sigma [w(F_o^2)^2] \}^{1/2}$

$R1 = \Sigma ||F_o| - |F_c|| / \Sigma |F_o|$

Table A-2: *X-ray diffraction data for [Li(Cl)(THF)$_2$][L$_3$U(Cl)] (**2.2**)*

Empirical formula	$C_{41}H_{72.34}Cl_2LiN_3O_2Si_3U$	
Formula weight	1039.50	
Crystal system	monoclinic	
Space group	$P2_1/c$	
Unit cell dimensions	a = 16.8114(16) Å	α= 90°
	b = 13.3779(13) Å	β= 90.146(2)°
	c = 22.306(2) Å	γ= 90°
Volume	5016.6(8) Å^3	
Z, Z'	4, 1	
Density (calculated)	1.376 Mg/m^3	
Wavelength	0.71073 Å	
Temperature	100(2) K	
F(000)	2105	
Absorption coefficient	3.447 mm^{-1}	
Absorption correction	semi-empirical from equivalents	
Max. and min. transmission	0.445 and 0.267	
Theta range for data collection	1.775 to 28.377°	
Reflections collected	115200	
Independent reflections	12559 [R(int) = 0.0483]	
Data / restraints / parameters	12559 / 319 / 589	
$wR(F^2$ all data)	$wR2$ = 0.0995	
$R(F$ obsd data)	$R1$ = 0.0404	
Goodness-of-fit on F^2	1.006	
Observed data [I > 2σ(I)]	10125	
Largest and mean shift / s.u.	0.002and 0.000	
Largest diff. peak and hole	2.674 and -2.857 e/Å^3	

$wR2 = \{ \Sigma [w(F_o^2 - F_c^2)^2] / \Sigma [w(F_o^2)^2] \}^{1/2}$

$R1 = \Sigma ||F_o| - |F_c|| / \Sigma |F_o|$

Table A-3: *X-ray diffraction data for $L_2U(Br)(\mu\text{-}Br)_3U(Br)L_2$ (**2.5**)*

Empirical formula	$C_{52}\ H_{88}\ Br_5\ Li\ N_4\ O_2\ Si_4\ U_2$	
Formula weight	1796.17	
Crystal system	monoclinic	
Space group	$P2_1/n$	
Unit cell dimensions	a = 16.9688(7) Å	α= 90°
	b = 20.1935(8) Å	β= 90.0076(7)°
	c = 19.7887(8) Å	γ= 90°
Volume	6780.8(5) Å^3	
Z, Z'	4, 1	
Density (calculated)	1.759 Mg/m^3	
Wavelength	0.71073 Å	
Temperature	100(2) K	
F(000)	3448	
Absorption coefficient	7.824 mm^{-1}	
Absorption correction	semi-empirical from equivalents	
Max. and min. transmission	0.573 and 0.106	
Theta range for data collection	1.008 to 27.833°	
Reflections collected	130697	
Independent reflections	16080 [R(int) = 0.0567]	
Data / restraints / parameters	16080 / 17 / 642	
$wR(F^2$ all data)	$wR2$ = 0.0547	
$R(F$ obsd data)	$R1$ = 0.0235	
Goodness-of-fit on F^2	1.005	
Observed data [I > 2σ(I)]	13904	
Largest and mean shift / s.u.	0.006and 0.000	
Largest diff. peak and hole	1.266 and -0.880 e/Å^3	

$wR2 = \{ \Sigma [w(F_o^2 - F_c^2)^2] / \Sigma [w(F_o^2)^2] \}^{1/2}$

$R1 = \Sigma ||F_o| - |F_c|| / \Sigma |F_o|$

Table A-4: *X-ray diffraction data for U[L]$_4$ (**2.6**)*

Empirical formula	$C_{44}H_{72}N_4Si_4U$	
Formula weight	1007.44	
Crystal system	tetragonal	
Space group	$P4_2/n$	
Unit cell dimensions	a = 14.4091(11) Å	α= 90°
	b = 14.4091(11) Å	β= 90°
	c = 11.5639(9) Å	γ= 90°
Volume	2400.9(4) Å^3	
Z, Z'	2, 1/4	
Density (calculated)	1.394 Mg/m^3	
Wavelength	0.71073 Å	
Temperature	100(2) K	
F(000)	1024	
Absorption coefficient	3.513 mm^{-1}	
Absorption correction	semi-empirical from equivalents	
Max. and min. transmission	0.743 and 0.262	
Theta range for data collection	1.999 to 28.320°	
Reflections collected	46696	
Independent reflections	3000 [R(int) = 0.0304]	
Data / restraints / parameters	3000 / 0 / 120	
$wR(F^2$ all data)	$wR2$ = 0.0361	
$R(F$ obsd data)	$R1$ = 0.0134	
Goodness-of-fit on F^2	0.987	
Observed data [I > 2σ(I)]	2566	
Largest and mean shift / s.u.	0.001and 0.000	
Largest diff. peak and hole	0.432 and -0.281 e/Å^3	

$wR2 = \{ \Sigma [w(F_o^2 - F_c^2)^2] / \Sigma [w(F_o^2)^2] \}^{1/2}$

$R1 = \Sigma ||F_o| - |F_c|| / \Sigma |F_o|$

Table A-5: *X-ray diffraction data for Th[L]$_4$ (**2.7**)*

Empirical formula	$C_{44}H_{72}N_4Si_4Th$	
Formula weight	1001.45	
Crystal system	tetragonal	
Space group	$I\bar{4}$	
Unit cell dimensions	a = 14.4058(15) Å	α= 90°
	b = 14.4058(15) Å	β= 90°
	c = 11.6263(12) Å	γ= 90°
Volume	2412.8(6) Å^3	
Z, Z'	2, 0.25	
Density (calculated)	1.378 Mg/m^3	
Wavelength	0.71073 Å	
Temperature	100(2) K	
F(000)	1020	
Absorption coefficient	3.222 mm^{-1}	
Absorption correction	semi-empirical from equivalents	
Max. and min. transmission	0.661 and 0.382	
Theta range for data collection	1.999 to 31.583°	
Reflections collected	13669	
Independent reflections	3757 [R(int) = 0.0248]	
Data / restraints / parameters	3757 / 224 / 248	
$wR(F^2$ all data)	$wR2$ = 0.0312	
$R(F$ obsd data)	$R1$ = 0.0146	
Goodness-of-fit on F^2	1.001	
Observed data [I > 2σ(I)]	3755	
Absolute structure parameter	0.30(3)	
Largest and mean shift / s.u.	0.005and 0.001	
Largest diff. peak and hole	0.600 and -0.214 e/Å^3	

$wR2 = \{ \Sigma [w(F_o^2 - F_c^2)^2] / \Sigma [w(F_o^2)^2] \}^{1/2}$

$R1 = \Sigma ||F_o| - |F_c|| / \Sigma |F_o|$

Table A-6: *X-ray diffraction data for $[L]_3U(THF)$ (**2.8**)*

Empirical formula	$(C_{37}H_{62}N_3OSi_3U)\cdot 0.5(C_6H_{14})$	
	$C_{40}H_{69}N_3OSi_3U$	
Formula weight	930.28	
Crystal system	monoclinic	
Space group	$P2_1/n$	
Unit cell dimensions	a = 11.2221(6) Å	α= 90°
	b = 18.7614(11) Å	β= 91.2144(10)°
	c = 21.4558(12) Å	γ= 90°
Volume	4516.3(4) Å^3	
Z, Z'	4, 1	
Density (calculated)	1.368 Mg/m^3	
Wavelength	0.71073 Å	
Temperature	100(2) K	
F(000)	1888	
Absorption coefficient	3.704 mm^{-1}	
Absorption correction	semi-empirical from equivalents	
Max. and min. transmission	0.424 and 0.240	
Theta range for data collection	1.899 to 31.396°	
Reflections collected	99602	
Independent reflections	14202 [R(int) = 0.0495]	
Data / restraints / parameters	14202 / 0 / 433	
$wR(F^2$ all data)	$wR2$ = 0.0503	
$R(F$ obsd data)	$R1$ = 0.0255	
Goodness-of-fit on F^2	1.002	
Observed data [I > 2σ(I)]	11427	
Largest and mean shift / s.u.	0.006and 0.000	
Largest diff. peak and hole	1.500 and -1.158 e/Å^3	

$wR2 = \{ \Sigma [w(F_o^2 - F_c^2)^2] / \Sigma [w(F_o^2)^2] \}^{1/2}$

$R1 = \Sigma ||F_o| - |F_c|| / \Sigma |F_o|$

Appendix B

X-ray diffraction data for complex described in Chapter 3

Table B-1: *X-ray diffraction data for [K][BDPP′]U(CH$_2$Ph)$_2$ (**3.1**)*

Empirical formula	$K^+ (C_{52} H_{62} N_3 U)^- \cdot 3(C_4 H_8 O)$	
	$C_{64} H_{86} K N_3 O_3 U$	
Formula weight	1222.48	
Crystal system	monoclinic	
Space group	$P2_1/c$	
Unit cell dimensions	a = 25.307(3) Å	α= 90°
	b = 23.069(3) Å	β= 111.822(2)°
	c = 19.679(2) Å	γ= 90°
Volume	10665(2) Å^3	
Z, Z'	8, 2	
Density (calculated)	1.523 Mg/m^3	
Wavelength	0.71073 Å	
Temperature	100(2) K	
F(000)	5008	
Absorption coefficient	3.173 mm^{-1}	
Absorption correction	semi-empirical from equivalents	
Max. and min. transmission	0.584 and 0.493	
Theta range for data collection	1.734 to 25.959°	
Reflections collected	126423	
Independent reflections	19671 [R(int) = 0.0514]	
Data / restraints / parameters	19671 / 15 / 1027	
$wR(F^2$ all data)	$wR2$ = 0.1593	
$R(F$ obsd data)	$R1$ = 0.0428	
Goodness-of-fit on F^2	0.999	
Observed data [I > 2σ(I)]	11466	
Largest and mean shift / s.u.	0.001and 0.000	
Largest diff. peak and hole	2.995 and -1.399 e/Å^3	

$wR2 = \{ \Sigma [w(F_o^2 - F_c^2)^2] / \Sigma [w(F_o^2)^2] \}^{1/2}$

$R1 = \Sigma ||F_o| - |F_c|| / \Sigma |F_o|$

Appendix C

X-ray diffraction data for complexes described in Chapter 4

Table C-1: *X-ray diffraction data for (L)$UCl_2(Py)_2$ (**4.1-(Py)**)*

Empirical formula	C_{34} H_{38} Cl_2 N_4 O_4 U	
Formula weight	875.61	
Crystal system	monoclinic	
Space group	*C2/c*	
Unit cell dimensions	*a* = 19.233(6) Å	α= 90°
	b = 19.034(6) Å	β= 122.796(3)°
	c = 12.202(4) Å	γ= 90°
Volume	3755(2) $Å^3$	
Z, Z'	4, 0.5	
Density (calculated)	1.549 Mg/m^3	
Wavelength	0.71073 Å	
Temperature	100(2) K	
F(000)	1712	
Absorption coefficient	4.504 mm^{-1}	
Absorption correction	semi-empirical from equivalents	
Max. and min. transmission	0.687 and 0.411	
Theta range for data collection	1.653 to 27.517°	
Reflections collected	24171	
Independent reflections	4301 [R(int) = 0.0666]	
Data / restraints / parameters	4301 / 0 / 204	
wR(F^2 all data)	*wR*2 = 0.1424	
R(*F* obsd data)	*R*1 = 0.0424	
Goodness-of-fit on F^2	1.020	
Observed data [I > 2σ(I)]	3346	
Largest and mean shift / s.u.	0.000 and 0.000	
Largest diff. peak and hole	2.368 and -2.619 e/$Å^3$	

$wR2 = \{ \Sigma [w(F_o^2 - F_c^2)^2] / \Sigma [w(F_o^2)^2] \}^{1/2}$

$R1 = \Sigma ||F_o| - |F_c|| / \Sigma |F_o|$

Table C-2: *X-ray diffraction data for (L)ThCl$_2$(Py)$_2$ (**4.2-(Py)**)*

Empirical formula	$(C_{34}\ H_{38}\ Cl_2\ N_4\ O_4\ Th) \cdot (C_5\ H_5\ N)$	
	$C_{39}\ H_{43}\ Cl_2\ N_5\ O_4\ Th$	
Formula weight	948.72	
Crystal system	monoclinic	
Space group	$P2_1/c$	
Unit cell dimensions	a = 16.806(13) Å	α= 90°
	b = 14.283(11) Å	β= 92.515(14)°
	c = 15.268(12) Å	γ= 90°
Volume	3661(5) Å^3	
Z, Z'	4, 1	
Density (calculated)	1.721 Mg/m^3	
Wavelength	0.71073 Å	
Temperature	100(2) K	
F(000)	1872	
Absorption coefficient	4.267 mm^{-1}	
Absorption correction	semi-empirical from equivalents	
Max. and min. transmission	0.726 and 0.675	
Theta range for data collection	2.268 to 22.464°	
Reflections collected	85853	
Independent reflections	4595 [R(int) = 0.2301]	
Data / restraints / parameters	4595 / 493 / 462	
$wR(F^2$ all data)	$wR2$ = 0.2203	
$R(F$ obsd data)	$R1$ = 0.1052	
Goodness-of-fit on F^2	1.071	
Observed data [I > 2σ(I)]	2708	
Largest and mean shift / s.u.	0.004 and 0.000	
Largest diff. peak and hole	2.233 and -1.716 e/Å^3	

$wR2 = \{ \Sigma [w(F_o^2 - F_c^2)^2] / \Sigma [w(F_o^2)^2] \}^{1/2}$

$R1 = \Sigma ||F_o| - |F_c|| / \Sigma |F_o|$

Table C-3: *X-ray diffraction data for* endo-*(L)U(N_3)$_2$(Py)$_2$* (***4.3*-Endo**)

Empirical formula	C_{34} H_{38} N_{10} O_4 U	
Formula weight	888.77	
Crystal system	monoclinic	
Space group	$P2_1/c$	
Unit cell dimensions	a = 16.872(4) Å	α= 90°
	b = 15.338(3) Å	β= 93.301(2)°
	c = 15.062(3) Å	γ= 90°
Volume	3891.3(14) Å^3	
Z, Z'	4, 1	
Density (calculated)	1.517 Mg/m^3	
Wavelength	0.71073 Å	
Temperature	100(2) K	
F(000)	1744	
Absorption coefficient	4.219 mm^{-1}	
Absorption correction	semi-empirical from equivalents	
Max. and min. transmission	0.237 and 0.154	
Theta range for data collection	1.897 to 26.257°	
Reflections collected	81766	
Independent reflections	7117 [R(int) = 0.1176]	
Data / restraints / parameters	7117 / 0 / 442	
$wR(F^2$ all data)	$wR2$ = 0.1202	
$R(F$ obsd data)	$R1$ = 0.0468	
Goodness-of-fit on F^2	1.001	
Observed data [I > 2σ(I)]	4959	
Largest and mean shift / s.u.	0.003 and 0.000	
Largest diff. peak and hole	1.574 and -1.971 e/Å^3	

$wR2 = \{ \Sigma [w(F_o^2 - F_c^2)^2] / \Sigma [w(F_o^2)^2] \}^{1/2}$

$R1 = \Sigma ||F_o| - |F_c|| / \Sigma |F_o|$

Note: This sample was a 3-component twin. The intensity data were effectively detwinned by the data reduction and scaling programs. A dichloromethane molecule was severely disordered and was eliminated using the Squeeze program.

Table C-4: *X-ray diffraction data for* exo-*(L)U(N$_3$)$_2$(Py)$_2$* (***4.3*-Exo**)

Empirical formula	$(C_{34}\ H_{38}\ N_{10}\ O_4\ U) \cdot (C_7\ H_8)$	
	$C_{41}\ H_{46}\ N_{10}\ O_4\ U$	
Formula weight	980.91	
Crystal system	triclinic	
Space group	$P\bar{1}$	
Unit cell dimensions	a = 9.572(5) Å	α= 76.878(2)°
	b = 13.791(7) Å	β= 86.987(2)°
	c = 16.103(2) Å	γ= 71.973(2)°
Volume	1968.2(15) Å^3	
Z, Z'	2, 1	
Density (calculated)	1.655 Mg/m^3	
Wavelength	0.71073 Å	
Temperature	100(2) K	
F(000)	972	
Absorption coefficient	4.179 mm^{-1}	
Absorption correction	semi-empirical from equivalents	
Max. and min. transmission	0.680 and 0.279	
Theta range for data collection	1.299 to 31.673°	
Reflections collected	90881	
Independent reflections	11866 [R(int) = 0.0574]	
Data / restraints / parameters	11866 / 1149 / 648	
$wR(F^2$ all data)	$wR2$ = 0.0945	
$R(F$ obsd data)	$R1$ = 0.0420	
Goodness-of-fit on F^2	0.990	
Observed data [I > 2σ(I)]	9414	
Largest and mean shift / s.u.	0.003 and 0.000	
Largest diff. peak and hole	2.478 and -1.960 e/Å^3	

$wR2 = \{ \Sigma [w(F_o^2 - F_c^2)^2] / \Sigma [w(F_o^2)^2] \}^{1/2}$

$R1 = \Sigma ||F_o| - |F_c|| / \Sigma |F_o|$

Note: The selected crystal was split. The intensity data were corrected by data reduction and scaling programs. Three parts of the structure were disordered. The occupancies of atoms C(1) and C(2) refined to 0.727(8) and 0.273(8) for the unprimed and primed atoms, respectively. The occupancies of atoms C(10) – C(15) refined to 0.750(5) and 0.250(5) for the unprimed and primed atoms, respectively. The occupancies of the toluene molecule refined to 0.660(5) and 0.340(5) for the A- and B-labeled atoms, respectively. Restraints on the positional parameters of the disordered atoms and the displacement parameters of all atoms were required.

Table C-5: *X-ray diffraction data for (L)U(Cp*)(Cl)(1,4-dioxane) (**4.5**)*

Empirical formula	$(C_{38}\ H_{51}\ Cl\ N_2\ O_6\ U) \cdot (C_4\ H_8\ O_2)$	
	$C_{42}\ H_{59}\ Cl\ N_2\ O_8\ U$	
Formula weight	993.39	
Crystal system	monoclinic	
Space group	$P2_1/n$	
Unit cell dimensions	a = 12.0835(6) Å	α= 90°
	b = 14.5754(7) Å	β= 95.3391(7)°
	c = 23.9974(11) Å	γ= 90°
Volume	4208.1(3) Å^3	
Z, Z'	4, 1	
Density (calculated)	1.568 Mg/m^3	
Wavelength	0.71073 Å	
Temperature	100(2) K	
F(000)	1992	
Absorption coefficient	3.973 mm^{-1}	
Absorption correction	semi-empirical from equivalents	
Max. and min. transmission	0.890 and 0.314	
Theta range for data collection	1.637 to 27.512°	
Reflections collected	43219	
Independent reflections	9663 [R(int) = 0.0446]	
Data / restraints / parameters	9663 / 357 / 546	
$wR(F^2$ all data)	$wR2$ = 0.0592	
$R(F$ obsd data)	$R1$ = 0.0270	
Goodness-of-fit on F^2	1.031	
Observed data [I > 2σ(I)]	8266	
Largest and mean shift / s.u.	0.015 and 0.000	
Largest diff. peak and hole	0.998 and -1.123 e/Å^3	

$wR2 = \{ \Sigma [w(F_o^2 - F_c^2)^2] / \Sigma [w(F_o^2)^2] \}^{1/2}$

$R1 = \Sigma ||F_o| - |F_c|| / \Sigma |F_o|$

Table C-6: *X-ray diffraction data for (L)U(Cp)$_2$(1,4-dioxane) (**4.6**)*

Empirical formula	$(C_{36}\ H_{46}\ N_2O_6\ U) \cdot (C_4\ H_8\ O_2)$	
	$C_{42}\ H_{54}\ N_2\ O_8\ U$	
Formula weight	952.90	
Crystal system	orthorhombic	
Space group	*Pna*2$_1$	
Unit cell dimensions	*a* = 21.513(3) Å	α= 90°
	b = 14.6224(15) Å	β= 90°
	c = 12.4258(12) Å	γ= 90°
Volume	3908.8(8) Å^3	
Z, Z'	4, 1	
Density (calculated)	1.619 Mg/m^3	
Wavelength	0.71073 Å	
Temperature	100(2) K	
F(000)	1904	
Absorption coefficient	4.208 mm^{-1}	
Absorption correction	semi-empirical from equivalents	
Max. and min. transmission	0.678 and 0.419	
Theta range for data collection	1.684 to 26.105°	
Reflections collected	44600	
Independent reflections	7734 [R(int) = 0.0401]	
Data / restraints / parameters	7734 / 335 / 536	
wR(F^2 all data)	*wR*2 = 0.0634	
R(*F* obsd data)	*R*1 = 0.0281	
Goodness-of-fit on F^2	1.016	
Observed data [I > 2σ(I)]	6705	
Absolute structure parameter	0.355(9) (inversion twin)	
Largest and mean shift / s.u.	0.001 and 0.000	
Largest diff. peak and hole	1.100 and -0.873 e/Å^3	

$wR2 = \{ \Sigma [w(F_o^2 - F_c^2)^2] / \Sigma [w(F_o^2)^2] \}^{1/2}$

$R1 = \Sigma ||F_o| - |F_c|| / \Sigma |F_o|$

Table C-7: *X-ray diffraction data for (L)Th(Cp)$_2$(1,4-dioxane) (**4.7**)*

Empirical formula	$(C_{38}H_{46}N_2O_6Th)\cdot 2(C_4H_8O_2)$	
	$C_{46}H_{62}N_2O_{10}Th$	
Formula weight	1035.01	
Crystal system	monoclinic	
Space group	$P2_1/c$	
Unit cell dimensions	a = 20.5126(7) Å	α= 90°
	b = 8.6783(3) Å	β= 95.8909(6)°
	c = 24.3505(9) Å	γ= 90°
Volume	4311.9(3) Å^3	
Z, Z'	4, 1	
Density (calculated)	1.594 Mg/m^3	
Wavelength	0.71073 Å	
Temperature	100(2) K	
F(000)	2088	
Absorption coefficient	3.519 mm^{-1}	
Absorption correction	semi-empirical from equivalents	
Max. and min. transmission	0.639 and 0.307	
Theta range for data collection	0.998 to 27.507°	
Reflections collected	89233	
Independent reflections	9911 [R(int) = 0.0307]	
Data / restraints / parameters	9911 / 766 / 670	
$wR(F^2$ all data)	$wR2$ = 0.0907	
$R(F$ obsd data)	$R1$ = 0.0294	
Goodness-of-fit on F^2	1.029	
Observed data [I > 2σ(I)]	9308	
Largest and mean shift / s.u.	0.003 and 0.000	
Largest diff. peak and hole	1.475 and -2.295 e/Å^3	

$wR2 = \{ \Sigma [w(F_o^2 - F_c^2)^2] / \Sigma [w(F_o^2)^2] \}^{1/2}$

$R1 = \Sigma ||F_o| - |F_c|| / \Sigma |F_o|$

Table C-8: *X-ray diffraction data for (L)U(Br)$_2$(Py)$_2$ (**4.8**)*

Empirical formula	$(C_{34}\ H_{48}\ Br_2\ N_4\ O_4\ U) \cdot (C_6\ H_5\ Cl)$	
	$C_{40}\ H_{43}\ Br_2\ Cl\ N_4\ O_4\ U$	
Formula weight	1077.08	
Crystal system	monoclinic	
Space group	P 2_1/c	
Unit cell dimensions	*a* = 16.858(3) Å	α= 90°
	b = 14.828(2) Å	β= 92.136(2)°
	c = 15.810(2) Å	γ= 90°
Volume	3949.3(10) Å^3	
Z, Z'	4, 1	
Density (calculated)	1.812 Mg/m^3	
Wavelength	0.71073 Å	
Temperature	100(2) K	
F(000)	2088	
Absorption coefficient	6.247 mm^{-1}	
Absorption correction	semi-empirical from equivalents	
Max. and min. transmission	0.745 and 0.521	
Theta range for data collection	1.209 to 26.022°	
Reflections collected	57696	
Independent reflections	7616 [R(int) = 0.0588]	
Data / restraints / parameters	7616 / 0 / 469	
wR(F^2 all data)	*wR*2 = 0.1375	
R(*F* obsd data)	*R*1 = 0.0622	
Goodness-of-fit on F^2	0.989	
Observed data [I > 2σ(I)]	5296	
Largest and mean shift / s.u.	0.001 and 0.000	
Largest diff. peak and hole	1.850 and -2.709 e/Å^3	

$wR2 = \{ \Sigma [w(F_o^2 - F_c^2)^2] / \Sigma [w(F_o^2)^2] \}^{1/2}$

$R1 = \Sigma ||F_o| - |F_c|| / \Sigma |F_o|$

Table C-9: *X-ray diffraction data for (L)U(O)$_2$(Py) (**4.11**)*

Empirical formula	$(C_{29}\ H_{33}\ N_3\ O_6\ U) \cdot (C\ D\ Cl_3)$	
	$C_{30}\ H_{33}\ Cl_3\ D\ N_3\ O_6\ U$	
Formula weight	877.99	
Crystal system	monoclinic	
Space group	*C*2/*c*	
Unit cell dimensions	*a* = 27.313(4) Å	α= 90°
	b = 9.2102(13) Å	β= 97.694(2)°
	c = 26.618(4) Å	γ= 90°
Volume	6635.7(17) Å^3	
Z, Z'	8, 1	
Density (calculated)	1.758 Mg/m^3	
Wavelength	0.71073 Å	
Temperature	295(2) K	
F(000)	3408	
Absorption coefficient	5.179 mm^{-1}	
Absorption correction	semi-empirical from equivalents	
Max. and min. transmission	0.860 and 0.297	
Theta range for data collection	1.505 to 28.359°	
Reflections collected	76032	
Independent reflections	8293 [R(int) = 0.0561]	
Data / restraints / parameters	8293 / 38 / 433	
wR(F^2 all data)	*wR*2 = 0.1016	
R(*F* obsd data)	*R*1 = 0.0355	
Goodness-of-fit on F^2	0.977	
Observed data [I > 2σ(I)]	6454	
Largest and mean shift / s.u.	0.001 and 0.000	
Largest diff. peak and hole	1.579 and -1.017 e/Å^3	

$wR2 = \{ \Sigma [w(F_o^2 - F_c^2)^2] / \Sigma [w(F_o^2)^2] \}^{1/2}$

$R1 = \Sigma ||F_o| - |F_c|| / \Sigma |F_o|$

Table C-10: *X-ray diffraction data for (L)U(Cl)$(N_3)_2(Py)_2$* ***(4.12)***

Empirical formula	$(C_{34}\ H_{38}\ Cl_{0.75}\ N_{7.76}\ O_4\ U) \cdot (C_5\ H_5\ N)$	
	$C_{39}\ H_{43}\ Cl_{0.75}\ N_{8.76}\ O_4\ U$	
Formula weight	962.95	
Crystal system	monoclinic	
Space group	$P2_1/c$	
Unit cell dimensions	a = 16.922(2) Å	α= 90°
	b = 15.136(2) Å	β= 94.0682(19)°
	c = 15.0499(18) Å	γ= 90°
Volume	3845.0(8) Å^3	
Z, Z'	4, 1	
Density (calculated)	1.663 Mg/m^3	
Wavelength	0.71073 Å	
Temperature	100(2) K	
F(000)	1900	
Absorption coefficient	4.326 mm^{-1}	
Absorption correction	semi-empirical from equivalents	
Max. and min. transmission	0.494 and 0.270	
Theta range for data collection	1.206 to 26.022°	
Reflections collected	74558	
Independent reflections	7575 [R(int) = 0.0383]	
Data / restraints / parameters	7575 / 306 / 573	
$wR(F^2$ all data)	$wR2$ = 0.1030	
$R(F$ obsd data)	$R1$ = 0.0387	
Goodness-of-fit on F^2	1.104	
Observed data [I > 2σ(I)]	6499	
Largest and mean shift / s.u.	0.002 and 0.000	
Largest diff. peak and hole	2.181 and -1.449 e/Å^3	

$wR2 = \{ \Sigma [w(F_o^2 - F_c^2)^2] / \Sigma [w(F_o^2)^2] \}^{1/2}$

$R1 = \Sigma ||F_o| - |F_c|| / \Sigma |F_o|$

Note: The azide and chloride groups were disordered as well as the separate pyridine. The occupancies of N5, N6, and N7 refined to 0.508(13), and the occupancy of Cl1 refined to 0.492(13). The occupancy of N8, N9, and N10 refined to 0.743(12), and the occupancy of Cl2 refined to 0.257(12). The occupancies of N1M – C5M refined to 0.579(19) and 0.421(19) for the unprimed and primed atoms, respectively. Restraints on the positional and displacement parameters of all disordered atoms were required.